Field-resolved studies of ultrafast light-matter interaction

Johannes Schötz

München 2021

Field-resolved studies of ultrafast light-matter interaction

Johannes Schötz

Dissertation
an der Fakultät für Physik
der Ludwig–Maximilians–Universität
München

vorgelegt von
Johannes Schötz
aus Hof

München, den 15.06.2021

Erstgutachter: Prof. Dr. Matthias Kling
Zweitgutachter: Prof. Dr. Emiliano Cortés
Tag der mündlichen Prüfung: 27.09.2021

Contents

Zusammenfassung **xv**

1 Introduction **1**

2 Theoretical foundations **9**
2.1 Few-cycle pulses and dispersion 9
2.2 Strong-field photoemission 11
2.2.1 Emission regimes 11
2.2.2 Simpleman's model 14
2.2.3 Strong-field photoemission spectra 17
2.3 High-harmonic generation 19
2.3.1 Phase matching of HHG 21
2.3.2 Phase-matching cutoff and critical ionization fraction 23
2.3.3 Gating techniques for isolated attosecond pulse generation 27
2.4 Field enhancement and confinement on nanotips 29

3 Experimental foundations **33**
3.1 Nanotip etching 33
3.2 Current measurements 34
3.2.1 Transimpedance amplification 34
3.2.2 Lock-in detection 35
3.3 Field-resolved measurement techniques 37
3.3.1 Attosecond streaking 37
3.3.2 Electro-Optic Sampling 41
3.3.3 Tunneling ionization with a perturbation for the time-domain observation of an electric field (TIPTOE) 43
3.3.4 Streaking of rescattering electrons 45
3.3.5 Nonlinear photoconductive sampling 47

4 The emergence of macroscopic optical-field-controlled currents in gases **49**
4.1 Classification of plasma regimes 51
4.2 Experimental setup and approach 52
4.3 Theoretical model and simulations 55

4.4 Experimental results . . . 61
4.5 Discussion . . . 64
4.6 Conclusion . . . 68

5 Transient field-resolved reflectometry from solid-state surfaces 71
5.1 Experimental foundations . . . 73
5.2 Theoretical background . . . 77
5.3 Experimental results . . . 84
5.3.1 Surface recombination dynamics in GaAs . . . 84
5.3.2 Buildup of collective excitations in GaAs . . . 86
5.3.3 Intervalley scattering in Ge . . . 88
5.3.4 Excitation-density dependence of the Drude scattering rate . . . 91
5.4 Conclusion and Outlook . . . 94

6 Phase matching of HHG with ionization reshaped few-cycle pulses 97
6.1 Introduction . . . 97
6.2 Experimental section . . . 99
6.2.1 Experimental setup . . . 99
6.2.2 Experimental approach . . . 101
6.2.3 Experimental results . . . 103
6.3 Theoretical modeling and analysis . . . 104
6.4 Discussion of the results . . . 106
6.4.1 Effects of the overdriven regime on HHG . . . 106
6.4.2 Phase matching in the overdriven regime . . . 110
6.4.3 Pressure and intensity variation . . . 114
6.5 Phase matching in the overdriven regime with long wavelength driving pulses 115
6.6 Conclusion . . . 122

7 Attosecond physics on metallic nanotips 125
7.1 Introduction . . . 125
7.2 Attosecond streaking from a metal nanotip . . . 128
7.2.1 Experimental setup and approach . . . 128
7.2.2 Theoretical approach . . . 129
7.2.3 Experimental results . . . 135
7.2.4 Discussion . . . 137
7.2.5 Conclusion and Outlook . . . 140
7.3 Attosecond field-resolved measurements using photocurrents . . . 142
7.3.1 Experimental setup . . . 142
7.3.2 Experimental approach . . . 144
7.3.3 Onset of space-charge effects . . . 145
7.3.4 Characterization of near fields at the apex of a nanotip . . . 152
7.3.5 Field and spatially resolved measurements of an OAM beam . . . 162
7.4 Discussion . . . 164

7.5 Conclusion and Outlook 167

A Dual-frequency demodulation 169

List of Figures

1.1 Attosecond field-resolved measurement techniques 3

2.1 Carrier-envelope phase 10
2.2 Strong-field photoemission 13
2.3 Simpleman's model 14
2.4 Above-threshold ionization photoemission spectrum 17
2.5 Rescattering trajectories and high-harmonic generation 19
2.6 Phase matching of HHG 22
2.7 Phase-matching cutoff of HHG 24
2.8 HHG dipole phase 25
2.9 HHG gating mechanisms for isolated attosecond pulse generation 28
2.10 Field enhancement on a nanotip 29

3.1 Nanotip etching process 33
3.2 Microscope image of a nanotip 34
3.3 Transimpedance amplifier 34
3.4 Attosecond streaking scheme 36
3.5 Attosecond streaking scheme 38
3.6 Streaking spectrogram of chirped XUV pulses 39
3.7 Electro-optic sampling 42
3.8 CEP-dependence of the current response function 44
3.9 Response function of the scattering cutoff variation 46
3.10 CEP-dependence of the current response fucntion 47

4.1 Classification of plasmas 51
4.2 Experimental setup and signal 53
4.3 Images of the electrodes 54
4.4 Homogeneous and inhomogeneous solution of the Poisson equation 55
4.5 Signal induction and Ramo-Shockley weighting potentials 56
4.6 Scattering and Coulomb-interaction 58
4.7 Microscopic origin of the signal in the simpleman's model 60
4.8 Pressure dependence 61
4.9 Electrode-distance dependence 62

4.10 Intensity dependence and signal trace reshaping 63
4.11 Role of scattering and Coulomb-interaction 65

5.1 Laser setup and pulse characterization 73
5.2 Experimental scheme and setup 74
5.3 Experimental pump-probe signal 76
5.4 Bandstructure of GaAs and Ge 78
5.5 Photoexcitation processes and timescales 79
5.6 Effect of an inhomogeneous excitation profile on the reflected field 82
5.7 Influence of surface recombination in GaAs 84
5.8 Femtosecond reflectivity buildup on GaAs 87
5.9 Intervalley scattering in Germanium 89
5.10 Scattering rates in Germanium 92
5.11 Transient reflectivity change from a graphene sample 94

6.1 Experimental setup 100
6.2 Experimental attosecond streaking spectrograms in argon and neon 102
6.3 Reconstructed streaking spectrograms and retrieved attosecond pulses . . . 105
6.4 Spatio-temporal pulse reshaping 107
6.5 Experimental signatures of pulse reshaping 107
6.6 Simulation of the XUV generation in argon and driving laser pulse evolution 108
6.7 Transient phase matching and XUV buildup 111
6.8 CEP-dependence of isolated attosecond pulse generation in argon 113
6.9 Intensity dependence 114
6.10 Pressure-dependence of the HHG process 115
6.11 Pulse-reshaping in the overdriven regime 116
6.12 Pressure-scaling of the HHG yield and phase-matching contributions 117
6.13 CEP-dependence and isolated pulse generation in helium 119
6.14 Spatio-temporal phase-matching map 121
6.15 Pulsefront and -profile reshaping in the overdriven regime 121

7.1 Experimental setup and approach for attosecond streaking experiments from a nanotaper 130
7.2 Attosecond streaking response function and surface field sensitivity in inhomogeneous fields 133
7.3 Attosecond streaking spectrograms from a nanotaper and reference gas . . 136
7.4 Reconstructed response function of the nanotaper 139
7.5 Experimental setup and approach for current detection from a nanotip . . 144
7.6 Energy-resolved electron spectra and charge interaction effects 146
7.7 Charge-interaction effects on the photoelectron spectral cutoff 148
7.8 Energy resolved CEP-asymmetry 149
7.9 Experimental signal and polarization dependence 152
7.10 Driving pulse characterization and optimization 153

7.11 CEP-dependence of the response function 155
7.12 Intensity dependence of pump and driving signal 157
7.13 Energy-resolved pump-probe spectra 160
7.14 Signal trace from an OAM driving beam 162
7.15 Spatially resolved measurement of an OAM beam 164
7.16 Spatio-temporally/-spectrally resolved measurement of an OAM beam . . . 165

A.1 Dual-frequency demodulation 169

List of Tables

5.1 Effective masses for Ge and GaAs 78

Abstract

The fastest light-matter interactions between electrons and optical laser pulses occur on attosecond timescales below the half-cycle oscillation period of the electric field. The investigation of such ultrafast processes and ultimately their control, therefore, requires field-resolved measurements. In this work, the understanding of well-established and newly emerging sub-cycle-resolved techniques for the characterization of optical pulses and ultrafast light-induced processes is expanded and the application of the methods includes gases, bulk solids, and nanostructures.

In the first part, the mechanism behind the macroscopic current generation in optical field-induced photocurrent measurements in gases is studied theoretically and experimentally. A rigorous model is developed that connects the measured current to the microscopic movement of charge carriers and includes scattering with atoms and the interaction of charges via the Coulomb force. The model is validated against an extensive set of experiments which measure the carrier-envelope-phase dependent strong-field photoemitted current induced on a pair of electrodes surrounding the focus of a few-cycle laser pulse. The role of the mean-free path as well as the Coulomb interaction is identified. The model provides a fundamental understanding of the signal generation mechanism in photoconductive sampling of laser pulses which had been missing before and which will allow to identify fundamental limitations and strategies for further optimization of the detection.

The second set of experiments aims at the transient change of the reflectivity after excitation with a near-infrared pump pulse. Electro-optic sampling is used for the field-resolved characterization of the mid-infrared probe pulses which covers a wavelength range from below $3\,\mu$m to above $6\,\mu$m. Measurements on semiconductors are performed and dynamics occuring on the femtosecond to the picosecond timescale after photoexcitation are studied. The demonstrated experiments represent an important milestone in pushing field-sampling methods from the THz into the PHz domain.

The investigation of the generation of isolated attosecond pulses in the extreme ultraviolet photon energy range using high-harmonic generation (HHG) in noble gases is the topic of the third section. The focus is put on the overdriven regime, where the driving laser undergoes severe reshaping due to plasma effects. Experimentally, attosecond streaking is used to demonstrate isolated attosecond pulses for the first time in this regime. Theoretically, the phasematching mechanism in this regime is studied using extensive numerical simulations. An extension of conventional phasematching expressions is introduced which describes the contribution of the HHG dipole phase due to the blue-shift of the driving

laser. The results are important for a complete understanding of HHG phasematching and might help to find routes towards more efficient HHG in the water window.

Finally, attosecond measurements on metal nanotips are presented. The attosecond field-resolved characterization of the nanoscale near-fields on a nanotip and the response function using attosecond streaking is demonstrated. Moreover, another field-reconstruction method based on the modulation of the strong-field photocurrent is used for the measurement of the enhanced near-fields at the nanotip apex and different aspects of the methods are studied. Combining the latter approach with the concept of the nanotip as nanoscale localized field sensor, the attosecond characterization of an orbital angular momentum beam in free-space below the diffraction limit is demonstrated. These results pave the way towards nanoscale attosecond field-resolved measurements on generic nanostructures.

Zusammenfassung

Die schnellsten Prozesse der fundamentalen Licht-Materie-Wechselwirkung zwischen Elektronen und sichtbaren Laserpulsen finden auf der Attosekunden-Zeitskala statt, unterhalb der halben Schwingungsperiode des elektrischen Feldes. Feldaufgelöste Messungen der beteiligten Laserpulse sind daher für die Untersuchung solch schneller Prozesse und ihrer Kontrolle unabdingbar. In der vorliegenden Arbeit wird das fundamentale Verständnis von etablierten als auch neu aufkommenden subzyklen-aufgelösten Messtechniken erweitert mit Anwendungen in Gasen, Festkörpern und Nanostrukturen.

Im ersten Teil wird der Mechanismus hinter der Erzeugung makroskopischer Ströme in den Messungen feld-induzierter Photoströme experimentell und theoretisch untersucht. Die Entwicklung eines rigorosen Models wird präsentiert, das die gemessenen Ströme mit der mikroskopischen Bewegung der Ladungsträger verknüpft. Es beinhaltet außerdem die Streuung an Atomen und die Coulomb-Wechselwirkung. Das Model wird in einer Reihe von umfassenden Experimenten bestätigt, in denen die Abhängigkeit der Ströme von der Phase der Trägerwelle zur Einhüllenden des Laserpulses gemessen werden. Zur Messung der Ströme wird ein Elektrodenpaar, das den Fokus eines intensiven Wenigzyklen-Pulses in verschiedenen Gasen umgibt, verwendet. Der Einfluss der mittleren freien Weglänge und der Ladungs-Wechselwirkung wird aufgeklärt. Das Model liefert ein fundamentales Verständnis der Signalerzeugung in der auf Photoleitung beruhenden Messung von Laserpulsen. Dies erlaubt die Identifizierung der fundamentalen Grenzen und eröffnet Wege zur Optimierung der Messmethode.

Die zweite Reihe von Experimenten hat die Messung der transienten Änderung der Reflektivität nach der Anregung durch einen Pumppuls in nahen Infrarotbereich zum Gegenstand. Elektro-optisches Sampling wird verwendet für die feldaufgelöste Charakterisierung der Probepulse im mittleren Infrarotbereich, von unter drei bis über sechs Mikrometern Wellenlänge. Messungen an Halbleitern werden durchgeführt und die Dynamik, die auf der Zeitskala von Femtosekunden bis Pikosekunden nach der Photoanregung stattfindet, wird untersucht. Die gezeigten Experimente sind ein wichtiger Meilenstein für die Erweiterung feldaufgelöster Messtechniken vom THz- in den PHz-Frequenzbereich.

Die Erzeugung von isolierten Attosekundenpulsen im extrem ultravioletten Wellenlängenbereich durch hohe Harmonische (HHG) in Edelgasen ist das Thema des dritten Abschnitts. Der Schwerpunkt liegt auf der Untersuchung des übersteuerten Regimes, in dem der Anregungslaser im Erzeugungsprozess eine starke Umformung durch Plasmaeffekte erfährt. Auf experimenteller Ebene wird die Attosekunden Streaking Technik angewendet,

um zum ersten Mal die Erzeugung isolierter Attosekundenpulse unter diesen Umständen nachzuweisen. Anhand umfangreicher numerischer Simulationen wird der Mechanismus der Phasenanpassung in diesem Regime theoretisch untersucht. Eine Erweiterung der konventionellen analytischen Beschreibung der Phasenanpassung wird eingeführt, die den Beitrag der Dipolphase der hohen Harmonischen aufgrund der Blauverschiebung des Anregungslasers berücksichtigt. Die Ergebnisse sind von grundlegender Bedeutung für ein vollständiges Verständnis der HHG-Phasenanpassung und helfen möglicherweise dabei, Wege zu effizienter HHG-Erzeugung im sogenannten Wasserfenster zu finden.

Zuletzt werden Attosekundenmessungen an metallischen Nanospitzen vorgestellt. Die feldaufgelöste Charakterisierung von Nahfeldern an einer Nanospitze auf der Attosekunden- und Nanometerskala und der entsprechenden Antwortfunktion durch die Attosekunden Streaking Methode werden demonstriert. Darüber hinaus wird eine andere Technik zur Feldrekonstruktion auf die Messung der verstärkten Nahfelder an dem Ende der Nanospitze angewandt. Verschiedene Aspekte der Messmethode, die auf der Modulation des durch Starkfeldemission erzeugten Photostroms beruht, werden untersucht. Schließlich wird die Kombination der demonstrierten Methodik mit dem Konzept der Nanospitze als nanolokalisiertem Feldsensor demonstriert. Damit wird die zeitlich und räumlich aufgelöste Charakterisierung eines frei propagierenden Laserstrahls mit Drehimpuls auf der Attoekunden-Skala und unterhalb des Beugungslimits gezeigt. Die Resultate ebnen den Weg hin zu feldaufgelösten Messungen im Nanometer-Attosekunden Bereich an beliebigen Nanostrukturen.

Chapter 1

Introduction

The first laser was demonstrated in 1960 by Maiman[1] and has developed into one of the most important tools in experimental physics due to its properties as a highly coherent light source. Within the same decade pulsed laser sources with nanosecond[2] and picosecond pulse duration became available[3]. From a scientific perspective pulsed lasers are particularly interesting since they enable the time-resolved measurement of physical processes using pump-probe experiments. Here, a pump pulse excites the system under study through the absorption of photons and a second pulse probes the state of the system at a later time. By varying the time-delay of the probe pulse in repeated measurements, the evolution of the system following excitation can be recorded. The availability of lasers with pulse durations below 100 fs[4] (1 fs=10^{-15} s) in the 1980s, enabled time-resolved studies of chemical reactions, i.e. the rearrangement of atoms[5] (Nobel prize in chemistry 1999[6]). Nowadays, laser pulses as short as a few femtoseconds, close to the oscillation period of visible light, can be produced[7].

The crucial insight to advance the time-resolution even further to the attosecond timescale (1 as=10^{-18} s), was that the light-matter interaction can effectively be confined to a fraction of a half-cycle oscillation of a laser pulse by using extremely nonlinear, non-perturbative processes, such as tunneling photoemission of an electron from an atom induced by the instantaneous electric field of a strong laser pulse. This concept has led to the birth of attosecond science[8] which now allows the study of electronic processes on their natural timescale. The close relation between attosecond and strong-field physics has led to the demonstration of isolated attosecond pulses (IAPs) in the extreme ultra-violet (XUV)[9] with pulse durations on the 100 as scale produced via high-harmonic generation[10, 11] (HHG) in the early 2000s. Since then, the attosecond streaking technique[12, 13] allows the field-resolved characterization of optical laser pulses. The method uses IAPs as pump pulses for triggering photoemission. The emitted electrons experience the electric field of a time-delayed probe laser pulse which leads to a delay-dependent change of their final kinetic energy.

The early research in attosecond science was mostly focused on the investigation of photoemission processes in atoms[14] and on solid surfaces[15]. However, the recent demonstration of optical-field induced currents in dielectrics[16], semiconductors[17] and in 2d-

materials[18] has opened an entirely new exciting perspective for the investigation of light-induced electronic processes inside solids on the attosecond timescale and for the development of solid-state based attosecond metrology. Moreover, combining this approach with the enhanced light-matter interaction on nanostructures[19], which is the subject of attosecond nanophysics[20], holds promise for the sub-cycle control of electronic currents on the nanoscale. This could form the basis of lightwave electronics[21] allowing processing speeds on the PHz-scale, 5-6 orders of magnitude faster than current electronics[22]. Importantly, for both the measurement and control of sub-cycle light-matter interaction in atoms, molecules, bulk solids, and on nanostructures, attosecond field-resolved measurement techniques are an indispensable prerequisite.

Attosecond streaking which has so far been one of the workhorses of attosecond science, is a well-established tool and it has been used for the measurement of the sub-cycle nonlinear polarization dynamics in solids[23]. The application of the technique to the field-resolved reconstruction of nanoscale near-fields on a nanostructure was demonstrated within the framework of this thesis (covered in Chap. 7 and Refs. [24, 25, 26, 27]). One major disadvantage of attosecond streaking is that the IAP generation process is very inefficient and the resulting low photon flux leads to long measurement times or may even inhibit certain experiments, especially if higher photon energies are required. A possible route to overcome this limitation is the exploration of new generation regimes, such as the overdriven regime[28], where the driving pulse undergoes strong pulse reshaping. The overdriven regime is investigated in this thesis (described in Chap. 6 and Ref. [29]) and isolated attosecond pulse generation is demonstrated. An even more severe disadvantage of attosecond streaking, however, is the required expensive and complex infrastructure for the generation and handling of the XUV/soft-x-ray pulses which has restricted the use of the method to a few laboratories around the world. Therefore, within the last few years, a number of simpler alternative sub-cycle field-resolved measurement techniques have been developed or pushed towards the attosecond regime, but their potential and fundamental limitations still need to be uncovered.

An overview of different attosecond field-resolved measurement techniques and the year of their first demonstration is given in Fig. 1.1. They can be categorized according to whether they originate from THz metrology (red shaded areas) or rely on isolated attosecond pulses (gray shaded area) or on the perturbation of a strong-field process (blue shaded area). Attosecond streaking, as mentioned above, was established almost two decades ago and can up to now be considered the gold-standard for sub-cycle optical field reconstruction. In contrast, the attosecond field measurement with the other techniques has only been demonstrated recently. The class of methods involving high-harmonic generation[34, 35, 36], which are also based on the perturbation of a strong-field process, have been omitted in this overview, since they pose similar infrastructure requirements as attosecond streaking and are not expected to be applicable to more complex systems such as nanostructures.

While the origins of THz field-resolved metrology date back to the 1980s[37, 38, 39, 40, 41], the electro-optic sampling (EOS) measurement of infrared waveforms down to 1.2 μm was only shown in 2016[31]. Electro-optic sampling is based on the polarization rotation

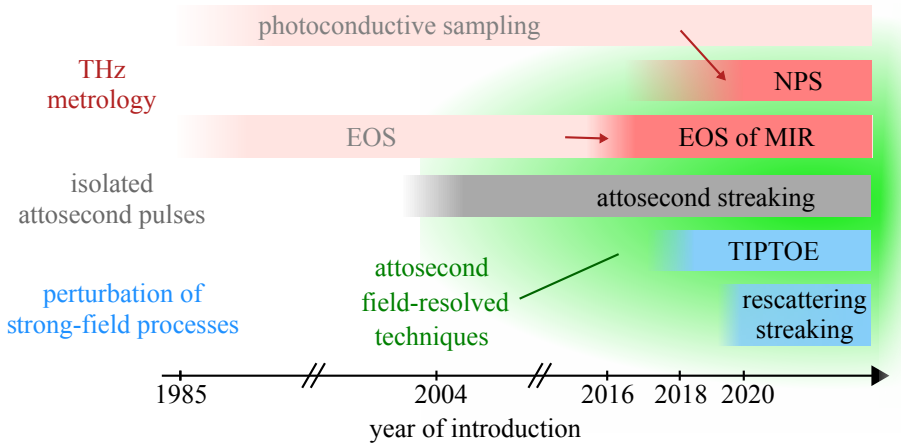

Figure 1.1: Overview of attosecond field-resolved measurement techniques: attosecond streaking was demonstrated almost two decades ago[12, 13]. The other techniques have only been demonstrated within the last few years. Nonlinear photoconductive sampling (NPS)[16, 30] and electro-optic sampling (EOS) of midinfrared pulses[31] have their roots in THz metrology. The perturbation of a strong-field process is used in tunneling ionization with a perturbation for the time-domain observation of an electric field (TIPTOE)[32] and streaking of rescattering electrons[33].

of the sampling pulse through the interaction with the signal pulse via the second order nonlinearity and is a heterodyne technique that allows sensitive measurements. However, it requires phasematching of the nonlinear optical processes which naturally limits the achievable bandwidth. Here, we demonstrate the application of the method for the ultrafast field-resolved pump-probe experiments on semiconductors with probe pulses at slightly longer wavelengths from below 3 μm to 6 μm (see Chap. 5). While the observed phenomena ranging from plasmon build-up to intervalley scattering to carrier recombination occur on the femtosecond to picosecond timescale, the experiments constitute an important milestone towards field-resolved pump-probe measurements in the optical regime.

Similarly, nonlinear photoconductive sampling (NPS)[16, 30] can be considered an extension of THz photoconductive sampling[37, 38]. Here, the sampling pulse creates free-charge carriers between a pair of electrodes and the signal pulse leads to a displacement of the carriers which induces a current on the electrodes. In nonlinear photoconductive sampling, as opposed to linear photoabsorption, the photoexcitation occurs nonlinearly. This provides a sub-cycle gate and the bandwidth should only be limited by the photoexcitation time. It is also possible to measure the waveform-dependent current of a single pulse. So far, despite the widespread use, the exact mechanism for the generation of the macroscopic optical field induced current on the electrode from the ultrafast strong-field microscopic charge carrier movement had not been clear. The mechanism is studied experimentally and theoretically and is elucidated within this thesis (described in Chap. 6). It is shown that electron scattering as well as the charge interaction poses fundamental limitations.

Methods based on the perturbation of strong-field processes are particularly easy to understand. The change of the strong-field observable depends linearly on the probe field, if the latter is weak enough such that a first-order Taylor-expansion is appropriate. One example is the streaking of rescattering electrons[33], where the probe field influences the rescattering electron trajectories, leading to a change of the cutoff energy in the photoelectron spectrum. Especially intuitive is the tunnel ionization with a perturbation for the time-domain observation of an electric field (TIPTOE)[32]. In a simple picture, the change of the ionization yield is proportional to the perturbing field at the time of the tunnel ionization burst. TIPTOE has originally been applied to gases. On nanostructures, the advantage is that the strong-field processes are confined to the enhanced near-fields, which is used in Chap. 7 to demonstrate the field-resolved characterization of the enhanced optical fields at the apex of a nanotip. With this approach in combination with the concept of the nanotip as a nanoscale field sensor, extensively used in tip-enhanced scanning near-field optical microscopy, we demonstrate the direct measurement of the electric field of a laser beam with orbital angular momentum on the attosecond timescale below the diffraction limit. The generalization of this concept would open the door for attosecond nanoscale reconstruction of optical fields on arbitrary nanostructures.

The outline of this thesis is as follows. In the second chapter, the theoretical foundations needed for the understanding of this work are briefly reviewed. The experimental basics as well as the field-resolved measurement techniques used in this thesis are discussed in more detail in chapter 3. Subsequently, the results obtained within this thesis are presented, starting with the developed model for the macroscopic signal generation mechanism in the optical field-induced current measurements and the comparison with experiments. In the fifth chapter, the pump-probe measurements on semiconductors using electro-optic sampling are presented. Chapter 6 discusses the experiments on the generation of isolated attosecond pulses in the overdriven regime. Finally, in the seventh chapter the attosecond field-resolved measurements on nanotips are presented.

List of publications by the author with high relevance to this thesis:

1. J. Schötz, L. Seiffert, A. Maliakkal, J. Blöchl, D. Zimin, P. Rosenberger, B. Bergues, P. Hommelhoff, F. Krausz, T. Fennel and M. F. Kling, *"Onset of space-charge effects in strong-field photocurrents from nanometric needle tips"*, arXiv:2106.00503, submitted to: Nanophotonics (2021)

2. J. Schötz, A. Maliakkal, J. Blöchl, D. Zimin, Z. Wang, P. Rosenberger, M. Alharbi, A.M. Azzeer, M. Weidman, V. S. Yakovlev, B. Bergues, and M. F. Kling, *"The emergence of macroscopic currents in photoconductive sampling of optical fields"*, arXiv:2105.10010, submitted to: Nature Communications (2021)

3. J. Schötz, B. Förg, W. Schweinberger, I. Liontos, H.A. Masood, A.M. Kamal, C. Jakubeit, N.G. Kling, T. Paasch-Colberg, S. Biswas, M. Högner, I. Pupeza, M. Alharbi, A.M. Azzeer and M.F. Kling, *"Phase-Matching for Generation of Isolated Attosecond XUV and Soft-X-Ray Pulses with Few-Cycle Drivers"*, Physical Review X 10, 041011 (2020)

4. J. Schötz, Z. Wang, E. Pisanty, M. Lewenstein, M. Kling and M. Ciappina, *"Perspective on petahertz electronics and attosecond nanoscopy"*, ACS Photonics 6, 3057 (2019)

5. B. Ahn, J. Schötz, M. Kang, W. Okell, S. Mitra, B. Förg, S. Zherebtsov, F. Süßmann, C. Burger, M. Kbel, C. Liu, A. Wirth, E. Di Fabrizio, H. Yanagisawa, D. Kim, B. Kim and M. F. Kling, *"Attosecond-controlled photoemission from metal nanowire tips in the few-electron regime"*, APL Photonics 2, 036104 (2017)

6. J. Schötz, B. Förg, M. Förster, W. Okell, M. Stockman, F. Krausz, P. Hommelhoff, M. F. Kling, *"Reconstruction of nanoscale near-fields by attosecond streaking"*, IEEE Journal of selected Topics in Quantum Electronics 23, 8700111 (2016)

7. B. Förg, J. Schötz, F. Süßmann, M. Förster, M. Krüger, B. Ahn, W. Okell, K. Wintersperger, S. Zherebtsov, A. Guggenmos, V. Pervak, A. Kessel, S. Trushin, A. Azzeer, M. Stockman, D. Kim, F. Krausz, P. Hommelhoff, M. F. Kling, *"Attosecond nanoscale near-field sampling"*, Nature Communications 7, 11717 (2016)

Other publications by the author:

8. A. Korobenko, P. Rosenberger, J. Schötz, A. Yu. Naumov, D. M. Villeneuve, M. F. Kling, A. Staudte, P. B. Corkum, and B. Bergues, *"Single-shot dispersion sampling for optical pulse reconstruction"*, Optics Express 29, 11845-11853 (2021)

9. D. Zimin, M. Weidman, J. Schötz, M.F. Kling, V.S. Yakovlev, F. Krausz and N. Karpowicz, *"Petahertz-scale nonlinear photoconductive sampling in air"*, Optica 8, 586-590 (2021)

10. P. Rosenberger, P. Rupp, R. Ali, M. S. Alghabra, S. Sun, S. Mitra, S. A. Khan, R. Dagar, V. Kim, M. Iqbal, J. Schötz, Q. Liu, S. K. Sundaram, J. Kredel, Markus Gallei, C. Costa-Vera, B. Bergues, A. S. Alnaser and M. F. Kling, *"Near-Field Induced Reaction Yields from Nanoparticle Clusters"*, ACS Photonics 7, 1885 (2020)

11. S. Mitra, S. Biswas, J. Schötz, E. Pisanty, B. Förg, G.A. Kavuri, C. Burger, W. Okell, M. Högner, I. Pupeza, V. Pervak, M. Lewenstein, P. Wnuk and M. F. Kling, *"Suppression of individual peaks in two-colour high harmonic generation"*, Journal of Physics B: Atomic, Molecular and Optical Physics, 53(13), p.134004. (2020)

12. S. Biswas, B. Förg, L. Ortmann, J. Schötz, W. Schweinberger, T. Zimmermann, L. Pi, D. Baykusheva, H.A. Masood, I. Liontos, A.M. Kamal, N.G. Kling, A.F. Alharbi, M. Alharbi, A.M. Azzeer, G. Hartmann, H.J. Wörner, A.S Landsman and M.F. Kling, *"Probing molecular environment through photoemission delays"*, Nature Physics 16, 778783 (2020)

13. M. Kubullek, Z. Wang, K. von der Brelje, D. Zimin, P. Rosenberger, J. Schötz, M. Neuhaus, S. Sederberg, A. Staudte, N. Karpowicz, M. F. Kling, and B. Bergues, *"Single-shot carrierenvelope-phase measurement in ambient air"*, Optica 7, 35-39 (2020)

14. T. Saule, S. Heinrich, J. Schötz, N. Lilienfein, M. Högner, O. de Vries, M. Plötner, J. Weitenberg, D. Esser, J. Schulte, P. Russbüldt, J. Limpert, M. F. Kling, U. Kleineberg, I. Pupeza, *"High-flux ultrafast extreme-ultraviolet photoemission spectroscopy at 18.4 MHz pulse repetition rate"*, Nature Communications 10, 458 (2019)

15. I. Yavuz, J. Schötz, M. Ciappina, P. Rosenberger, Z. Altun, M. Lewenstein, M. F. Kling, *"Control of molecular dissociation by spatially inhomogeneous near fields"*, Physical Review A 98, 043413 (2018)

16. J. Schötz, S. Mitra, H. Fuest, M. Neuhaus, W. Okell, M. Förster, T. Paschen, M. Ciappina, H. Yanagisawa, P. Wnuk, P. Hommelhoff, M. Kling *"Nonadiabatic ponderomotive effects in photoemission from nanotips in intense midinfrared laser fields"*, Physical Review A 97, 013413 (2018)

17. M. Neuhaus, H. Fuest, M. Seeger, J. Schötz, M. Trubetskov, P. Russbüldt, H-D. Hoffmann, E. Riedle, Z. Major, V. Pervak, M. F. Kling and P. Wnuk, *"10 W CEP-stable few-cycle source at 2 μm with 100 kHz repetition rate"*, Optics Express 26, 16074 (2018)

18. H. Yanagisawa, M. Ciappina, C. Hafner, J. Schötz, J. Osterwalder, M. F. Kling *"Optical control of Youngs type double-slit interferometer for laser-induced electron emission from a nano-tip"*, Scientific Reports 7, 12661 (2017)

19. L. Ortmann, J. A. Pérez-Hernández, M. Ciappina, J. Schötz, A. Chacón, G. Zeraouli, M. F. Kling, L. Roso, M. Lewenstein and A. Landsman, *"Emergence of a higher energy structure in strong field ionization with inhomogeneous electric fields"*, Physical Review Letters 119, 053204 (2017)

20. H. Li, N. Kling, T. Gaumnitz, C. Burger, R. Siemering, J. Schötz, Q. Liu, L. Ban, Y. Pertot, J. Wu, A. Azzeer, R. de Vivie-Riedle, H. J. Wörner and M. F. Kling, *"Sub-cycle steering of the deprotonation of acetylene by intense few-cycle mid-infrared laser fields"*, Optics Express 25, 14192 (2017)

21. M. Ciappina, J. A. Pérez-Hernández, A. Landsman, W. Okell, S. Zherebtsov, B. Fïg, J. Schötz, L. Seiffert, T. Fennel, T. Shaaran, T. Zimmermann, A. Chacón, R. Guichard, A. Zar, J. Tisch, J. Marangos, T. Witting, A. Braun, S.A. Maier, L. Roso, M. Krüger, P. Hommelhoff, M. F. Kling, F. Krausz and M. Lewenstein, *"Attosecond physics at the nanoscale"*, Reports on Progress in Physics 80, 054401 (2017)

22. Q. Liu, P. Rupp, B. Förg, J. Schötz, F. Süßmann, W. Okell, J. Passig, J. Tiggesbäumker, K.-H. Meiwes-Broer, T. Fennel, E. Rühl, M. Fürster, P. Hommelhoff, S. Zherebtsov, M. F. Kling, *"Photoemission from nanomaterials in strong few-cycle laser fields"*, bookarticle in: Nano-Optics: Principles Enabling Basic Research and Applications ISBN: 978-94-024-0848-5 (2017)

23. B. Ahn, J. Schötz, W. Okell, F. Süßmann, B. Förg, S. C. Kim, M. F. Kling and D. Kim, *"Optimization of a nanotip on a surface for the ultrafast probing of propagating surface plasmons"*, Optics Express 24, 92 (2016)

24. H. Li, A. Alnaser, X.-M. Tong, K. Betsch, M. Kübel, T. Pischke, B. Fürg, J. Schötz, F. Süßmann, S. Zherebtsov, B. Bergues, A. Kessel, S. Trushin, A. Azzeer and M. F. Kling, *"Intensity dependence of the attosecond control of the dissociative ionization of D2"*, Journal of Physics B 47, 124020 (2014)

Chapter 2

Theoretical foundations

In this chapter the theoretical foundations of attosecond physics and its extension to nanostructures are briefly reviewed. The major building block of attosecond science consists of strong-field electron processes driven by intense laser pulses. Strong-field tunneling photoemission confines the electron emission to a fraction of a half-cycle of the driving laser pulse. Furthermore, the laser field determines the dynamics of the emitted electrons, giving rise to a number of different processes. Their experimental detection allows to obtain information about the electron dynamics on attosecond timescales. One of the most intriguing processes is high-harmonic generation (HHG), where the recollision of the electron with the parent ion leads to the coherent emission of a photon with a multiple times higher photon energy than that of the driving laser pulse. Driven by waveform-controlled laser pulses, HHG allows the generation of isolated attosecond pulses (IAPs), forming a powerful tool for attosecond pump-probe spectroscopy. Combining experimental techniques of attosecond science with nanophysics provides attosecond temporal and nanometer spatial resolution. However, due to the nanometer confinement of the electromagnetic near fields around nanostructures, the electron dynamics might be strongly affected and requires careful consideration.

This chapter is organized as follows: First, the description of waveform-controlled few-cycle laser pulses is presented. Secondly, strong-field photoemission and electron dynamics in strong laser fields are discussed. Thirdly, in a slightly more detailed section, high-harmonic generation, phasematching and isolated attosecond pulse generation are considered. Finally, the description of electromagnetic near-fields around nanostructures and their influence on the electron dynamics are discussed.

2.1 Few-cycle pulses and dispersion

Within this thesis, the laser pulses are described classically in terms of their time-dependent electric field $\vec{E}(t)$. For a linearly polarized laser a single component is sufficient. The electric field $E(t)$ can be decomposed into a carrier wave $\exp(i\omega t + i\phi)$ and an envelope function

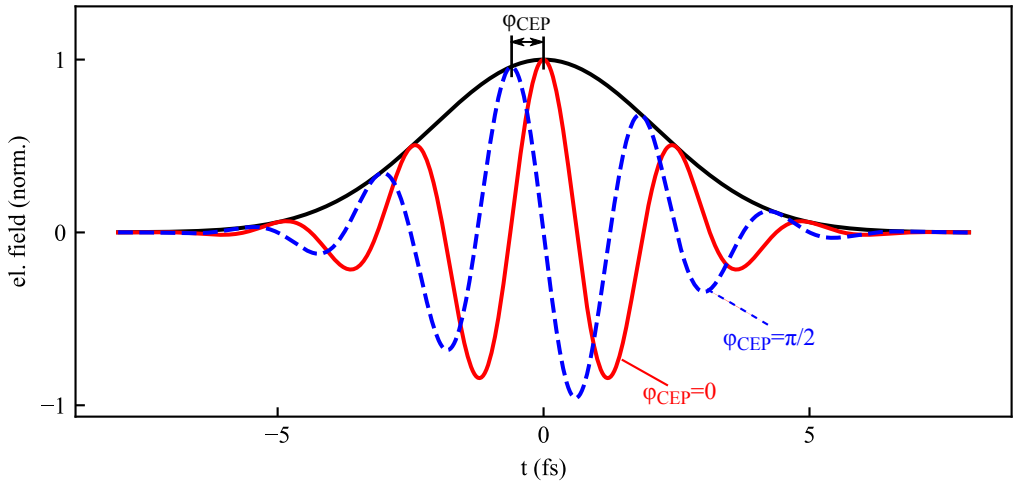

Figure 2.1: Illustration of the electric-field of a few-cycle laser-pulse for an carrier-envelope phase (CEP) of 0 (red line) and $\pi/2$ (blue dashed line). The Gaussian envelope ($T_{\mathrm{FWHM}} = 3.5\,\mathrm{fs}$) is shown as black solid line. The carrier wavelength is 750 nm.

$g(t)$. The most common choice for the envelope is a Gaussian[42]:

$$E(t) = E_0 \cdot \exp\left(-2\ln 2 \frac{t^2}{T_{\mathrm{FWHM}}^2} \right) \cdot \exp(i\omega t + i\phi_{\mathrm{CEP}}), \tag{2.1}$$

where T_{FWHM} is the intensity full-width at half maximum (FWHM) and E_0 is the electric field amplitude. The physical electric field is described by the real part. The carrier-envelope phase ϕ_{CEP} (or CEP) is defined as the phase of the carrier wave with respect to the peak of the envelope (here at t=0). Fig. 2.1 shows the electric field of a few-cycle pulse for two different CEPs (red solid and blue dashed lines) together with the envelope (black line). As can be seen, for the laser pulses in the visible and near-infrared wavelength region used in this thesis, the half-cycle duration is on the order of 1 fs (1 femtosecond=10^{-15}s).

The carrier-envelope phase of few-cycle pulses plays an important role in attosecond physics. Firstly, by varying the CEP and detecting the change of experimental observables, processes that depend on the field (rather than the intensity envelope) can be identified. Conversely, such processes also allow the determination of the CEP. Secondly, by controlling ϕ_{CEP}, dynamics unfolding on a sub-cycle timescale can be controlled with attosecond precision and the contribution of an individual half-cycle can be separated. In this thesis the former concept is used in the investigation of laser-field-dependent currents in plasmas (Chap. 4) and photoemission from nanotips (Chap. 7). The latter is utilized in the generation of isolated attosecond pulses (IAPs) in Chap. 6 and Chap. 7. Often the term waveform-controlled is encountered which usually refers to CEP-controlled.

In order to be able to observe CEP-effects, few-cycle pulses are required, since the electric field strength difference between neighboring half-cycles increases as the pulse duration decreases. Pulse duration and spectral bandwidth are connected through the Fourier

transform. The required spectral intensity FWHM $\Delta\omega$ can be obtained through the time-bandwidth product, which for a Gaussian pulse is given by $\Delta\omega \cdot T_{\mathrm{FWHM}} \geq 2\pi \cdot 0.441$ [43]. For a 1.5-cycle pulse at a central wavelength of 750 nm, this results in a spectral bandwidth ranging from 650 nm to 880 nm. However, the miminum duration is only reached if all frequency components are in phase. Since any material exhibits dispersion, i.e. a frequency dependent refractive index, propagation of few-cycle pulses generally results in a frequency-dependent spectral phase and temporally broadened pulses. A major part of setting up an experiment therefore consists in managing and optimizing the dispersion in order to achieve few-cycle pulses.

The strong-field regime of laser-matter interaction is reached once the electric field strength becomes comparable to the Coulomb force acting on the bound electrons (see the next section for a more rigorous discussion). A simple estimate, obtained from the condition that the electric field multiplied by the spatial dimension of the electron orbital (order 1 Å) equals the binding energy ($\gtrsim$1 eV), results in a peak intensity $\gtrsim 10^{13}\mathrm{W/cm^2}$. For a 5 fs-pulse and a typical focal spotsize of 100 μm, a pulse energy of $\gtrsim$10-100μJ is required. Nowadays, such pulses can routinely be produced from kHz repetition rate chirped pulse amplifier laser systems (CPA)[44] with Watt-level average power. One compelling feature of nanostructures is the enhancement of the electric near-field (see Sec. 2.4), which relaxes the requirement on the pulse energy by a factor of 10-100 and in principle allows the use of MHz-repetition rate laser oscillators (see e.g. [45]).

Within this thesis, laser beam propagation is described in the scalar wave equation, or within the framework of Maxwell's equations when considering reflections from surfaces or the interaction with nanostructures (see Chap. 7). A Gaussian laser beam is assumed if not stated otherwise. Note that within this thesis generally the $+i\omega t$-convention is used, except for quantum mechanical wavefunctions, where $-i\omega t$ is imposed by the Schrödinger equation.

2.2 Strong-field photoemission

2.2.1 Emission regimes

One major building block of attosecond science is strong-field photoemission. When the photon energy $\hbar\omega$ of a laser is below the ionization potential I_p of an atom or molecule (or work function ϕ of a solid) photoemission can still occur through the absorption of several photons, as depicted in Fig. 2.2 a). The number of required photons is given by $n = \lceil I_\mathrm{p}/\hbar\omega \rceil$. The ionization rate for multiphoton ionization w_MPI can be described by lowest order perturbation theory (LOPT)[46]:

$$w_\mathrm{MPI} = \sigma_n I^n, \tag{2.2}$$

where I is the laser intensity and σ_n is the generalized cross-section for n-photon ionization[46]. Once the laser intensity is increased, more photons than the minimum number n can be absorbed and the potential of the atom starts to get deformed by the electric field of the

laser. Eventually, the electric field becomes so strong that the emission process is dominated by tunneling of the electron through the potential barrier at the peak of the electric field, as illustrated in Fig. 2.2 b). In the tunneling regime the ionization rate $w(t)$ is given by[47]:

$$w(t) \propto \exp\left(-\frac{2(2I_\mathrm{p})^{3/2}}{3E(t)}\right), \tag{2.3}$$

where $E(t)$ is the instantaneous electric field strength. If the electric field is further increased the barrier-suppression regime is reached[48, 49]. There, the potential barrier is decreased even below the binding energy of the initial state E_i. This latter regime is, however, not considered in this thesis.

The cycle-averaged strong-field photoemission rate in the multiphoton, tunneling and intermediate regime can be described by Keldysh theory[50]. The different regimes are classified by the Keldysh parameter γ:

$$\gamma = \sqrt{\frac{I_\mathrm{p}}{2U_\mathrm{p}}}, \tag{2.4}$$

where I_p is the ionization potential and U_p is the ponderomotive potential, the average kinetic energy of the oscillatory motion of a free electron in an oscillating electric field. The ponderomotive potential is given by:

$$U_\mathrm{p} = \frac{e^2 E_0^2}{4m\omega^2} = 9.22\,\mathrm{eV} \cdot I[10^{14}\mathrm{W/cm^2}] \cdot \lambda[\mu\mathrm{m}]^2, \tag{2.5}$$

with the electron charge e and mass m and the laser electric field amplitude E_0, angular frequency ω, intensity I and wavelength λ. The multiphoton regime is reached in the limit $\gamma \gg 1$ and the tunneling regime for $\gamma \ll 1$ and it can be shown that Eq. 2.2 and Eq. 2.3 emerge from Keldysh theory in the respective limit[51]. The intensity range for which both expressions are good approximations is discussed below.

Keldysh theory can be applied to the ionization of atoms, transitions in solids and has also been extended to metal surfaces[53] and is valid under the condition $I_\mathrm{p} \gg \hbar\omega$. The calculation of the rates involves the summation over all multiphoton orders as well as integration over one oscillation cycle. The extension of the Keldysh theory by Perelomov, Popov, and Terentev (PPT)[54, 55, 56] usually shows good agreement with experimental data for simple atoms[57]. For complex systems or when intermediate resonances occur, the numerical solution of the time-dependent Schrödinger equation (TDSE) might be required.

The intensity-dependence of the PPT rate (red line) according to the formulation in Ref. [57] is shown in Fig. 2.2 c). The considerably simplified expression for the tunneling regime (Eq. 2.3) has been derived by Ammosov, Delone and Krainov (ADK)[47] from PPT theory. By comparing the expressions for the tunneling regime (black line) and the multiphoton regime (blue line, Eq. 2.2) with the PPT rate, it can be seen that the approximations are valid for $\gamma \lesssim 1$ and $\gamma \gtrsim 5$, respectively.

In the intermediate region, in the transition from the multiphoton to the tunneling regime, characteristic kinks appear that are connected to so-called "channel closings"[54,

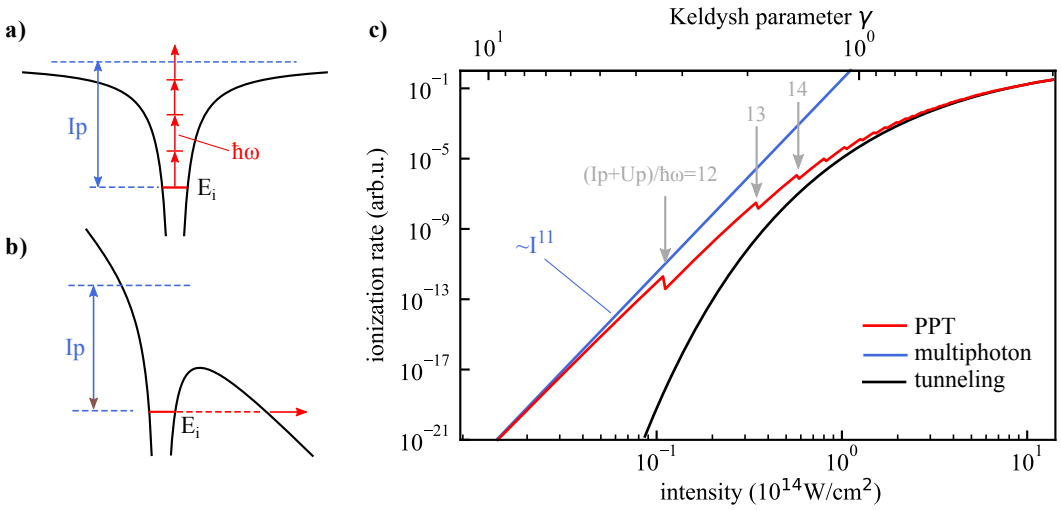

Figure 2.2: strong-field photoemission: schematic illustration of the a) multiphoton and b) tunneling regime. c) PPT rate (red line) compared to the multiphoton (blue line) and tunneling rate (black line). Channel closings are indicated by gray arrows. The prefactor of the multiphoton scaling has been fixed to match the PPT rate at the lowest intensities. The PPT rate has been calculated for an ionization potential of 15.79ėV and orbital quantum numbers l=1, m=0 and photon energy of 1.5 eV ($\lambda \approx 825$nm), [a-b adapted from [52]]

46, 57]. The nth-order multiphoton channel closes above a certain value of the ponderomotive potential, when the absorption of n photons can not provide the required energy, the sum of ionization and ponderomotive potential, for the transition from the ground state to a free electron in the laser field anymore, i.e. $n \cdot \hbar\omega < I_\mathrm{p} + U_\mathrm{p}$. The first three channel closings are indicated in Fig. 2.2 b) by the gray arrows. Channel closing can also be seen in the photoelectron spectrum, by the down-shift or suppression of the lowest photon peak[58, 59, 46].

The timing of the strong-field photoemission process, especially the question how long it takes an electron to tunnel through the barrier, has already been considered in the work of Keldysh[50] and has been studied in the context of attosecond science experimentally[60, 61] and theoretically[62, 63]. A recent experiment has measured small but finite delays in strong-field tunneling photoemission from helium (on the order of 10 as) which could be explained by theory[64]. For most practical purposes, such as the semi-classical modeling of strong-field processes below, however, these tunneling times will be negligible and tunneling can be considered to occur quasi-instantaneously. Moreover, it has been shown theoretically that even in the intermediate regime with a large multiphoton contribution, the emission is still strongly centered around the electric-field maximum[62].

In this thesis, the experimental conditions are generally in the tunneling regime $\gamma \lesssim 1$. Therefore, for the description of photoionization rates, we use the modified ADK-rates for noble gas atoms of Ref. [65] and the Fowler-Nordheim tunneling rate for nanostructures[66], unless stated otherwise.

2.2.2 Simpleman's model

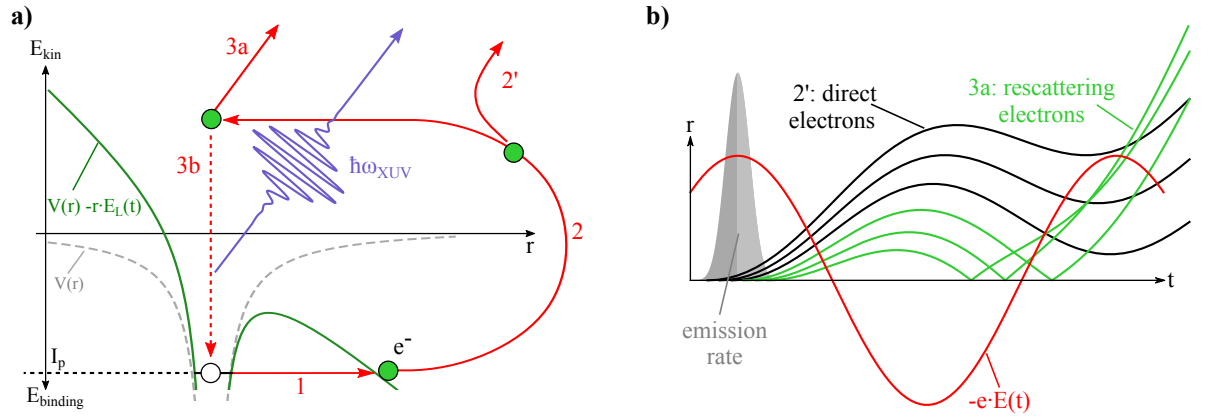

Figure 2.3: The simpleman's model: a) the three steps, as indicated by the red arrows: (1) tunneling photoemission and (2) electron acceleration and propagation. Upon recollision the electron can rescatter (3a) or recombine with the parent ion (3b) leading to the emission of an XUV photon (blue line). Additionally, electrons can escape from the ion without recollision (2') . The combined potential of the atom and the laser is shown (green) and compared to the unperturbed atomic potential (gray dashed line) [adapted from [27]]. b) Electron trajectories under the strong-field approximation: Electrons emitted before the half-cycle crest are direct electrons (black lines), while electrons emitted after the peak may recollide with the ion giving rise to rescattered electrons (green lines).

The second major foundation of attosecond science is the understanding of the electron propagation in the continuum after the strong-field ionization process. Historically, a major breakthrough came with the interpretation of the dynamics in terms of classical electron trajectories[67] in the so-called simpleman's model (SMM) also referred to as three-step model. As the latter name suggests, the strong-field photoemission process is separated into three different steps as depicted with red arrows in Fig. 2.3 a):

1. Tunneling photoemission of the electron through the potential barrier
2. Acceleration of the electron in the oscillatory electric field. Due to the oscillatory nature of the field the electron can be accelerated back to the parent ion.
3. recollision of the electron with the parent ion

Several different processes can take place in the recollision event. First, the electron can elastically rescatter from the ion core and then propagate away from the core as a photoelectron (3a). Secondly, the electron can recombine with the parent ion (3b), leading to the emission of an extreme ultraviolet (XUV) photon (blue wiggly line) with an energy given by the sum of the ionization potential and kinetic energy of the recolliding electron[67]. This process is at the core of high-harmonic generation (HHG), which is discussed below.

There are further processes, such as non-sequential double ionization (NSDI)[68, 69], where the rescattering electron leads to the ionization of another electron[70, 71]. Moreover incoherent recombination, Bremsstrahlung[72] or excitation of the ion can take place[73]. The phenomena investigated in this thesis are based on the first two recollision processes (3a and 3b). Additionally, there are also trajectories that do not recollide (2').

In the SMM, the electron is assumed to be born in the continuum at the origin without initial velocity. In the description of the electron propagation usually the strong-field approximation (SFA) is applied. In the SFA, after the tunneling step, the electric field due to the ionic potential is neglected compared to the laser electric field. With these assumptions the equation of motion for the classical electron becomes especially simple:

$$\frac{\mathrm{d}\vec{v}}{\mathrm{d}t} = -\frac{e}{m}\vec{E}(r,t). \tag{2.6}$$

Assuming a homogeneous field $E(r,t) = E(t)$ this equation is readily solved for an electron emitted at time t_0:

$$\vec{v}(t,t_0) = \frac{e}{m}\cdot\left(\vec{A}(t) - \vec{A}(t_0)\right) + v(t_0) \tag{2.7}$$

where $\vec{A}(t) = -\int_{-\infty}^{t}\mathrm{d}t'\,\vec{E}(t')$ is the vector potential and $v(t_0)$ is the initial velocity. As mentioned above, we assume here an initial velocity of zero. The electron position is given by:

$$\vec{r}(t,t_0) = \frac{e}{m}\cdot\left(\vec{B}(t) - \vec{B}(t_0) - \vec{A}(t_0)\cdot(t-t_0)\right) \tag{2.8}$$

where we have defined $\vec{B}(t) = \int_{-\infty}^{t}\mathrm{d}t\vec{A}(t)$. The condition for recollision is given by $\vec{r}(t_\mathrm{r},t_0) = 0$ for the rescattering time $t_\mathrm{r} > t_0$. This equation can easily be solved numerically and in the case of a linearly polarized laser pulse reduced to one dimension. For a continuous wave (cw) laser with $E(t) = -E_0\cos(\omega t)$ the vector potential is given by $A(t) = \frac{E_0}{\omega}\sin(\omega t)$ and $B(t) = -\frac{E_0}{\omega^2}\cos(\omega t)$.

The resulting trajectories for a single cycle of a cw laser are shown Fig. 2.3 b) together with an exemplary tunnel emission rate (gray area). Several important observations can be made within this simple model: Firstly, electrons emitted before the peak of the electric field do not recollide and are therefore called direct electrons (black line). Secondly, the other electrons rescatter about 3/4 of an optical cycle after their emission (green line), close to the zero-crossing of the field. Finally, if the electrons rescatter elastically, their velocity $v(t_\mathrm{r},t_0)$ is reversed upon recollision. Therefore, they can be accelerated for roughly an additional half-cycle compared to direct electrons and can reach higher velocities as evident from the slope of the depicted curves. We will revisit this point when discussing strong-field photoelectron spectra below.

It is worth mentioning that in the SFA, the classical equations of motion can be made dimensionless by the transformation $t \to \varphi/\omega$, where φ is the phase of the driving laser, and introducing the ponderomotive potential U_p as characteristic energy scale. This transformation results in a characteristic length scale which is the amplitude of the oscillatory electron motion (Fig. 2.3 b), the so-called quiver amplitude given by $l_\mathrm{q} = eE_0/m\omega^2 \approx 1.36\,nm\cdot\lambda[\mu m]^2\cdot\sqrt{I[10^{14}W/cm^2]}$.

In order to be able to describe for quantum effects such as interferences in strong-field photoelectron spectra or the phase of the dipole in HHG (see Chapter 6), we shortly have to consider the quantum solution to the problem. This paragraph closely follows Ref. [74]. We recommend Ref. [75] for more detailed derivations and Ref. [76] for a more extensive overview. In the dipole approximation, the Schrödinger equation for a free electron (SFA) in the velocity gauge,[75] and momentum space reads:

$$i\hbar\partial_t\psi(k,t) = \frac{1}{2m}\Big(k + eA(t)\Big)^2\psi(k,t), \tag{2.9}$$

where k is the canonical momentum and $\hbar$ is the reduced Planck constant. This equation is solved by straight-forward integration and yields the eigenstate of an electron in an oscillating electric field, the so-called Volkov-state ψ_V:

$$\psi_\mathrm{V}(k,t) = \psi_\mathrm{V}(k,t_0)\cdot\exp\left(-\frac{i}{\hbar}\int_{t_0}^{t}\frac{1}{2m}\Big(k+eA(t')\Big)^2\mathrm{d}t'\right). \tag{2.10}$$

The term in the exponent is commonly referred to as Volkov-phase. In the velocity gauge the instantaneous velocity v is related to the canonical momentum by $mv = k + eA$. Furthermore, from Eq. 2.7, $mv = e[A(t)-A(t_0)] = eA+k_0$, which means that the expression under the integral can be identified with the time-dependent kinetic energy of a classical particle. Therefore, the Volkov-phase is just the classical action integral[77]. Furthermore, the canonical momentum k is identical to the final kinetic momentum k_0 (since $A(t\rightarrow\infty) = 0$ for an oscillating laser field). This also allows to attribute a quantum phase to a classical trajectory. The quantum-classical correspondence and the success of the three-step model is related to the Ehrenfest theorem[74] and the fact that the Volkov-state describes a free-electron.

Fully quantum mechanical descriptions of ATI[78] and HHG (Lewenstein model)[79] generally apply the SFA and use the Volkov-solution to expand the continuum wavefunction. The resulting integral equations are typically solved by applying the saddle-point approximation making use of the rapidly oscillating Volkov-phase. The solutions of the saddle-point equation can be identified with quantum orbits that are closely related to the classical trajectories. However, unless the ionization potential is neglected[79], generally complex emission times, rescattering times and momenta and tunnel exits are required[63], where the complex parts can be related to probability amplitudes. These complex trajectories can also be understood in terms of Feynman path integrals[80].

Besides full-TDSE simulations[81] and time-dependent density-functional theory (TDDFT)[82], recently Classical Trajectory Monte Carlo (CTMC)[83] or Classical Wigner Propagation (CWP) methods[84], where an ensemble of electrons with initial conditions derived from the initial wavefunction are propagated classically, have become increasingly popular in modeling attosecond experiments. These quasiclassical methods allow the incorporation of complex effects and typically show a much more favorable scaling of the calculations.

In this thesis, we will mostly stay in the classical picture, especially for the description of photoemission in spatially varying near-fields from nanostructures (Chapter 7). However,

the classical-quantum correspondence is used in the description of the phase of the HHG dipole, and the numerical simulations of HHG in Chapter 6 make use of the Lewenstein model. Note, that the electron dynamics in the continuum for attosecond streaking is described in the same theoretical framework as discussed here, by considering an electron that is born by linear photoemission through an isolated attosecond pulse with an initial velocity v_0. A brief overview of attosecond streaking is presented in Sec. 3.3.1.

2.2.3 Strong-field photoemission spectra

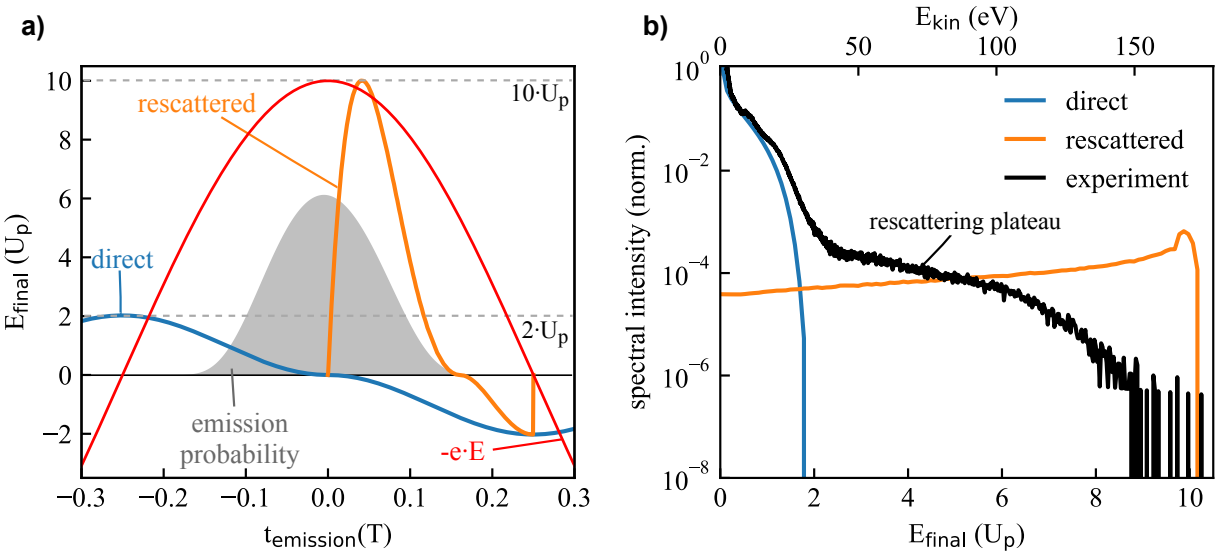

Figure 2.4: ATI spectra in the SMM: a) final electron kinetic energies of direct (blue) and rescattered (orange) electrons calculated for the central cycle of a multicycle pulse. The sign indicates the final emission direction. The force of the laser electric field is also shown (red line) together with the tunnel emission probability (gray area). b) Spectral contribution of the half-cycle considered above and comparison with an experimental ATI spectrum recorded in nitrogen using a time-of-flight spectrometer (see Chapter 7 for details; central wavelength 750 nm, T_{FWHM} =4.5 fs). The transition from the direct electrons to the rescattering plateau is visible as a kink in the spectrum and occurs close to $2\,U_p$. In the calculation a uniform rescattering probability of $5 \cdot 10^{-3}$ has been assumed.

One major success of the SMM is that it can explain the main features of strong-field photoemission spectra, also often called above-threshold ionization spectra (ATI), that stem from the different contributions of direct and rescattered electrons. This difference is illustrated in Fig. 2.4 a) which shows the relation between the emission time and the final kinetic energy of the photoelectrons for the central half-cycle of a multicycle laser field calculated in the three-step-model in one dimension. The sign of the curves indicate the final emission direction. The force of the electric field (red line) and ADK-emission rate (gray area) are also shown. Direct electrons (blue line) can reach a maximum final

kinetic energy of $2\,U_p$, which is determined by the vector potential $A(t_0)$ (see Eq. 2.7). In contrast, rescattered electrons (orange line) can acquire up to $10.007\,U_p$, since they can be accelerated effectively up to two consecutive half-cycles due to the reversal of their velocity upon rescattering, as mentioned above (see Fig. 2.3 b)). Note that the direct electrons that are emitted after $t = 0$ cross the origin but do not interact with the parent ion due to the finite rescattering probability.

The contribution to the photoelectron spectrum can be calculated by weighting the final energies emitted in the positive direction with the emission rate, which is shown in b) together with an experimental ATI spectrum (black line) from molecular nitrogen. Direct electrons (blue line) lead to a distribution peaking at zero and quickly decaying with increasing energy up to $2\,U_p$. In contrast, rescattered electrons (orange line) form a plateau-like structure that reaches up to $10\,U_p$, the so-called "rescattering plateau".

The difference in the shape of the two contributions originates from the relation of the final energy curves to the emission probability shown in a). Direct electrons are emitted with close to zero final kinetic energy around the maximum of the emission rate at $t = 0$ and the maximum energy of $2\,U_p$ is only reached when the tunneling rate is effectively vanishing ($t = -0.25T$). For rescattered electrons the final kinetic energy is also zero at $t = 0$ but quickly increases and reaches its maximum at $t_{max} \approx 0.04T$ before decaying again. The fact that the maximum is reached at a finite tunneling probability leads to the plateau. Moreover, since emission times around t_{max} all result in similar final energies, a peak is formed at the cutoff.

In the experimental spectrum the rescattering plateau with the $10\,U_p$-cutoff is clearly visible and the $2\,U_p$-cutoff of direct electrons appears as a kink in the spectrum. These two features can be used to estimate the experimental U_p and intensity in the experiment (see Eq. 2.5), here roughly 17 eV and $3.3 \cdot 10^{14}\mathrm{W/cm^2}$, respectively. The direct cutoff and rescattering cutoff and plateau are a universal feature of ATI spectra since they are a consequence of the electron dynamics in free space and have been observed from atoms[85], molecules[86] and nanosystems[45, 87]. However, if the electric fields around nanostructures vary on a spatial scale comparable to the quiver amplitude, significant modifications can occur[88, 89], which are briefly discussed in Sec. 2.4.

In the experimental data the peak at the cutoff is suppressed compared to the simple calculation, which can be explained by the drastic simplifications in the 1d-model, most importantly the omission of any quantum mechanical aspects, the spreading of the wavefunction in the other two dimensions[90] and the double-differential scattering cross-section for the rescattering[91] with the parent ion. Moreover, in the experiment several half-cycles with different cutoff energies contribute and averaging over the focal region occurs. Nevertheless, the contributions at the cutoff of different half-cycles usually cause characteristic CEP-dependent variations in the rescattering plateau, which can be resolved experimentally (see e.g. [92]).

Finally, for laser pulses with smaller bandwidth than in Fig. 2.4 b), i.e. longer pulses, pronounced multiphoton peaks are visible in the kinetic energy spectrum. In the time-domain they can be understood in terms of the interference of the contributions from different cycles. Since they are separated by the oscillation period T of the driving laser,

interference leads to oscillations in the energy domain of $\hbar\frac{2\pi}{T}$, which equals the photon energy of the driving laser. For this picture the term temporal multislit (see e.g. [87]) has been coined, since the more cycles contribute, the sharper the photon peaks become analogous to a multislit interference experiment.

2.3 High-harmonic generation

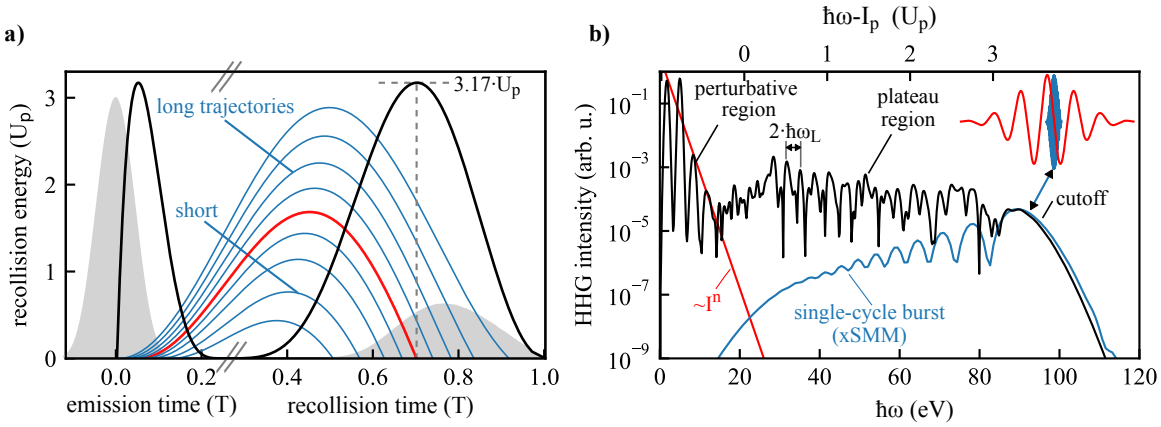

Figure 2.5: a) Recollision energy versus the phase of the laser field at the time of emission (left) and recollision (right) together with the electron trajectories (blue lines) calculated using the SMM. The emission probability and recollision rates are also shown (gray area). A maximum recollision energy of $3.17\,U_p$ is reached. Below the cutoff, two trajectories lead to the same final energy and are classified into short and long trajectories. b) HHG spectrum of a single atom calculated using the Lewenstein model[79] together with the single cycle burst of the extended simpleman's model (xSMM). The laser pulse and single-cycle burst are shown in the top right corner. Photon peaks are spaced by double the photon energy.

Besides rescattering, HHG is one of the processes that can occur upon recollision of the electron with the parent ion, leading to the emission of a photon with an energy given by the sum of the kinetic energy and the binding energy. In this thesis we will focus on HHG in noble gases as a source for isolated attosecond pulses. What makes HHG an intriguing source for attosecond physics is the intrinsic temporal sub-cycle synchronization of the emitted radiation with the driving laser and the coherent nature of the generation process. The latter implies that the HHG radiation has laser-like spatial and temporal coherence properties at photon energies far beyond the region where traditional active laser media are available.

The intrinsic temporal synchronization to the driving laser field can be understood in terms of the recolliding electron trajectories in the SMM model within the SFA. This is

illustrated in Fig. 2.5 a) where the dynamics within an individual laser cycle is considered. The emission time of the electrons is confined through the tunneling rate (gray area) to the fraction of a half-cycle around the peak of the laser field. As mentioned above, for a constant electric field amplitude considered here, only electrons emitted after the maximum lead to recolliding trajectories (blue lines). Since the process is driven by the electric field, the recollision times are determined by the emission time, resulting in the sub-cycle synchronization between emitted HHG and driving laser.

The recollision energy (black line), shown for both the emission and recollision phase, reaches up to $3.17\,\mathrm{U_p}$. For lower energies, two different trajectories lead to the same final energy. Depending on the time of recollision with respect to the cutoff trajectory (red line), they can be classified into long and short trajectories. However, due to phasematching, usually only short trajectories are observed in experiment (see Sec. 2.3.1). In a laser pulse each half-cycle leads to an emission burst resulting in an attosecond pulse train (APT). In order to extract an isolated attosecond pulse (IAP), gating techniques are required as discussed below in Sec. 2.3.3.

The simulated HHG spectrum of a single atom using the quantum-mechanical Lewenstein model [79, 93](black line) is shown in Fig. 2.5 b). The driving laser pulse is depicted in the top right corner. Similar to the ATI spectra, a plateau region below the cutoff of $3.17\,\mathrm{U_p}$+$\mathrm{I_p}$ is observed, as predicted in the three-step model in a). The low photon energy region below I_p can not be understood in terms of the SMM, since it is dominated by bound and quasi-bound electrons, which results in a perturbative scaling of the spectrum $\propto I^n$, where n is the photon order. Multiphoton peaks are visible at odd harmonics that are spaced by two times the photon energy $\hbar\omega_\mathrm{L}$ since every half-cycle contributes ($\Delta t = T/2 \rightarrow \Delta E = 2\hbar\omega_\mathrm{L}$), leading to spectral interference. Note that in the cutoff region only a single half-cycle burst contributes and therefore no interference occurs. Even harmonics can only be observed for systems breaking inversion symmetry, either in the electronic system, e.g. for a molecule, or in the driving field(see e.g. [94]).

For comparison, the single cycle burst from a) is also shown (blue line). It is calculated by approximating the HHG dipole $d(t)$ as the product of the squareroot of the recollision rate $r(t)$ as envelope function with an instantaneous carrier-wave frequency given by the sum of the rescattering energy $E_\mathrm{rec}(t)$ and the ionization potential and subsequent Fourier transformation, similar to Refs. [95, 96]:

$$d(t) = r(t) \cdot e^{+i\int_{-\infty}^{t} E_\mathrm{rec}(t')+I_\mathrm{p}\,\mathrm{d}t'} \tag{2.11}$$

We have used the same approach in Ref. [94] and refer to it as extended SMM (xSMM). The visible fringes originate from the intraburst interference of short and long trajectories. Since phasematching suppresses long trajectories, as discussed in Sec. 2.3.1, these interferences are again usually not prominent in experiments.

So far, the coherent nature of the HHG process has only been mentioned, however it has important consequences. In order to understand its origin, we have to consider the quantum mechanical picture. The electron wavefunction $|\psi\rangle$ can be approximated as the sum of the ground state $|0\rangle$ and the continuum wavefunction expressed in terms of

Volkov-solutions $|\psi_V\rangle$ (Eq. 2.10) [75]:

$$|\psi\rangle = a(t)\,|0\rangle + \int \mathrm{d}k\, b_\mathrm{k}(t)\,|\psi_{\mathrm{V,k}}\rangle\,, \tag{2.12}$$

where $a(t)$ and $b_\mathrm{k}(t)$ are the amplitudes of the ground state and the Volkov-state with quantum number k, respectively. The expectation value of the HHG-dipole $P(t) = \langle\psi|r|\psi\rangle$ can now be calculated:

$$P(t) = a(t) \int \mathrm{d}k b_\mathrm{k}(t)\,\langle 0|r|\psi_{\mathrm{V,k}}\rangle + c.c., \tag{2.13}$$

where *c.c.* is the complex conjugate and we have ignored continuum-continuum-transitions and assumed a ground state without dipole moment. The important point to notice is that the ground state amplitude $a(t)$ appears in the expression, as the HHG-dipole is a consequence of the interference of the bound state with the continuum wavefunction. For a fully-depleted ground-state no HHG occurs. When visualizing the electron probability density in space, this interference leads to rapid oscillations in the region with non-negligible bound state density. This finding also implies that the strong-field recollision of electrons is not enough, but the coherence of the ground state is equally important for HHG emission. The most significant consequence is that due to the coherence the emitted electromagnetic fields of an ensemble of N atoms can add up constructively, if properly phasematched, leading to a scaling of N^2 in intensity. This is in contrast to the intensity of incoherent processes that only scales with N. For small N, however, as found e.g. in the first experiments that tried to produce HHG in the enhanced near-fields of nanostructures[97, 98, 99, 100, 101], incoherent processes can dominate the emitted radiation.

In this thesis, HHG is driven by few-cycle pulses centered at around 750 nm and intensities of around $5 \cdot 10^{14}\mathrm{W/cm}^2$ which lies in the tunneling regime and results in HHG cutoffs of around 100 eV in the extreme ultraviolet region (XUV). Going to higher energies is in principle possible by either increasing the intensity or the wavelength since $U_\mathrm{p} \propto \lambda^2 I$. Unfortunately the single atom HHG efficiency in a given energy range drops dramatically with the driving wavelength, scaling as $\propto \lambda^{-5.5\pm0.5}$, which can only partly be explained by the longer diffusion time of the wavepacket in the continuum[102, 103, 104]. Going to higher intensities is ultimately limited by the depletion of the ground state, but already at much lower intensities phasematching problems occur. Phasematching is discussed in the next section.

2.3.1 Phase matching of HHG

In order to obtain a coherent buildup of HHG along the propagation axis (z) as the driving laser travels through the medium, the newly emitted HHG radiation at z_0 must interfere constructively with the radiation arriving from prior positions $z_0 - \Delta z$. This is referred to as phasematching and is quantified in terms of the phase-mismatch Δk. Compared to conventional, perturbative harmonic generation, such as second harmonic generation,

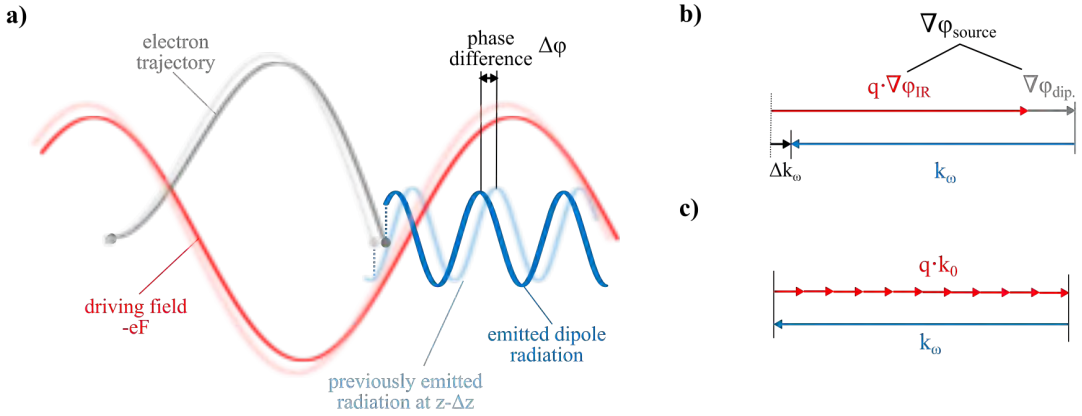

Figure 2.6: Phase matching of HHG: a) illustration of the different contributions to the phase mismatch. In addition to different phase-velocities of driving laser pulse (red) and HHG radiation (blue), the change of the driving pulse, which in turn affects the electron trajectory, influences the phase of the HHG dipole thereby contributing to the phase mismatch. Semitransparent lines indicate the fields and trajectory at an earlier position along the propagation direction. b) schematic representation of the HHG phase mismatch: source term contribution can be separated into the driving field (red) and dipole source term (gray) which has to be compared to the wavevector of the HHG radiation (blue). c) Simplified situation when only the wavevectors of the driving field and the HHG radiation contribute to the phase mismatch.

phasematching of HHG is considerably more complicated, mainly because of three factors. Firstly, the order of the harmonics q is generally much higher ($q \sim 15-100$), thereby phase changes of the driving laser result in a factor q higher phase change for the harmonics. Secondly, ionization changes the properties of the medium during the driving laser pulse duration. Finally, the phase of the HHG dipole for a given photon energy depends non-trivially on the intensity and wavelength of the driving laser.

The phase-mismatch Δk at the q-th harmonic is defined as[105]:

$$\Delta k(\omega_q) = k_{\omega_\mathrm{q}} + \nabla\phi_{\mathrm{source}}, \tag{2.14}$$

where k_{ω_q} is the wavevector of the harmonic, ∇ is the spatial gradient and ϕ_{source} is the phase of the source term. Note that the '+'-sign is a consequence of the employed $\exp(+i\omega t - kx)$-convention (therefore $k = -\nabla\phi$). The source contribution can be separated into the phase of the driving laser ϕ_{IR} multiplied by the harmonic order q and the intrinsic phase of the HHG dipole ϕ_{dipole}, which results in:

$$\Delta k(\omega_q) = k_{\omega_q} + q \cdot \nabla\phi_{\mathrm{IR}} + \nabla\phi_{\mathrm{dipole}}. \tag{2.15}$$

The three different contributions to the phase-mismatch are illustrated in Fig. 2.6 a). The intrinsic dipole phase is a result of the electron propagation in the continuum and therefore affected by the details of the driving laser pulse between emission and recollision. The classical respresentation of the phase-mismatch in terms of wavevectors is shown in b).

The advantage of Eq. 2.15 is that it allows to discuss the individual contributions separately. In the following, we will first consider how the ionization induced dispersion of the driving laser affects the HHG phase matching, leading to the concept of the critical ionization fraction and phase-matching cutoff. Subsequently, we will focus our discussion on the intrinsic HHG dipole phase. Both aspects are important in order to understand the results in Chap. 6. The presentation below will closely follow our discussion in Ref. [29].

2.3.2 Phase-matching cutoff and critical ionization fraction

For a driving laser pulse that is slowly varying, the gradient of the dipole phase as well as the Gouy phase can be neglected. The phase-mismatch is therefore simply given by the wavevector difference of the driving laser (multiplied by q) and HHG radiation, which depends on the contribution of the neutral atoms and the plasma generated by ionization through the driving laser. Thus, Δk is determined by the fraction of ionized gas atoms η[106, 107, 108]:

$$\Delta k = q \cdot k_0 \cdot \frac{\rho}{\rho_0} \cdot \left[(1-\eta)\cdot(n_{\omega_q} - n_{\omega_0}) - \eta \cdot \frac{\rho_0 e^2}{2\epsilon_0 m \omega_0^2} \cdot \left(\frac{1}{q^2} - 1\right)\right], \tag{2.16}$$

with the electron mass m, the particle number density ρ, and wavevector k_0 and angular frequency ω_0 of the driving laser. The angular frequency of the q-th harmonic is given by $\omega_\mathrm{q} = q \cdot \omega_0$. The refractive indices n_{ω_0} and $n_{\omega\mathrm{q}}$ at the fundamental and harmonic

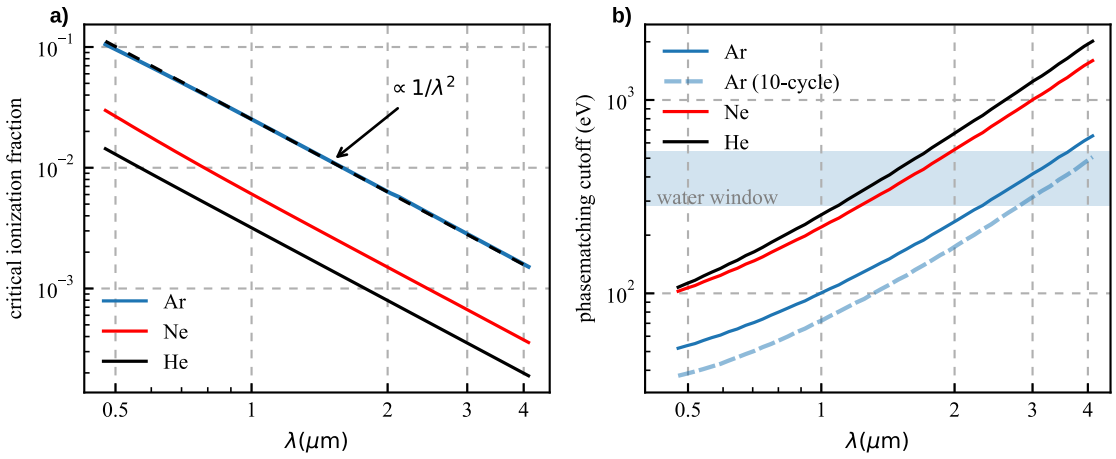

Figure 2.7: Critical ionization fraction and phase-matching cutoff for a 1.5-cycle pulse (intensity FWHM): a) Wavelength-dependence of the critical ionization fraction for argon (blue), neon (orange) and helium (green), which is to a very good approximation proportional to $1/\lambda^2$ (dashed black line). b) The resulting phase-matching cutoff calculated with the tunneling rate of Ref. [65]. For argon, also the result for a 10-cycle pulse is plotted (thick blue dashed line) for comparison. The water window is indicated by the light blue area.

frequency are given for the reference number particle density ρ_0 . The first term in the bracket describes the neutral gas contribution while the second term represents the plasma dispersion. For high harmonic orders q the XUV contribution to the phase-mismatch can be neglected ($n_{\omega q} \approx 1$ and $1/q^2 \approx 0$) for most practical applications[107], implying that the generated XUV propagates with the speed of light c. With this assumption, independent of the pressure $p \propto \rho$, the contribution of the neutral gas atoms is negative, while the plasma term is positive, and only at the so-called critical ionization fraction η_{cr} perfect phase-matching $\Delta k = 0$ is realized[106]. As soon as geometric dispersion effects of the driving laser have to be considered, the critical ionization fraction becomes pressure dependent (see .e.g. [109, 110]), which is, however, not discussed here.

For a laser pulse, the plasma density increases during each half-cycle due to tunneling photoemission. If the critical ionization fraction is exceeded, no phasematching of HHG is possible anymore under the above assumptions. The highest XUV energy that can be phasematched is therefore determined by the intensity for which the critical ionization fraction is reached at the central cycle of the pulse. This is the so-called phase-matching cutoff. If the intensity is further increased, phase-matching is achieved already before the main peak at lower XUV cutoff energies. Additionally, if the phase-mismatch in the preceding and following half-cycle is significantly different from zero, i.e. for high particle densities ρ (high pressures), this transient phase-mismatch can be used for gating in isolated attosecond pulse generation [111, 112, 113, 114, 108] (see also Sec. 2.3.3 and Fig. 2.9 b).

The wavelength dependence of the critical ionization fraction for argon, neon and helium

is shown in Fig. 2.7 a) which is calculated using the refractive indices of Refs. [115, 116]. The wavelength scaling is close to $1/\lambda^2$. With increasing ionization potential I_p of the noble gas atom, the neutral gas dispersion at a considered wavelength decreases and thereby also the critical ionization fraction. Nevertheless, larger I_p leads to a higher phasematching cutoff, as illustrated in b), due to the highly nonlinear tunneling rate. The shown curves are calculated for a 1.5-cycle pulse using the ADK-tunneling rate[65]. For comparison, we also show the curve for a ten-cycle pulse in argon (blue dashed line), which has a lower phasematching cutoff since more cycles contribute to the ionization before the maximum intensity is reached. The blue area indicates the photon energy range of the so-called water window, which would allow interesting applications in biological samples immersed in a natural water environment (see Chap. 6 for more details).

Phase-matching contribution of the dipole phase

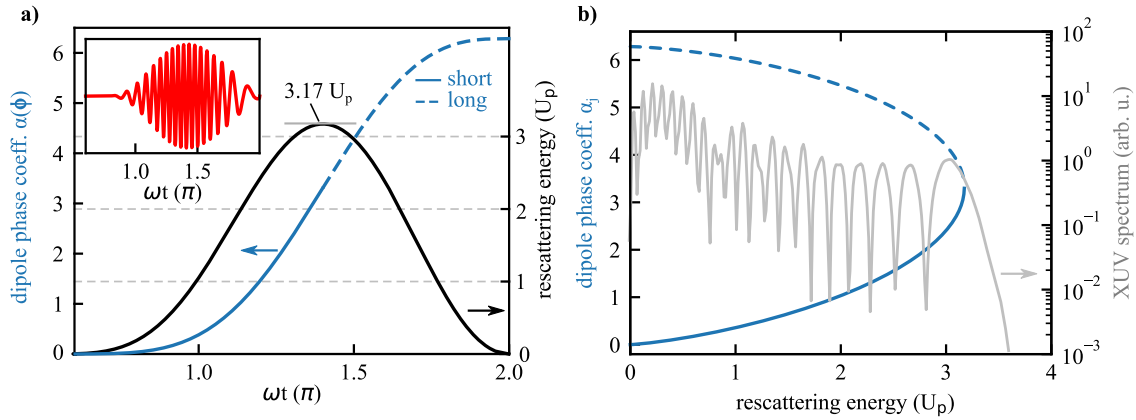

Figure 2.8: The dipole phase coefficient: a) in the temporal domain: short (long) trajectory contributions are indicated by solid (dashed) lines. The derivative of the dipole phase coefficient equals the rescattering energy (black line). The inset shows the dipole oscillation. b) dipole phase coefficient in the spectral domain. The XUV spectrum from a 1.5-cycle pulse in argon obtained by the Lewenstein model is also shown (driving wavelength 1 μm, intensity $2.8 \cdot 10^{14}\mathrm{W/cm^2}$) (gray line).

The HHG dipole is the result of the interference of the recolliding electron wavepacket and the part of the wavefunction left in the ground state, as discussed in Sec. 2.3. Nevertheless, utilizing the SFA, the quantum-classical correspondence and the fact that the electron dynamics in the continuum can be expressed in terms of the characteristic energy and and time scale, a relatively simple expression for the HHG dipole phase can be derived. For a continuous-wave driving laser at frequency ω_0 and a HHG photon energy $\hbar\omega_q$, it can be written as[105, 117]:

$$\phi_{\mathrm{dipole}}(\omega_q) = \alpha \frac{U_p}{E_{\mathrm{photon}}} + \frac{I_p}{\hbar}(t_{\mathrm{rec}} - t_0) - \omega_q \cdot t_{\mathrm{rec}}, \tag{2.17}$$

where U_p is the ponderomotive potential, $E_\mathrm{photon} = \hbar\omega_0$ the photon energy of the driving laser, t_rec is the recollision time at which the XUV photon is generated, t_0 is the corresponding emission time and I_p is the ionization potential. The first term originates from the electron dynamics in the continuum. The HHG dipole coefficient α is a function of the recollision phase $\phi = \omega_0 t_\mathrm{rec}$ and further discussed below. The second term stems from the evolution of the ground state between emission and recollision time. The dipole phase has to be determined with respect to a reference wave $\exp(i\omega_\mathrm{q} t)$ which is responsible for the last term.

Within the Simple Man's Model (SMM)[67], for an electron emitted at phase ϕ_0 initially at rest, the dipole coefficient at the recollision phase ϕ is given by:

$$\alpha(\phi) = 2 \cdot \int_{\phi_0}^{\phi} \left(\sin\phi_0 - \sin\phi'\right)^2 \mathrm{d}\phi', \tag{2.18}$$

which is basically the integral over the normalized electron kinetic energy (compare to Eq. 2.7 with $E(t) \propto \cos\omega_0 t$). The dipole phase coefficient α therefore corresponds to the normalized phase of the electron wavefunction at the time of recollision and is shown in Fig. 2.8 a) (blue line). Consequently, the derivative with respect to ϕ results in the normalized rescattering energy (black curve) with the well known 3.17-U_p-cutoff.

For practical purposes it would be more convenient to express α in terms of the HHG photon energy, which is observable experimentally. For this goal, we briefly reconsider the relation of the high-harmonic photon energy to the recollision time (phase) and recollision energy, which is given essentially by the time derivative of the first two terms in Eq. 2.17:

$$\omega_\mathrm{q} = \left(\frac{\mathrm{d}\alpha}{\mathrm{d}t}\right)\frac{U_\mathrm{p}}{E_\mathrm{photon}} + \frac{\mathrm{d}}{\mathrm{d}t}\left(\frac{I_\mathrm{p}}{\hbar} \cdot (t_\mathrm{rec} - t_0)\right). \tag{2.19}$$

From the inspection of above equation, we see that in addition to the sum of the ionization potential and the rescattering energy, the ground state evolution adds a small additional term to the photon energy through the dependence $t_0(t_\mathrm{rec})$, which is in agreement with more rigorous quantum models[79]. The relation between photon energy and recollision energy is now given by $E_\mathrm{recollision}/U_\mathrm{p} \approx (\hbar\omega_\mathrm{q} - 1.32 \cdot I_\mathrm{p})/U_\mathrm{p}$[117, 79, 118, 63].

The dipole phase coefficient in terms of the recollision energy is shown in b) (blue curve). Since two trajectories lead to the same energy, short trajectories (solid line) and long trajectories (dashed line) have to be distinguished which is accomplished by the index j. By comparing a) and b) the connection between the temporal and energy domain becomes obvious. For the rest of the thesis, we will utilize the dipole coefficient in the energy domain α_j.

We are now finally in a position to calculate the contribution of the dipole phase ϕ_dipole to the phase-mismatch by performing the derivative of Eq. 2.17 with respect to the propagation direction. Due to Eq. 2.19 most terms cancel and we are left with:

$$\frac{\mathrm{d}\phi_\mathrm{dipole}}{\mathrm{d}z} = \alpha_j \frac{\mathrm{d}}{\mathrm{d}z}\left(\frac{U_\mathrm{p}}{E_\mathrm{photon}}\right). \tag{2.20}$$

Since $U_\mathrm{p} \propto I/\omega_0^2$, with the driving laser intensity I and $E_\mathrm{photon} \propto \omega_0$, the dipole phase contribution to the phase-mismatch depends on the change of the driving laser intensity and carrier-frequency. This finding will be important in Chap. 6, where HHG phasematching with strongly reshaped laser pulses is investigated.

Several phenomena connected to phase-matching can be explained from Fig. 2.8 b) and Eq. 2.20. Firstly, it can be seen, why usually only short trajectories can be phase-matched if the driving laser varies in intensity along the medium. For short trajectories in the plateau region the contribution of the dipole phase coefficient varies from 0 to about 1, compared to 5-6 for long trajectories. Long trajectories can only be phase-matched efficiently under special conditions. Secondly, by noticing that Eq. 2.20 is in principle also valid for the derivative perpendicular to the propagation direction, we can conclude that compared to the short trajectories, the phase of the long trajectory contribution changes more rapidly when moving away from the propagation axis due to the intensity decrease. This results in a higher curvature of the phasefront of long trajectories and thereby a larger divergence as confirmed by experiments[119, 120, 121]. Finally, under normal conditions phase matching is achieved by putting the generating medium about half the Rayleigh length behind the focus. Ignoring the contribution of the medium, the positive phase-mismatch contribution of the Guoy-phase can be balanced by the negative dipole phase contribution caused by the decrease in driving laser intensity. This is in contrast to the regime where the driving pulse undergoes strong reshaping due to plasma effects, as discussed in Chap. 6.

2.3.3 Gating techniques for isolated attosecond pulse generation

In order to extract an isolated attosecond pulse, i.e. the contribution of a single half-cycle from the attosecond XUV/soft-x-ray pulse train, several gating techniques exist. Within this thesis we classify these techniques depending on whether the gating works on the single-atom level or on the macroscopic level, but other classification schemes exist (see e.g. [122]).

An example for a single-atom gating technique is amplitude gating[9], which is utilized in the experiments in this thesis and further illustrated in Fig. 2.9 a). The technique requires a CEP-stabilized few-cycle laser (red line; top). The instantaneous photon energy is shown as orange line. For the right CEP, only one half-cycle burst from the XUV emission (blue shaded area) contributes above a certain photon energy. By filtering out lower photon energies, i.e. using a transmission filter or multilayer mirror, an isolated attosecond pulse can be extracted. Another gating technique working on the single atom level is polarization gating[123, 124] and variants thereof[125, 126, 127], which make use of the fact that the recollision probability drastically decreases for elliptic polarization. Finally, in above-saturation gating, the ground state wavefunction is depleted in the leading part of the pulse through tunnel ionization, confining the highest XUV energies to a single half-cycle[128].

On the other hand, gating techniques on the macroscopic level work by ensuring that constructive interference of the HHG emitters only occurs for a single half-cycle. One example is phase-matching ionization gating[129, 114, 130], as illustrated in Fig. 2.9 b).

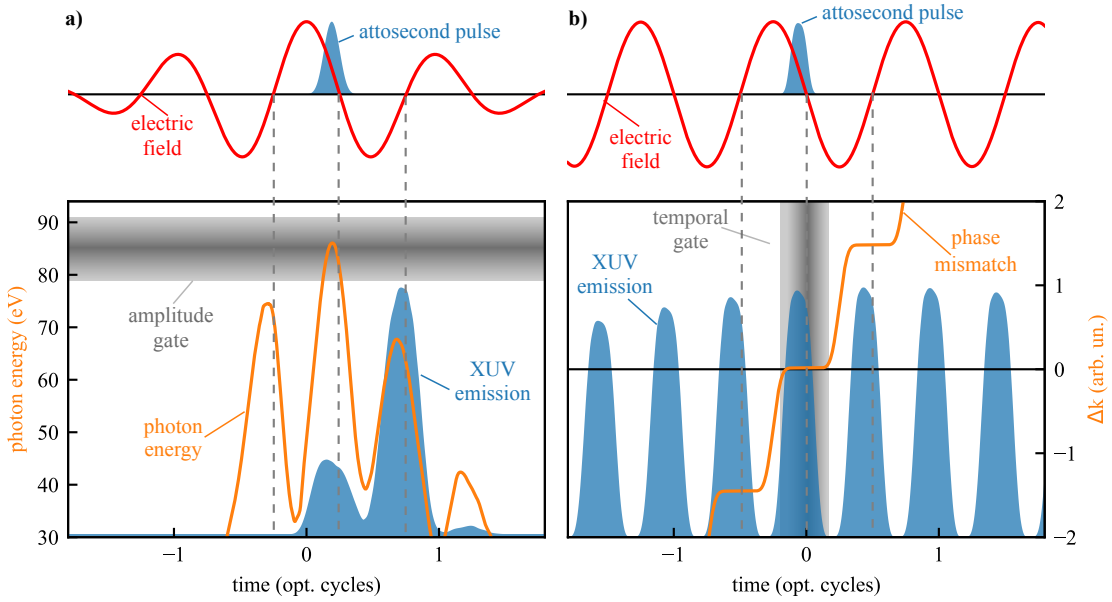

Figure 2.9: Illustration of different gating mechanisms for isolated attosecond pulse generation: a) amplitude gating and b) ionization gating. The driving laser pulse (red) and the resulting IAP (blue area) is shown above the panels. The maximum photon energy (orange line) reaches into the spectral gating window (gray area) only for one half-cycle emission burst. b) Ionization gating works on the macroscopic level by making use of phasematching. Due to the varying ionization degree, perfect phasematching is achieved only for a single half-cycle. Neighboring half-cycles are suppressed in the macroscopic buildup of the XUV pulse.

This technique also works for multicycle lasers and relies on the instantaneous HHG phase mismatch (orange line, see Sec. 2.3.1). In the beginning of the laser pulse, the dispersion of the neutral gas determines the phase mismatch. Since the plasma density keeps accumulating for later half-cycles, which counteracts the dispersion of the neutral gas, perfect phase matching can be reached for a single half-cycle. In neighboring half-cycles the coherent buildup of HHG is suppressed due to the phase mismatch, which results in an isolated attosecond pulse in the far-field even though the single-atom contribution consists of a pronounced APT. Another example is the attosecond lighthouse[131, 132], where a rotation of the wavefront of the driving laser field in the HHG focus leads to emission of the attosecond burst in separate directions.

Isolated attosecond pulses with a duration on the order of few 100 as can nowadays be produced fairly routinely. The shortest attosecond pulse demonstrated up to now had a duration of 43 as generated by a driving laser pulse centered at around 1600 μm wavelength and a duration of 11 fs utilizing amplitude gating[133].

2.4 Field enhancement and confinement on nanotips

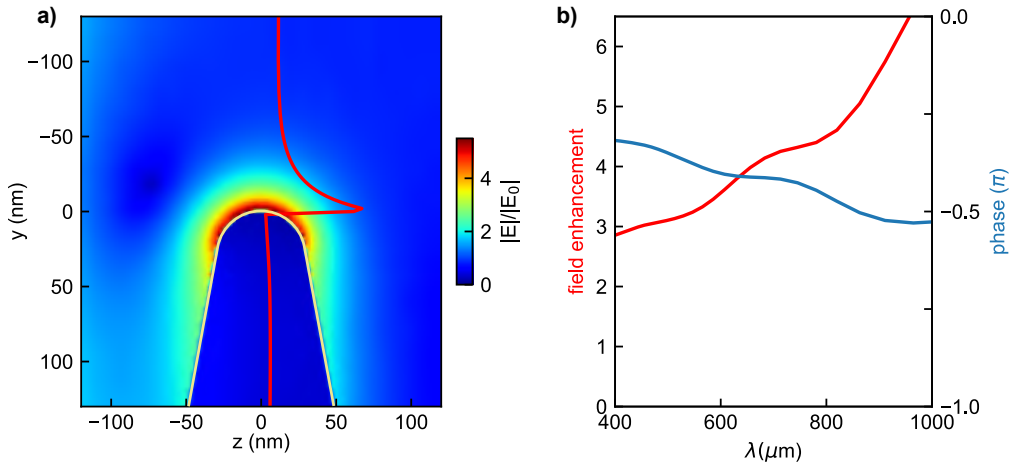

Figure 2.10: Field enhancement and response function of a nanotip: a) Field enhancement and field confinement on a tungsten nanotip with a radius of 30 nm and an opening angle of 10° calculated at a wavelength of 780 nm. The incident laser pulse is propagating in z-direction and polarized vertically. The red line shows the field amplitude on the nanotip axis. b) Amplitude (red line) and phase (blue line) of the response function at the apex of the nanotip.

The interaction of light with nanostructures leads to confinement and enhancement of the electromagnetic fields near the surface which constitutes the basis of nano-optics[134]. The length scale for the near-field decay (confinement) around the sharp geometric features

is given by its radius[135] which has found various applications for example in optical near-field microscopy well below the diffraction limit of light (see Sec. 7.1 for more examples). Moreover, mostly due to an analog of the lightning rod effect, the near-fields are enhanced at these hotspots[135] which can be used for sensing. The details of the field enhancement and confinement depend on the wavelength of the incident light λ_{inc} as well as the optical properties and exact geometry of the nanostructure.

Metal nanotips and their interaction with ultrashort laser pulses is the focus of Chap. 7. Nanotips represent a prototypical nano-optical hotspot and are therefore an ideal model system for studying the interaction ultrafast laser pulses with nanostructures. They are easy to produce by electro-chemical methods (see Sec. 3.1) and the obtained apex radii can routinely reach 50 nm and below, much smaller than the wavelength of the incident laser pulse. Compared to isolated nanospheres, nanotips can be electrically contacted and precisely placed within the focus.

The field enhancement compared to the incident field around the apex of a tungsten nanotip is shown Fig. 2.10 a) for an incident wavelength of 780 nm and an apex radius of 30 nm. The outline of the nanotip is shown as white line. The calculation has been performed with a commercial finite-difference time-domain (FDTD) software (Lumerical FDTD). The incident field is polarized along the y-axis. The magnitude of the near-field along the nanotip axis (red line) clearly shows the confinement to the length scale of the apex radius. A field enhancement factor up to 5 can be observed, which translates into more than an order of magnitude increase in intensity. Besides the lightning rod effect that dominates the response here, two resonant mechanisms can contribute to the field enhancement[135]. Firstly, for plasmonics materials, the localized surface plasmon resonance can contribute. Secondly, if the length of the nanostructure happens to be an odd multiple of $\lambda_{\mathrm{inc}}/2$, an antenna resonance might occur.

The wavelength dependence of the amplitude (red line) and phase (blue line) of the spectral near-field response function at the apex of the nanotip is shown in Fig. 2.10 b) for the spectral range covered by the laser pulses used in this thesis. From the near-field response the electric field in time for can be calculated for any incident pulse (see Sec. 7.2.2 for more details on the response function). As can be seen, the field enhancement increases with wavelength from around 3 at 400 nm to above 6 at 1000 nm. In the absence of resonances the field enhancement generally increases with the incident wavelength. Our laserpulses are mostly confined within 600-900 nm which results in an enhancement between 4 and 5. The relative phase only decreases slightly from around -0.4 π to marginally below -0.5 π.

The near-fields around nanostructures can significantly influence the strong-field photoemission dynamics. Firstly, due to the field enhancement, the strong-field emission regime can be reached with much lower input pulses that are available from oscillators at MHz repetition rates compared to the kHz rate provided by chirped amplifier systems. Moreover, the near-field confinement can affect the strong-field electron dynamics once the quiver amplitude is on the order of the field decay length[88], since the field that would drive the electrons back to the surface has already significantly decreased at the turning point. This quenching of the quiver motion leads to a reduction of the rescattering cutoff

well below 10 Up and can be characterized by an adiabaticity parameter δ, defined as the ratio of near-field decay length and quiver amplitude. Additionally, as shown in a publication by the author[89] which is not represented in this thesis, a shift of the low-energy peak to higher energies can be observed which can be interpreted in terms of a non-adiabatic ponderomotive shift. Since the quiver amplitude scales with λ^2, these two effects mostly play a role at longer wavelengths and can be ignored for our visible laser pulses. Additionally, the near-field decay also affects the attosecond streaking amplitude and phase for electrons emitted from the nanostructure and a related adiabaticity parameter has been introduced by the author in Refs. [25, 26] which is discussed in more detail in Chap. 7.

Chapter 3

Experimental foundations

3.1 Nanotip etching

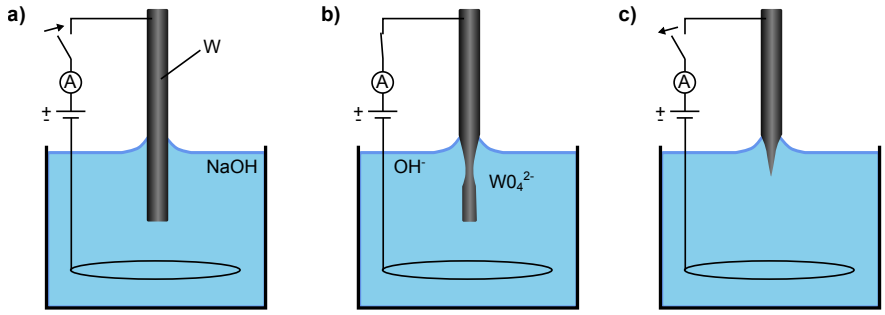

Figure 3.1: Overview over the nanotip etching process: a) a tungsten wire is immersed in NaOH and the etching process is initiated by applying an etching voltage. b) Thinning of the immersed wire through etching. Tungsten is dissolved into soluable tungstate ions WO_4^{2-}. c) Fast switch-off of the etching voltage after the etching process is finished.

The tungsten nanotips used in the photocurrent experiments presented in Sec. 7.3 were produced by an electrochemical etching setup described in Ref. [136] and built by Hirofumi Yanagisawa. The basic principle is shown in Fig. 3.1. A tungsten wire with a diameter on the order of 100 μm is immersed into a 5M NaOH solution (a). When a voltage is applied between the tungsten wire and the submerged ring electrode, the etching process starts which occurs predominantly around the meniscus at the interface of etchant solution, air and wire (b). Once the lower part is etched away, a nanotip is formed (c). In order to avoid further bluntening of the nanotip, the etching process has to be stopped as soon as possible. Since the sudden drop of the etching current indicates that the lower part of the wire is etched away, this can be achieved by switching off the etching voltage with the

help of a dedicated analog electronic circuit that measures the etching current (for further details see Ref. [136]).

A microscope image of a tungsten nanotip is shown in Fig. 3.2. The diameter of the tungsten wire is around 100 μm. The characteristic shape towards the nanotip stems from the etching process. The chemical etching process usually results in a very smooth surface on the shank of the nanotip[137] which is crucial for the spatially resolved experiments performed in Chap. 7. The gold nanotips in the attosecond streaking experiments were supplied by the group of Prof. Hommelhoff[51].

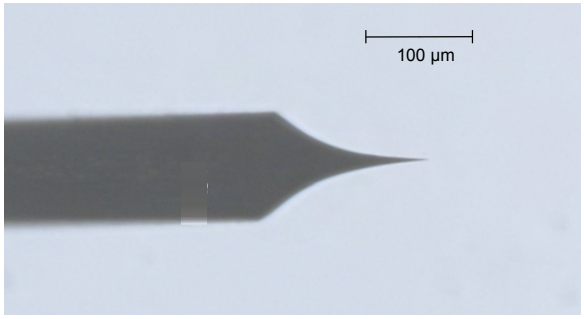

Figure 3.2: Microscope image of a tungsten nanotip produced with our nanotip etching setup.

3.2 Current measurements

3.2.1 Transimpedance amplification

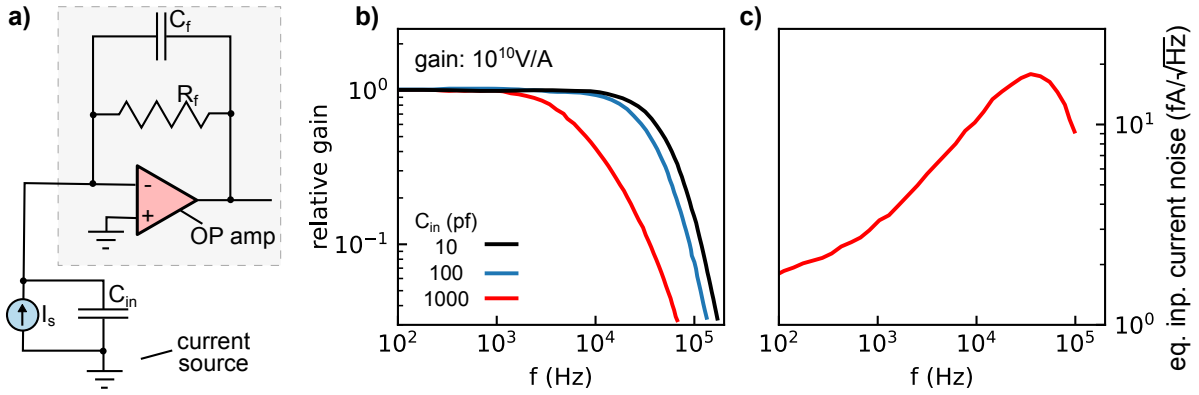

Figure 3.3: Transimpedance amplifier: a) schematic measurement circuit consisting of the current source and the transimpedance amplifier (gray box). b) Frequency dependence of the relative gain for various input capacitances and c) equivalent input current noise (data extracted from Ref. [138]).

For the sub-cycle resolved current measurements presented in Chap. 7 and Chap. 4 a transimpedance amplifier (TIA) is a key component which is also commonly found in e.g. photodiodes. TIAs convert a small current signal into a voltage signal. The conversion factor is given in units of $\frac{\mathrm{V}}{\mathrm{A}}$. Here, only the basic principle is presented, details can be found elsewhere (e.g. Ref. [139]).

The fundamental building block of a TIA is an operational amplifier (OP amp) and a feedback resistor with resistance R_f, as shown in Fig. 3.3 a). First, we consider low frequencies where any capacitances can be ignored. Here, the OP amp tries to cancel any voltage difference between its inputs due to the sensor current I_S by sending an opposite feedback current through the feedback resistor. Thus, R_f determines the current-to-voltage gain. For higher frequencies the input capacitance C_in starts to play a role. In order to avoid oscillations of the transimpedance amplifier, a feedback capacitance C_f has to be added[140].

Commercial high-gain, low-noise TIAs (FEMTO DLCPA-200) are used for our measurements. The relative gain and equivalent input current noise density of a comparable TIA (NF Corp. SA-607F2) with a fixed transimpedance gain of $10^{10}\,\frac{\mathrm{V}}{\mathrm{A}}$ are shown in Fig. 3.3 b) and c), respectively. The gain bandwidth decreases with increasing C_in. Moreover, at these high transimpedance gains, the 3dB-bandwidth of TIAs is limited to a few kHz-100kHz, which is significantly slower than would be required for the direct amplification of the fs-ns photocurrent in our measurements. As further discussed in Chap. 4, the detected signals in our experiments can therefore be better understood in terms of the total induced charge on the electrodes or equivalently as the temporal integral of the current. The equivalent current input noise (c) determines the minimum amount of current variation that can be measured and is fundamentally limited by Johnson (thermal) noise of the electronic components.

3.2.2 Lock-in detection

In addition to transimpedance amplifiers discussed above, for the sensitive detection of weak signals a lock-in amplifier is another crucial instrument and is used for both the current measurements in Chaps. 4 and 7 as well as the electro-optic sampling in Chap. 5. Usually, the modulation of the laser pulse is required at a reference frequency f_ref either by an optical chopper or by changing the CEP. This section closely follows Ref. [141] to which we refer for more details.

The fundamental working principle of lock-in amplification relies on the detection of an input signal within a narrowband frequency window around the reference frequency f_ref, thereby discarding noise at other frequencies. This is schematically illustrated in Fig. 3.4 a), which shows the signal (red line) and the detection bandwidth (blue area). In addition to the spectrally flat white noise (light blue area), there also appears so-called 1/f-noise at lower frequencies from various sources, such as mechanical and acoustical vibrations. As can be seen, with the help of the spectral gating, the lock-in amplifier is able to resolve signal amplitudes below the low frequency noise amplitude.

In the lock-in amplifier the input voltage signal V_s is multiplied with a reference signal

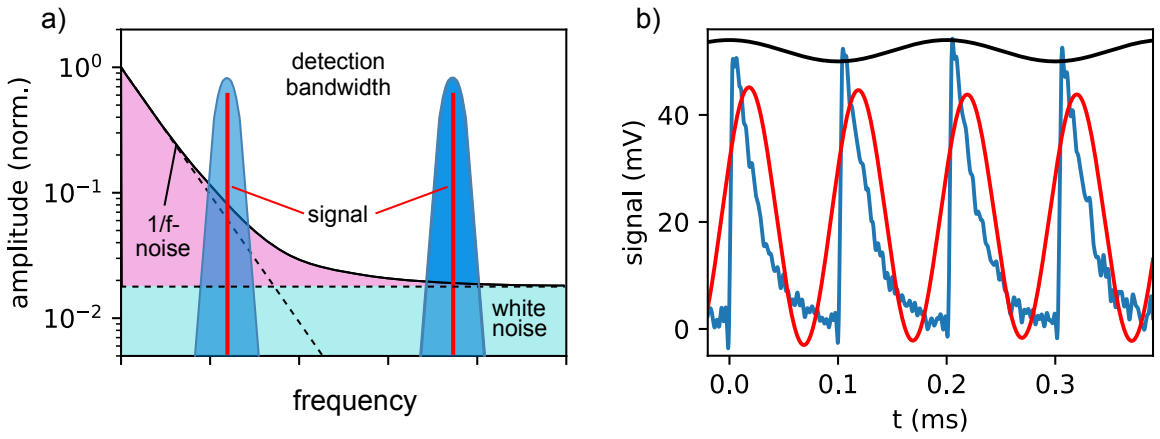

Figure 3.4: Lock-in detection: a) Signal (red line) and detection bandwidth (blue area). For lower frequencies, considerable $1/f$-noise is present while for higher frequencies practically only white noise is left. Due to the limited detection bandwidth, even signals that lie below the low-frequency noise amplitude can be resolved (adapted from Ref.[141]). b) Experimental input signal (blue line) together with the demodulation at the repetition rate f_{rep} (red) and $f_{\mathrm{rep}}/2$ (black line).

V_{ref} which is either a cosine or sine wave oscillating at f_{ref}. Modern lock-in amplifiers can perform both demodulations simultaneously which is most conveniently described in the complex domain as $V_{\mathrm{ref}} = \sqrt{2}\exp(-i\omega_{\mathrm{ref}}t)$. The multiplication yields the signal Z':

$$Z' = V_{\mathrm{s}} \cdot V_{\mathrm{ref}} = R \cdot \left(e^{+i\cdot(\omega_{\mathrm{s}}-\omega_{\mathrm{ref}})t+i\phi_0} + e^{-i\cdot(\omega_{\mathrm{s}}+\omega_{\mathrm{ref}})t-i\phi_0} \right), \tag{3.1}$$

where $\sqrt{2}R$ is the signal amplitude at f_{s}. Whether or not an additional factor $\sqrt{2}$ appears, depends on the details of the modulation (see also Appendix A), the convention of the lock-in manufacturer and how the signal amplitude is defined. If $f_{\mathrm{s}} = f_{\mathrm{ref}}$, the first term is quasi constant while the second term is oscillating with twice the reference frequency. The latter is eliminated by low-pass filtering of Z' resulting in the lock-in signal Z:

$$Z = Re^{i\phi_0} = X + iY. \tag{3.2}$$

The relation between the lock-in detection and an experimental input signal is further illustrated in Fig. 3.4 b). The input voltage pulses (blue line) after transimpedance amplification represent the signal from consecutive laser pulses. The signal component contributing to the demodulation at the repetition rate f_{rep} of the laser is shown as red solid line. Additionally, the signal was modulated at f_{rep} (black solid line), which is however not visible here due to noise components at other frequencies and only appears after averaging over many signal pulses. For completeness, boxcar averaging, where the signal is integrated over a well-defined temporal window can be advantageous over lock-in detection, if the signal of interest has a low duty cycle, i.e. is temporally well confined and most

of the time only noise is present[142]. This condition is not fulfilled for our signals and therefore lock-in detection is preferred.

3.3 Field-resolved measurement techniques

This section serves as an overview of the field-resolved techniques used in this thesis and is also intended as a reference for the discussion of more specific details. It might be helpful for some readers to first go through the experimental description in the later chapters to get a glimpse of the experimental implementation and applications, and then come back to this section.

Attosecond streaking is used for the characterization of isolated attosecond pulses and their driving laser pulses in the overdriven regime in Chap. 6 as well as for the characterization of nanoscale near-fields on a gold nanotaper (Chap. 7). The pump-probe measurements on semiconductors presented in Chap. 5 rely on electro-optic sampling (EOS). Tunneling ionization with a perturbation for the time-domain observation of an electric field (TIPTOE) and streaking of rescattering electrons are utilized in the measurement of the enhancend near-fields of a nanotip apex and the application to the spatio-temporal characterization of a vortex beam (Chap. 7). Finally, Chap. 4 studies the fundamental mechanism through which macroscopic currents in photoconductive sampling of optical fields are generated on the electrodes.

3.3.1 Attosecond streaking

Description

Attosecond streaking[12, 13] is a pump-probe scheme that relies on an isolated attosecond pulse (IAP) in the XUV/soft-x-ray range generated through HHG. It is used to characterize a co-propagating near-infrared laser pulse (red line) with a variable time-delay Δt. As shown in Fig. 3.5 a), the IAP (blue line) leads to the photoemission of an electron (black dot) from an atom (green circle) through linear absorption of an XUV photon. The emitted photoelectron is accelerated by the near-infrared laser pulse (red line) which leads to an increase or decrease of its final kinetic energy (or momentum) depending on the time-delay. The final momentum p_{final} can be calculated classically within the simpleman's model (see Sec. 2.2.2) for an electron emitted at time t_0:

$$p_{\text{final}}(t_0) = p_0 - eA(t_0), \tag{3.3}$$

where p_0 is the field-free final momentum. The change of the photoelectron spectrum thus allows the reconstruction of the vector potential $A(t)$ and thereby the electric field $E(t)$ of the streaking laser pulse. Usually, the IAP is generated by the streaking laser pulse in the first place resulting in intrinsic timing synchronization between both pulses.

A simulated attosecond streaking spectrogram, i.e. delay-resolved photoelectron spetra, is depicted in Fig. 3.6 a) (see e.g. also Figs. 6.2 and 7.3 for experimentally measured spectrograms). The central momentum shift closely follows $-eA$ (red dashed line).

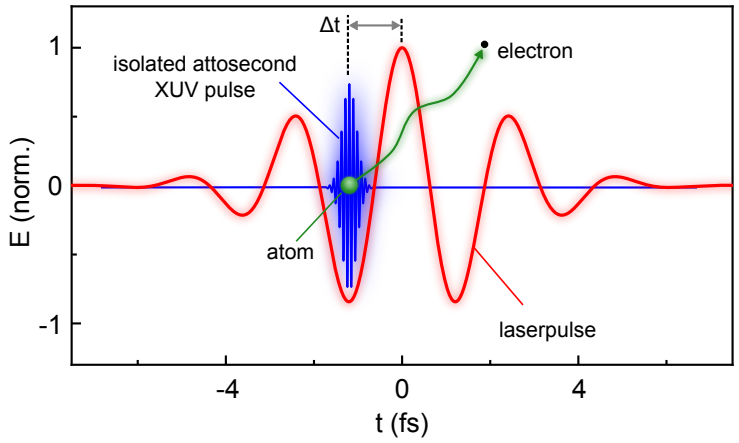

Figure 3.5: Principle of attosecond streaking: an isolated attosecond XUV pulse (blue line) photoemits an electron (black dot) from an atom (green ball) via linear photoemission and with variable delay Δt with respect to a near-infrared laser pulse (red line). After the emission, the electron experiences the electric field of the latter, leading to a variation of its final kinetic energy.

Attosecond streaking does not only allow the reconstruction of the laser pulse but also of the attosecond XUV pulse. This is qualitatively illustrated in Fig. 3.6 b) for a positively chirped XUV pulse, i.e. where the central photon energy under the envelope increases with time. Here, the width of the photoelectron distribution for a fixed delay changes depending on whether $-eA$ is decreasing or increasing in contrast to an unchirped XUV pulse (a). The reason can be seen in Fig. 3.6 c)-e), which shows the temporally resolved initial momentum distribution (false color plot) that directly reflects the temporal structure of the XUV pulse together with $-eA$ (red dashed line) which corresponds to the momentum shift induced by the streaking field. For an unchirped pulse (c), integration along the time axis results in the same final momentum distribution independent on whether the vector potential increases or decreases. In contrast, for the chirped pulse, the emission time-dependent momentum shift (black arrows) leads to narrowing (broadening) of the final momentum distribution for decreasing (increasing) $-eA$ as shown in d) (respectively e). Thereby, temporal information on the XUV pulse is encoded into the streaking spectrogram.

Pulse retrieval

For the retrieval of both the XUV and the streaking pulse from the attosecond streaking spectrogram $S(p, \Delta t)$, the quantum mechanical expression based on the dipole transition from the initial state to the Volkov state (see Eq.2.10) has to be used[79, 143, 144]:

$$S(p,\Delta t) = \left| \int_{-\infty}^{\infty} \mathrm{d}t\, \vec{E}_{\mathrm{XUV}}(t-\Delta t)\vec{d}\big(p+A(t)\big) e^{+i(p^2/2+I_\mathrm{p})t} \cdot e^{-i\int_t^\infty \mathrm{d}t'\,[p\cdot A(t')+A(t')^2/2]} \right|^2, \quad (3.4)$$

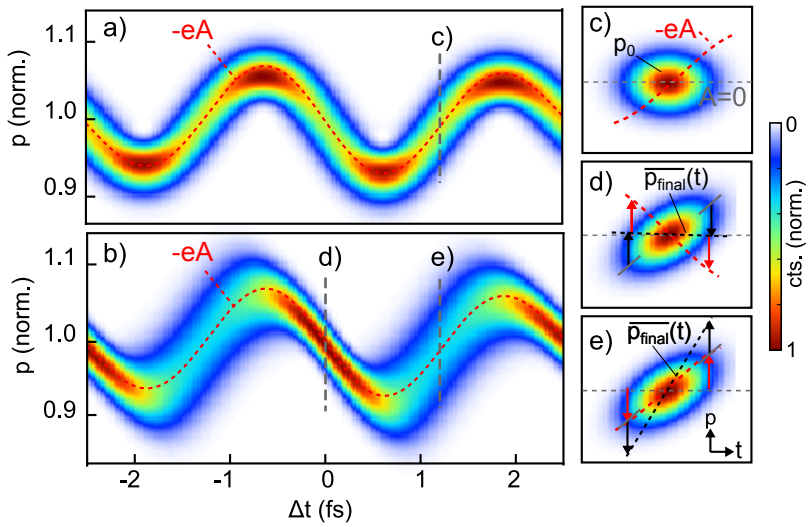

Figure 3.6: Streaking spectrogram and the signature of chirped XUV pulses: photoelectron streaking spectrogram of a) an unchirped XUV pulse and b) a positively chirped XUV pulse together with the vector potentials (red dashed line). c)-e) Schematic illustration of the effect of the XUV pulse structure on the spectral width at a given pump-probe delay: The false color plots indicate the momentum of the electrons directly after photoemission thereby carrying the signature of the XUV pulse. The final momentum is shifted by the vector potential (red line) indicated by the black dashed line. For a chirped pulse this leads to a change of the width of the final momentum distribution which manifests itself as a broadening or narrowing of the streaking trace.

where $\vec{E}_{\mathrm{XUV}}$ is the electric field of the XUV pulse, $\vec{d}$ is the dipole matrix element, p is the final momentum and I_{p} is the ionization potential. For notational simplicity, atomic units are employed. The integral in the last exponential originates from the Volkov state.

Commonly, the central momentum approximation (CMA) is being adopted where it is assumed that the central momentum p_{c} is much larger than the range of momenta to be considered. In this case, p in the Volkov integral can be replaced with p_{c} and the dipole matrix element can be considered constant. The advantage of the CMA is that it allows the use of well established fast Fourier-transform-based methods for the retrieval of both the attosecond XUV and streaking pulse such as frequency-resolved optical gating for the complete reconstruction of attosecond bursts FROG-CRAB[145, 143, 146] or ptychographic reconstruction algorithms[147]. In this thesis, a ptychographic reconstruction algorithm is implemented under conditions for which the CMA holds.

For broadband XUV pulses, the CMA has been shown to lead to errors in the extraction of timing information[148]. Recently, a reconstruction algorithm that does not rely on the CMA has been demonstrated, the so-called Volkov transform generalized projection algorithm (VTGPA)[144] which has enabled the absolute complex dipole transition matrix element reconstruction (ACDC)[149] from attosecond streaking spectrograms.

For completeness, there also exist frequency domain interferometric methods[149] for the attosecond pulse retrieval, such as RABBITT[150], PROOF[151] or iPROOF[152]. However, they are limited to perturbative intensities and narrowband driving pulses and are thus not appropriate for reconstructing the broadband driving laser pulses employed in our experiments.

Another problem can originate from incoherent contributions which can arise due to fluctuations or different final states of the unobserved ion, e.g. caused by shake-up processes. Indeed, the retrieved photoemission time-delay (see discussion below) between different initial states in neon[14] could only be explained by considering additional shake-up channels[153, 154, 155]. Incoherent processes can not be described by the coherent expression in Eq. 3.4. A fully consistent retrieval therefore requires a density matrix approach as in quantum state tomography, which has only very recently been demonstrated within the field of attosecond science[156].

Attosecond photoemission delays

Attosecond streaking has been successfully applied for the measurements of photoemission time delays in atoms[14, 155], molecules[84] and solids[15, 157]. These photoemission time delays manifest themselves as a time shift τ_{s} between the streaking traces originating from different initial states. Photoemission time delays do not play a role for the final interpretation of the attosecond streaking experiments in this thesis. Nevertheless, they could, in principle, affect the field reconstruction and are therefore discussed in Chap. 7. Hence, a brief overview is given here. For a more illustrative introduction, we refer to Ref [158]. The streaking time delay can be decomposed into several contributions[159]:

$$\tau_{\mathrm{s}} = \tau_{\mathrm{EWS}} + \tau_{\mathrm{CLC}} + \tau_{\mathrm{dLC}}, \tag{3.5}$$

where τ_{EWS} is the so-called Eisenbud-Wigner-Smith time-delay, τ_{CLC} is the Coulomb laser coupling term and τ_{dLC} is the dipole laser coupling time delay. Again, as for the strong-field dynamics in the simpleman's model (see Sec. 2.2.2), the streaking delays are generally very well described by the classical equations of motion due to the Ehrenfest theorem[159, 160].

τ_{EWS} originates from the short-ranged potential and is specific to the type of medium on which the attosecond streaking measurement is performed. It corresponds to the time-shift an electron experiences when leaving the potential compared to a free electron with the same asymptotic kinetic energy. The latter implies that the Eisenbud-Wigner-Smith time delay for an attractive potential is negative, since the electron has a higher velocity within the range of the potential. However, τ_{EWS} is not automatically negative. Depending on the orbital angular momentum l of the final continuum state, the centrifugal potential $l(l+1)/2r^2$ can act as a repulsive potential[159, 161].

The emitted electron is subject to both the Coulomb and the streaking laser field. This coupled motion leads to the Coulomb laser coupling time delay which, in atomic units, is given to first order by[159]:

$$\tau_{\mathrm{CLC}} = \frac{Z}{(2 \cdot E_{\mathrm{kin}})^{3/2}}[2 - ln(E_{\mathrm{kin}} T_{\mathrm{IR}})], \tag{3.6}$$

where Z is the charge of the ion, E_{kin} is the final kinetic energy and T_{IR} is the oscillation period of the streaking laser field. τ_{CLC} does neither depend on the specific target nor, somewhat surprisingly, on the streaking field strength and is usually negative. The magnitude of τ_{EWS} and τ_{CLC} increases with lower kinetic energy and generally ranges between 100 as and 10 as for kinetic energies between 20 eV and 100 eV. The dipole laser coupling τ_{dLC} originates from the interaction of the streaking laser with the (induced) dipole of the initial or final state which in turn affects the outgoing electron.

Generally, photoemission time-delays can only be measured relative to a reference. Only recently, the absolute timing of photoemission delays could be demonstrated[157] through comparison of experimental data with simulations for helium, which can be treated exactly.

3.3.2 Electro-Optic Sampling

Electro-optic sampling (EOS) is an all-optical field-resolved method. In this thesis, EOS is used for the transient field-resolved reflectometry experiments on semiconductors presented in Chap. 5. EOS has been employed for the measurement of THz-pulses for almost three decades[41]. Only recently, the extension of the concept down to 1.2 μm[31] (near-infrared) could be demonstrated.

A schematic illustration of an EOS setup is shown in Fig. 3.7 a). The MIR pulse (blue line) to be sampled is focused into a nonlinear EOS crystal together with a gating pulse (red line) at a variable delay Δt. The gating pulse duration generally needs to be shorter than one half-cycle. The nonlinear crystal is tuned for phase-matching of the sum-frequency generation (SFG) process with the resulting electric field E_{SFG} approximately given by:

$$E_{\mathrm{SFG}}(t, \tau) \propto E_{\mathrm{gate}}(t) \cdot E_{\mathrm{MIR}}(t + \tau). \tag{3.7}$$

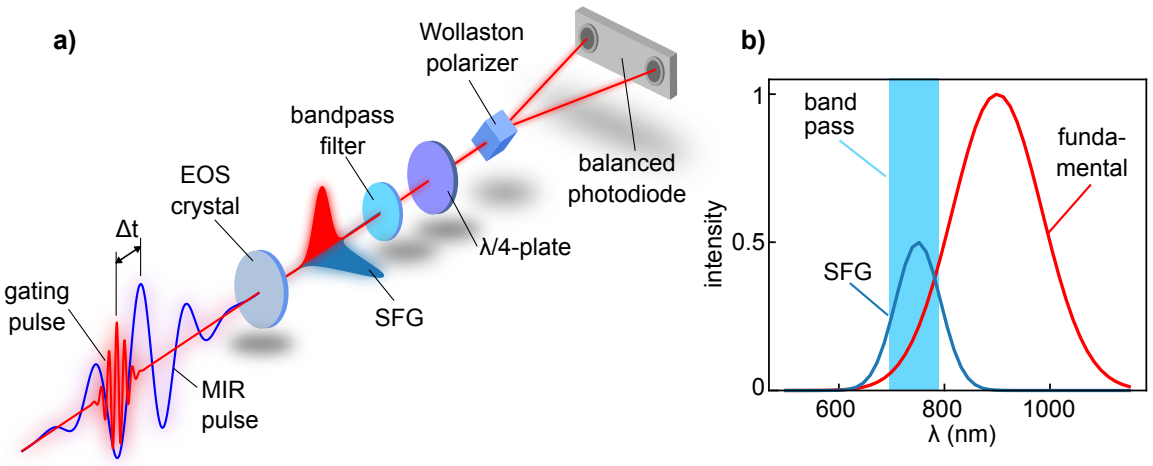

Figure 3.7: Electro-optic sampling: a) Setup for electro-optic sampling of an MIR pulse via an NIR gate pulse. b) Schematic spectrum of the SFG-signal (blue line) and of the fundamental NIR gating pulse (red line) which serves as a local oscillator and additionally the range of the bandpass filter (light blue shaded area). The figure is adapted from Ref. [162].

Strictly speaking Eq. 3.7 also contains a difference frequency generation (DFG) term, which could also be used in EOS. Here, we neglect it, since our considerations focus on the proportionality. Through the SFG process the MIR signal is transfered to the optical/NIR range. As shown in Fig. 3.7 a), the SFG signal is normally orthogonal to the gating pulse. In order to allow for a sensitive detection of the SFG signal, an optical heterodyne ellipsometric detection scheme is employed where the transmitted gating pulse serves as a local oscillator[31]. A bandpass filter is applied to limit the detected spectral range to a region where both pulses interfere, as schematically shown in Fig. 3.7 b). Using a $\lambda/4$-plate and a Wollaston polarizer, the rotation of the polarization induced by the SFG-signal can be detected in a balanced manner. Qualitatively, the signal intensity at the detector is proportional to:

$$I_{\mathrm{EOS}} \propto |E_{\mathrm{gate}} + E_{\mathrm{SFG}}|^2 \propto E_{\mathrm{gate}}^2 + 2 \cdot E_{\mathrm{gate}} E_{\mathrm{SFG}} + E_{\mathrm{SFG}}^2. \tag{3.8}$$

The first term on the r.h.s is delay-independent and eliminated by the balanced detection. Since the SFG-signal is usually weak, the last term can be neglected and only the interference term is left. By using Eq. 3.7, it can be seen that the latter is proportional to the MIR field at time τ which yields for the EOS signal $S_{\mathrm{EOS}}(\tau)$:

$$S_{\mathrm{EOS}}(\tau) \propto E_{\mathrm{gate}} \cdot E_{\mathrm{SFG}}(\tau) \propto I_{\mathrm{gate}} \cdot E_{\mathrm{MIR}}(\tau) \tag{3.9}$$

Due to the interference, where the small E_{SFG} is multiplied by the strong local oscillator given by E_{gate}, even very weak SFG signals and thereby small MIR fields can be detected. EOS generally shows outstanding sensitivity[163] and has been used to measure vacuum fluctuations[164].

In a more rigorous treatment, the spectral response function $S(\Omega)$ of EOS detection can be derived[31]:

$$S(\Omega) = \int_{\Omega}^{\infty} \mathrm{d}\omega_{\mathrm{LO}} R(\omega_{\mathrm{LO}}) |E_{\mathrm{gate}}(\omega_{\mathrm{LO}})| |E_{\mathrm{gate}}(\omega_{\mathrm{LO}} - \Omega)| e^{i[\phi(\omega_{\mathrm{LO}}) - \phi(\omega_{\mathrm{LO}} - \Omega)]}, \tag{3.10}$$

where Ω is the MIR frequency, ω_{LO} is the local oscillator frequency, ϕ is the spectral phase of the gating pulse and R is the response of the detection system.

3.3.3 Tunneling ionization with a perturbation for the time-domain observation of an electric field (TIPTOE)

A particularly intuitive method based on the perturbation of field driven processes is the tunneling ionization with a perturbation for the time-domain observation of an electric field (TIPTOE)[32]. The mechanism is depicted in Fig. 3.8 a) for the case of a surface. A strong pump field E_{p} (red solid line) leads to tunneling emission (blue shaded area) from the surface constituting a sub-cycle gate at around t_0=0. Here, emission only occurs when the electric force for an electron $-e \cdot E$ points away from the surface. The emission rate gets modified (dashed black line) by a weak time-delayed perturbing signal field E_{s} (red dashed line). This leads to a change of the total emitted charge ΔQ depending of whether the total electric field magnitude during the gate, i.e. the magnitude of the sum of pump and probe field at t_0=0, decreases or increases.

The total emitted charge Q at time delay τ in the presence of the signal field can be calculated from the instantaneous tunneling rate $w\big(E(t)\big)$[32, 165]:

$$Q(\tau) \propto \int w\Big(E_{\mathrm{p}}(t-\tau) + E_{\mathrm{s}}(t)\Big)\mathrm{d}t, \tag{3.11}$$

where the time integral extends over the pulse length. Since the signal field is weak, the kernel of the integral can be Taylor-expanded up to first order:

$$Q(\tau) \propto \int w\Big(E_{\mathrm{p}}(t-\tau)\Big) + \left.\frac{\mathrm{d}w}{\mathrm{d}E}\right|_{E_{\mathrm{p}}(t-\tau)} \cdot E_{\mathrm{s}}(t)\mathrm{d}t, \tag{3.12}$$

where the last term corresponds to the cross-correlation of the gating function with the signal field[165]. The first term corresponds to the rate without signal field. Moreover, the gating function for a tunneling emission burst at t_0 can be approximated as a delta-function $\delta(t - \tau - t_0)$, yielding an expression for ΔQ:

$$\Delta Q(\tau) \propto \int \left.\frac{\mathrm{d}w}{\mathrm{d}E}\right|_{E_{\mathrm{p}}(t-\tau)} \cdot E_{\mathrm{s}}(t)\,\mathrm{d}t \propto \left.\frac{\mathrm{d}w}{\mathrm{d}E}\right|_{E_{\mathrm{p}}(t_0)} \cdot E_{\mathrm{s}}(t_0+\tau). \tag{3.13}$$

For a single emission burst, the charge modulation is thus approximately proportional to the electric field.

For several tunneling emission bursts, the last expression on the left hand side in Eq. 3.13 becomes a sum over all burst times t_k. This is illustrated in Fig. 3.8 b) for a pump pulse (not shown) with CEP=0, where two dominating equal emission bursts occur. As can be seen, in this case, signal frequencies at $0.5\,f_0$ (red line) and $1.5\,f_0$ (black line), where f_0 is the pump pulse frequency, do not lead to a modulation of the emitted charge. The reason is that the emission modulation of the first burst is counteracted by the second burst since the signal fields point into opposite direction. This is not the case for CEP=π.

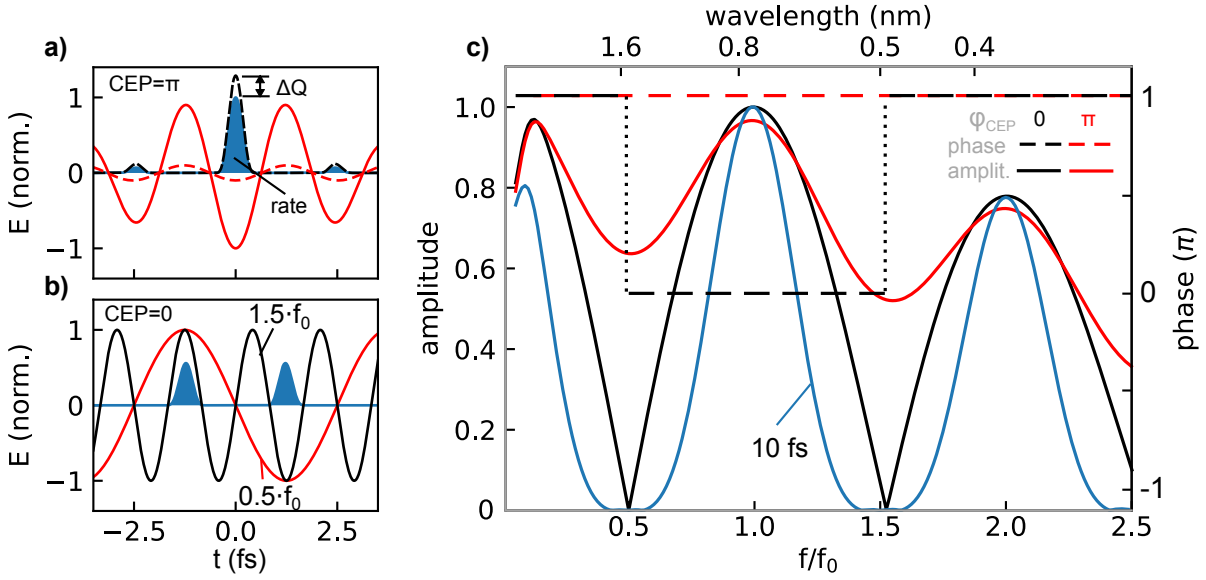

Figure 3.8: TIPTOE response function for surface emission: a) TIPTOE-principle: The ionization rate (blue line area) of a strong pump pulse (red line) is perturbed by a weak signal pulse (red dashed line). The change in ionization is essentially proportional to the perturbing electric field at the time of the emission peak. At a surface, electron emission only occurs if the electric field points into the surface. b) Amplitude (solid lines) and phase (dashed lines) of the response function for CEP=0 (red) and CEP=π (black) for a pulse width of 4.5 fs (FWHM) calculated using the Fowler-Nordheim rate. For a 10 fs-pulse (blue line), practically no CEP-dependence is observed (intensity $3{\cdot}10^{14}$W/cm^2, work function=4.5 eV). c) Illustration of the reason for the minima in the amplitude response for CEP=0 at $0.5 \cdot f_0$ (red line) and $1.5 \cdot f_0$ (black line). The results shown here use a Fowler-Nordheim emission rate[66] assuming a work function of 4.5 eV and a pump pulse at an intensity-FWHM of 4.5 fs, a central wavelength of 750 nm and intensity of approximately $3 \cdot 10^{13}$W/cm^2. In order to obtain a large bandwidth, we chose a signal pulse duration of 1 fs at 375 nm wavelength and a relative field strength of 10^{-5}.

This leads to a CEP-dependence of the spectral response function, as can be seen in Fig. 3.8 c), and which has been extensively discussed in Ref. [165]. The spectral response function can be calculated either by Fourier transforming the gating function in Eq. 3.12, or by evaluating the full expression for the emitted charge for a given pump and signal

field in Eq. 3.11 and subsequently forming the ratio of ΔQ and E_s in the Fourier-domain. We chose the latter approach, since it does not rely on the first-order Taylor-expansion.

The amplitude (solid lines) and phase (dashed lines) of the spectral response function for a CEP of 0 (black) and π (red) are shown in Fig. 3.8. As discussed above, for CEP=0, the amplitude response exhibits zeros at $f = 0.5\, f_0 + n \cdot f_0$, where n is an integer. The response function for CEP=π only shows a slight modulation caused by the small satellite emission bursts one cycle earlier and later as shown in Fig. 3.8 a). Around f_0 the phase of the response function changes with the CEP of the pump pulse. As pointed out in Ref. [165], if both pump and signal pulse originate from the same laser source, this allows the auto-characterization of the pulse without CEP-stabilization, since the relative phase of both pulses does not change. However, this statement only holds true, if the bandwidth is relatively narrow: we demonstrate in Chap. 7, that the change of the amplitude of the response function $|H|$ with the CEP can be measured with broadband pulses. For comparison, we also show $|H|$ for a pump pulse with the same parameters as above, but a pulse duration of 10 fs (solid blue line). In the latter case, the CEP-dependence is not visible anymore.

Originally, TIPTOE has been employed in gas as an ionizing medium[32] and has been used to characterize an optical near-single-cycle pulse[166] and multicycle laser pulses from the UV to the IR[167]. It has also been shown that the condition that the signal pulse is only a minor perturbation can be relaxed[167]. The TIPTOE principle is not limited to charge measurements, but also can be used for ionization-induced fluorescence[168]. Finally, the method has successfully been applied to the measurement of the near-field in a nanostructure array[165]. We employed TIPTOE as the main method for measuring enhanced near-field on the apex of a metallic nanotip based on the photocurrent in Chap. 7.

3.3.4 Streaking of rescattering electrons

It has been shown very recently that also the perturbation of the electron trajectories contributing to the cutoff of the ATI rescattering plateau can be used for field-resolved measurements[33]. The approach is illustrated in Fig. 3.9 a). A strong pump field (red solid line) accelerates electrons after their emission and a fraction of the electron trajectories rescatters with the parent ion or surface. The classical trajectory (black solid line) leading to the highest electron energy in the SMM (see Sec. 2), is emitted shortly after the field crest at $t = 0$ and rescatters around $t = 0.7\,T$, where T is the oscillation period. If a weak perturbing signal field (red dashed line) is added, the cutoff trajectory is slightly modified (blue dashed line), resulting in a shift of the cutoff energy $\Delta E_{\mathrm{cutoff}}$ in the ATI spectrum, as shown in Fig. 3.9 b). This approach is especially appealing for near-field measurements from nanostructures and is one of the methods used in Chap. 7. Here, the strong-field emitted electrons from the enhanced nanoscale near-field itself are used to measure the very same field, similar to the TIPTOE approach described above.

The description is simplified in terms of the final momentum shift $\Delta p_{\mathrm{cutoff}}$. In the SMM,

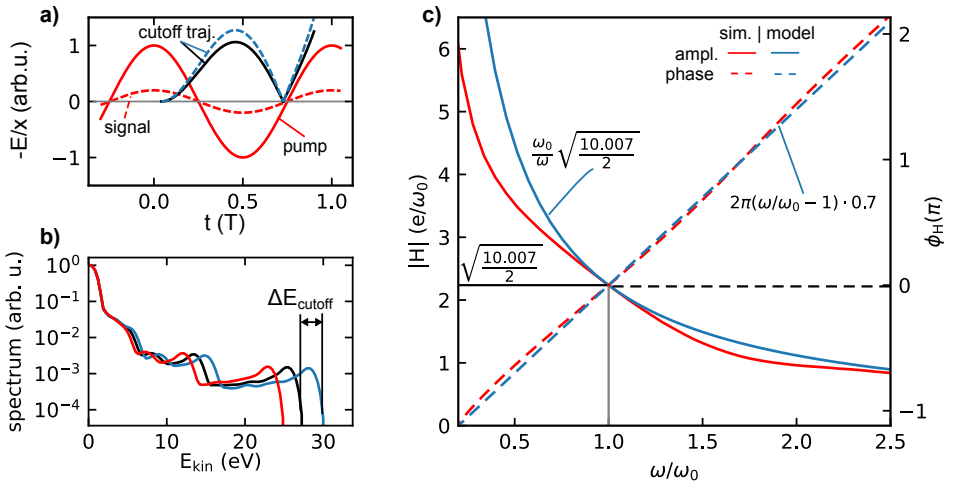

Figure 3.9: Response function of the cutoff rescattering streaking: a) principle: a weak signal field (red dashed line) influences the cutoff trajectory (black and blue dashed line, respectively) driven by the strong pump pulse (red solid line). b) the perturbation leads to a variation in the spectral cutoff that is proportional to the weak field. c) Response function of the rescattering cutoff variation with respect to the perturbing electric field strength calculated using the SMM. The amplitude (solid red line) and phase (red dashed line) response is compared with a heuristic model (blue solid and dashed lines).

it is approximately given in terms of the vector potential of the signal field A_s by[33]:

$$\Delta p_\mathrm{cutoff}(\tau) = -2A_\mathrm{s}(t_\mathrm{r} - \tau) + \frac{1}{t_\mathrm{r} - t_\mathrm{i}} \int_{t_\mathrm{i}}^{t_\mathrm{r}} A_\mathrm{s}(t - \tau)\mathrm{d}t, \tag{3.14}$$

where t_i and t_r are the ionization and rescattering times in the absence of the signal field, respectively.

We have calculated the spectral response function to the electric field using pump and signal fields with constant amplitude within the SMM. The amplitude (solid red line) and phase (dashed red line) of the response function are shown in Fig. 3.9 c). At the pump frequency ω_0, the pump and signal fields are degenerate, which means that the amplitude is related to the $10\,U_\mathrm{p}$-cutoff and the phase is zero (see gray solid and dashed lines). Since Δp_cutoff is dominated by the vector potential at the rescattering time (first term on the r.h.s. in Eq. 3.14), the amplitude follows an approximate $1/\omega$-dependence and the phase increases almost linearly by $2\pi \cdot 0.7 \cdot (T_0/T - 1)$. A simplified heuristic spectral response based on both previous findings is shown in blue.

A similar approach exists based on the HHG cutoff modulation[35]. The advantage of the rescattering streaking approach over TIPTOE is that it allows in principle the straightforward determination of the absolute signal field strength, but it requires an electron spectrometer. Moreover, it can be measured simultaneously with the TIPTOE approach (see Sec. 3.3.3) as done in Chap. 7. Since the approach assumes single electron dynamics, it might not work anymore in the multielectron emission regime when charge interaction

dominates the dynamics.

3.3.5 Nonlinear photoconductive sampling

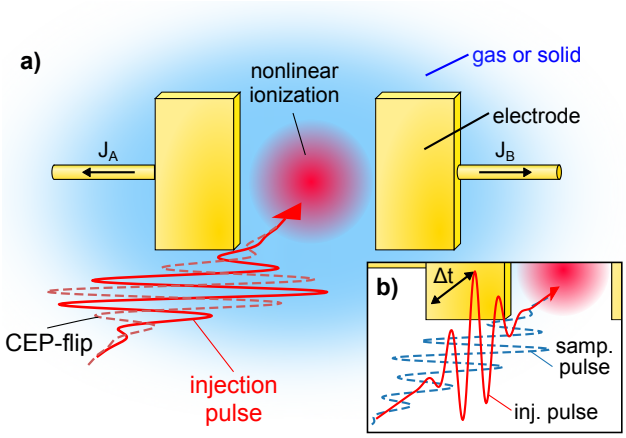

Figure 3.10: Optical field-induced currents: a) schematic setup for the detection of optical field-induced currents. A few-cycle laser pulse (red line) induces nonlinear ionization within a medium, either a gas or a solid. The charge carriers are driven by the laser inbetween an electrode pair, which induces a current flow from the electrodes. In the depicted geometry, CEP-dependent currents can be detected which is enabled by a CEP-flip (red dashed line) between consecutive pulses. b) For the sampling of a laser pulse, a different geometry has to be used. The strong injection pulse (red line) is polarized parallel to the electrode surface and does not induce currents. On the other hand, the pulse to be sampled (blue dashed line) is polarized orthogonally, driving the carriers towards the electrodes.

Optical-field-induced currents in dielectrics were demonstrated in 2013[16] which since has had profound impact on the recent development of attosecond science. Here, a strong laser pulse induces a nonlinear transition of an electron from the valence into the conduction band on a sub-cycle timescale which leads to a sudden rise in the conductivity. A schematic setup is depicted in Fig. 3.10 a). A focused laser pulse leads to the strong-field nonlinear ionization of the medium between an electrode pair. In the given polarization the laser pulse can drive the charge carriers towards the electrodes, thereby inducing a measurable current. After amplification using a transimpedance amplifier, the current signal is recorded via lock-in detection. As depicted here, for the measurement of CEP-dependent currents, the CEP between consecutive pulses is flipped.

Recently, also the field-resolved measurement of UV to MIR waveforms has been demonstrated [30] based on this approach. The technique has been named nonlinear photoconductive sampling (NPS) and can be considered a generalization of the photoconductive Auston switch used for the sampling of THz-fields[169]. As shown in Fig. 3.10 b), a slightly different configuration has to be used. The strong injection pulse is polarized perpendicular to the electrodes and therefore does not induce a current on them. The carriers are steered

towards the electrodes by a weak orthogonally polarized sampling pulse (blue dashed line). The resulting current depends on the time-delay Δt between signal and injection pulse and allows the reconstruction of the signal pulse.

The measurement principle has also been extended to gases as the nonlinear photoconductive medium[170, 171, 172]. Here, one advantage is that the medium can not be damaged unlike a solid which has to be driven close to the damage threshold in these experiments. Moreover, the densitiy of the medium can be changed by varying the pressure, which allows to obtain further information on the signal generation mechanism.

Despite the widespread use of the current-based detection in the attosecond science community in recent years, the details on how the laser-induced charge dynamics leads to the measured macroscopic currents from the electrodes has so far not been very well understood. In the literature, two different contributions are commonly discussed, namely either charge carriers directly reaching the electrodes[16] (current contribution) or the formation of a macroscopic dipole between the electrodes that induces the measured current (dipole contribution)[171, 172]. In Chap. 4, a rigorous theoretical model is presented which provides a unified picture and overcomes these heuristic models.

Chapter 4

The emergence of macroscopic optical-field-controlled currents in gases

Attosecond science has been heavily relying on photoelectron spectroscopy and XUV spectroscopy on atoms and molecules since the beginning[173, 122]. Experimentally, the disadvantage of both methods is that they require (ultra-)high-vacuum environments. Most attosecond experiments, therefore, have to be conducted in dedicated vacuum beamlines [174, 175, 176]. These setups are expensive to build and are considerably bulky, restricting the number of laboratories that can conduct these types of experiments.

Within the effort to investigate attosecond dynamics in solid-state samples[16, 177], it has been demonstrated that intense few-cycle pulses can drive currents in dielectrics that depend on the driving waveform with switching times on the sub-cycle timescale ($\sim$100 attoseconds)[16]. Since then, CEP-dependent currents have been measured in various materials[17, 178, 179, 180] and 2D-structures[18]. Moreover, by realizing that the sub-cycle current injection event could be used as a temporal gate, in a generalization of the concept of THz photoconductive field-sampling[37, 181], the field-resolved measurement of optical waveforms up to PHz-frequencies has been shown[30]. The involved currents can simply be measured by a set of electrodes fabricated on the sample, with relatively inexpensive measurement devices and under atmospheric conditions which makes these experiments accessible to a far broader range of laboratories.

Very recently, the same concepts have been applied to CEP- and field-resolved current measurements in air[170, 171, 172], which offers additional advantages[172]: Firstly, the electrodes don't need to be fabricated on the sample. Secondly, the medium (air) can not get damaged. Finally, the microscopic response on the atomic/molecular level can be numerically calculated using time-dependent Schrödinger equation (TDSE) and may be well understood in the framework of the strong-field approximation and the simpleman's model[67].

Moreover, the general experimental setup of strong-field sub-cycle controlled currents is almost identical to broadband THz generation in gases[182, 183, 184] and both processes

are expected to be closely linked. Furthermore, the plasma density and mean kinetic electron energy of the resulting non-thermal partially ionized plasma fall into a regime utilized not only for plasma spectroscopy[185] but also for a vast number of technological and industrial applications[186], such as catalysis.[187], biotechnology[188], medicine[189] and food processing[190].

Regarding the ultrafast current experiments in solids and gases the macroscopic aspects of signal formation have largely been ignored even though processes such as scattering of the electrons are expected to play an important role[171]. Apart from Refs. [191, 162] where the role of the electrode distance has been investigated, no systematic studies exist. Even worse, there currently seems to be no rigorous model that connects the microscopic single electron dynamics to the macroscopic current signal induced on the electrodes. Consequently, the role of the charges reaching the electrodes compared to the formed dipoles has not been understood.

In this chapter, we present experimental measurements investigating the macroscopic aspects of signal formation of CEP-dependent currents in gases by varying the gas pressure, gas type, electrode distance and driving pulse intensity. Moreover, we present a rigorous theoretical model that describes the induced currents in terms of the propagation of the individual electrons which is based on the Ramo-Shockley description for moving point charges[192, 193, 194, 195]. Furthermore, by comparison of the experimental results with extensive numerical particle-in-cell (PIC) simulations, we are able to identify the role of the electron-atom scattering cross sections. We find a surprisingly large influence of the Coulomb interaction that leads to maximum in the current signals at around 1-10 mbar pressure for most conditions. Our results also imply that most of the heuristic models utilized so far will need to be modified. We believe that this work presents an important step in the understanding of the macroscopic signal formation not only for gases but also for solids and therefore will strongly help in the further development of the experimental techniques. The work presented here has led to a manuscript that is submitted for review[196].

This chapter is organized as follows. First, the characteristic time- and lengthscales and the classification of plasmas is briefly reviewed. Secondly, the experimental setup is presented before the theoretical model and simulations are discussed. Then, the experimental results are shown followed by the discussion. Finally, a short conclusion is given.

First preliminary measurements were performed together with Dmitry Zimin who also helped with the initial build-up of the setup. Final implementation and further development of the setup, electrode design and detection were done by the author and Ancyline Malliakal (A.M.). Johannes Blöchl (J.B.) and Zilong Wang (Z.W.) helped with the improvement of the setup. Philipp Rosenberger and Z.W. helped with operating the laser. A.M., J.B. and the author performed the measurements. The experimental data was analyzed together with A.M. and discussed with A.M., J.B., Z.W., Boris Bergues and Matthias Kling. The author developed the theoretical model, implemented the code, performed the simulations and analyzed the numerical data. The presentation of the results has been done by the author. The results and interpretation were discussed with all the authors of the submitted manuscript[196].

4.1 Classification of plasma regimes

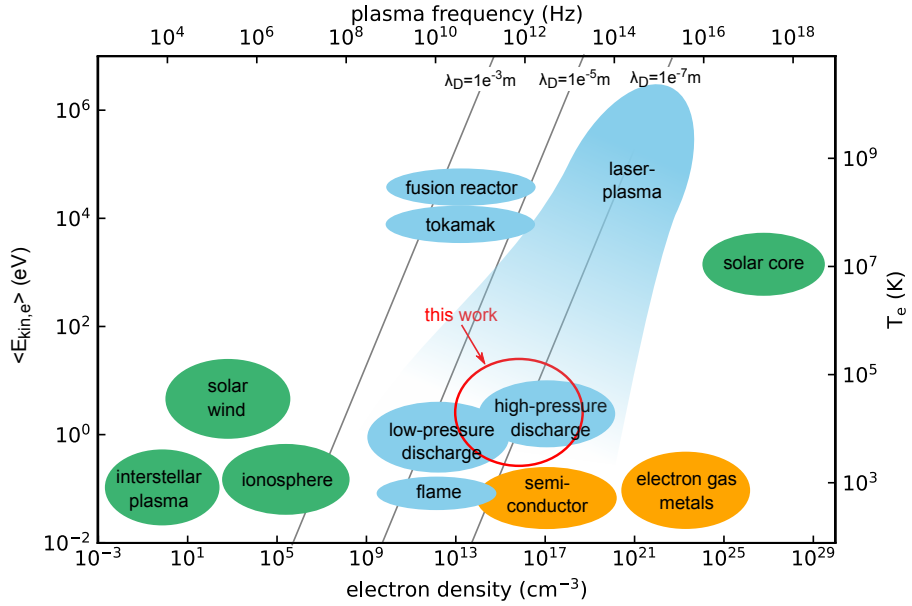

Figure 4.1: Classification of plasmas according to the charge density and mean electron kinetic energy. The diagonal lines show the Debye length. Adapted from Refs. [197, 198, 199, 200].

In our experiment (see below), laser pulses are focused into a gas medium with intensities on the order of 10^{14}W/cm^2 which, through strong-field ionization, leads to partially ionized atoms and molecules. The emitted electrons together with the parent ions form a plasma where both species interact via the Coulomb force. This section will give only a very brief overview, for more details we refer to the literature (e.g. Refs [197, 198, 199, 200]).

The behavior of plasmas is mainly determined by two factors, the charge density and the mean electron kinetic energy (or temperature)[200]. An overview over different types of plasmas is shown in Fig. 4.1. Naturally occuring plasmas (green areas) can for example be found inside the sun, interstellar medium and the earth's ionosphere. Furthermore, electrons inside metals and semiconductors can often be approximated using a plasma description (orange areas). Finally, man-made plasmas (blue area) span from flames to artificial fusion. The field of laser-plasma research is currently pushing towards relativistic high-density plasmas, but a huge parameter range can be accessed by laser matter interaction (indicated by the blue-shaded gradient). As mentioned above, most technological applications utilize gas discharges, which lie in a similar parameter range as our experiments. Moreover, these technical plasmas are also non-thermal which means that the electron ensemble is not in thermal equilibrium with the ions and neutrals.

The characteristic timescale over which collective charge oscillations occur is given by

the plasma frequency ω_p:

$$\omega_\mathrm{p} = \sqrt{\frac{\eta e^2}{\epsilon_0 m_\mathrm{e}}}, \tag{4.1}$$

where η is the charge density and ϵ_0 is the vacuum permittivity. Collective oscillations only unfold if ω_p is larger than the scattering rate of the electrons. Nevertheless, the plasma frequency can be used as an estimate for the time it takes the plasma to adjust to a charge imbalance.

The Debye length λ_D on the other hand is a measure for the lengthscale over which charge imbalances are shielded through the collective motion of charges and is given by:

$$\lambda_\mathrm{D} = \sqrt{\frac{\epsilon_0 k T_\mathrm{e}}{\eta e^2}}, \tag{4.2}$$

where k is the Boltzmann-constant and T_e the electron temperature. In our case, the Debye length is only a good estimate for the order of magnitude of the typical lengthscale, since the plasma in our experiment is not in thermal equilibrium but quickly relaxes. Moreover, the plasma is confined within 10 μm due to the laser focal spot size. Both Debye length and plasma frequency are indicated in Fig. 4.1.

4.2 Experimental setup and approach

The experiment utilizes laser pulses with pulse durations down to 4.0 fs (FHWM) and pulse energies up to 18 μJ which are provided by a commercial Ti:Sa laser system (Femtopower HR/CEP-4) that has been described in detail in Ref. [201]. In short, a Kerr-lens mode-locked oscillator (Femtolasers Rainbow) produces 7 fs pulses at a central wavelength of 780 nm and at a repetition rate of 75.8 MHz which are CEP-stabilized in a feed-forward scheme (Femtolasers CEP-4). The pulses are further amplified in a 9-pass Ti:Sa chirped-pulse amplifier (Femtopower HR) up to 0.7 mJ pulse energy with 27 fs pulse duration at 10 kHz repetition rate. For spectral broadening the pulses are sent through a hollow-core fiber filled with argon at 0.5 mbar and subsequently compressed using chirped mirrors (Ultrafast Innovations PC70) and a pair of fused silica wedges (Lens Optics, custom).

The experimental setup is shown in Fig. 4.2 a). The fused silica wedges are mounted on a motorized stage which is utilized to control the dispersion. The laser pulses are focused by an off-axis parabola (OAP, f=101.6mm) to a spotsize below 10 μm, as determined by a CCD camera. Additionally a mirror-based telescope can be introduced in front of the setup leading to an approximately factor three larger spotsize. The focused laser creates an ionization region between the two cylindrical copper electrodes. The propagation of photoemitted electrons induces currents on the electrodes which are individually amplified by two transimpedance amplifiers (Femto DLPCA-200) with a gain of 10^9. The resulting voltage pulses are detected via a two channel lock-in amplifier (Zürich Instruments HF2LI). The focusing mirror and electrodes are placed in a UHV-chamber which is used to change

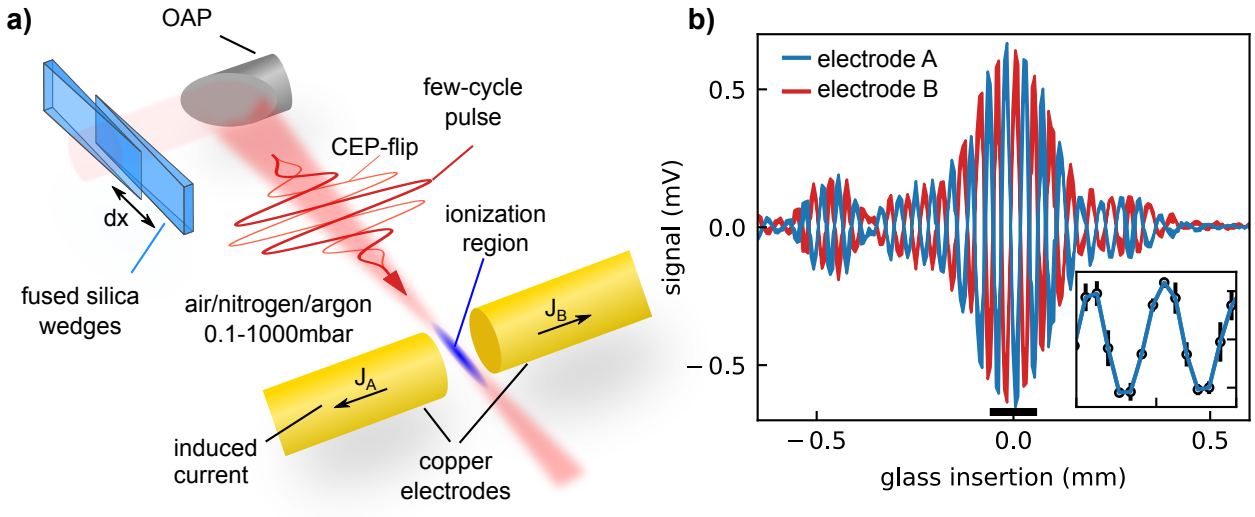

Figure 4.2: Experimental overview: a) experimental setup. The thin red line indicates the flip of the CEP between consecutive pulses. b) current dispersion scan trace obtained by moving the fused silica wedges from electrode A (blue line) and B (red line). The line thickness corresponds to the standard deviation of three measurements. The inset shows a zoomed view (black bar in a) of the signal from electrode A with individual datapoints marked as dots.

the gas species (air, nitrogen and argon) and vary the pressure (0.1 to 1000 mbar) in the ionization region.

In order to be able to measure the CEP-dependence of the currents, the CEP is flipped between ϕ_0 and $\phi_0+\pi$ for consecutive laser pulses (indicated by the thick and thin red line) using an acousto-optic dispersive programmable filter (Fastlite Dazzler). Consequently, the demodulation of the voltage signals in the lock-in amplifier is performed at half the repetition rate $f_{\mathrm{rep}}/2$. An exemplary signal trace obtained by scanning the glass insertion is depicted in b) for both electrodes. The observed oscillations are caused by the change of the CEP ϕ_0 with dispersion, while the envelope reflects the pulse duration and peak intensity. Since the electrodes measure the current in opposite directions, both signals are 180° out of phase (a more detailed discussion can be found below). Additionally, the signal demodulated at f_{rep} is proportional to the total created charge separation sensed by the electrodes. It thereby proved useful for finding the laser focus and for the initial optimization of the electrode position and pulse dispersion.

The electrodes are produced from a copper wire with a diameter of approximately 500 μm. The end of the wires forming the flat surface of the cylindrical electrodes was mechanically polished, the other end was soldered into an SMB-pin. The pin was connected to a BNC cable via an SMB-plug. The current signal was fed out of the vacuum chamber via a BNC-feedthrough with floating shield and finally amplified outside. A photo of the electrode assembly is shown in Fig. 4.3 a). The electrodes are mounted individually on miniature stages (Mechonics MS15) which allows to vary the distance between them. The

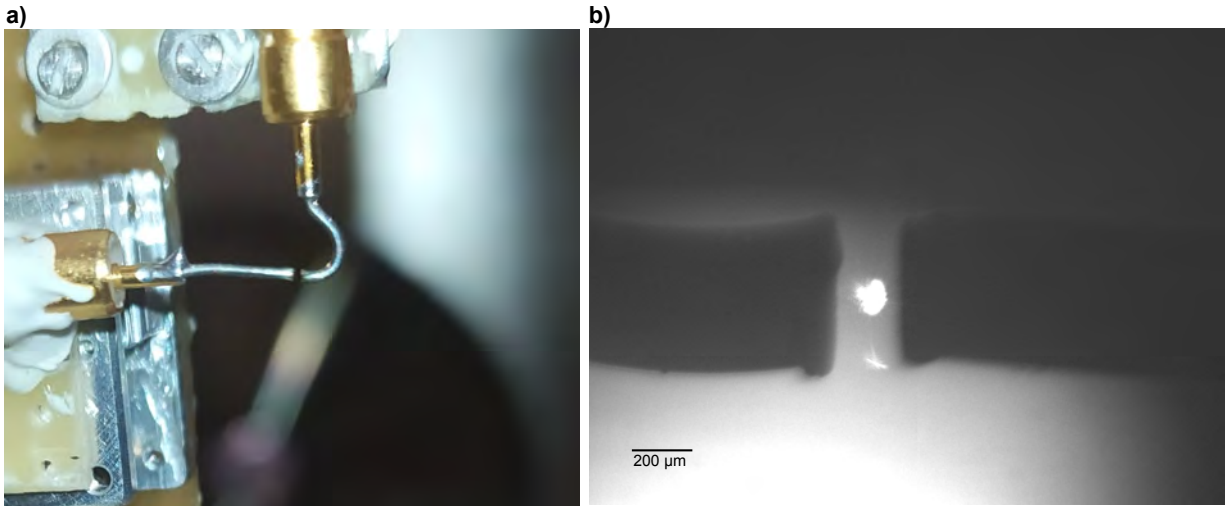

Figure 4.3: Electrode images: a) Photo of the electrode assembly. The shape of the right wire is chosen to allow the placement of the electrodes in front of the time-of-flight detector. b) In-situ imaging of the electrodes including the laser beam (white spot) in the center. The laser beam is strongly saturated in the image.

electrode assembly is placed on a linear closed-loop 3d-stage (Smaract SLC24) for fine positioning with respect to the ionization region with few nanometer precision. The electrode distance and positioning can be checked by an in-situ imaging system (shown in Fig4.3 b). The results presented in this chapter do not depend on the exact electrode geometry. We have measured similar results with different electrode materials and geometries.

For the calibration of the intensity, we measured the focal spotsize inside the experimental chamber via a CCD camera. Moreover, the relative peak intensity compared to the Fourier limit for our 4.5 fs laser pulses was determined from a d-scan measurement in front of the chamber. We obtained a conversion factor from pulse energy measured by a powermeter to peak intensity in the experimental focus of $1.1 \cdot 10^{14} \frac{\mathrm{W}}{\mu J \cdot \mathrm{cm}^2} \pm 20\%$. For the situation including the telescope a factor of $0.11 \cdot 10^{14} \frac{\mathrm{W}}{\mu J \cdot \mathrm{cm}^2} \pm 50\%$ is determined. Here, a higher relative uncertainty is obtained, since the telescope introduces a slight astigmatism, affecting the accuracy of the focal spotsize determination. Generally, we found that it is necessary to check the experimental focus on a daily basis, since the off-axis parabola is rather sensitive to small misalignments. Therefore, we expect any errors to be mostly systematic. Additionally, we used a time-of-flight spectrometer for intensity calibration via the $2U_\mathrm{p}$ and $10U_\mathrm{p}$ spectral cutoffs (see Sec. 2.2.3). A conversion coefficient smaller by roughly a factor 2 compared to the value stated above was determined. This discrepancy can be explained by focal averaging and the inability to optimize the focus prior to the experiment due to the vacuum requirements of the detector. In the following, we will use the above values.

4.3 Theoretical model and simulations

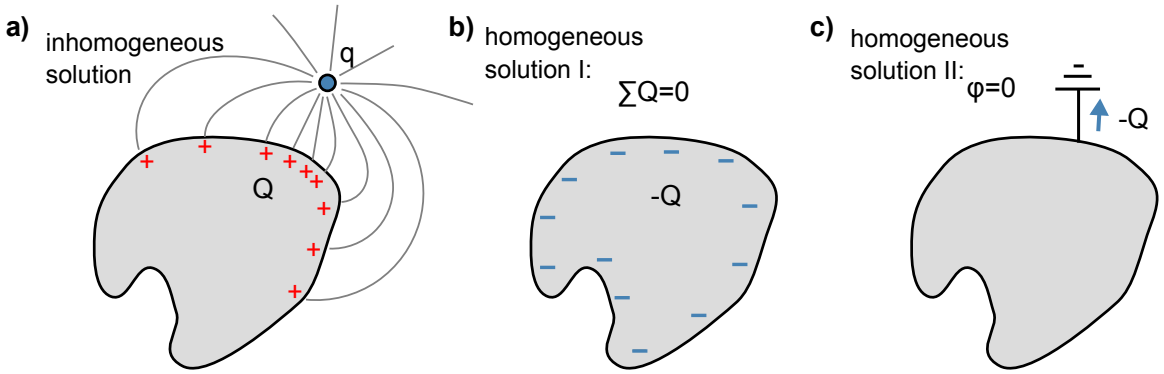

Figure 4.4: Inhomogeneous and homogeneous solution of the Poisson equation at a single electrode by placing a charge q in the vicinity: The solution to the electrostatic problem is the sum of the inhomogeneous and the homogeneous solution. a) The inhomogeneous solution is determined the external charge q and can be interpreted in terms of an induced surface charge Q. b) The homogeneous solution is determined by the boundary condition on the electrode. If charge neutrality is required, a surface charge $-Q$ is spread over the surface of the electrodes and the potential at the surface changes. c) If the electrode is set to a fixed potential the surface charge $-Q$ flows from the electrode towards the ground and is detectable as a current.

The mechanism through which the signal on the conducting electrodes is formed is based on a simple electrostatic principle: The induced charge Q on an electrode is given by the surface charge that is induced by placing the charged particle q in the vicinity. If the electrode is grounded, the charge $-Q$ flows from the electrode and can be measured as a current[192, 193].

This can be better understood in terms of the homogeneous and inhomogeneous solution to the Poisson equation as is schematically illustrated in Fig. 4.4 a) for a negatively charged particle. The induced surface charge represents the inhomogeneous solution of the Poisson equation and ensures that electric field lines (gray lines) are normal to the metal electrode surface. In contrast, the boundary condition imposed on the electrode fixes the homogeneous solution. If the electrode is isolated, then the total charge on the electrode needs to be zero, which leads to a surface charge $-Q$ distributed according to the homogeneous solution and a change of the potential of the electrode surface, as depicted in Fig. 4.4 b). If the electrode is grounded, as in our experiments, the charge $-Q$ flows to ground as a current which is amplifed with the transimpedance amplifier. Practically, it is impossible to create a charge out of nowhere in front of the electrode and it it is instead the change of the induced charge Q caused by a movement of the particle that is measured.

For our experiments, immediately after the emission process electron and parent ion are still at same position and since their charges have opposite signs, the induced surface charges cancel. A net charge is only induced if one charge gets displaced with respect to

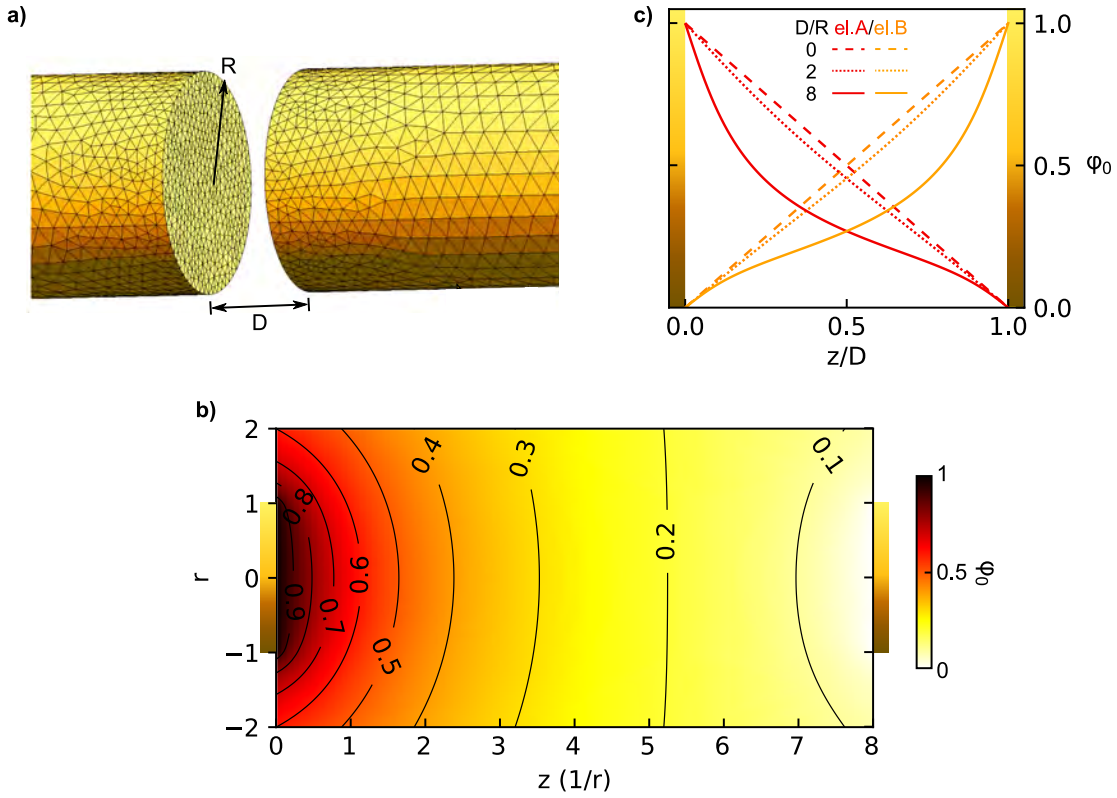

Figure 4.5: The Ramo-Shockley weigthing potential: a) Illustration of the geometry and surface mesh used in the numerical calculation. b) Radially-resolved weighting potential for a ratio of the distance D to the radius R of D/R=8. c) Weighting potentials on the cylinder axis for different ratios D/R for electrode A (red, left) and B (orange, right).

the other. For practical applications it would be tedious to calculate the induced surface charge for each position of the electron/ion and then integrate over the electrode surface. This approach would be feasible only for very simple, highly symmetric geometries.

Fortunately, the calculation is considerably simplified through the Ramo-Shockley theorem [194, 195] which states that the induced charge Q and current I on the electrode caused by a particle with charge q at position $\vec{r}$ and velocity $\vec{v}$ is given by[192, 193]:

$$Q = -q\phi_0(\vec{r}) \tag{4.3}$$

$$I = q\vec{v}\vec{E}_0(\vec{r}), \tag{4.4}$$

where ϕ_0 is the weighting potential and $\vec{E}_0$ is the weighting field. For an arrangement of electrodes the weighting potential can be calculated by setting the potential on the electrode under consideration to unity (1V in SI units) and to zero on all other electrodes. For an ensemble of charges, the induced charge is given by the sum over the individual particle contributions.

For infinitely extended parallel plates, the weighting potential can be obtained analytically and has a very simple form: It depends on the position between the electrodes and is one at electrode under consideration and linearly decays to zero at the other electrode. For realistic geometries the weighting potential has to be calculated numerically. The results for two opposing cylinders is shown in Fig. 4.5. The electrodes were meshed (see Fig. 4.5 a)) using GMSH[202, 203] and the electrostatic calculation was performed using the boundary-element implementation of scuff-em[204, 205]. Figure 4.5 b) shows the radially resolved cylindrical symmetric weighting potential of the left electrode for a rather large distance D to radius R ratio of 8. As can be seen in Fig. 4.5 c), the weighting potential along the cylinder axis (solid line) decays much faster when moving away from the considered electrode compared to the infinite plate solution (dashed line). However, for a still considerable ratio of 2, ϕ_0 only slightly deviates from the latter (dotted line). The weighting potentials for electrode B are mirror symmetric with respect to the mid-plane. As a sidenote, an idealized single infinitely extended plane electrode is not suited for measuring the displacement of charges. Independent from the distance to the surface, the full charge of the particle q is induced as surface charge (given by the image charge $-q$) which makes the single infinitely extended flat electrode insensitive to any charge movement.

The Ramo-Shockley theorem is heavily used for the modeling of radiation detectors in particle physics (see e.g. Refs. [206, 207, 208, 209]) and has recently also been applied for the design of optoelectronic probe circuits[210]. However, so far, the presented model of signal induction has not been employed in any study of field-dependent ultrafast current measurements[16, 17, 178, 179, 18, 180, 30, 170, 171, 172]. Moreover, modeling of the signal generation on the fundamental single-charge level using the Ramo-Shockley theorem seems to be largely ignored for the conventional simulation of THz photoconductive sampling even for the classical Auston switch[211, 212, 213].

For the numerical simulations of our experiments, an electrostatic particle-in-cell model (PIC), developed and implemented by the author, is used. After emission by the laser, the electron propagation under the influence of scattering and electric fields is considered. The

laser is modeled as a Gaussian beam with Gaussian pulse envelope of 4.5 fs (FWHM). Due to computational limitations, the model had to be restricted to two spatial dimensions perpendicular to the laser beam propagation direction. This is a good approximation mainly because the spatial scale perpendicular to the focus, the focal spotsize ω_0, is much smaller than the dimension along the propagation direction, the Rayleigh length z_R.

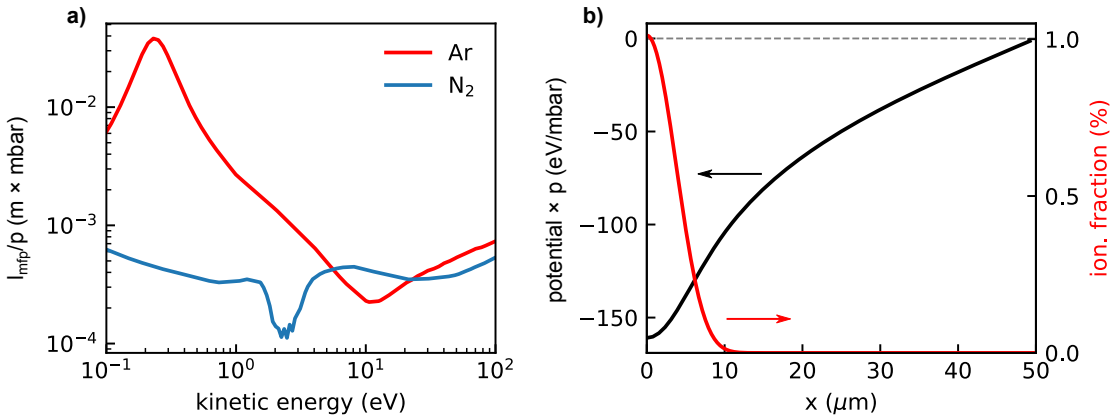

Figure 4.6: Scattering mean-free path and Coulomb interaction: a) Mean-free path for argon (red) and nitrogen (blue) at 1 mbar. b) ionization fraction (red) and electrostatic potential (black line) due to the background ions at 1 mbar calculated for argon and a laser with $\omega_0 = 25\,\mu$m and $I = 1.6 \cdot 10^{14}$W/cm^2

The electrons are modeled as an ensemble of pseudoparticles with an effective charge given by the total emitted charge divided by the number of pseudoparticles N. We usually use $N = 5 \cdot 10^5$. The total charge is obtained by radially integrating the final ionization fraction calculated by the ADK-rate[65] multiplied by the atomic number density ($\propto$ pressure p). For simplicity, we use atomic ADK-tunneling rates also for the molecules. The I_p values are taken from Ref. [214]. For nitrogen (I_p=15.58 eV), the same tunneling rate as for argon (I_p=15.76 eV) is employed. In order to model the contribution of oxygen in air, which has a much lower ionization potential (I_p=12.56 eV)[214] than nitrogen, we use the ADK-parameters of xenon (I_p=12.13 eV), but with angular momentum quantum numbers of l=2 and m=1. The latter is important since it takes into account the symmetry of the molecular wavefunction of O_2 in the tunneling region which leads to a significantly lower tunneling rate than in xenon (l=1, m=0)[214]. For simplicity, we model air as consisting of 80 % nitrogen and 20 % oxygen as an approximation to the literature values for dry air (78.1 % nitrogen, 20.9 % oxygen, 0.9 % argon and trace gases)[215].

In a Monte-Carlo approach, the initial position of a pseudoelectron and the corresponding pseudoion is randomly sampled from the radially-resolved ionization fraction and the emission time from the tunneling rate. From the latter the final emission velocity of the pseudoelectron is calculated in the SMM with the SFA under the assumption that effectively only direct electrons contribute, which appears to be justified considering the experimental TOF-spectra (see Fig. 2.4 b)). Pseudoelectrons have a charge-to-mass ratio

of e/m_e such that they behave like normal electrons during propagation. Pseudoions are assumed to stay fixed at the birth position.

The propagation of pseudoelectrons is performed via the Velocity-Verlet algorithm[216] using a timestep of 20 fs, or smaller if required, over a timespan of 1 ns. For each timestep the electron-neutral (atom or molecule) scattering probability is calculated via the mean free path l_{mfp} and Monte-Carlo sampling. l_{mfp} is obtained from the MagBoltz[217] cross-sections available via the xcat-database[218], that contain elastic, excitation and ionization cross-sections. The mean free path for argon (red line) and nitrogen (blue line) at 1 mbar are shown in Fig. 4.6 a). While both l_{mfp}s are of similar magnitude above 10 eV, for argon it increases below the threshold of ionization and excitation by more than an order of magnitude at electron kinetic energies around 0.5 eV. In nitrogen, on the other hand, there are a lot more open excitation channels at lower energies due to the molecular structure, resulting in a minimum in l_{mfp} at around 2 eV. It is important to note that the mean-free path scales as $\propto 1/p$, so l_{mfp} is on the order of 1mm for 1 mbar, while for 1000 mbar it is around 1 μm. The scattering time is above 10^{-13} s even at atmospheric pressure. For the inelastic channels we assume a uniform probability for the energy loss from the threshold of the inelastic process, e.g. the ionization potential for the ionization channel, up to the electron kinetic energy. Secondary electrons are neglected. For simplicity, we assume isotropic scattering in the lab frame for all processes. Since we deal with ionization fractions of around 1 % and below, scattering and recombination with the ions is neglected. For simplicity, for air the scattering cross-sections of nitrogen are used, neglecting differences in the mean free path to the other constituents (see above).

In order to calculate the electrostatic interaction, the Poisson equation is solved on a 2D-grid for each timestep. The dimension of the rectangular simulation region in x-direction is given by the electrode distance D, and by $3 \cdot D$ in the other direction. The laser focus is positioned in the center of the rectangle. The grid resolution is typically better than 200 nm. The pseudoelectrons are sampled onto the grid using a linear weighting scheme. We impose the Dirichlet boundary condition for the potential $\phi = 0$ at all four edges of the simulation region using the method of image charges. To this end, the grid is doubled in size and a charge of opposite sign is injected at the position mirrored along the positive edge. Due to the implicit periodicity of the Fast-Fourier Transform (FFT) used for solving the Poisson equation, all contributions of the otherwise infinite sum of mirror charges are contained in the calculation. The electric field is obtained in the same step and linearly interpolated onto the positions of the pseudoelectrons. If a particle leaves the simulation region it is not considered anymore in the electrostatic interaction. Across the boundary perpendicular to the electrodes the propagation is continued whereas it is stopped if the pseudoelectron reaches the electrodes. For the pseudoions, the potential and field calculation on the grid is only calculated once at the start of the simulation. The algorithm is tested against the analytic solution of a uniform cylindrical charge distribution. Fig 4.6 b) shows the ionization fraction (red line) and the electrostatic potential of the ion background (blue line) from the center of the simulation towards one electrode for a laser with $\omega_0 = 25\,\mu$m and $I = 1.6 \cdot 10^{14}\mathrm{W/cm}^2$ at 1 mbar argon. The strength of the ion potential also explains why related experiments that measure the generated charge via

bias voltages[32], are conducted at low pressures or have to apply kV-level biases in order to separate electrons and ions.

At each timestep, the induced charge Q on both electrodes is calculated using the linear weighting potential of the infinite parallel plates shown above and summing over the ensemble of pseudoelectrons. Since the induced current decays over a timescale of 100 fs-1 ps (see discussion below), much faster than the bandwidth of measurement electronics, the measured signal is assumed to be proportional to the induced charge averaged from 0.5 ns-1 ns after the start of the simulation. In order to obtain the signal in the experiment from the 2d-simulation, the simulated induced charge density is multiplied by the repetition rate of the laser (10 kHz), the transimpedance gain (10^9 V/A) and the effective ionization length $\Delta z_{\mathrm{ion,eff}}$ which is a free parameter. A 3D-version of the code is being developed utilizing the fast-multipole method (FMM) for the electrostatic interactions. However, the FMM libraries tested so far, which were mostly not parallelized, proved too slow for meaningful simulations and especially the parameter scans presented in this work and a dedicated, highly optimized FMM implementation would be required. All calculations are carried out on the high-performance computing (HPC) cluster Cobra of the Rechenzentrum Garching (RZG).

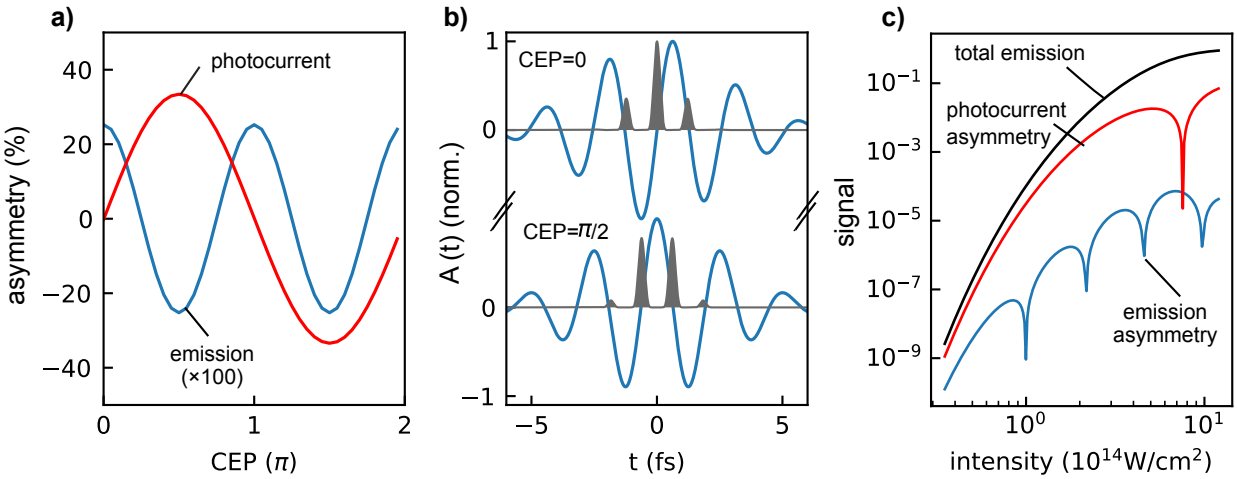

Figure 4.7: Signal origin in the single-atom picture calculated using SMM/SFA: a) CEP-variation relative to the mean-value of the total emission rate (blue) and the photocurrent (red). b) Final velocity of electrons ($\propto A(t)$, blue line) and the emission rate (gray area) for CEP=0 and CEP=$\pi/2$. c) Intensity-scaling for CEP=0 of the emission asymmetry (blue), photocurrent (red) and the total emission rate (black).

Before turning our attention to the comparison of experimental and numerical results, the microscopic origin of the measured signal in our model is briefly reviewed by considering the signal from a single argon atom at $I = 10^{14}\mathrm{W/cm^2}$. The CEP-dependence of the asymmetry, defined as the deviation from the mean-value averaged over the CEP, for different signals is shown in Fig. 4.7 a). The photocurrent, $\int v_{\mathrm{final}}(t)w(t)\,\mathrm{d}t$, (red line) asymmetry reaches several 10 %, whereas the total emission $\int(t)w(t)\,\mathrm{d}t$ asymmetry is about

a factor 100 weaker. Moreover, in contrast to the former which is direction-dependent, the total emission shows a periodicity of π and therefore can not be measured with the experimentally employed CEP-flipping scheme.

At first glance, it is surprising that the photocurrent asymmetry peaks at CEP=$\pi/2$. The reason becomes clear when realizing that $v_{\mathrm{final}} \propto A(t)$ as depicted in b). While the emission rate (gray area) is an even function in time for both ϕ_{CEP}, the vector potential (blue curve) is odd for CEP=0 and even for CEP=$\pi/2$. Therefore, the time-integral yields zero in the former and a maximum in the latter case. This is an important realization if the CEP-asymmetry is used to obtain the CEP of the pulse. The direct electrons might, however, be influenced by the Coulomb interaction as Ref. [172] suggests, so a more in-depth theoretical study might be needed for further clarification.

Moreover, when scanning the intensity at a fixed CEP (=0), as can be seen in c), the emission asymmetry yields pronounced minima stemming from the vanishing CEP-effect[219]. In contrast, the photocurrent only yields a single dip which originates from the depletion of the ground-state reducing the emission rate in the trailing part of the pulse.

4.4 Experimental results

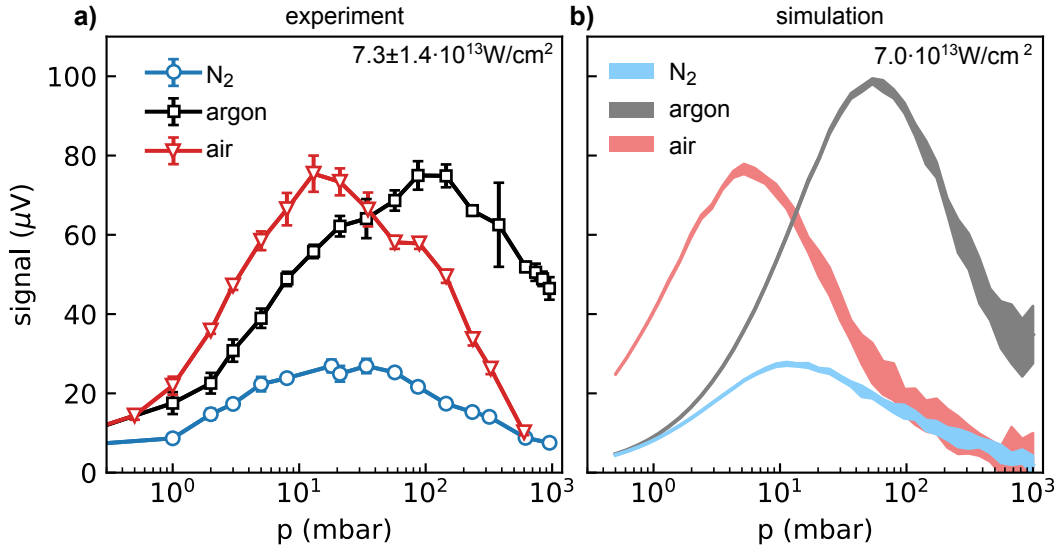

Figure 4.8: Pressure dependence of the maximum signal amplitude: a) Experimental measurement. Parameters can be found in the text. b) Simulation results. The thickness of the curves indicates the standard deviation of 10 Monte-Carlo simulations with different initial random seed ($\omega_0 = 8\,\mu$m, $I = 7 \cdot 10^{13}\mathrm{W/cm}^2$, $D = 100\,\mu$m and $\Delta z_{\mathrm{ion,eff}} = 7\mu$m).

The dependence on pressure of the maximum signal amplitude for nitrogen (blue line), argon (black line) and air (red line) are shown in Fig.4.8 a). The experimental data

has been obtained by averaging over three dispersion scans per data point (see Fig. 4.2 b) and the errorbars indicate the standard deviation. Performing these measurements via dispersion scans is necessary. Since, due to the optical path length of around 0.5 m in the vacuum chamber before the focus, increasing the pressure leads to a shift of the maximum to lower glass insertions. The electrode distance was around 100 μm. A rather low intensity of $7.3{\cdot}10^{13}$ W/cm^2 was used, in order to avoid reshaping of the dispersion trace with increasing pressure. Starting from low pressure, all three curves are increasing and reach a maximum at different pressures, nitrogen at around 30 mbar, argon at 100 mbar and air at 10 mbar. They subsequently decay going towards 1000 mbar. The maximum signal amplitude in argon and air is roughly equal, whereas it is around a factor of three lower for nitrogen.

The simulations reproduce the main features of the pressure-dependence very well, as can be seen in Fig.4.8 b), especially the relative maximal amplitudes and the pressures at which the maximum is reached. An intensity of $7.0 \cdot 10^{14}$W/cm^2 is used, close to the experimental value. Since the individual pseudoelectrons have a larger weight for higher pressure, a larger standard deviation of the Monte-Carlo simulations is obtained for higher pressures. The simulated distributions are slightly narrower than the experimental ones, which is likely due to the 2D-approximation.

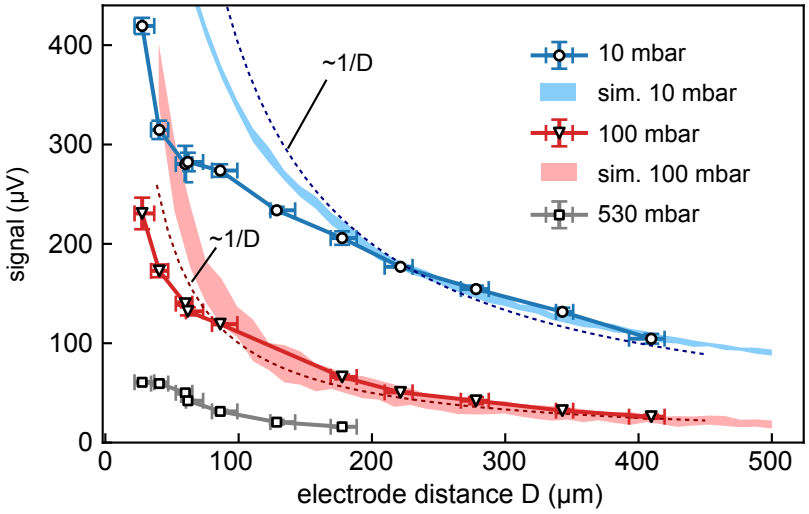

Figure 4.9: Electrode-distance dependence of the maximum signal amplitude for pressures of 10 mbar (blue), 100 mbar (red) and 530 mbar (gray) at an intensity of $8.3 \pm 1.8 \cdot 10^{13}$W/cm^2. Simulation for 10 mbar (light blue area) and 100 mbar (light red area) for $\omega_0 = 8\,\mu$m, intensity of $8.0 \cdot 10^{13}$W/cm^2, and $\Delta z_{\mathrm{ion,eff}} = 44\,\mu$m. For comparison the 1/D-dependence is shown (dotted lines).

Figure 4.9 shows the electrode-distance dependence of the maximum signal amplitude in nitrogen for pressures of 10 mbar (blue line), 100 mbar (red line) and 530 mbar (gray line)

at a peak intensity of approximately $8.3 \pm 1.8 \cdot 10^{13}\mathrm{W/cm^2}$. Again, each datapoint has been obtained from the average of three dispersion scans. The inter-electrode-distance D is changed via a miniature piezo-stage and determined via the imaging system. The signal amplitude increases nonlinearly by almost a factor of four when decreasing the distance from 420 μm to roughly 30 μm. At even lower distances, the laser starts to visibly hit the electrodes which we intentionally avoid. The different amplitude for the various pressures reflects the pressure dependence discussed above. The simulations (light blue and light red areas, peak intensity $8.0 \cdot 10^{13}\mathrm{W/cm^2}$) reproduce the distance dependence above roughly 150 μm, however, they slightly overestimate the signal for lower distances, which is further discussed below. For comparison, two curves proportional to $1/D$ (dashed lines) are shown, which reproduce the evolution of experiment and theory for higher distances.

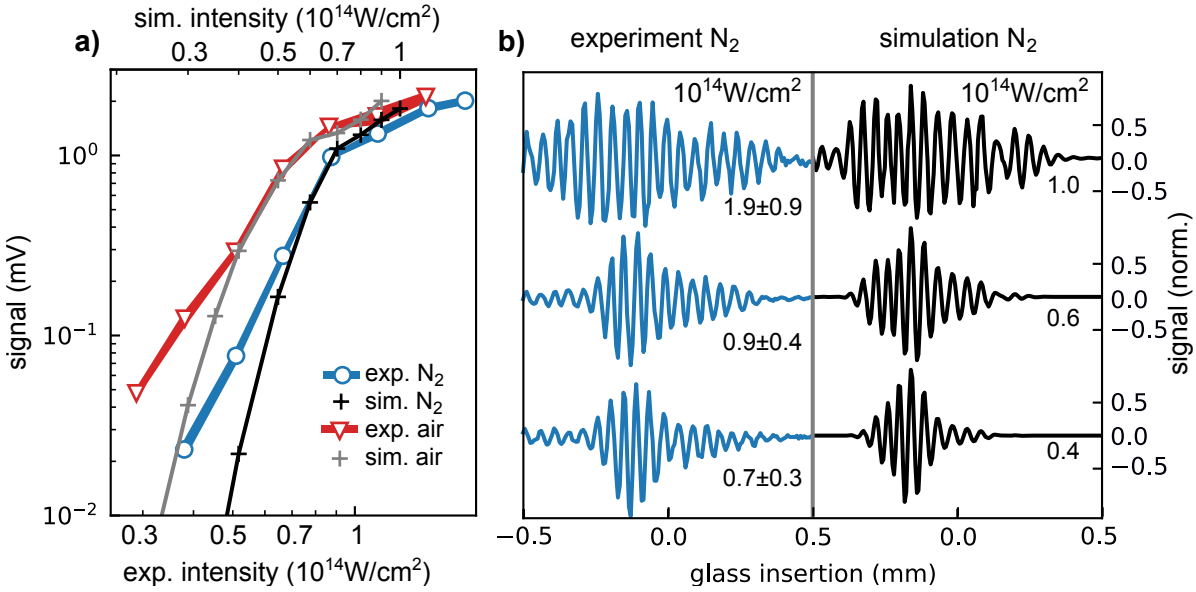

Figure 4.10: Intensity dependence and signal trace reshaping: a) Intensity-dependence of the maximum signal amplitude for nitrogen (blue dot) and air (red triangles) together with the respective simulations (black and gray crosses) at 25 mbar. b) Comparison of experimental and simulated signal traces for different peak intensities. Parameters for the simulation: $\omega_0 = 25\,\mu$m, $\Delta z_{\mathrm{ion,eff}} = 47\,\mu$m.

The scaling of the maximum signal strength with intensity can be seen in Fig. 4.10 a) for nitrogen (blue dots) and air (red triangles) at 25 mbar. The additional telescope was placed in the beampath, increasing the focal spotsize by around a factor of three. The signal amplitudes grow rapidly by almost two orders of magnitude when increasing the experimental intensity from about 4.0· to $8.0 \cdot 10^{13}\mathrm{W/cm^2}$. Above, a kink is formed that is connected to the saturation of the signal. In air the kink is reached slightly earlier and below the kink the signal amplitude is roughly a factor 3-5 higher compared to nitrogen. The simulations ($\omega_0 = 25\,\mu$m) for nitrogen (black crosses) and air (gray crosses) reproduce relative amplitudes and the initial transition from the rapid increase to the kink extremely

well. For the lowest intensities the simulations underestimate the measured signal, which can be traced back to the fact that the ADK rate is not appropriate anymore in this regime and a more complete theory for photoemission would need to be employed[57].

In order to better illustrate the connection between signal saturation and the formation of the kink, the experimentally measured dispersion traces in nitrogen are shown in Fig. 4.10 b) (blue curves, left side) and compared to the simulated traces (black curves, right side). The laser pulse for the calculation is obtained from a d-scan-measurement at the entrance of the vacuum chamber. Again, overall good agreement is observed. The low-intensity wings of the traces are underestimated in the simulation which can largely be explained by the finding above. Most importantly, the saturation of the signal trace is reproduced. It is connected to a quenching of the amplitude growth for the highest intensities above the kink observed in Fig. 4.10 a). In contrast, for other glass insertion and correspondingly lower relative intensities the signal still keeps growing rapidly. The simulations suggest that the occurrence of the kink is not connected to a saturation of the ionization (or the vanishing CEP-effect as shown in Sec. 4.3) since the maximum ionization fraction is around 1%. Instead the saturation is rather a consequence of scattering and the rapidly increasing Coulomb interaction. For higher ion densities, the charge interaction limits the asymmetric expansion of the electron distribution and thereby the induced charge on the electrode. The mechanism is further discussed in the following.

4.5 Discussion

In order to illustrate the effect of scattering and Coulomb interaction, we investigate their influence on the signal formation in the simulation. Figure 4.11 a) shows the time-dependence of the induced charge Q on one electrode normalized by the total emitted charge with scattering and Coulomb interaction selectively disabled for nitrogen at 100 mbar, $7.0 \cdot 10^{13}\mathrm{W/cm^2}$ and $\omega_0 = 8\,\mu$m. With neither scattering nor charge interaction (black line), the relative induced charge increases rapidly and reaches several 10 % as would be predicted from the photocurrent. Indeed, the initial slope of all three curves is proportional to the standard expression for the photocurrent $I = \sum q \cdot v$. However, when scattering is enabled (blue line), the rise of the induced charge is quickly damped and reaches close to the asymptotic value of about 1 % after 0.2 ns. Qualitatively, this observation can be understood by considering that electron propagation leads to charge induction only up to the first (isotropic) scattering event, since afterwards, on average, the charge is induced in our model (if one neglects that the electrodes limit further propagation). If additionally the charge interaction is switched on (red line), the rise is damped even faster and an asymptotic value of 0.2 % is reached, since the Coulomb interaction counteracts any charge imbalance and pulls the electrons back. Additionally, small, fast-decaying oscillations can be seen on the charge signal, that are connected to plasma oscillations. The figure also illustrates why the experimental signal is calculated from the total induced charge several 0.5 ns after the initial rise. The transient initial current burst is not resolved experimentally.

Additionally, we simulated the pressure-dependence with and without both effects, as

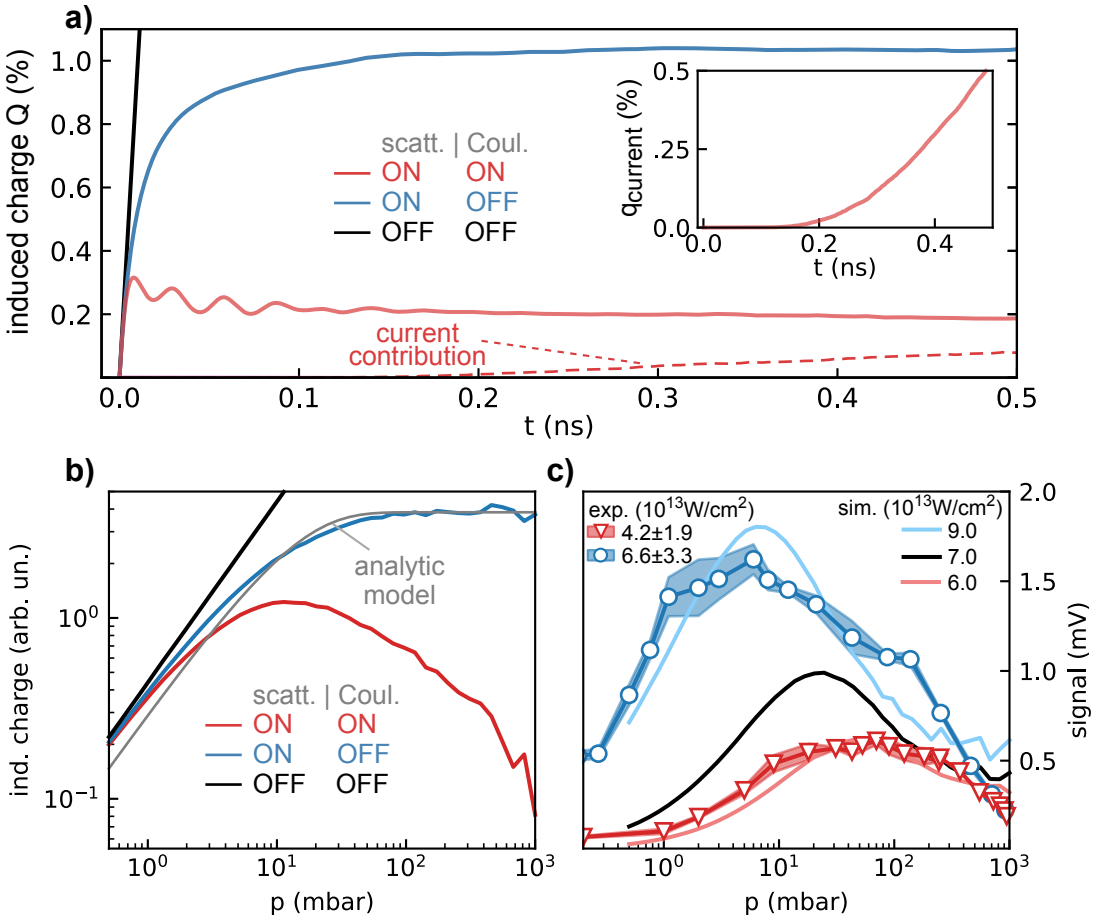

Figure 4.11: Role of scattering and the Coulomb-interaction: a) time-resolved induced charge at electrode A with selectively disabled scattering and Coulomb-interaction at 100 mbar. The relative charge that reaches the electrode is shown in the inset. The difference between the charges that have reached the left and right electrode can be identified with the current contribution (red dashed line, main panel) . b) Pressure-dependence of the induced charge for various conditions as indicated. c) Scaling of the pressure-dependence with different laser-intensities in argon. Simulations are shown as solid lines and compared with experimental measurements (symbols). The standard deviation of three dispersion scans is shown as shaded area. Further experimental parameters can be found in the text. Simulation parameters: a,b) $\omega_0 = 8\,\mu$m and $I = 7.0 \cdot 10^{13}$W/cm^2, c) $\omega_0 = 25\,\mu$m, $\Delta z_{\mathrm{eff,ion}} = 25\,\mu$m.

can be seen in Fig.4.11 b). Without any interactions (black curve), the signal is simply proportional to the pressure. Once scattering is considered, the signal saturates above around 50 mbar. Again, intuitively, for high pressures the contribution of a single charge is proportional to the distance it travels until the first scattering occurs, i.e. the mean-free path which scales as $1/p$. On the other hand, the number of charges scales linearly with p, therefore, the signal is constant at high pressures. Since the distance between the electron and the parent ion is limited by the electrodes, the signal drops once the mean-free path is on the order of the electrode distance.

This behavior can be described analytically. An electron with charge q undergoing the first scattering event at a distance x in electrode direction from its birth position $x_0 = 0$, contributes on average $q \cdot x/D$ to the induced charge Q on the electrode. Electrons reaching the electrodes contribute $q \cdot D/2D$ (assuming the electron is born in the center between both electrodes). Integrating the scattering probability over both regions ($[0, D/2]$ and $]D/2, \infty]$) and considering that the number of electrons is proportional to p results in:

$$Q \propto \frac{qp \cdot l_{\mathrm{mfp}}}{D}(1 - e^{-0.5\, D/l_{\mathrm{mfp}}}), \tag{4.5}$$

which is shown as gray line in Fig.4.11 b). The best fit to the simulated curve is obtained by using a mean-free path twice as large as the one used in the simulation. The expression also contains the approximate $1/D$-dependence observed in the distance scans. The reasoning leading to Eq. 4.5 also suggests that instead of the velocity v_{x} as for the photocurrent, the weighting factor for the macroscopic contribution of an individual electron should be the effective mean free path l_{eff} in the electrode direction:

$$l_{\mathrm{eff}} = \frac{v_{\mathrm{x}} \cdot l_{\mathrm{mfp}}}{\sqrt{v_{\mathrm{x}}^2 + v_{\perp}^2}}, \tag{4.6}$$

where v_{x} and $v_{\perp}$ is the velocity in detection direction and perpendicular to it, respectively, and where l_{mfp} is energy-dependent. The same considerations are applicable to both femtosecond streaking[171]/PHz-scale nonlinear photoconductive sampling[172] in gases.

Additionally, taking into account the Coulomb interaction leads to electrons experiencing the positive ion background. Qualitatively, in the simplified picture above, after the first scattering event, the electron motion is not isotropic anymore but the Coulomb field acts to undo the created charge imbalance. Therefore, the contribution of an individual electron, the average electron displacement, falls below the mean-free path. For a given intensity, this effect becomes more pronounced at higher pressures, since the concentration of free charges and the strength of the Coulomb interaction grows proportionally to the pressure. As a consequence, the measured signal is maximal at the gas pressure that maximizes the mean displacement, which for most intensities in this study is in the range of 1 to few 10 mbar.

The influence of the Coulomb interaction is further illustrated in Fig. 4.11 c) which shows the pressure-dependence in argon measured for two different peak intensities of $4.2{\cdot}10^{13}\mathrm{W/cm}^2$ (red triangles) and $6.6{\cdot}10^{13}\mathrm{W/cm}^2$ (blue dots) with the additional telescope

in the beam. For comparison, the corresponding simulations at three distinct intensities of (ω_0=25 μm) at $6.0 \cdot 10^{13}$W/cm^2 (light red line) and $9.0 \cdot 10^{13}$W/cm^2 (light blue line) and additionally at $7.0 \cdot 10^{13}$W/cm^2 (black line). Again, a slight systematic shift between experimental and theoretical intensity values is observed which can be explained by the uncertainty in the intensity calibration. At higher intensities, due to the increased number of charges the maximum signal grows, as does the Coulomb interaction leading to a shift of the maximum to lower pressures. A similar effect is observed in Fig. 4.8, when comparing the pressure-dependence of nitrogen and air. While very similar total scattering cross-sections can be assumed for both gases, as is done in the simulation, the air contribution peaks at lower pressures since a higher number of charges is generated due to the oxygen contribution. At the same time, once the peak intensity is so high that the maximum occurs at lower pressures than where the measurement is taken, saturation occurs. This, in turn, leads to a convolution of the intensity and pressure dependence.

Regarding the signal generation mechanism, there is some debate on the roles of the asymmetric charge distribution (dipole contribution) compared to the charges that reach the electrodes (current contribution). In the framework presented here, there is no real difference on the single charge level. The weighting potential of the electrode smoothly reaches a value of one at the electrode surface (see Fig. 4.5 b,c), meaning that the total charge of the particle q is induced in the electrodes regardless of whether the charge q has entered the electrode or sits close to the surface. Moreover, for the idealized situation of an infinite parallel plate electrodes, the induced charge Q just scales linearly with decreasing distance of the particle to the electrode. In order to further clarify the roles of current and dipole contribution, we specifically looked at the maount of free charges that reaches the electrodes q_{current}, as shown in the inset of Fig. 4.11 a). and its' contribution to the induced charge (red dashed line, main panel, current contribution). As can be seen, q_{current} constitutes a considerable fraction of the total free charge. Moreover, both the dipole contribution as well as the current contribution take part in forming the total induced charge (solid red line) that is measured in the end.

However, realistic electrode configurations can be more sensitive to charges closer to the electrodes (see Fig. 4.5c)), if the weighting potential is not linear. In an intuitive picture, this is the case, if more electric field lines of the particle charge do not end up on the electrodes but escape to the surroundings. This situation applies to all real experiments, especially to most solid-state experiments, where thin electrodes are deposited on the surface. As this finding suggests, the linearity of these measurements could be affected. It also implies that the scaling of the signal with electrode distance investigated in Refs. [191, 162], will depend on the actual electrode geometry.

We have also observed some deviations between experimental results and theoretical model, which is likey connected to idealizations in the latter. The employed infinite parallel plate model would predict that the induced charge on one electrode has the opposite sign than on the other electrode flipping with CEP. In the experiment, however, we observe that both signal pulses after the transimpedance amplifier, observed on an oscilloscope, exhibit the same sign and the CEP-dependence only manifests itself as a small variation of the signal height. We observe that the signal pulses from both electrodes have similar

shape only if the laser focus is close to the center of the electrodes. However, while the voltage signal pulse shape is strongly affected by the laser focus positioning, the CEP-dependence measured at $f_{\mathrm{rep}}/2$ is not. There are a lot of different effects that might play an additional role here, such as the surface roughness of the electrodes, potentially dielectric passivation layers and charging of the electrodes and consequently the interaction with the electron dynamics. Nevertheless, we believe that in a carefully designed experiment with well characterized electrodes and modeling of the whole electric circuit, in-situ information on the weighting potentials could be obtained. This could be achieved by scanning the laser focus between the electrodes and measuring the voltage signal pulse in addition to the CEP-dependence.

Our model describes the experiments very well despite the approximations. The most severe simplification is likely the pure mean-field treatment of electrostatic interactions, that neglects electron-electron and electron-ion scattering as well as electron-ion recombination. The former two effects likely have a similar influence as electron-neutral scattering. For our experimental parameters with ionization degrees below roughly 1 %, this simplification seems justified, but a microscopic extension might be necessary at higher intensities, where additional reshaping of the laser pulse due to the generated plasma[29] has to be considered. Moreover, the effect of ion movement has been neglected as well as the role of dynamic electromagnetic fields. The latter are the foundation for the production of THz radiation in plasmas in almost the same experimental setting[182, 183, 184]. Finally, the plasma produced light could lead to electron emission from the electrodes. Theoretically, particle-particle particle-mesh PIC-codes should be able to describe most of these effects. Nevertheless, surprisingly good agreement with our measurements has been obtained with our simple model. Experimentally interesting aspects might be learned from experiments that simultaneously measure both the generated electromagnetic radiation (THz, possibly down to GHz) and the electrode current.

4.6 Conclusion

In this chapter the macroscopic aspects of laser waveform dependent photocurrent signal generation measured by nearby electrodes has been investigated. Experimental measurements of the pressure-dependence of the signal amplitude for nitrogen, argon and air are presented. A maximum of the current signal is found at few mbar to several tens of mbar. Moreover, the electrode-distance dependence has been measured for different pressures and a nonlinear increase of the signal with decreasing electrode separation is found. Finally, the intensity-dependence is investigated for air and nitrogen. After a fast increase, the signal amplitude starts to saturate slightly below $1.0 \cdot 10^{14}\mathrm{W/cm}^2$. The signal in air is roughly a factor 3-5 higher and starts to saturate slightly earlier.

We present a theoretical model for the signal generation mechanism on the electrodes based on the Ramo-Shockley-theorem which resolves the artificial separation into dipole and current contribution. Using 2D particle-in-cell simulations, an excellent agreement with the experimental results is obtained. Through a series of simulations, the role of scat-

tering and the Coulomb interaction is discussed. Scattering damps the directional motion of the electrons after photoemission, limiting the buildup of an asymmetric charge distribution which causes the macroscopic signal. The Coulomb-interaction reduces the signal even further by suppressing the formation of charge imbalances. Finally, open questions and potential further experiments are discussed.

Our findings present a way to boost the current signal measurements in gases, that have so far been done at atmospheric pressures, by more than an order of magnitude by going to lower pressures, thereby reducing scattering. At the same time our results also seem to indicate that the Coulomb interaction is an important limitation for these experiments. We believe that this work represents an important step for the understanding of current measurements in attosecond science and will lay the basis for exploring further optimizations and fundamental limitations.

Chapter 5

Transient field-resolved reflectometry from solid-state surfaces

Electro-optic sampling (EOS, see Sec. 3.3.2) has been for decades an invaluable tool for the investigation of solid-state material properties in THz-time-domain spectroscopy (THz-TDS)[220, 221] and especially in optical-pump THz-probe (OPTP) experiments[222]. These techniques have found a vast variety of applications from the study of bulk and nanostructured semiconductors[223], polymers[224], biological relevant molecules[225] pushing for medical applications[163] to dynamical processes in strongly correlated systems such as pair-breaking and state recovery in superconductors[226]. A particularly important example for our work is the buildup of collective excitations, i.e. plasmons, after photoexcitation of a semiconductor as studied in Refs. [227, 228].

Time-domain spectroscopy via THz-EOS has several advantages over other approaches [220]. Firstly, since field-sampling provides both amplitude and phase of the THz field, a direct measurement of real and imaginary parts of the refractive index and its transient changes becomes possible without having to resort to the Kramers-Kroning relation. This may sound like a mere technicality but has profound consequences if the relevant optical transition is not fully contained within the sampled frequency range. For our data, for example, the real and imaginary parts of the transient reflectivity change caused by a plasmon peak can be extracted even though our measured frequency window lies considerably above the plasmon resonance frequency.

Furthermore, compared to FTIR, the information on the THz-field gets encoded in the sum-frequency signal that lies in the wavelength range of the VIS-NIR EOS gating pulse, allowing for a much simpler, more sensitive detection via conventional photodiodes compared to MIR detectors that usually require cryo-cooling. Moreover, the EOS-signal is typically recorded in a heterodyne configuration which allows the detection of much smaller signals compared to sampling via photoconductive antennas. In addition, the time-gated coherent detection scheme allows to record signals way below the background black-body radiation level[229]. For pump-probe experiments, the generation of the THz-radiation via femtosecond optical pulses means that well synchronized laser pulses are intrinsically available[222]. Finally, EOS as a field-resolved measurement technique offers sub-cycle

time resolution.

Currently, field sampling via EOS is developing in two aspects. Firstly, the technique is driven towards extreme sensitivity. EOS with a dynamic range of 12 orders of magnitude[163] and the measurement of vacuum fluctuations could be demonstrated[164]. Moreover, the former study could show a time resolution down to the attosecond range[163] due to the high stability and phase resolution. Secondly, EOS field sampling is being pushed towards shorter wavelengths from the THz to the short wavelength IR around 1.2 μm[31]. However, pump-probe implementations in the short-wavelength region have not been demonstrated so far.

In principle, information on the transient dynamics of photoexcited carriers in solid samples can be obtained either in transmission or reflection geometry. While transmission measurements are easier to realize, they require transparent or very thin samples. The latter are usually hard to produce in the desired quality. Moreover, thin-films or nanostructured or otherwise functionalized samples usually require substrates that do not necessarily transmit the MIR probe light which limits the applicability of pump-probe studies. In contrast, all these limitations are absent in the reflection geometry.

Here, we report the implementation of a pump-probe reflectometry setup in the 3-6 μm wavelengths region which represents to our knowledge the shortest wavelength range for pump-probe reflectometry measurements using EOS reported to date. The focus of this chapter lies on the experimental implementation. In order to demonstrate the capabilites of our instrument, measurements of the fs-ps dynamics of highly excited semiconductors are presented. The field-resolved capability is used to measure the real and imaginary change of the reflectivity, but the application to sub-cycle field-dependent processes is anticipated.

The outline is as follows: First, we describe the experimental setup and measurement approach. Subsequently, we briefly discuss the theoretical basics for the interpretation of our measurements with a focus on bandstructures and effective masses in semiconductors as well as macroscopic aspects. Then, we describe the experimental measurements of transient reflectivity changes Δr. We find a strong influence of carrier diffusion and surface recombination on GaAs on a 10 ps timescale. We are also able to measure the 100 fs buildup time of collective excitations in GaAs in agreement with Ref. [227]. A significant difference of Δr between GaAs and Ge on the few ps timescale is observed which can be attributed to the intervalley scattering of electrons in the conduction band and the accompanied change of the effective mass. Furthermore, we discuss the dependence of the carrier-scattering rate on the excited carrier density. Finally, we provide an outlook on 2D-materials by presenting a measurement from a graphene sample and give a conclusion.

The NOPA laser system has been developed by Marcel Neuhaus (M.N.). The measurement approach including the MIR generation and pulse compression was developed and implemented by the author, M.N., Zilong Wang (Z.W.) and Mario Aulich (M.A.). The chirped mirrors are provided by Volodymyr Pervak (V.P.). The experimental data has been taken by the author together with M.N. and M.A. The presented experimental data has been analyzed and interpreted by the author and the results were discussed with M.N., M.A., Z.W. and the Burgdörfer group.

5.1 Experimental foundations

Setup and approach

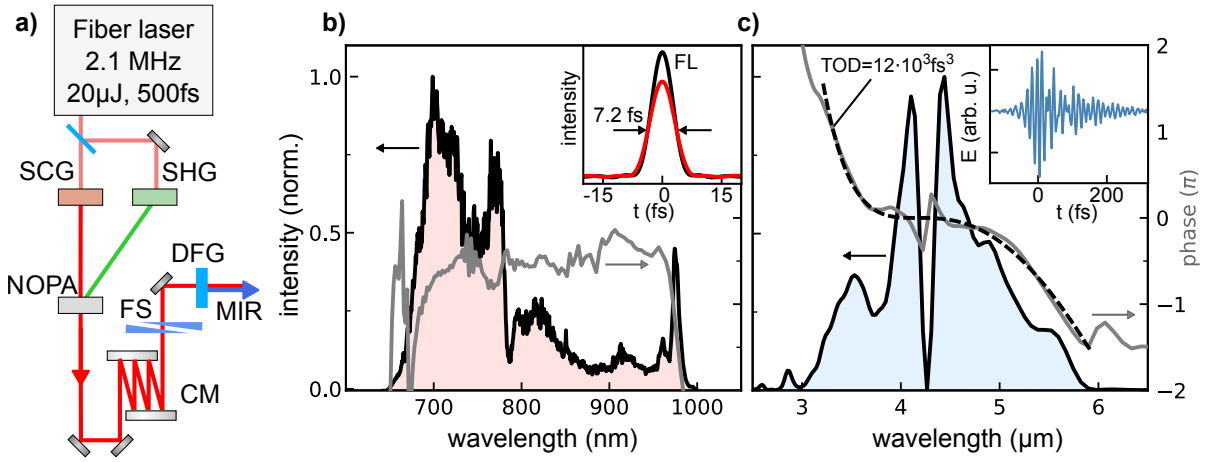

Figure 5.1: Laser setup and pulse characterization: a) schematic overview of the NOPA seed laser including the iDFG crystal for MIR generation (adapted from Ref. [230]). b) NIR spectrum (black line and red shaded area) and phase (gray line) reconstructed via a d-scan measurement. The inset shows the temporal intensity (red line) compared to the Fourier-limit (black line). c) MIR spectrum (black line and blue shaded area) and phase (gray) as measured by EOS. The inset shows the temporal evolution of the electric field.

The laser system and experimental setup for MIR field-resolved transient reflectometry will be presented in detail in another publication[230]. In short, the laser frontend consists of a non-collinear optical parametric amplifier (NOPA) delivering sub-8 fs pulses at around 800 nm which is , in turn, used to excite the samples under investigation and generate and sample mid-infrared radiation. The NOPA is driven by a commercial fiber laser (Active Fiber Systems) at a wavelength of 1030 nm and approximately 500 fs pulse length, as shown in Fig. 5.1 a). A part of the output is used for super-continuum generation (SCG) in YAG which leads to significant spectral broadening serving as the seed for the NOPA process. Another part is used for second harmonic generation acting as the pump. A broadband NIR pulse is achieved at the NOPA output spanning from 650-980 nm. The NIR pulses are compressed by a combination of fused-silica wedges and a set of complementary chirped mirror pairs to a pulse duration below 8 fs at an energy of around 2 μJ. The NIR pulses also drive the intrapulse difference frequency generation process (iDFG) in a $LiIO_3$-crystal[231] through which MIR pulses are produced.

The NIR laser spectrum (black line and red shaded area) is shown in Fig. 5.1 b). The spectral phase (gray line) has been reconstructed from a d-scan measurement obtained by scanning the wedge position and taken at the position of the EOS sampling focus in the pump-probe setup. The inset shows the reconstructed pulse intensity (red line) and duration of 7.2 fs in comparison to the Fourier limit (black line; FL).

Figure 5.1 c) shows the mid-infrared spectrum (black line and blue shaded area) and phase (gray line) measured by electro-optic sampling. Here, the bandwidth spans from 3-6 μm, but can be extended down to roughly 2 μm by slightly adjusting the DFG crystal. The strong absorption line at around 4.25 μm originates from CO_2 absorption[232] in air since the measurements presented here are taken at ambient conditions. The spectral phase is dominated by a strong third-order phase. While the group-delay dispersion is largely compensated by the combination of normal and anomalous dispersive materials in the beampath, the third order dispersion is always positive and adds up. As a consequence, even though the intensity FWHM can be as short as 30 fs, the MIR pulse always exhibits considerable postpulses, as shown in the inset. While the residual phase of the MIR could be compensated in the future by specially designed chirped mirrors, here, we used the pulse as is. As further discussed below the time resolution in the experiments was not affected by the MIR pulse shape.

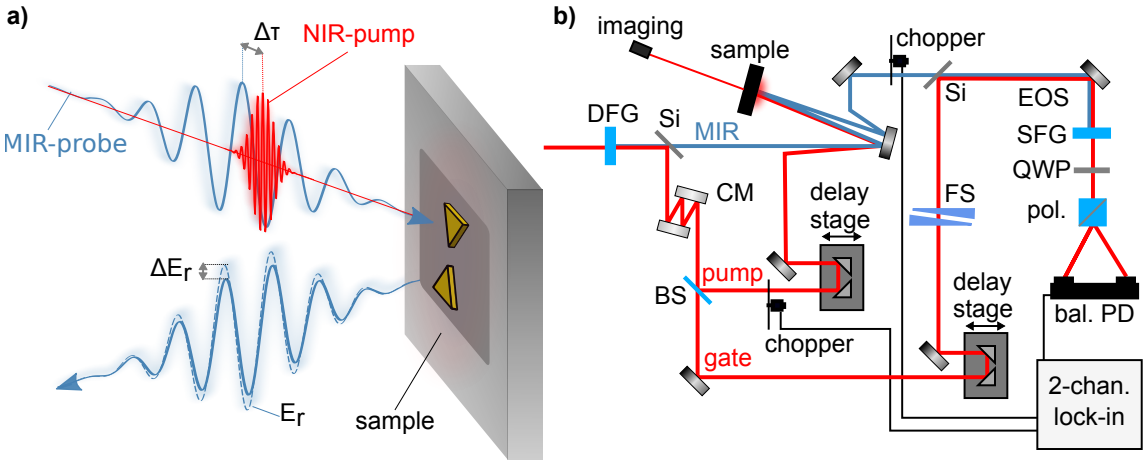

Figure 5.2: Experimental setup: a) Illustration of the measurement scheme. A MIR-probe pulse and a NIR-pump pulse impinge on a sample. The pump pulse leads to a change of the reflected field. b) Experimental setup: 3-arm interferometer with MIR-arm, pump arm and EOS gating arm. Optical choppers are placed in the pump and MIR arms for lock-in-detection at two different reference frequencies (adapted from Ref. [230]).

The measurement approach is illustrated in Fig. 5.2 a). A MIR probe pulse (blue waveform) and a time-delayed NIR pump pulse (red waveform) are focused onto the sample. The reflected field E_r and the pump induced change of the reflected field ΔE_r are measured simultaneously with EOS as a field-resolved measurement technique (see Sec. 3.3.2). Since the measurements are performed in reflection, arbitrary complex samples from bare semiconductor surfaces to nanostructure enhanced thin-layer films on opaque substrates with arbitrary thickness (as in the illustration) can be measured. The price to pay is a slightly more complex procedure for changing samples. Nevertheless, using two CCD cameras at different positions for referencing the beam reflected from the surface, a sample change can typically be performed in less than 30 minutes. The work presented here focuses on

measurements from GaAs wafers (<110>, Freiberger Compounds) and a monocrystalline Ge sample (<111>, Edmund optics), since they allow good comparison with literature.

A scheme of the measurement setup is shown in Fig. 5.2 b). After the DFG crystal, a 1mm-thick silicon window separates MIR and NIR pulses. The NIR pulses undergo four reflections from a chirped mirror pair for pre-compensating the dispersion and are further split into pump and EOS gating beam. Both pump and gate pulse can be time-delayed individually via separate delay-stages. The pump beam is recombined with the MIR pulse and focused onto the sample. The overlap of both pulses can be checked using a microbolometric camera (FLIR systems) or even a CCD using a residual long-wavelength contribution from the supercontinuum generation. A maximum NIR fluence of up to around $400\mu\mathrm{J/cm}^2$ is reached at the sample surface. For transmissive samples, the NIR spot on the sample can be imaged. The reflected MIR is recollimated with the same focusing mirror under a slight angle before being recombined collinearly with the gate pulse on another Si-window. Thereafter, the MIR pulse and the pump-induced change is sampled using an electro-optic sampling setup.

Two chopper wheels are employed in the experimental setup. One chopper wheel is placed in the MIR beampath after the sample and another chopper in the pump arm. They are running at different non-commensurate reference frequencies f_{MIR} and f_{PP}, respectively. A 2-channel lock-in amplifier (Anfatec eLockin204) simultaneously demodulates the signal from the balanced photodiode at both reference frequencies and allows to measure the reflected field E and the pump-induced change ΔE at the same time. Some care needs to be taken when assigning the measured signals to the field quantities, which is derived in appendix A.1. First, since the MIR beam that carries the modulation due to the pump beam is also chopped at f_{MIR}, ΔE is proportional to two times the signal at f_{PP}. Secondly, the pump induced reflectivity change also affects the average field amplitude and therefore E is proportional to the signal at f_{MIR} minus the signal at f_{PP}.

Several issues are being tackled by M.N., M.A. and Z.W., which had affected the performance of the system. The achievable signal-to-noise ratio in the setup was often limited by the stability of the white light generation in combination with the fiber laser. We performed in-situ noise measurements and optimization via a photodiode and digital oscilloscope while aligning the laser system which is, however, rather cumbersome and does not aid the long-term stability during the measurements. Currently, an active stabilization scheme similar to Ref. [233] is being implemented.

Moreover, the system is being installed in a vacuum chamber, which allows to suppress the CO_2-absorption peak. Furthermore chirped mirrors for the MIR are developed by V.P. which could allow 20 fs MIR pulses. Additionally, here it is suggested to replace the silicon beam combiner in front of the EOS setup, where the MIR is currently being transmitted, by an ITO-coated sample, where the MIR would be reflected and the NIR gating pulse is transmitted. This way, dispersion and phase distortions of the MIR pulse between the sample and the detection would be minimized, which is important in order to truly achieve sub-cycle resolution for the fields reflected from the experimental sample.

Experimental measurements

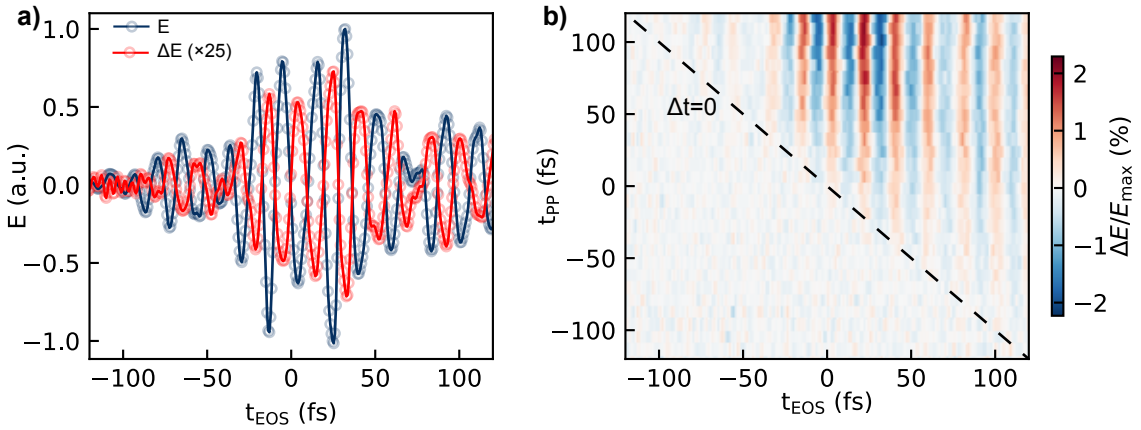

Figure 5.3: Experimental signal: a) EOS measurement of the reflected field (darkblue dots and line) and the pump-field induced change (red dots and line) on GaAs for a fixed pump-probe delay of 150 fs. b) Pump-probe delay t_{PP} resolved relative change of the reflected field. The diagonal (dashed line) indicates the propagation of the pump-pulse through the EOS sampling window.

An exemplary experimental signal trace is illustrated in Fig. 5.3 a), which shows the reflected MIR field (dark blue open dots) and the change of the reflected field (red open dots) at a fixed pump-probe delay from a GaAs sample. The solid lines have been obtained by Fourier-filtering out wavelength components below 1.2 μm and above 14 μm, lying outside the MIR spectrum. The measured ΔE is out of phase with E, which means that under the presence of the NIR pump pulse on the sample, the MIR reflectivity is reduced. Figure 5.3 b) shows a pump-probe delay resolved measurement of the relative change of the reflected field. It can clearly be seen how the signal builds up as the pump pulse starts to arrive before the MIR pulse (positive $\mathrm{t_{PP}}$), which is manifested in the diagonal structure. The dashed diagonal line indicates how the peak of the pump pulse gets temporally displaced with respect to the MIR pulse due to the pump-probe delay.

The measurement of E and ΔE allows to determine the pump induced relative electric field reflectivity change $\Delta r/r$:

$$\frac{\Delta r(\omega)}{r(\omega)} = \frac{\Delta E_{\mathrm{r}}(\omega)}{E_{\mathrm{r}}(\omega)}, \tag{5.1}$$

where r is the unexcited reflectivity and the relation is expressed in the spectral domain. Furthermore, in terms of the change of the reflected intensity $\Delta R = |r + \Delta r|^2 - |r|^2$, the relative reflectivity change $\Delta R/R$ is given by:

$$\frac{\Delta R}{R} = 2\mathcal{R}\left(\frac{\Delta r}{r}\right) + \mathcal{R}\left(\frac{\Delta r}{r}\right)^2 + \mathcal{I}\left(\frac{\Delta r}{r}\right)^2, \tag{5.2}$$

where $\mathcal{R}$ and $\mathcal{I}$ are the real and imaginary parts, respectively. Interestingly it can be seen, that the imaginary part of $\Delta r/r$ only enters quadratically in the intensity expression. The

field-resolved measurements are therefore more sensitive to $\mathcal{I}(\Delta r/r)$, which is connected to electron scattering in the Drude model, compared to intensity resolved approaches.

Since the MIR pulse is measured in a field-resolved fashion, the time resolution in our pump-probe experiments is not limited by the MIR pulse duration, but rather the NIR pump pulse duration at the sample (∼8 fs). In our case, the temporal resolution is slightly limited by the dispersion of the MIR pulse between the pump-probe sample and the EOS focus. Nevertheless, we expect it to be on the order of 10 fs or slightly above.

5.2 Theoretical background

Before we can turn our attention to the experimental results, we briefly have to review the bandstructures and the mechanisms that can lead to a change of the optical properties under excitation. Furthermore, the relation to the experimentally measured change of the reflectivity has to be established. Finally, we discuss how to treat an inhomogeneous excitation as well as excited carrier diffusion.

Bandstructure and density of states

The bandstructure of GaAs and Ge is shown in Fig. 5.4 a) and b), respectively. The presentation is simplified as details of heavy-hole, light-hole and split-off hole band are neglected. The direct transitions from the valence band (blue line) to the conduction band (red line) that can be driven by our NIR pump laser are indicated as black arrows. The ranges where transitions are possible given the spectral extent of the pump pulse (1.2-1.9 eV) are also shown (green shaded areas). Here, an immediate difference between both materials becomes apparent. For GaAs, direct transitions are only possible close to the Γ-point into the bottom of the conduction band due to the relatively high bandgap of around 1.4 eV. In contrast, for Ge the transitions occur away from the Γ-point mostly into a non-parabolic region in the conduction band. Moreover, since the energy at the X-valleys (0.85 eV) and L-valleys (0.66 eV) is significantly lower than at the point in the conduction band where the transitions happen, these valleys can be expected to be easily reached by intervalley scattering, which has been well studied for Ge (e.g. Refs. [234, 235, 236, 237, 238, 239]).

An important aspect regarding the properties of excited electrons in the conduction band is schematically illustrated by the shape of isoenergy surfaces around the Γ-valley (blue), X-valleys (red) and L-valleys (green), as shown in Fig. 5.4 c). The elliptic shape for X- and L-valleys indicates that two different effective masses have to be attributed to the electrons in the conduction band valleys: a longitudinal effective mass m_L along the longer axis of the ellipsoid and the transverse effective mass m_T perpendicular to it. Since the effective mass is connected to the inverse of the curvature of the bandstructure: $m_\mathrm{L} > m_\mathrm{T}$. Which effective mass is relevant for the electron dynamics depends on the direction in which it is driven, e.g. the orientation of an external electric field. An overview of the effective masses for GaAs and Ge used in this work is given in Tab. 5.1 based on Ref. [244].

Another quantity that is connected to the effective masses is the density of states of

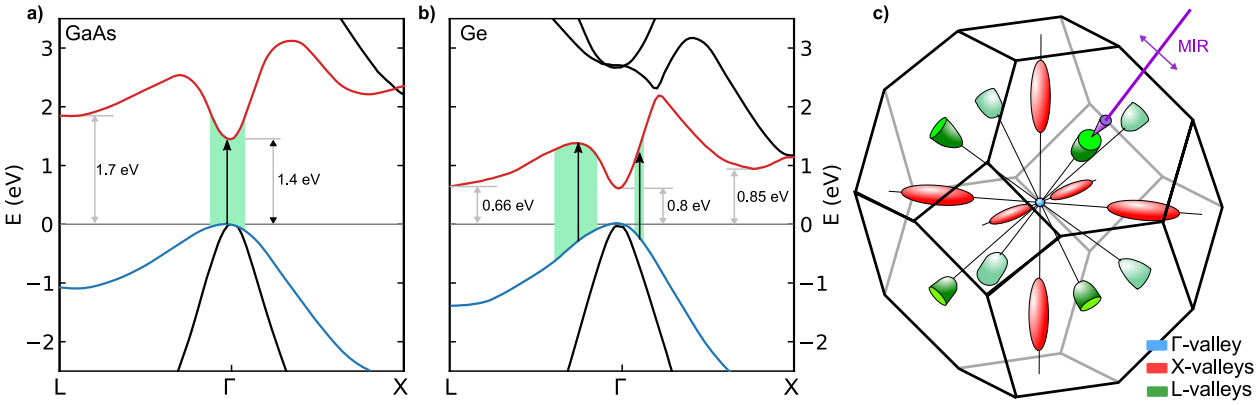

Figure 5.4: Bandstructures and Brillouin zone: a) Bandstructure of GaAs adapted from Ref. [240]. b) Bandstructure of Ge based on Ref.[241]. The bandgap values are from Ref.[242]. c) Brillouin zone of Ge and schematic illustration of the elliptic isoenergy surfaces around the Γ-, X- and L-valleys (adapted from Ref. [243]).

material	Γ	X,l	X,t	L,l	L,t	lh	hh	so
Ge	0.038	1.35	0.29	1.57	0.081	0.042	0.32	0.095
GaAs	0.064	1.90	0.19	1.90	0.075	0.083	0.59	0.154

Table 5.1: Effective masses for Ge and GaAs at the Γ-, X- and L-valley as well as for the light-hole (lh), heavy-hole (hh) and split-off hole (so) in terms of the free electron mass. Both longitudinal (l) and transverse (t) effective masses are given where appropriate. All values are from Ref. [244].

different valleys. Intuitively, for a higher effective mass, the curvature of the band is lower and therefore the density of states is higher. For anisotropic valleys, the relation to the density of states $g(E)$ is given via $g(E) \propto m_{\mathrm{dos}}^{3/2}$, where m_{dos} is the effective mass for density of states calculations. In turn, m_{dos} is connected to the transversal and longitudinal effective mass for an elliptic band minimum through[245]:

$$m_{\mathrm{dos}} = M_{\mathrm{c}}^{3/2} \sqrt[3]{m_{\mathrm{l}} m_{\mathrm{t}} m_{\mathrm{t}}}, \tag{5.3}$$

where M_{c} is the multiplicity of the respective band minimum in the Brillouin zone (6 and 4 for the X-valley and L-valley, respectively). Note that at the Γ-point, the relevant terms under the cube root is m_{Γ}^3. In Ge, due to the large effective longitudinal mass compared to the Γ-valley and the multiplicity, the following approximate ratios between the density of states in the valleys: $g_{\mathrm{X}} : g_{\mathrm{L}} : g_{\Gamma} \approx 8.3 : 1 : 3 \cdot 10^{-3}$ is obtained. In Fig. 5.4 c) this is qualitatively illustrated by the different volumes of the ellipsoids.

Transitions and influence of pump excitation

An exhaustive presentation of the optical properties of semiconductors is given in several specialized books, e.g. Ref. [247] which is beyond the scope of this work. Here, we try to

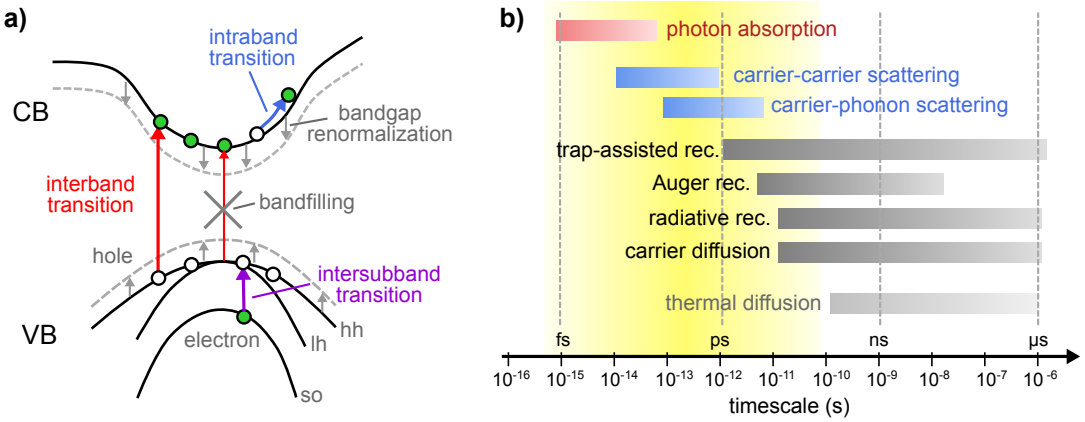

Figure 5.5: Photoexcitation processes and timescales: a) Schematical illustration of the possible optical transitions and the effect of an excited carrier population. b) Timescale of different processes leading to excitation (red), thermalization (blue) and carrier removal (dark gray) as well as heat diffusion (gray). The yellow area indicates the timescales covered by our experiments (adapted from Ref. [246]).

capture the relevant aspects needed for the interpretation of our experiments in a simplified qualitative picture, as schematically illustrated in Fig. 5.5 a). We consider three types of optical transitions in a semiconductor: Firstly, interband transitions (red arrows) from the valence (VB) to the conduction band and secondly intersubband transitions (purple arrows) between subbands in the VB or CB, both driven by absorption of a photon. Finally, intraband transitions (blue arrows) within one subband for a charge carrier driven by the electric fields. We neglect the influence of impurities and excitons.

In a semiconductor, there will be a number of thermally excited eletrons and holes in the CB and VB, respectively due to the small bandgap. The intrinsic carrier concentration is about $2 \cdot 10^6 \mathrm{cm}^{-3}$ in GaAs[248] and $2 \cdot 10^{13} \mathrm{cm}^{-3}$ in Ge[249]. Generally, which type of transition dominates, depends on the photon energy. Around the bandgap energy, interband transitions dominate, which can be driven by the NIR pump, while for considerably longer wavelengths intraband transitions play the major role, as for the MIR probe[250]. The pump pulse excites electrons from the valence into the conduction band via interband transitions leading to charge densities on the order of $10^{18} \sim 10^{19} \mathrm{cm}^{-3}$ for our experimental conditions, much higher than the intrinsic densities. This changes the optical properties of the semiconductor for the MIR probe pulse in several regards, whose photon energy is significantly below the bandgap. Firstly, the impact of intraband transitions increases due to the much higher electron (hole) density in the CB (VB), which can be described via the Drude model[250] introduced below. Secondly, intersubband transitions might open due to the excited electrons and holes. For example, transitions from the split-off hole band (so) to the light hole (lh) or heavy hole (hh) band[251] might occur. For photon energies around the bandgap, two additional effects would be visible, namely blocking of transitions due to bandfilling and the renormalization of the bandgap due to the high free-

carrier density[252, 253]. Most aspects of our measurements can be described within the Drude model even though intersubband transitions might play a role in certain wavelength regions.

An overview of the different processes within semiconductors in our pump-probe experiments and their respective timescales is given in Fig. 5.5 b). After the initial excitation, the non-equilibrium distribution of excited electrons and holes thermalizes via carrier-carrier collisions as well as interactions with the lattice via phonons. The former is usually much faster (10-100 fs)[246] which leads to the notion of separate effective temperatures of the excited electrons (holes) in the conduction (valence) band and the phonon system in the so-called two-temperature model[254, 255]. The interaction between the excited carriers and phonon system and the equilibrium of their respective temperatures typically occurs on the 100 fs-∼10 ps timescale[246]. The electron-phonon interaction is also responsible for scattering electrons from one conduction band valley to another (intervalley scattering)[256]. Finally, recombination and diffusion lead to a reduction of the carrier density at the surface after pump excitation. There are a number of different carrier recombination mechanisms, such as radiative band-to-band recombination and non-radiative Shockley-Read-Hall (defect/impurity assisted)[257, 258], Auger (three-carrier interaction)[259] and surface recombination (surface-defect assisted)[260, 261]. Recombination rates in semiconductors depend significantly on the sample parameters, such as impurity densities. The timescale for diffusion and recombination typically lies in the range of ∼10 ps-∼100 ns[246]. Although recombination is not the central topic of this work, we will discuss surface recombination in more detail below since it leads to a modification of the macroscopic excited carrier distribution that can be measured in our setup.

Relation to experimental measurements

We express the permittivity of the sample that has been excited by the pump pulse ϵ_{exc}, as follows:

$$\epsilon_{\mathrm{exc}}(\omega) = \epsilon_{\mathrm{unexc.}}(\omega) + \Delta\epsilon(\omega), \tag{5.4}$$

where $\epsilon_{\mathrm{unexc.}}$ is the permittivity of the unexcited sample and $\Delta\epsilon$ is the pump-induced change. The photon energy of our probe pulses (0.2 eV-0.4 eV) is below the bandgaps of GaAs and Ge and can therefore not drive interband transitions between the valence and conduction band. Hence, we only consider the intraband motion of excited electrons and holes in the conduction and valence band, respectively. This results in a Drude-type change of the permittivity:

$$\Delta\epsilon = \frac{-n_{\mathrm{fc,k}} \cdot e^2}{m_{\mathrm{eff,k}} \cdot \epsilon_0} \cdot \frac{1}{\omega^2 - i\omega\Gamma_{\mathrm{k}}}, \tag{5.5}$$

where n_{fc} is the free-carrier density, e is the electron charge, m_{eff} is the effective mass, ϵ_0 is the vacuum permittivity and Γ is the Drude scattering rate (i.e. momentum relaxation rate). The index k distinguishes electrons and holes and also valley contributions (see Sec. 5.3.3 below). The total $\Delta\epsilon$ is therefore a sum of terms described by Eq. 5.5. Here, we only consider the case where the carrier density due to photoexcitation is much higher

than due to any impurity doping, such that the density of electrons approximately equals the density of holes. Due to the denominator in Eq. 5.5, the Drude permittivity change is larger for longer wavelengths (i.e. THz pulses) which are therefore a particular sensitive probe of free-carriers.

More complete expressions that take bandgap renormalization and band occupations into account exist[253, 262], but are not necessary for our purposes. A complete quantum mechanical first-order description of pump-induced changes is given in Ref. [263]. Our approach neglects virtual intersubband transitions as well as interband transitions of electrons (holes) between different conduction (valence) bands. As has been shown in the framework of quantum mechanical calculations, even if interband transitions are taken into account, the Drude-term can still provide a decent functional description[262, 252, 263].

The pump-induced change of the optical properties can be measured by the change of the reflectivity. For simplicity, we will first consider a homogeneously excited sample, which we refer to as homogeneous approximation. At normal incidence, the reflectivity can be calculated by the Fresnel equation:

$$r_{\mathrm{exc}} = \frac{1 - n_{\mathrm{exc}}}{1 + n_{\mathrm{exc}}}, \tag{5.6}$$

where n_{exc} is the refractive index of the excited sample which is given by:

$$n_{\mathrm{exc}} = \sqrt{n^2 + \Delta\epsilon}. \tag{5.7}$$

Here, n is the refractive index of the unexcited sample and $\Delta\epsilon$ is the change of the relative permittivity given in Eq. 5.5. For small changes of the refractive index Δn, the change of the reflectivity Δr can be approximated by:

$$\Delta r = r_{\mathrm{exc}} - r_{\mathrm{unexc.}} \approx \frac{-2\Delta n}{(1+n)^2}, \tag{5.8}$$

i.e. for a real valued refractive index of the unexcited sample, the real and imaginary part of the refractive index change can be readily obtained from Δr.

Macroscopic aspects

The pump pulse only has a finite penetration depth into the sample due to absorption which means that also the excitation profile from the surface will not be homogeneous as assumed so far. Whether this inhomogeneity plays a role depends on the relative penetration depth l_{p} of pump and probe pulses which can be calculated from the absorption coefficient (or the complex refractive index). For the NIR pump pulses in Ge we obtain $l_{\mathrm{p}} \approx 0.25\mu$m, whereas the sample is transparent for the MIR pulse. The opposite limit to the homogeneously excited sample is a thin-film with conductivity σ and effective thickness d. The reflectivity is described by:

$$r = \frac{n_1 \cos\theta_1 - n_2 \cos\theta_2 - Z_0 \sigma d}{n_2 \cos\theta_2 + n_2 \cos\theta_2 + Z_0 \sigma d}, \tag{5.9}$$

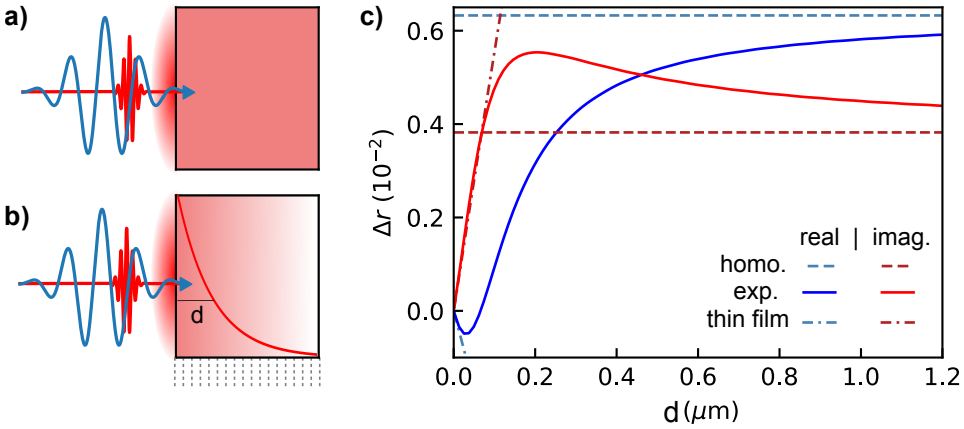

Figure 5.6: Influence of inhomogeneous excitation: a) ilustration of a homogeneous excitation compared with b) an inhomogeneous excitation with an exponential decay. c) Real (blue) and imaginary part (red) of the reflectivity change upon excitation for different excitation depths calculated from the transfermatrix approach (solid lines), the thin-film approximation (dashed-dotted line) and the homogeneous approximation (dashed lines). The calculations were performed on Ge at a wavelength of 5.5 μm, surface excited electron density of $2.4{\cdot}10^{18}\mathrm{cm}^{-3}$ using the transverse effective mass in the L-valley and a Drude-scattering rate of $2{\cdot}10^{14}$Hz.

where n_1 is the refractive index of the first medium (here air $n_1 \approx 1$) and n_2 of the second medium and θ_1 and θ_2 are the angles with respect to the surface normal in medium 1 and 2, respectively. $Z_0 = 1/\epsilon_0 c$ is the vacuum impedance.

For an arbitrary refractive index distribution along the propagation direction of the beam, the transfer-matrix approach can be employed[264, 223, 265]. Here the medium is divided into thin slabs of length L with constant refractive index, as illustrated by the gray dashed lines in Fig. 5.6 b). The electric field $E(z+L)$ and magnetization field $H(z+L)$ are related to the fields at position z via:

$$\begin{pmatrix} E(z+L) \\ H(z+L) \end{pmatrix} = M \cdot \begin{pmatrix} E(z) \\ H(z) \end{pmatrix}, \tag{5.10}$$

where M is the transfer-matrix which is determined by the wavevector $k' = n\omega/c$ within the slab:

$$M = \begin{pmatrix} \cos(k'L) & \sin(k'L) \\ -k'\sin(k'L) & \cos(k'L) \end{pmatrix}. \tag{5.11}$$

The transmission matrix M_s of a sample is simply given by:

$$M_\mathrm{s} = M_\mathrm{N} \cdot \ldots \cdot M_2 \cdot M_1, \tag{5.12}$$

where M_i is the transmission matrix of the i-th slabs. The reflectivity r and transmittivity t can then be calculated from M_s. For a purely exponential decay of Δn, analytic solutions exist[266, 267].

Figure 5.6 c) compares the real (blue) and imaginary (red) components of Δr for the homogeneous approximation (dashed lines), the thin-film approximation for different effective thicknesses (dashed dotted lines) and the transfer-matrix calculation (solid lines, TMC) for different decay lengths of an exponentially decaying Drude contribution (as indicated in b). As can be seen, only for very small decay length, the thin-film approximation and the TMC agree. For increasing L, the transfer-matrix calculation converges towards the homogeneous solution but generally yields smaller real and larger imaginary contributions in comparison.

Over longer timescales (>1 ps), the excited electron distribution can not be considered static but changes in the spatial profile are caused by diffusion. In 1D the diffusion equation is given by[268, 264]:

$$\frac{\partial n(z,t)}{\partial t} = D\frac{\partial^2 n(z,t)}{\partial z^2} - \frac{n(z,t)}{\tau_{\mathrm{rec}}}, \tag{5.13}$$

where D is the diffusion coefficient and τ_{rec} is the recombination rate. The carrier diffusion coefficient is given by the Einstein relation:

$$D = \frac{\mu}{e} k_{\mathrm{B}} T \tag{5.14}$$

where μ is the carrier mobility given by $\mu = e\tau/m_{\mathrm{eff}}$[269], which establishes a direct relation to the Drude-expression in Eq. 5.5. The carrier mobility determines the electrical conductivity which explains the widespread use of the Drude-model in THz-TDS approaches for the characterization of material properties[270]. We adopt here a simplified picture where electron and hole diffusion is treated as interdependent with an effective, so-called ambipolar diffusion coefficient[264]. For a more precise description, electrons in the different conduction band valleys and holes would have to be treated separately and any resulting electric fields, that can e.g. lead to THz emission via the photo-Dember effect[271, 239, 272], need to be taken into account[273]. Despite the highly interesting aspects that would be added in the context of our pump-probe experiments, any dependence of the mobility on the excited charge density[268] or on the above-bandminimum energy for hot electrons[274] is neglected.

At the air-bulk interface, so-called surface recombination occurs that is caused by surface states which can help the recombination of excited carriers[260, 261]. In diffusion simulations this leads to a special boundary condition, given by:

$$\frac{\mathrm{d}n(0,t)}{\mathrm{d}t} = \frac{\mathrm{d}J(0,t)}{\mathrm{d}z} + \frac{\mathrm{d}J_{\mathrm{s}}(0,t)}{\mathrm{d}z}, \tag{5.15}$$

where $J = \mathrm{d}n/\mathrm{d}z$ and $J_{\mathrm{s}} = -v_{\mathrm{s}} \cdot n(0,t)$ with the surface recombination velocity v_{s}. An analytic solution of the diffusion problem for a purely exponential initial distribution is available[268, 264], but suffers from convergence problems for small and large diffusion times. Therefore, we solve Eq. 5.13 by employing a Crank-Nicholson propagator, and use the analytic solution for benchmarking.

5.3 Experimental results

We are finally in a position where we can consider the experimental results. We will first look at the effect of surface recombination on the reflectivity on GaAs on the 10 ps timescale. Then, we investigate the buildup of collective excitations in GaAs on the 10 fs timescale and subsequently intervalley scattering in Ge on the 1 ps timescale. Finally, we discuss the excitation density dependence of the Drude scattering rate.

5.3.1 Surface recombination dynamics in GaAs

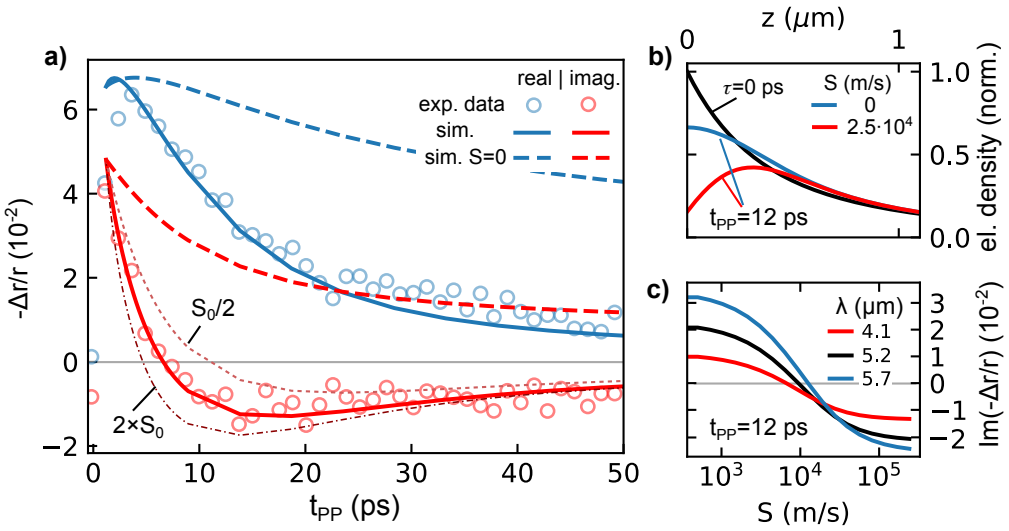

Figure 5.7: The effect of surface recombination in GaAs: a) Measured real (blue dots) and imaginary (red dots) relative reflectivity change at 5.2 μm. For comparison, simulation results including diffusion with surface recombination (solid line) and without (dashed line) are shown. Simulation for a initial surface excited electron density of $6.3 \cdot 10^{18}\mathrm{cm}^{-3}$, Drude scattering rate of $9 \cdot 10^{13}$Hz, bulk carrier recombination rate of 30 ns and a surface recombination velocity of S_0=2.5·10^{4}m/s. For comparison simulations with $2 \cdot S_0$ and $S_0/2$ are also shown. b) Simulated initial (black line) and diffused excited carrier density with (red line) and without (blue line) surface recombination at a pump-probe delay of 12 ps. c) Simulated surface recombination velocity dependence of the imaginary reflectivity change at a pump-probe delay of 12 ps for different wavelengths.

Diffusion and recombination influence the dynamics of excited carriers on intermediate (few ps) to longer timescales and leave clear signatures in our measurements. Figure 5.7 a) shows the evolution of the real (blue open dots) and imaginary parts (red open dots) of the negative transient reflectivity change $-\Delta r/r$ measured from GaAs at a wavelength of 5.2 μm. The real part shows a slightly delayed maximum and decays with a time constant of roughly 20 ps towards zero. In contrast, the imaginary part decays much quicker and $\Delta r/r$ even reaches positive values around 10 ps, which might mistakenly be interpreted

as a sign of optical gain (Note that positive means below the gray line). This behavior is qualitatively uniform in the measured wavelength range from 3 μm to 6 μm. We have consistently observed this behavior in intrinsic and as well as p-doped GaAs samples.

In order to clarify to reason for the observation, we performed simulations where we solve the diffusion equation (see Eq. 5.13) for the excited carrier density. The initial distribution within the bulk is calculated from the experimental pump spectrum and the wavelength-resolved linear absorption coefficient of GaAs. The transient reflectivity change is calculated in the frequency domain by the transfer-matrix approach. We use an initial excited carrier density at the surface of $6.3 \cdot 10^{18}\mathrm{cm}^{-3}$, and a Drude scattering rate of $9 \cdot 10^{13}$Hz. These two values determine the initial magnitude $|\Delta r|$ and relative strength of the imaginary component, respectively. The range of possible values is very well confined by comparison with the experimental data. A bulk recombination time of 30 ns has been employed, which can, however, also be neglected for the considered timescale. An ambipolar diffusion constant of 25 cm^2/s was used which is only slightly above the value of 15-20 cm^2/s of Ref. [275], but gave the best fit to the data. As can be seen in Fig. 5.7 a), using a surface recombination velocity $S_0 = 2.5 \cdot 10^4$m/s (solid lines), which is well within the range of values expected from literature (see further discussion of surface recombination below), excellent agreement with the experimental data is observed. By comparison with simulations using a two times higher (lower) S_0, it can be seen that the surface recombination velocity in our simulations is relatively well defined by the slope of the initial decreases and the maximum value of the positive imaginary part in the experimental data. In contrast, the simulations without surface recombination (thick dashed lines in Fig. 5.7 a) show a much slower decay of $-\Delta r/r$ and do not exhibit a transient positive imaginary part. Remarkably, this observation indicates that the decay of the transient reflectivity can be understood in terms of diffusion and surface recombination alone without having to invoke bulk recombination. Similar findings have been made e.g. in Ref. [251].

In order to understand the reason for the positive imaginary transient relative reflectivity change, the carrier density profile within the bulk (surface at z=0), is shown in Fig. 5.7 b) at $t_{\mathrm{pp}} = 0$ (black line) and at $t_{\mathrm{pp}} = 12$ ps with (red line) and without (blue line) surface recombination, respectively. Interestingly, the calculated density profile with surface recombination exhibits a peak density not at the surface but at a certain distance within the bulk. This profile is responsible for the transient positive imaginary part. The effect is also expected to be more pronounced in our measurements than in THz-experiments, due to the much smaller wavelength.

The question remains, for which ranges of surface recombination velocity S, the transient positive imaginary reflectivity change can be observed. The simulated dependence of the imaginary part of $-\Delta r/r$ on S at a pump-probe delay of 12 ps is shown in Fig. 5.7 c) for different wavelengths. The other parameters are kept at the values stated above. All curves only significantly decrease above 10^3 m/s and yield a zero-crossing around 10^4 m/s. For lower wavelengths the zero-crossing is reached at smaller S. For $S > 10^5$m/s, the negative transient reflectivity change flattens again at negative values. The magnitude of $\mathcal{I}(-\Delta r/r)$ is larger for longer wavelengths. These findings are in agreement with our wavelength-resolved experimental data.

The neglect of bulk recombination can be understood by looking at the timescales of the different processes. The Auger recombination coefficients in GaAs are about $6 \cdot 10^{-31}\mathrm{cm}^6\mathrm{s}^{-1}$[276]. Auger recombination could play a role at carrier densities obtained in attosecond transient absorption spectroscopy (ATAS) experiments of about $10^{21}\mathrm{cm}^{-3}$[277], where it reaches down to the ps-timescale. However, the excited carrier densities in our experiment of about $10^{18} - 10^{19}\mathrm{cm}^{-3}$ result in ns-recombination times, two to three orders of magnitude above the timescales considered here. Similarly, trap-assisted recombination in the bulk might contribute on the ps-timescale in extremely defect-rich nanocrystalline samples used for ATAS-experiments[241], but is expected to unfold on the ns-timescale for our single-crystalline wafer with no to moderate doping defects[278].

Surface recombination affects the excited carrier lifetime and the performance of optoelectronic devices especially for III-V semiconductors such as GaAs, InGaAs, GaSb and InP since surface oxidation does not provide a passivation layer[260] and therefore, the whole surface can be considered as consisting of defects unlike e.g. silicon. Measured surface recombination velocities of untreated GaAs surfaces lie in the range of $10^4 - 10^5\mathrm{m/s}$[279], which is consistent with the value in our simulations of $2.5 \cdot 10^4\mathrm{m/s}$. Various surface passivation techniques exist, such as sulfur passivation, atomic layer deposition or plasma treatment which leads to S below $5 \cdot 10^2$[280]. At such low values of S the impact of surface recombination for our measurements would be drastically reduced, as can be seen in Fig. 5.7 c). Surface passivation of our samples, might therefore be an important step in the improvement of the measurement approach to investigate bulk dynamics. In contrast, germanium yields already lower intrinsic surface recombination velocities on the order of $S \sim 2 \cdot 10^3\mathrm{m/s}$[261].

For our measurements, we will study the 100 fs dynamics in GaAs. For the investigation of few-ps processes we focus on Ge. In the interpretation of the experiments, it has to be considered that the results might be slightly influenced by diffusion and surface recombination especially for longer pump-probe delays.

5.3.2 Buildup of collective excitations in GaAs

After photoexcitation, buildup of collective excitation such as plasmons does not occur instantaneously but a certain amount of time is required until correlations between excited carriers are established, which can be resolved in our experiments. Figure 5.8 a) shows the rise of the real part of the reflectivity on GaAs integrated over the MIR spectrum, for a slightly lower excitation than in the previous section. A Fermi function (red line) is fitted to the experimental data (open dots) and yields a 20-80 % risetime of 82 fs. A comparison of the wavelength resolved $\mathcal{R}(-dr/r)$ at pump-probe delays of 12 fs (red open dots) and 175 fs (blue open dots) is shown in Fig. 5.8 b), which are marked by arrows in in a). For the larger delay (blue open dots), the experimental response shows a characteristic increase with wavelength which can be described fairly well by a Drude-term (blue solid line, see Eq. 5.5) in the homogeneous approximation. An excited carrier density of $1.2 \cdot 10^{18}\mathrm{cm}^{-3}$ is obtained. In contrast, the lower delay (red open dots) exhibits a rather flat response.

As shown by Huber et al.[227, 228], the above observations can be interpreted in terms

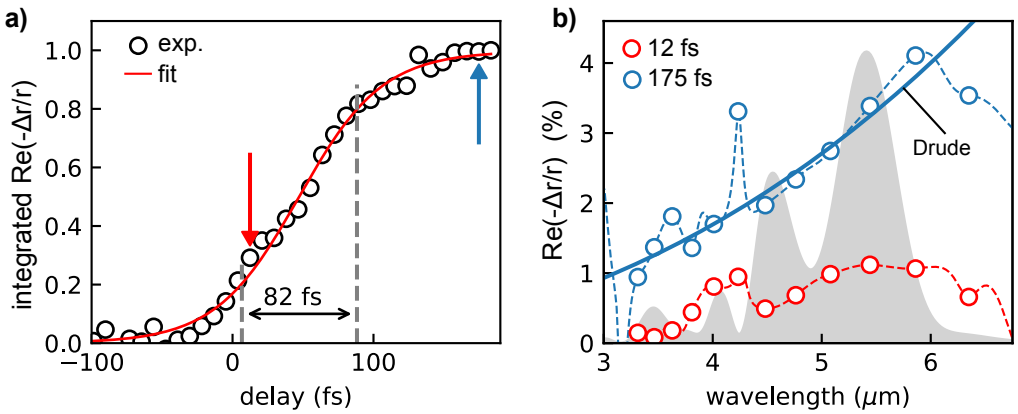

Figure 5.8: Buildup of the reflectivity from GaAs: a) Normalized real part of the experimentally measured relative reflectivity change (dots) integrated over the wavelength range 3.5-6.4 μm and Fermi-fit (red). Dashed lines indicate the determined 20-80% rise time of 82 fs. b) Wavelength resolved real part of $\Delta r/r$ for a delay of 12 fs (red dots and dashed line) and 175 fs (blue dots and dashed line). For the later delay the calculated Drude expression in the homogeneous approximation is also shown (blue solid line) which yields an excited carrier density of $1.2{\cdot}10^{18}\mathrm{cm}^{-3}$ and a plasma oscillation period of $\sim$60 fs which would yield an expected buildup time of roughly 96 fs.

of the buildup of dressed particles and the formation of Coulomb correlations in the photoexcited electron-hole plasma, which manifests itsef in the plasmon response described by the Drude model.

In order to understand how the measurements reveal information about the particle interactions, we have to briefly consider charge interactions in solids. The presentation here closely follows Ref. [227]. In a solid, the Coulomb interaction is altered by many-body effects and around each charge carrier a screening cloud of opposite charge is formed, which together is also referred to as dressed particle. The bare Coulomb interaction potential between two charges in momentum space $4\pi e^2/q^2$ (q is the momentum transfer) is altered by the dielectric function ϵ_q which results in the effective interaction potential W_q[227]:

$$W_\mathrm{q}(\omega, t_\mathrm{D}) = \frac{4\pi e^2}{\epsilon_\mathrm{q}(\omega, t_\mathrm{PP})q^2}, \tag{5.16}$$

where a dependence on the pump-probe delay t_PP has been added in order to account for the dynamical evolution of ϵ_q after pump excitation of the sample. With optical experiments $\epsilon_{\mathrm{q}=0}$ is measured. The Coulomb interaction between dressed particles becomes time dependent through the ω dependence in frequency space. The real part of the dielectric function shows how much the bare charges are screened, while the imaginary part is proportional to the energy loss of the carriers. The latter is also the basis for most calculations of inelastic electron scattering in solids[281, 282].

Huber et al.[227] performed optical-pump-terahertz-probe (OPTP) experiments also on GaAs. For similar excited carrier densities ($2 \cdot 10^{18}\mathrm{cm}^{-3}$), they found buildup times of the

plasmon on the timescale of 70-100 fs close to our observation. The finite delay for the buildup of correlations and resonances can be described by calculations using nonequilibrium Green's functions[228]. The time-delay for the buildup of the plasmon peak τ_{cor} is on the order of the plasmon oscillation period T_{pl}[228], more precisely $\tau_{\mathrm{cor}} \approx 1.6 \cdot T_{\mathrm{pl}}$. Our observations are in close agreement with this finding: The Drude response takes about 82 fs to buildup compared to the predicted 96 fs, deduced from the plasma oscillation period of 60 fs.

To be precise, for our MIR wavelength region the pump-probe response is not completely described by the intraband picture underlying the Drude model. Ganikhanov et al.[251] found in pump-probe experiments that intersubband transitions from electrons in the split-off band into hole states in the light and heavy hole band occur around 3.8 μm and 3.1 μm, respectively. These transitions are also the basis of split-off band MIR detectors[283]. However, the results of Ref. [251] also suggest that in reflection the response is dominated by free-carriers and that intersubband transitions should not play a role beyond 4 μm. In our data, while oscillations in the reflectivity between 3-4 μm could provide a hint of these transitions, they could not clearly be resolved. Upcoming experiments with an improved SNR, higher spectral resolution and removal of the CO_2 absorption peak could potentially be sensitive enough to identify their influence on the transient reflectivity.

Attosecond transient XUV absorption measurements pumped by few-cycle NIR pulses have been performed on GaAs by Schlapefer et al.[277] at excited carrier densities of $1^{20} - 10^{21}\mathrm{cm}^{-3}$. They found that in this regime interband transitions as well as intraband motion lead to carrier excitation which results in a non-linear increase of carrier density with intensity. The transient decrease of the transmission of highly pumped solids has been applied in Ref. [284] as a gating method for laser pulse reconstruction over a broad wavelength range. It would be interesting to investigate how the risetime of the plasmon response evolves with carrier densities up to $10^{21}\mathrm{cm}^{-3}$, since there, the plasma frequency would lie on the few fs scale which corresponds to the expected temporal resolution of our measurement setup. The required intensities might be reachable after a change of the setup and tighter focusing.

5.3.3 Intervalley scattering in Ge

We observed a striking difference of the transient reflectivity $\Delta R/R$ between Ge and GaAs on the few ps timescale, which can be explained by the intraconduction band dynamics of excited electrons in Ge, especially intervalley scattering, as discussed below. The comparison between Ge and GaAs is shown in Fig. 5.9 a). The signal on GaAs (blue open dots) rises rapidly within 100 fs and subsequently decays with a time constant of around 20 ps. In contrast, on Ge (red open dots) the reflectivity reaches its maximum only after about 3 ps. On the other hand, for longer delays on the 50 ps timescale, the dynamics is overall similar, as can be seen in the inset. We have consistently observed this behavior on Ge in our measurements over several weeks of measurements. An explanation for the evolution of the transient reflectivity in GaAs and Ge on the short timescale can be obtained based on Fig. 5.4 and the related discussion in Sec. 5.2.

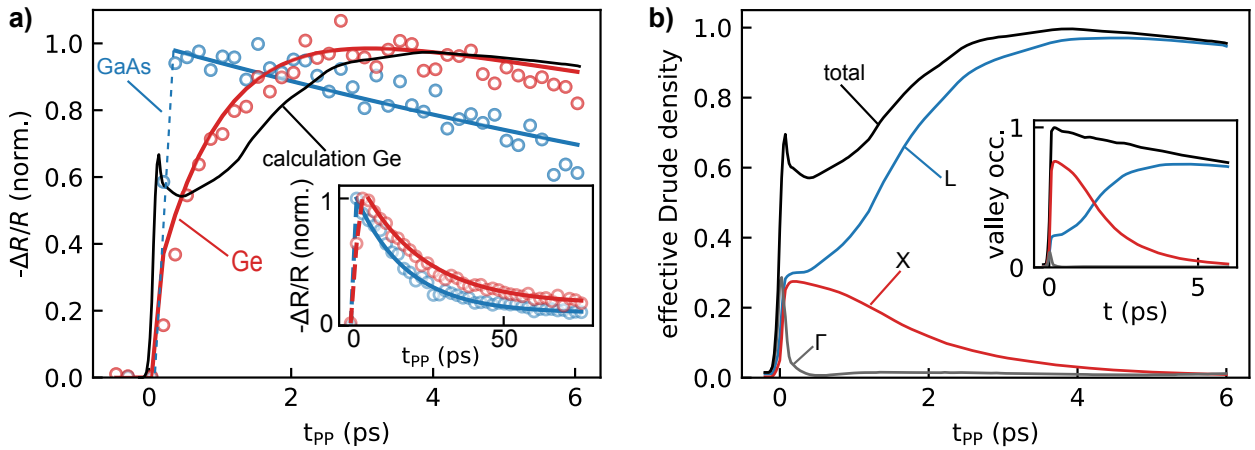

Figure 5.9: Intervalley scattering in Ge: a) Comparison of the experimentally measured rise in reflectivity between Ge (red dots) and GaAs (blue dots). The lines are a guide to the eye, the curves are normalized. The black line shows the calculated Drude reflectivity change for Ge based on the evolution of the conduction band valley occupations simulated in Ref. [237] for an excitation with $\hbar\omega = 1.5\,\mathrm{eV}$ and the effective masses from Ref. [244]. The inset shows the long term evolution with a double-exponential fit (solid lines). b) Contribution of the individual conduction band valleys to the effective Drude density, defined as the carrier density divided by the relative transverse effective mass. The inset shows the valley occupations extracted from Ref. [237] assuming a recombination time constant of 20 ps.

For GaAs the interband excitation by the NIR pump beam occurs from the top of the valence band into the bottom of the conduction band around the Γ-point, as shown in Fig. 5.4 a). Since the other bandgap minima at the L- and X-valleys lie significantly higher in energy, most of the electron population is expected to stay centred around the Γ-point. Moreover, the holes are expected to quickly relax into the heavy-hole band.

In contrast for Ge, as can be seen in Fig. 5.4 b), the electron excitation occurs away from the Γ-point, higher up into the valence band from which the X- and L-valleys are accessible via horizontal transitions mainly through electron-phonon scattering. The inset of Fig. 5.9 b) shows the time evolution of the electron population in the different valleys after pump excitation extracted from Ref. [237] based on Monte-Carlo simulations which model the electron-phonon interaction via deformation potentials. In their simulations, the excited carrier density is around $1 \cdot 10^{18}\mathrm{cm}^{-3}$ and the photon energy is 1.5 eV. As can be seen, the initial population around the Γ-point (gray line) is quickly scattered within 100 fs into the X-valleys (red line) and L-valleys (blue line) due to the much higher available density of states. At first, most of the excited electrons end up in the X-valley since there the density is highest. However, within 4-5 ps almost the whole electron population will relax to the L-valley as it constitutes the conduction band minimum. For better agreement with the experimental data, we added an exponential decay of the effective excited carrier density with $\tau = 20\,\mathrm{ps}$ which represents mostly diffusion and surface recombination, as discussed in Sec. 5.3.1 above.

A qualitative approximation for the evolution of the transient reflectivity is obtained by combining the extracted time-dependent conduction band valley populations with the transverse effective masses shown in Tab. 5.2. We use the sum of three Drude terms (Eq. 5.5) to represent the contribution of the Γ-, X- and L-valleys. For each valley, an effective Drude density is defined as the ratio of valley population density and transverse effective mass, which is shown in Fig. 5.9 b). Since $m_{\mathrm{X,t}}/m_{\mathrm{L,t}} \approx 3.6$, the total effective density (black line) rises with the population transfer from X- to L-valley. As can be seen in Fig. 5.9 a) with this model (black line) the slow increase of the transient reflectivity in Ge can be reproduced. Here, we use an excited carrier density of $\sim 5 \cdot 10^{18}\mathrm{cm}^{-3}$ and a Drude scattering time of 10 fs, but the exact values are not important for the qualitative shape.

Several aspects of the above model need to be discussed. First of all, we neglect the hole contribution, which can be justified by the simulation results of Ref. [237], which show that the hole contribution gets localized in the heavy-hole band within a fraction of a picosecond and therefore doesn't contribute to the few-picosecond time-dependence. Secondly, the initial peak of the simulated reflectivity around $t_{\mathrm{pp}} = 0$ which can be attributed to the Γ-valley contribution is absent in the experimental data. This can again be explained by looking at Fig. 5.4 b) considering that the initial excitation occurs into a non-parabolic region of the conduction band. There, the effective mass is expected to be considerably larger than at the Γ-point which suppresses this contribution to the effective Drude density. An increased effective mass has also been predicted for strong-field excitation of semiconductors[252, 262, 263] which has been attributed to the same effect[252]. Finally, the use of only the transverse masses is a severe approximation. In principle, for

each separate degenerate valley the effective mass would need to be calculated from the polarization vector of the MIR and the present assumption overestimates the effective Drude density. However, tor the given surface orientation (111) and normal incidence of the MIR probe beam, as can be seen in Fig. 5.4 c), two sub-L-valleys are always driven transversely irrespective of the polarization orientation. A slight dependence on whether an X-valley is driven transversely could exist and might be interesting to investigate further.

Intervalley scattering is a fundamental process for the relaxation excited carriers in the conduction band and was invoked for the explanation of optical-pump optical-probe experiments of Ge already more than three decades ago[234, 235, 236]. The timescale of the X-L-intervalley scattering of around 2-3 ps is consistent with attosecond transient reflection measurements on Ge where a time constant of 3.2±0.2 ps was deduced[285]. In the OPTP experiments of Ref. [269] the same evolution of the transient reflectivity seems to have been observed where it was, however, not interpreted (there also the excited carrier density seems to be overestimated through the use of the heavy-hole mass as effective mass). Theoretically, a similar conduction band valley population transfer has been simulated by the use of deformation potentials[237, 238, 239]. Since there are countless theoretical and experimental pump-probe investigations on semiconductors, especially on Ge, it is almost certain that many more studies, that are not cited here, have observed very similar phenomena. Overall, the main reason for the observed delayed buildup of the reflectivity is that the electrons are excited way above the conduction band minimum towards which they relax via intervalley scattering which leads to a change of the effective mass. It can therefore be generalized to other semiconductors. For example, in GaAs related dynamics have been measured when exciting the sample with a photon energy well above the bandgap (e.g. 3.1 eV)[286]. Nevertheless, our measurements present a particularly clear demonstration of the power of the concept of effective masses in solids.

5.3.4 Excitation-density dependence of the Drude scattering rate

Our setup can not only measure changes in the reflected intensity, but provides more information in terms of the complex valued reflectivity change for the electric field, as discussed above. Figure 5.10 a) shows the few picosecond evolution of $\Delta r/r$ on Ge. While the real part (blue open dots) keeps rising after the sharp initial increase around $t_{\mathrm{pp}} = 0$, the imaginary part (red open dots) quickly flattens and even starts to decrease.

As a side note, slight oscillations seem to be observable especially on the imaginary part with a period of approximately 375 fs. The sudden excitation of electron into the conduction bands affects the interatomic binding forces and therefore can lead to the generation of coherent phonons in Ge which is detectable as oscillations in the reflectivity[287, 288] [289] under similar excitation densities. However, a significantly faster oscillation period of ∼100 fs would be expected. Potentially, future, more sensitive experiments could be able to detect such oscillations.

We therefore focus on the difference in the increase of real and imaginary parts in Fig. 5.10 a) which gives information on the scattering rate. For feasibility, the homogeneous approximation is applied, but the eventual shortcomings discussed in Sec. 5.2 have to be

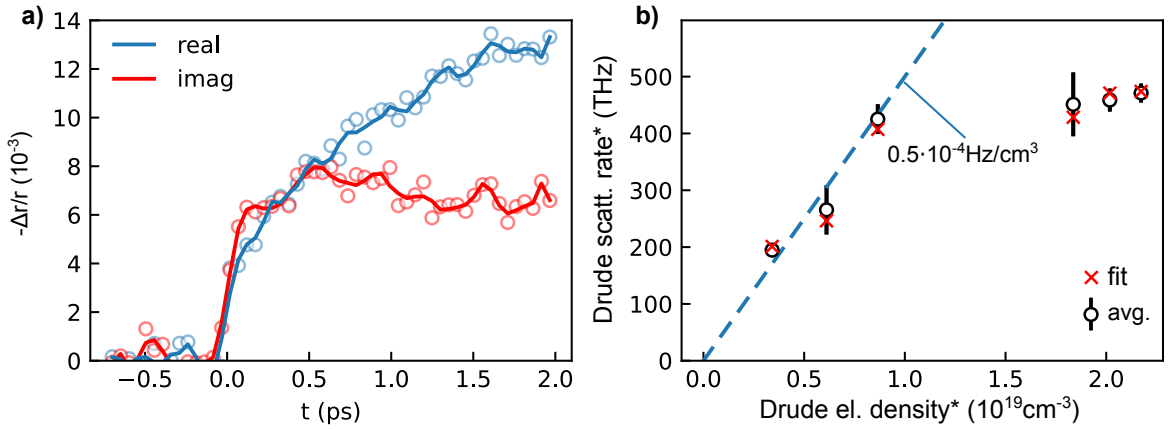

Figure 5.10: Drude scattering rates in Ge: a) exemplary evolution of the real (blue) and imaginary parts (red) of the reflectivity change in Ge at 5 μm. b) Dependence of the Drude scattering rates on the Drude density for Ge both evaluated using the approximation for an homogeneously excited sample (marked by *) at a pump-probe delay of 1.5 ps. The average and standard deviation calculated in the wavelength range from 4.5-5.5 μm are shown (black open dots and errorbars) together with the results of a Drude fit (red crosses). Each datapoint represents a separate measurement. The data was taken on different occasions. The blue dashed line indicates a linear dependence for lower densities.

kept in mind. In the homogeneous approximation and within the Drude model, it can be shown that for small relative changes of the refractive index in first order Taylor expansion the following relation holds:

$$\frac{\mathcal{I}(\Delta r/r)}{\mathcal{R}(\Delta r/r)} \approx \frac{\Gamma}{\omega}, \tag{5.17}$$

if the unperturbed refractive index is real in the frequency range of interest. $\mathcal{R}$ and $\mathcal{I}$ denote the real and imaginary parts and Γ is the Drude scattering rate. The evolution of the real and imaginary part of $\Delta r/r$ after the sharp initial increase around $t_{\mathrm{pp}} = 0$, seems to suggest that while the effective density increases through intervalley scattering, the Drude scattering rate decreases. The measurement therefore shows that the Drude scattering rate under strong excitation is time-dependent, which is mostly caused by the dependence on the excited carrier density[266] but also the temperature[290].

Here, we investigate the dependence of the extracted Drude scattering time on the excited carrier density, as illustrated in Fig. 5.10 b). The mean (open dots) and standard deviation (errorbar) of the Drude-scattering time in the homogeneous approximation from Ge is shown, evaluated at $t_{\mathrm{pp}} = 1.5$ ps, when most of the density is in the L-valley and in the wavelength range from 4.5 μm to 5.5 μm. Moreover, the results of a Drude fit in the same wavelength region is shown (red cross). Excellent agreement between both approaches is observed. Note that the effective Drude density might be underestimated by up to a factor of 4 by the use of the transverse effective mass, as discussed above. The low densities

between $0.5 - 1 \cdot 10^{19}\mathrm{cm}^{-3}$ suggest an initial linear increase of the Drude scattering rate, as indicated by the blue dashed line. On the other hand, the highest datapoints seem to indicate saturation at a scattering rate slightly below 500 THz (2 fs). More systematic intensity scans, that could be performed at a single pump-probe delay, would be highly desirable.

The topic of Drude scattering times in strongly pumped semiconductors and especially the transient excited carrier density dependence is highly debated (Ref. [266] and references therein). Most of the work concerns silicon but the qualitative behavior is expected to be similar to germanium such that we can relate it to our experiments. According to Ref. [266], for low densities, carrier-phonon scattering is the major contribution which leads to a quasi-constant Drude scattering time on the order of 200 fs. The carrier-carrier scattering rate which linearly increases with carrier density starts to dominate above $\sim 5 \cdot 10^{17}\mathrm{cm}^{-3}$ up to around $5 \cdot 10^{19}\mathrm{cm}^{-3}$ where it reaches a maximum (20 fs) due to the reduction of available final states for electron-electron and hole-hole scattering. The qualitative dependence is consistent with our experimental data but we extract even lower carrier scattering times. Upon a further increase of the density, the rate is expected to decrease again as the number of available final states reduces further, but it is not clear whether all relevant effects in this regime where considered in Ref. [266]. The linear increase of the scattering rate with carrier density in the intermediate regime seems to be well accepted and has been confirmed for example by another experimental study that additionally included the temperature dependence[290]. However, the question of how low the Drude scattering time can reach is debated, since several other measurements have also reported values on the 1 fs scale[291, 253] or a much faster increase of the scattering rate with excited carrier density[292].

Within the framework of TDDFT simulations of pump-probe experiments in silicon[252, 262], Drude fits to the calculations yielded scattering times on the 1 fs timescale even though no explicit collision effects were taken into account in the model. There, it was argued that interband transitions, excited electrons or holes which undergo intersubband transitions driven by the probe pulse, are responsible for the finding[262]. The role of interband transitions on the apparent Drude response was further investigated and confirmed in Ref. [263]. In this case, the classical interpretation of the Drude model where a particle is considered that travels through the crystal and randomly scatters, becomes questionable and extensions for explicit inclusion of interband transitions would be desirable. Regarding electron-phonon scattering times, first principle calculations have shown that hot electrons in GaAs, i.e. electrons significantly above the conduction band minimum, exhibit carrier-phonon scattering times also down to the 1 fs timescale[293]. These studies show that additional effects not considered in Ref. [266] could contribute to the effective Drude scattering times.

For our experimental results, as shown in Fig. 5.6, with the employed approximation of an homogeneously excited sample, the imaginary part of Δr is overestimated compared to the real part, which results in a too high value for the extracted scattering rate. This can likely only be accounted for with macroscopic simulations. Moreover, the role of interband transitions, which are especially expected for the hole bands would need to be identified, as

discussed above. Finally, as pointed out by Ref [266], a reliable extraction of the scattering rate in pump-probe experiments based on intensity measurements, ideally includes the plasmon peak in the detected wavelength range, since the scattering time determines its width. Even though this requirement might be relaxed for our field resolved measurements, extending the wavelength range by changing the nonlinear crystals in our setup would be desirable for further investigation of scattering times in highly excited semiconductors.

5.4 Conclusion and Outlook

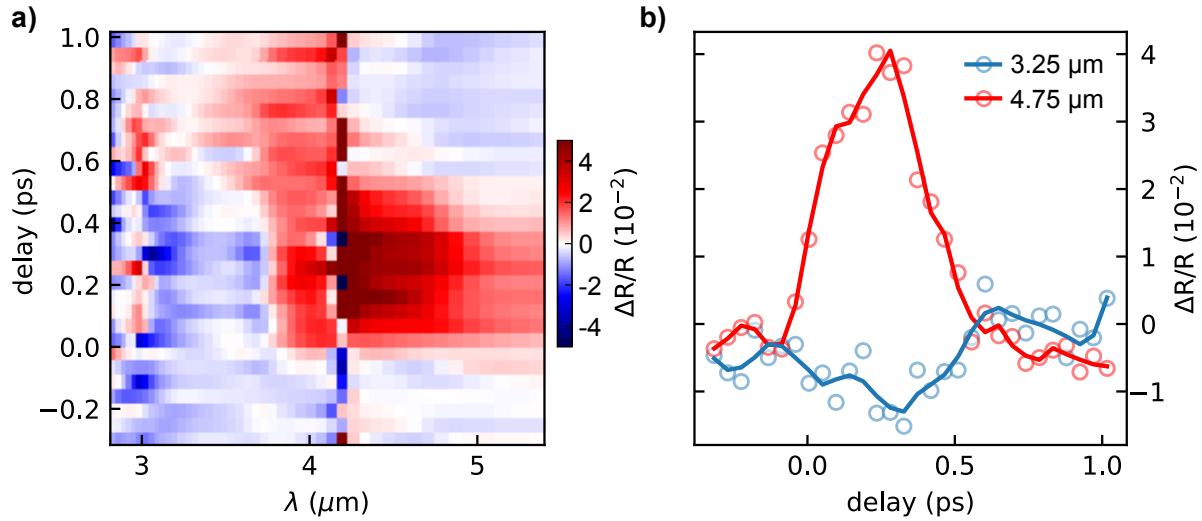

Figure 5.11: Transient reflectivity change from a graphene sample: a) Wavelength resolved transient reflectivity change. b) Evolution of the reflectivity change at 3.25 μm (blue dots) and 4.75 μm (red dots). The solids line are smoothed using a Savitzky-Golay filter and intended as a guide to the eye.

In conclusion, this chapter describes a newly developed field-resolved NIR-pump MIR-probe setup based on electro-optic sampling. To our knowledge, with a probe spectrum from 3-6 μm, the presented experimental results constitute the shortest-wavelength field-resolved pump-probe reflectometry measurements using EOS ever reported.

Theoretically, the foundations for the understanding of pump-probe experiments on semiconductors are discussed. Emphasis is laid on the description of effective masses and intervalley processes as well as macroscopic aspects.

Experimentally, we show that the decay of the transient reflectivity on the 10-100 ps timescale is dominated by diffusion and surface recombination. Furthermore, measurements on the rise of the reflectivity from GaAs reveal the buildup times of collective plasmon excitations on the 100 fs timescale in agreement with earlier studies[227]. From Ge a few picosecond increase of the transient reflectivity is observed, which can be explained by the intervalley scattering and the different transverse effective masses. The

same measurements also indicate an increased effective mass within more than few 100 fs after photoexcitation due to excitation into a non-parabolic region of the bandstructure. Finally, the dependence of the scattering rate on the excited carrier density is discussed.

The measurements shown here, were mostly intended as a demonstration of the capabilities of the setup and variety of effects to be studied, but are, nevertheless, of significance for the field of semiconductor optoelectronics. Considerably improved data is expected after the currently performed updates of the setup, purging of the experiment in order to suppress the CO_2-absorption peak and most notably the implementation of an active laser intensity stabilization. Furthermore, an increase of the pump power will enable studies of extremely highly excited semiconductors as well as nonlinear excitations. Moreover, expansion of the wavelength region might enable many more interesting studies. With these improvements, several important aspects might be clarified such as the identification of intersubband transitions of photoexcited carriers discussed above, or the excitation dependence of the Drude scattering rate.

Apart from semiconductors, a significantly higher diversity of systems can be studied with our setup such as 2D-structures. Figure 5.11 a) shows the wavelength resolved transient reflectivity from a graphene sample on a silicon nitride substrate provided by the Atwater group (Caltech). As can be seen, the dynamics unfolds on a much faster timescale (500 fs) compared to semiconductors. Moreover, the dynamics is not qualitatively uniform for different wavelengths (see Fig. 5.11 b). Graphene is especially interesting, because it allows to tune the Fermi-level and thereby the effective bandgap for interband transitions in the few 100 meV region, which is reachable with our wavelengths, by an external bias voltage[294]. Our setup was partly build to investigate electron-plasmon coupling which could allow gain in the MIR (also Ref. [294]). Moreover the wavelength region covers the range of almost all stretching vibrations in functional groups in molecules (2500 nm-6500 nm)[295]. In combination with the pump-probe scheme, a vast variety of photochemical reactions can be investigated. Overall, we believe that the developed setup will enable many interesting applications from femtosecond- to picosecond timescales.

Chapter 6

Phase matching of HHG with ionization reshaped few-cycle pulses

6.1 Introduction

High-harmonic generation (HHG) is a nonlinear process during which an intense laser pulse is focused into a medium to non-perturbatively generate high harmonic orders of the fundamental photon energy[10, 11, 296] (see Chap. 2). The emitted high-harmonic radiation exhibits two key properties. Firstly, it possesses longitudinal and transverse coherence through the coherent generation process. Secondly, HHG is intrinsically synchronized to the driving laser field on a sub-cycle timescale and has therefore become one of the founding pillars of attosecond science[150, 9, 8, 297, 122, 298].

High-harmonic radiation is generally emitted in sub-cycle bursts, forming an attosecond pulse train (APT). The generation of isolated attosecond pulses (IAPs) by extracting a single sub-cycle burst has been made possible through advances in laser technology and waveform control of the driving laser[299, 7], extending the resolution of pump-probe spectroscopy to the electronic timescale (1 as=10^{-18}s)[12, 300, 301, 13] (see Sec. 2.3.3).

Isolated attosecond pulses based on HHG have allowed a vast number of experiments, such as the studies on the fundamental timing of the photoemission process in atoms[14, 302, 155], molecules[84], liquids and solids[15, 303]. Moreover, the bound-state dynamics on its fastest timescale has been measured by attosecond transient absorption[304, 177, 305, 306, 307, 308, 277, 309, 310, 311] and very recently attosecond transient reflection[176, 312]. In the context of this thesis, the attosecond streaking measurements on isolated nanospheres[313, 314] as well as the reconstruction of the near fields around a nanotip on attosecond temporal and nanometer spatial scales [25] deserve a special mention. The latter experiment has been performed within the framework of this thesis and published in Refs. [26, 27], and several aspects of it are discussed in Chap. 7. For completeness, while also APTs have extensively been used in attosecond photoemission experiments[150, 315, 316, 317, 318, 319, 320], for general applications the temporal resolution is given by the few fs duration of the APT[321, 322, 323]. We will therefore focus here on the generation

of IAPs.

In recent years, another source of ultrashort (soft) x-ray pulses has emerged in the form of x-ray free-electron lasers (XFELs). XFELs are especially appealing due to the enormous photon flux compared to HHG-based sources[324]. However, while progress is being made to produce sub-fs pulses[325] and to overcome pulse fluctuations problems[326], the timing jitter between the XUV pulse and external laser sources is on the order of few fs[327] and, generally, single shot-techniques are necessary[328, 326, 325]. Most imortantly, XFELs can only be realized in dedicated large-scale facilities[329]. HHG will therefore remain an important tool for attosecond science even in the long-term future.

So far, most HHG-based attosecond experiments have been performed at photon energies of around 100 eV and below. Especially promising are, however, pump-probe experiments in the so-called water window between the K-shell absorption edges of carbon and oxygen (284 eV-543 eV)[330, 132]. In this photon energy range water is transparent for soft x-ray pulses, which would allow the investigation of biological molecules in their natural environment and therefore the fundamental processes of life with unprecedented temporal resolution.

In recent years, an increasing number of research groups has shown HHG potentially supporting IAPs in the water window[331, 132, 332, 322, 28, 333], and lately IAP generation has been demonstrated by attosecond streaking[334]. However, the problem is that HHG at higher photon energies becomes inefficient for two reasons (see Chap. 2). First, since ionization limits the maximum intensity for which phase matching of the HHG process is possible, longer driving wavelengths are required. This, however, dramatically reduces the rescattering probability due to the longer excursion of the electron before recollision. Secondly, the phase-matching process itself becomes increasingly difficult over longer distances with increasing harmonic order[28]. This opens the quest to explore new regimes of HHG phase matching[324, 335]. A recent study has demonstrated that these limitations might partly be overcome in the so-called overdriven regime, where ionization-induced plasma leads to severe pulse reshaping of the driving laser pulse[28] strongly influencing the HHG buildup. A demonstration of IAP generation as well as a detailed analysis of the phase-matching conditions was, however, missing.

In this chapter, we present experiments demonstrating the generation of IAPs at 80 eV through HHG in argon and neon by attosecond streaking driven by 750 nm laser pulses. With the help of experimental signatures and numerical calculations, it is shown that the IAP generation process in argon takes place in the overdriven regime. An extended phase-matching expression for the HHG dipole contribution is derived that takes into account the blue-shift of the driving laser. With this expression the description of HHG phase matching even under extreme pulse reshaping conditions is possible. We show through simulations that the mechanism is important for the phase matching of long-wavelength, tightly-focused laser beams in high-pressure gas targets, which are currently being employed for scaling isolated attosecond pulse generation to water window photon energies.

The structure of this chapter is as follows: First, the fundamentals of HHG and phase matching are reviewed. Then, the experimental setup and the experimental results are described. Thirdly, through simulations and comparison with experiment the HHG regime

for argon is identified. The fourth section describes the extended phase-matching expression and applies it to the simulations. Then, the simulations for longer wavelength drivers are discussed and the importance of the blue-shift contribution to the HHG dipole is demonstrated. Finally, a short outlook and conclusion is given. The results of this chapter have been published in Ref. [29] and the presentation here closely follows the one given therein.

6.2 Experimental section

6.2.1 Experimental setup

The setup for attosecond streaking spectroscopy at the Attosecond Science Laboratory of the King Saud University is shown Fig. 6.1. A description of this setup has been given in Ref. [27], which we will closely follow in this section and to which we refer for further details. The pulses used in the experiment are delivered by a commercial laser system consisting of an oscillator (Spectra-Physics^{TM} ; rainbow^{TM} DFG seed) pumped by a solid-state diode laser (Coherent Inc.; Verdi V6 UNO) as depicted in Fig. 6.1 a). The carrier-envelope offset frequency is measured and controlled in a CEP module (Menlo Systems GmbH, XPS 800 Femtosecond Phase Stabilization) via a feedback to the pump power. The oscillator delivers 4 nJ pulses at a repetition rate of 75 MHz in the spectral range between 675 nm and 930 nm. The pulses are further amplified by a ten-pass chirped-pulse amplifier (Spectra-Physics^{TM} ; FEMTOPOWER^{TM} compact PRO HP/HR 3 kHz) which is pumped by a pulsed solid-state diode laser (Photonics Industries International Inc.; DM 30 Q-Switched DPSS Laser). After the fourth pass, a Pockels cell selects pulses at a repetition rate of 3 kHz and an acousto-optic programmable dispersive filter (AOPDF; DAZZLER by FASTLITE) allows shaping of the pulse spectrum and phase. After the amplification, the pulses are compressed via a grating compressor to approximately 25 fs with an energy of 800 μJ. A small portion of the pulses is sent into a carrier-envelope phase (CEP) module (APS800 by Menlo Systems), which stabilizes long-term drifts via feedback-controlled insertion of one of the prisms in the stretcher. The pulses are spectrally broadened in a hollow-core fiber filled with neon at about 2 bar to a width of 300 nm centered at 750 nm, supporting sub-two-cycle pulses. The pulses are compressed by a set of chirped mirrors (Ultrafast Innovations PC70). A pair of fused silica wedges is used for dispersion fine tuning. Finally, phase-stable few-cycle pulses with 450 μJ at 3 kHz repetition rate are delivered to the experiment.

The vacuum beamline is shown in Fig. 6.1 b). The laser is focused with a concave mirror (f=75 cm) into the HHG chamber. An iris is used to regulate the pulse power that reaches the experiment. The gas target consists of a hollow metal tube with laser-drilled entrance and exit holes and has a length of roughly 1.5 mm. It is kept at a constant gas pressure of few 100 mbar of either neon or argon by controlling the gas flow. XUV and fundamental beam are spatially separated by using a concentric Zr-foil filter and the focusing double mirror. The Zr-foil blocks the fundamental spectrum in the beam center that hits the inner mirror. The inner part of the double mirror (custom-made, Ultrafast

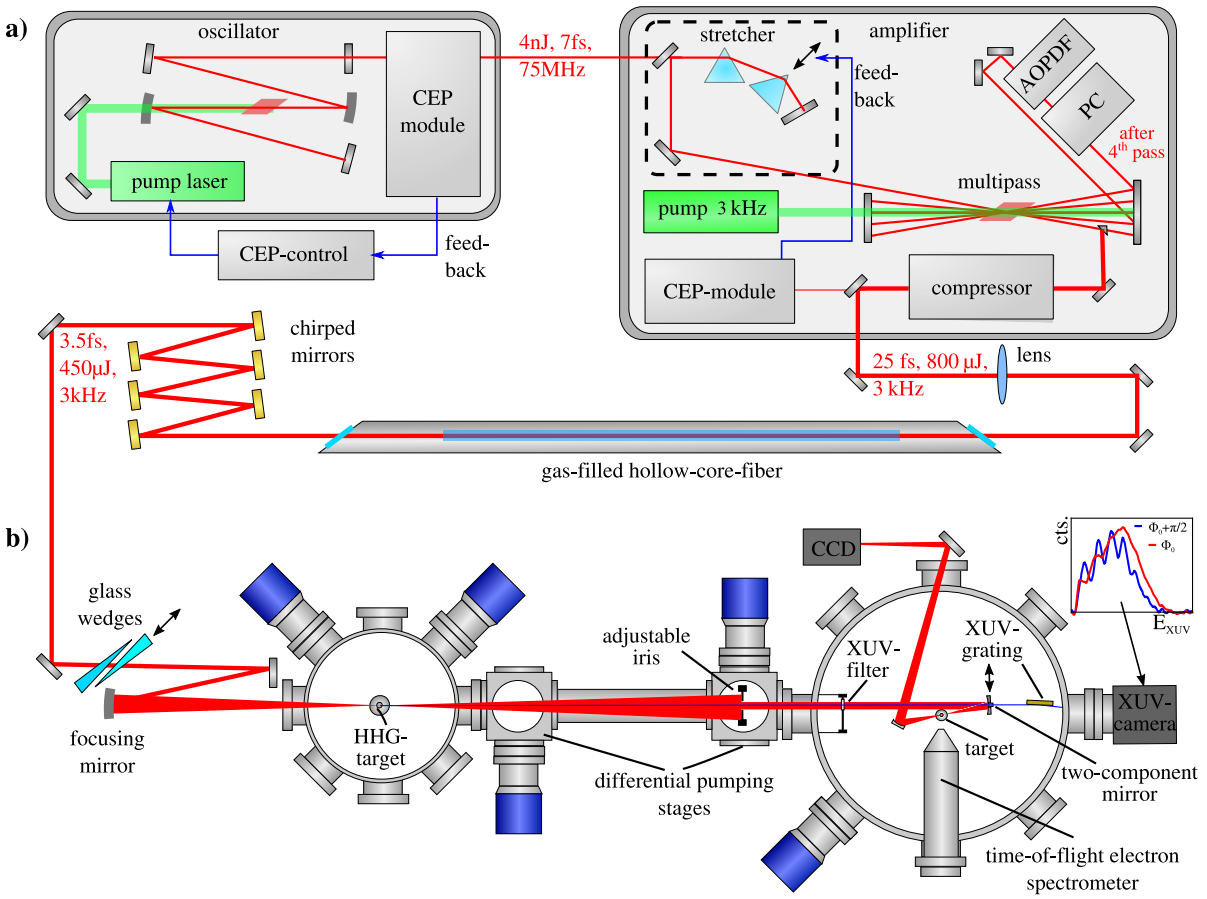

Figure 6.1: Overview of the experimental setup: a) the laser system consists of the CEP-stabilized oscillator that seeds the chirped-pulse amplifier which contains another slow-loop CEP-stabilization system. The amplified pulses are spectrally broadened in a noble-gas-filled hollow-core-fiber and subsequently compressed to below 4 fs using chirped mirrors. b) Fused silica glass wedges are used for fine-tuning of the dispersion. The laser beam is focused into the HHG chamber of the attosecond vacuum beamline for XUV generation in the HHG target. An iris is used to adjust the IR power in the experimental chamber. The XUV-filter and the two-component multilayer XUV-mirror spectrally select the isolated attosecond pulse. The synchronized XUV and IR pulses are focused into the streaking gas-target (neon) and photoelectron momenta are detected using a time-of-flight spectrometer. The double-mirror can be removed from the beampath to allow spectral characterization of the XUV pulses (adapted from Refs. [27, 29]).

Innovations) has a special multilayer coating to reflect XUV with a bandwidth of 6.4 eV and a flat spectral phase around a central energy of 80 eV. The outer mirror substrate (fused silica) is coated with 10 nm of B_4C in order to achieve a reflectivity of about 10 % for the driving laser pulse. The position of the outer and inner mirror can be changed with nanometer-precision by a closed-loop piezo stage (PI Hera 620). The double-mirror focuses both beams into a neon gas jet produced by the streaking target, and a time-of-flight-spectrometer (STEFAN KAESDORF ETF10) is used to record the kinetic energy of the generated photoelectrons. Moreover, the double mirror can be removed such that the beam falls onto an XUV spectrometer for optimizing HHG flux and coarse alignment.

6.2.2 Experimental approach

The gas flow through the HHG gas target is controlled via an automatic valve at the gas tube feedthrough in order to guarantee a stable pressure within the target over longer timescales. The feedback to the controller is the background pressure within the HHG vacuum chamber. This is a slight drawback since this does not permit to exactly determine the backing pressure within the actual HHG gas target. The latter is also not possible calibrate either since the dependence between HHG target backing pressure and the measured chamber pressure is nonlinear. Moreover, it depends on the entrance and exit hole sizes in the target, which slightly changes due to ablation on the timescale of a few days during an experimental campaign. For our experimental parameters, maximum flux in neon is usually achieved between 100-300 mbar. We observed similar flow rates for argon and neon and therefore assumed a similar target pressure for both gas types of about 150 mbar. These pressures also give excellent agreement with experimental observations, as discussed below. The exact pressure is not critical, since the phase-matching mechanism relying on blue-shift and intensity-decay becomes significant already at much lower pressures, as we show below in Sec. 6.4.3.

We used variable HHG target gas pressure, HHG focusing mirror position, and dispersion control via fused silica wedge insertion to optimize the IAP generation. Experimentally, we start with HHG in neon by first optimizing the gas pressure for maximum XUV flux. We then continue by fine adjusting the fused silica wedge insertion for maximum CEP-dependence in the cutoff region of the XUV spectrum. Subsequently, a streaking spectrogram in neon is recorded by inserting the double-mirror. We then switch to argon after evacuating the gas supply line. Besides gas pressure and dispersion, we also change the position of the focusing mirror and optimize again flux, stability and CEP-dependence in the XUV spectrum. Originally, as inferred from plasma generation in low-pressure air, the HHG gas target had been placed several mm behind the focus. With this procedure, for argon compared to neon, we end up with a shift of the focusing mirror by about 5.5 mm towards the target, an additional insertion of roughly 260 μm of fused silica and similar gas flow rates. Afterwards, again the streaking spectrograms are recorded.

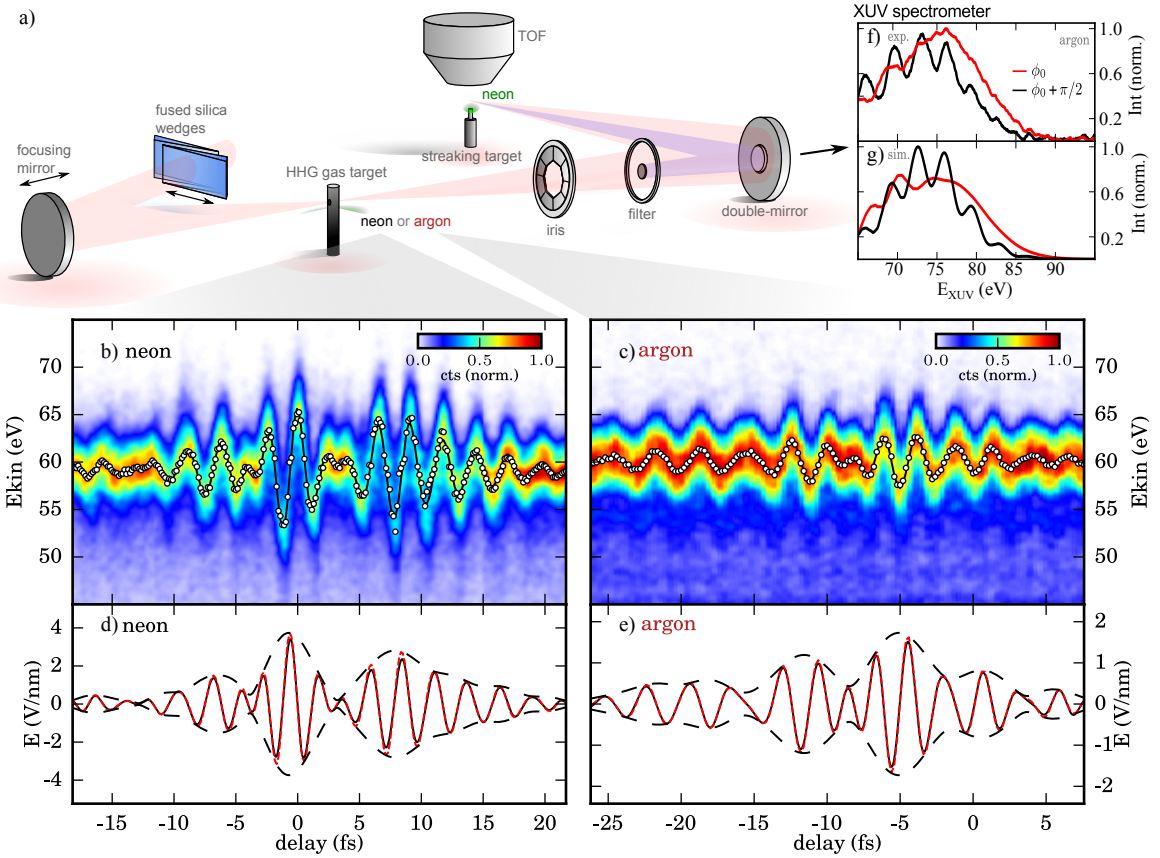

Figure 6.2: Description of the experiment: a) Principle components: The pulses are focused into the HHG gas target either filled with neon or argon. Fused silica wedges are used for fine-tuning of the dispersion in front of the movable focusing mirror. A special filter spatially separates the IR and XUV pulses. The double mirror introduces the XUV-IR delay by displacing the inner multilayer XUV-mirror and focuses the pulses into the streaking gas target filled with neon. b) and c) attosecond streaking spectrograms recorded using the time-of-flight spectrometer in neon and argon, respectively. The streaking curve (black line) is extracted through a Gaussian fitting procedure for each delay (dots) and subsequent Fourier-filtering. d) and e) retrieved driving laser in the streaking target obtained through the Gaussian peak fitting procedure (red dashed line) and the ptychographic retrieval algorithm (black line). f) and g) experimentally measured and simulated CEP-dependent HHG spectra, respectively (adapted from Ref. [29]).

6.2.3 Experimental results

An overview of the experimental results is given in Fig. 6.2 b)-f) while the main elements of the experimental setup are depicted in a). The measured attosecond streaking spectrograms for XUV generated in neon and argon are shown in b) and c), respectively. Here, both spectrograms are normalized. Note, however, that the XUV photon flux for argon is roughly a factor of three lower than for neon. From the streaking spectrograms precise information about the electric field of the IR laser pulses and the isolated attosecond XUV pulses can be obtained [12].

For a coarse reconstruction of the electric field, a streaking curve is extracted from the central energy of the fit of a Gaussian function to the photoelectron spectrum for each delay step (white dots). This curve is subsequently smoothed by filtering out frequency components beyond the laser bandwidth, i.e. below 450 nm and above 1050 nm. From the streaking curve, the vector potential and thereby the electric field can be calculated, as shown in d) and e) as red dashed lines (see e.g. Ref. [26] for more details).

In order to reconstruct the attosecond XUV-pulses a ptychographic reconstruction algorithm based on the description in Ref. [147] was implemented by the author. The algorithm is easy to realize and can simultaneously reconstruct the IR laser pulse. However, it relies on having a good initial guess for the IR streaking field. The latter is derived from the Gaussian fits above. We found that the bare reconstruction algorithm introduced considerable high frequency components to the reconstructed streaking field due to noise in the experimental measurements. We circumvented this by filtering out wavelength components below 100 nm in the streaking field and, in contrast to the original algorithm, by averaging over the corrections over all delay steps in an iteration step instead of subsequently applying the corrections after every delay step. The standard deviation of the corrections also provides an estimate for the variation of the reconstruction. Furthermore, we dynamically adjusted the correction factor from 0.25 for the first 20 iterations to 0.1 for the remaining iterations to improve the quality and speed of convergence. With this approach, we achieved considerably more consistent results and better convergence than with a FROG-CRAB algorithm [143, 146].

The results of the ptychographic retrieval are shown Fig. 6.3. The reconstructed a)-b) and input streaking spectrograms c)-d) agree very well. Since the algorithm can not deal with incoherent contributions, the background below (above) an unstreaked photoelectron energy of 51.8 eV (68.3 eV) has been removed (compare to Fig. 6.2). The reconstruction yields XUV temporal profiles (blue lines) for HHG in neon (e) and argon (f) with 309 ± 9 as and 323 ± 4 as full-width-at-half-maximum (FWHM) duration, respectively, with negligible chirp (red line) and almost no satellite pulses (contrast better than 50:1) as is also evident from the shape of the experimental spectrograms. In the spectral domain, a bandwidth of around 6.4 eV for neon g) and 6.0 eV for argon h) is obtained, which is close to a Gaussian with 6.4 eV bandwidth (orange line) and the expectation from the reflectivity curve of the multilayer mirror (black dashed line). The retrieved streaking laser pulses for argon and neon are shown in Fig. 6.2(d) and (e) in black. Both streaking pulse shapes agree very well with the ones obtained through the Gaussian fits.

At a closer look, our experimental results regarding the generation of IAPs in argon are surprising. Firstly, the CEP of the measured streaking pulses is close to $\pi/2$, in contrast to neon and what would be expected for amplitude gating, even when considering the focussing mirror adjustment. Secondly, for our experimentally measured pulse shape, the phase-matching cutoff would be expected at around 70 eV, while we observe HHG up to 90 eV. The latter also implies that the ionization fraction should be above several 1 %, for which strong plasma effects on the driving laser pulse propagation are to be expected. In order to be able to turn our discussion to these intriguing findings, we first have to introduce our theoretical model that will prove to be a valuable tool afterwards for the interpretation of the experimental results.

6.3 Theoretical modeling and analysis

In order to gain insight into the pulse propagation dynamics in the HHG target, we performed numerical simulations with a HHG code developed by Maximilian Högner which is described in detail in Ref. [336] and part of which can be accessed online[337]. In short, for both the driving field and the XUV field, linear refraction and absorption is considered in the paraxial approximation with cylindrical symmetry. Moreover, for the driving laser field the Kerr effect and the plasma generation, leading to ionization loss, plasma defocussing, and blueshift, are taken into account. For the XUV emission, the dipole response of individual atoms is modeled using the strong-field approximation (SFA) with hydrogen-like dipole moments including ground state depletion through a static tunneling ionization rate[65]. Even though the use of hydrogen-like dipole moments means that we cannot expect absolute quantitative agreement in terms of photon flux, phase-matching effects are adequately described within the SFA. Converting attosecond pulses from the frequency into the time domain is done by utilizing a Gaussian window with 6.4 eV spectral bandwidth at 80 eV central photon energy and Fourier transformation.

For the propagation of the laser pulses through the beamline into the streaking focus, we utilize the propagator of the cylindrically symmetric Helmholtz equation in the paraxial approximation (see SI of Ref. [29]), as it allows to conveniently incorporate irises and filters. The input pulse for the simulations is obtained from the measured streaking trace in neon by iteratively simulating the HHG process and propagation through the beamline to the streaking focus and correcting the input pulse in the frequency domain for the observed difference in phase and amplitude between simulated streaking pulse and measurement. This approach is justified since the propagation through the HHG target is almost linear for neon. The input pulse for the argon experiment is obtained by adding the dispersion of 260 μm fused-silica to the neon pulse, which originates from the HHG optimization. Also the focal mirror position adjustment is accounted for in the simulations. For the XUV pulses the 2-step Fresnel propagator[336] is used to propagate the pulses onto a spherical screen. The sphere of the screen is centered at the HHG gas target position and has a radius given by the distance of the target to the double-mirror. For the calculation of the XUV spectra, additionally, the geometry of the spectrometer is taken into account.

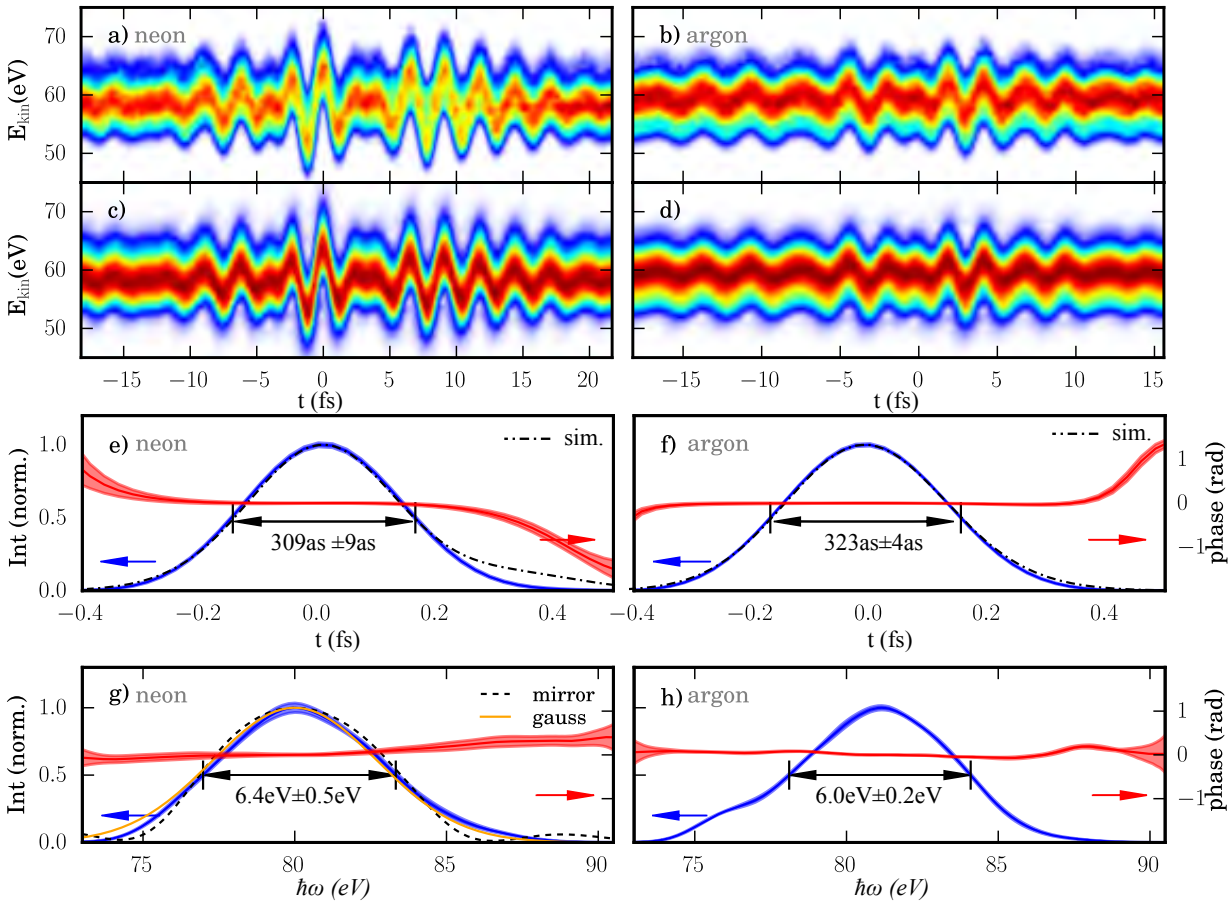

Figure 6.3: IR and XUV pulses retrieved using the pytchographic reconstruction algorithm: a) and b) experimental input streaking trace and c) and d) reconstructed streaking spectrogram for neon and argon, respectively. e) and f) temporal reconstruction of the intensity (blue) and phase (red) of the isolated attosecond XUV pulses for neon and argon, respectively, and the intensity obtained from simulations (black dashed-dotted line). The colorscale is the same as in Fig. 6.2. g) and h) spectral reconstruction of the intensity (blue) and phase (red), together with the reflectivity of the XUV multilayer mirror (black dashed line, maximum reflectivity ≈42 %) and a Gaussian (orange line, 6.4 eV FWHM). The shaded areas indicate the standard deviation of the single delay corrections in the final retrieval iteration. The arrows denote the intensity FHWM. (adapted from Ref. [29]).

Excellent agreement of our simulations with the experimental results is observed, as we want to point out with several examples. Firstly, the experimental and simulated CEP-dependent XUV-spectra shown in Fig. 6.2 f) and g), respectively, match almost perfectly. Secondly, the simulated and experimentally retrieved isolated attosecond pulses agree very well, as depicted in Fig. 6.3 e) and f). Finally, the CEP that optimizes the isolated attosecond pulse generation in argon in the simulation excellently reproduces the CEP of the measured streaking laser field (see also Fig. 6.5), which is one of the intriguing experimental observations, as mentioned above and further discussed below.

In order to assess the fit of analytical phase-matching expressions for the conditions of our experiment and simulations, we had to devise a method that allows the extraction of the time-dependent phase-mismatch from the calculated spatio-spectral HHG source-term. We chose a straight-forward approach using an energy-windowed fast Fourier transform (FFT). Unless noted otherwise, for all the conversions between frequency and time, we utilize the Gaussian window mentioned above (6.4 eV bandwidth at 80 eV). The thus obtained time-resolved complex source-term allows the extraction of the phase ϕ_{source} from which the phase mismatch can be calculated using Eq. 2.14. Since our simulations are performed in a co-moving frame of reference moving at the speed of light, we neglect the XUV dispersion (i.e. $v_{\text{phase}} = c$). As we restrict ourselves to the on-axis phase mismatch along the propagation direction z, the phase mismatch is simply given by $\partial_z \phi_{\text{source}}$. We find this method to work quite well. One drawback is that the phase is not well defined when there is negligible amplitude. It also occurs that the instantaneous frequency away from the maximum of the calculated source bursts, can be significantly different from the central energy of the Gaussian window. Possible improvements could be achieved by utilizing a Wigner transform that allows a fully consistent time-frequency picture.

We are not aware of any study that uses a similar method for the analysis of the time-dependent phase mismatch from full numerical simulations of the HHG process. As shown below, the developed approach represents a crucial step in the understanding of phase matching under strong pulse-reshaping conditions of the driving laser.

6.4 Discussion of the results

6.4.1 Effects of the overdriven regime on HHG

The overdriven regime of HHG is "characterized by strong spatio-temporal reshaping of the laser pulse by laser induced ionization over a short spatial extent" according to Ref. [28], which gives a definition based on the clamping of the driving laser pulse intensity. Indeed, in our simulations for argon we observe a strong spatio-temporal pulse reshaping as illustrated in Fig. 6.4 which shows the driving pulse electric field at the entrance (a) and exit (b) of the HHG target. After the maximum of the pulse (around 0 fs), a strong reduction of the electric field amplitude is observed close to the propagation axis which is accompanied by a blue-shift. Both effects can mostly be attributed to plasma defocussing which is caused by the plasma density gradient in transverse direction from the propagation axis due to

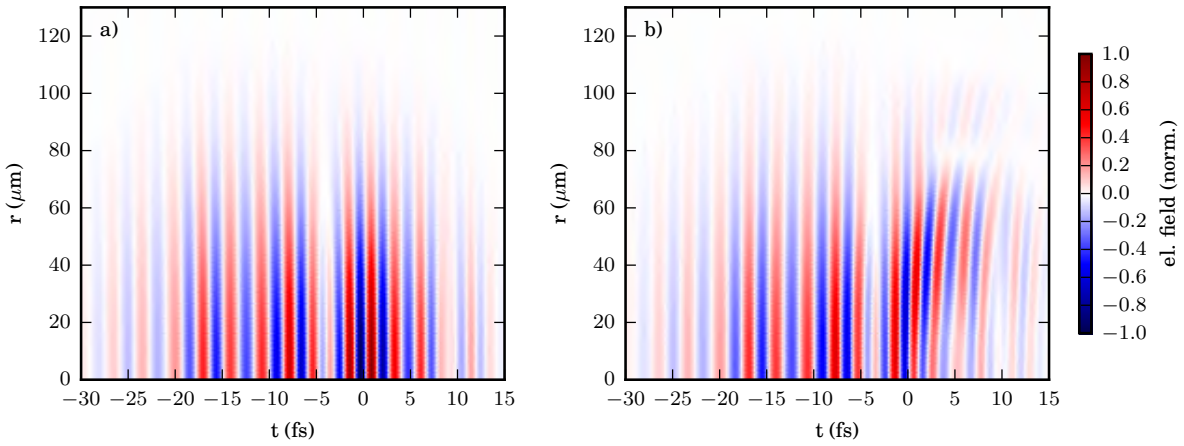

Figure 6.4: Simulated spatio-temporal profiles of the driving pulse in argon at the entrance (a) and the end (b) of the HHG target. A strong plasma-induced modification of the driving pulse is observed after the main peak at around 0 fs (adapted from Ref. [29]).

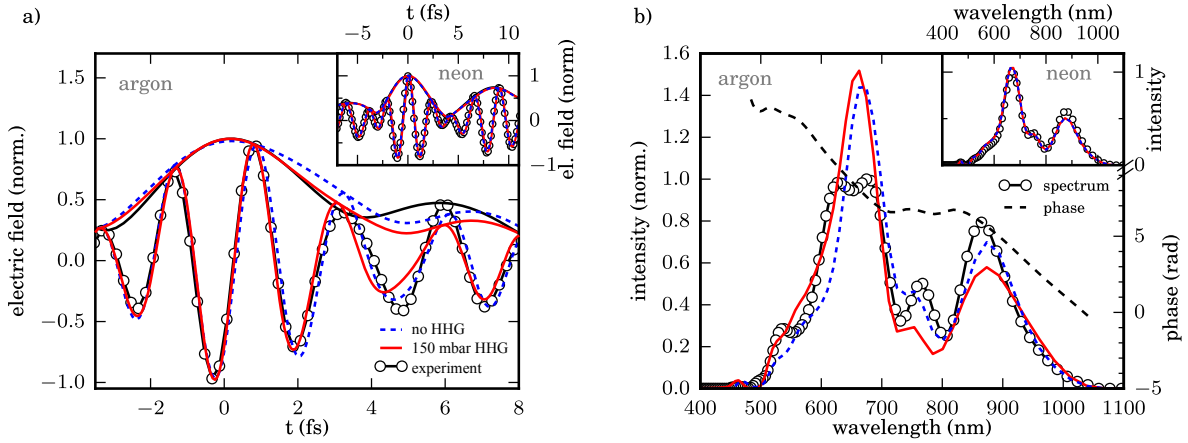

Figure 6.5: Signatures of pulse reshaping in the measured streaking field: Comparison of the experimentally measured laser waveforms (white dots with black solid line) to the simulated pulses for the case of 150 mbar pressure in the HHG target (red solid line) and the case with no high-harmonic generation (blue dashed line). Panels a) and b) show the comparison in the temporal domain and spectral domain, respectively. The main panels show the case of HHG in argon while the insets show the results for neon. In b), in addition to the spectral intensity, the spectral phase of the experimentally measured pulse is shown (black dashed line). The figure has been adapted from Ref. [29].

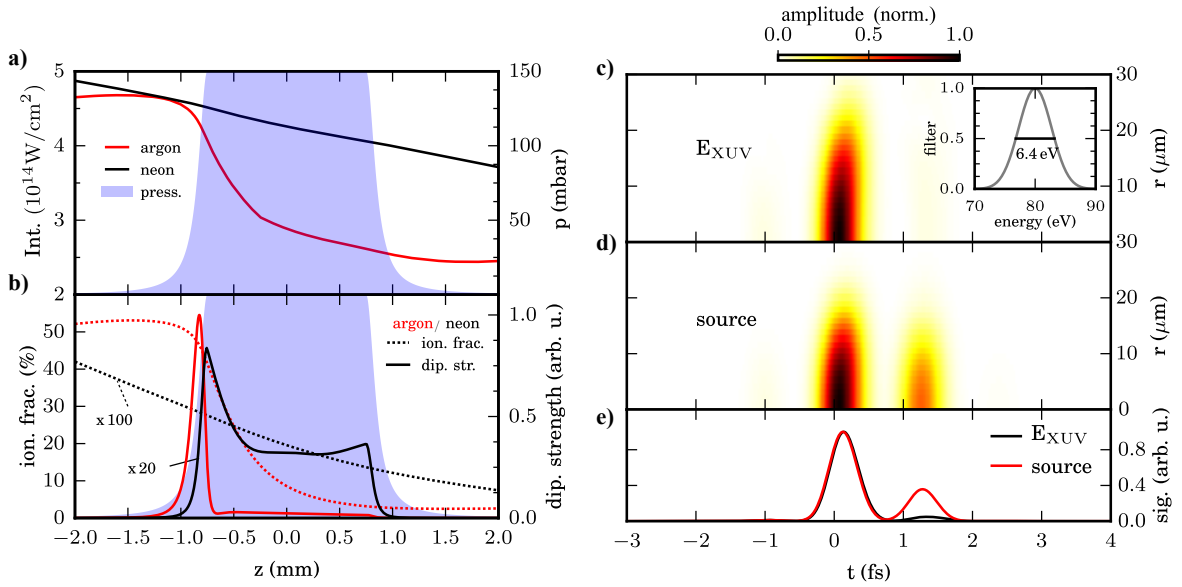

Figure 6.6: Simulation of the driving laser pulse evolution in neon and argon (left column) and XUV generation in argon (right column): a) Maximum on-axis intensity for argon (red) and neon (black). The shaded area indicates the pressure distribution. b) Ionization fraction (dashed line) and dipole strength (solid line) in the energy window defined in a) for argon (red) and neon (black), respectively. Note the different scaling of the quantities for argon and neonc) spatio-temporally resolved XUV pulse at the end of the HHG target in the energy window defined in the inset. d) the source term in the same energy window integrated along the propagation direction. e) Comparison of the radially integrated source term and XUV pulse. The absence of the second peak around 1.2 fs in the XUV pulse compared to the source contribution indicates the occurence of transient phasematching. (adapted from Ref. [29]).

the intensity profile of the driving laser. The plasma contribution reduces the refractive index of the gas medium and acts as a defocussing lens leading to an extra curvature of the wavefronts. The defocussing based on the plasma induced refractive index change scales as λ^2 (see Drude model Eq. 5.5). Together with the time-dependent reduction of the refractive index during the plasma build-up, this explains the effective on-axis blue-shift.

A comparison of the effects of pulse reshaping on the streaking field between experiment and simulation is shown in Fig. 6.5 in the temporal (a) and spectral domain (b). For neon (depicted in the insets), practically no change is observed regardless of whether the nonlinear propagation through the HHG target is considered (red solid line) or not (blue dashed line) and excellent agreement with experiment (white dots) is evident. In the case of argon in the temporal domain, a strong reshaping after the main peak occurs that leads to an intensity decrease and blue-shift when propagation in the HHG target is taken into account. This reshaping is also evidenced in the experimental measurement (white dots) in the region relevant for HHG up to 3 fs. Afterwards, some deviation occurs. In the spectral domain a blue-shift can be observed both in experiment and simulation (500 nm-600 nm). Part of the deviation that is present can possibly be explained by the experimental setup, that blocks the central part of the HHG driving pulse before the streaking chamber which might make a more precise modeling of the laser beam and the filter necessary.

An analysis of how the HHG process is affected by the pulse reshaping in the simulations is shown in Fig. 6.6. The peak on-axis laser intensity for argon (red line) and neon (black) can be seen in a). While the intensity evolution for neon practically follows a Gaussian beam, in argon the peak intensity quickly decays once the pulse enters the gas target (blue shaded area) from about $4.6{\cdot}10^{14}\mathrm{W/cm}^2$ to $3.0{\cdot}10^{14}\mathrm{W/cm}^2$ over a distance of a few 100 μm. The distinct behavior originates from the vastly different ionization rates as illustrated by the fraction of ionized atoms at the end of pulse as shown in b) for argon (red dashed line) and neon (black dashed line), respectively. For argon the ionization is more than a factor of 100 higher, leading to a much stronger plasma loss and defocussing. The final fraction of ionized atoms is also more than an order above the critical ionization fraction for HHG phase-matching (see Fig. 2.7 b)). We can thus conclude that the experiments in argon were done in the overdriven regime. The fast driving pulse intensity decay also leads to a confinement of the XUV dipole term in the considered energy window to the entrance of the HHG target for argon (red solid line). In contrast, the dipole term extends over the full target in neon (black solid line) . Due to the higher ionization rate, the dipole strength is considerably larger in argon than in neon for our simulation.

The strong spatio-temporal reshaping naturally raises the question on how the off-axis contribution, not considered above, is influenced. In our simulations the time-resolved XUV pulse profile at the end of the HHG target, depicted in Fig. 6.6 (a) seems to be hardly affected. This is in contrast to Ref. [338], where HHG was dominated by off-axis emission. However, their experiments were done under considerably different conditions, especially much tighter focusing. Generally, care needs to be taken to account for potential off-axis contributions.

Nevertheless, an intriguing observation can be made, when comparing the time-resolved XUV amplitude Fig. 6.6 (c) to the integrated XUV source term amplitude (d). The latter

has been obtained by calculating the time-resolved XUV source term (again in the Gaussian window given above) at each position on the simulation grid, and subsequently adding up the time-resolved absolute values of the source term along the propagation direction. Apart from the main peak centered slightly after 0 fs there is another prominent contribution one half-cycle later at around 1.3 fs, which is suppressed in the XUV pulse. This is further illustrated in e), which shows both quantities radially integrated. As shown below, the suppression of the satellite peak is a consequence of phase matching.

Before we can discuss how phase matching of HHG is possible under these strong spatio-temporal reshaping conditions and seemingly high plasma densities, and how this can explain the finding in the previous paragraph, we have to make a few fundamental considerations on the description of phase matching in the overdriven regime.

6.4.2 Phase matching in the overdriven regime

Extension of the HHG dipole contribution

Even though the term overdriven regime has only been coined recently[28], several important aspects of HHG under similar conditions have already been revealed theoretically. Generally, since the phase-mismatch is proportional to the harmonic order, for high photon energies and a driving pulse undergoing reshaping, perfect phase-matching can only be achieved locally and transiently[28, 96]. Furthermore, the HHG dipole phase can counteract the plasma-induced phase increase of the driving laser, either through a blue-shift [339] or an intensity decrease [96], leading to perfect phase-matching and XUV buildup over propagation lengths of 10-100 μm. While, the former has been used to explain experiments with an XUV cutoff significantly above the phase-matching cutoff up to the keV energy range [340, 341, 342, 343], due to the low photon flux, it is not clear whether phase-matching has been achieved. Finally, simulations of HHG with long-wavelength drivers and high-pressure gas targets with realistic pressure distributions have shown a pronounced intensity clamping of the driving laser and identified different contributions to the phase-mismatch[344].

On the experimental frontier, there have been several studies involving long wavelength drivers or tight focusing conditions or both [345, 331, 338], including one with additional plasma density measurement [28], indicating the importance of plasma defocusing and pulse reshaping.

However, while the intensity-decay is usually included in the analysis, none of these studies has presented an expression for the phase-mismatch that contains explicitly the blue-shift contribution to the dipole phase. Indeed, except for the 1d-simulations in Refs. [339, 346], the latter is usually ignored. Here, we introduce an expression that includes all the effects of pulse-reshaping on the HHG dipole phase, thereby allowing the description of phase-matching in the overdriven regime:

$$\Delta k(t,z) = +q\partial_z\phi_{\mathrm{IR}}(t,z) + \alpha \cdot U_p/\hbar\omega_0 \cdot \left(\frac{\partial_z I(t,z)}{I} - 3 \cdot \frac{\partial_z \omega_0(t,z)}{\omega_0}\right), \tag{6.1}$$

which is a straight-forward extension of Eq. 2.15 and Eq. 2.20 through the addition of the last term which describes the effect of the driving laser blue-shift on the dipole phase, once the proportionality $U_p/E_{photon} \propto I\dot{\lambda}^2/\omega_0 \propto I/\omega_0^3$ is recognized. As a reminder, since we are in the co-propagating frame and neglect XUV dispersion, the XUV wavevector does not appear. Note that the numerically calculated ϕ_{IR} from the beam propagation simulation contains all the effects of plasma and neutral dispersion and any geometric phase, such as the Gouy-phase. We limit ourselves to the phase-mismatch in propagation direction, but Eq. 6.1 can be easily generalized by replacing the partial derivative ∂_z with the gradient ∇. Since the focus in this chapter lies on photon energies close to the HHG cutoff, we will generally assume an α of 3.2 unless mentioned otherwise.

Analysis of the experimental phase-matching in argon

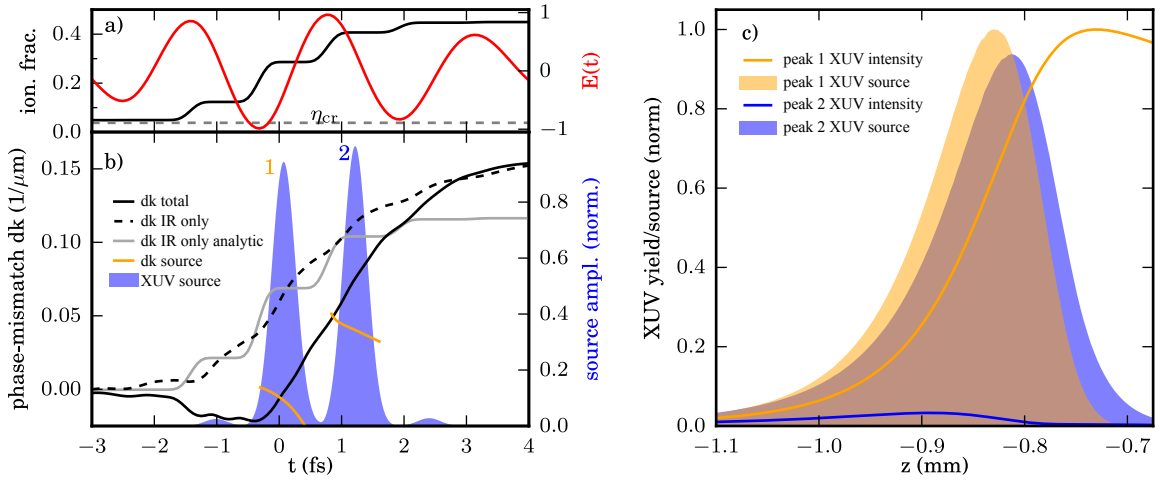

Figure 6.7: On-axis transient phase matching and XUV generation in argon: a) The driving laser pulse (red) and the time-dependent fraction of ionized atoms (black). (b) The on-axis phase mismatch in the analytic expression without dipole (gray) and the calculated phase-mismatch accroding to Eq. 6.1 with the dipole contribution (black) and without (black dashed). The numerical phase mismatch calculated from the complex source term (orange) and the source term amplitude (blue shaded area) is also shown. The quantities are shown at the entrance of the target at $z = -0.8$ mm. c) The on-axis source term amplitude (shaded area) and evolution of the XUV amplitude from the full simulation (solid line). The color indicates the first (orange) or second (blue) half-cycle centered around 0.1 fs and 1.2 fs, respectively, as shown in b). The figure has been adapted from Ref. [29].

An analysis of the phase-matching for our experimental conditions in argon is shown in Fig. 6.7 at the entrance of the HHG target (z=-0.8 mm). Here, the XUV source term in the considered energy window peaks and a strong driving pulse intensity decrease is observed (see Fig. 6.6). The driving laser pulse (red line) and the fraction of ionized atoms (black

line) together with the critical ionization fraction (black dashed line) of 3.8% is illustrated in a). Already at the beginning of the pulse, the ionization fraction is at 4.8 % due to the prepulse (see Fig. 6.2 e) and rises up to around 13 % even before the main cycle.

Two strong bursts of the on-axis time-resolved XUV source term (blue shaded areas) can be observed at around 0.1 fs and 1.3 fs, as shown in Fig. 6.7 b). Considering the phase mismatch calculated according to Eq. 6.1 (black line), it can be understood why, nevertheless, a single IAP is generated. Only up to the first main burst, the phase mismatch is close to zero, while it rapidly increases afterwards, such that the second burst already experiences a considerable Δk, limiting its coherent buildup to distances of only several tens of micron. The buildup of the XUV intensity of the first burst (orange line) and second burst (blue line) is compared in c). Both bursts exhibit similar source strengths (shaded areas), however, only the first pulse is effectively phase-matched, whereas the buildup of the second pulse is strongly suppressed.

In order to validate the phase-matching expression further, we compare it to the numerical phase mismatch calculated from the simulated source term (orange lines), as shown in b). Relatively good agreement is achieved. Remarkably, the numerical phase mismatch exhibits a different curvature, i.e. it decreases within a burst. This observation can, however, be explained considering that the instantaneous frequency of the calculated bursts is changing and that α grows for increasing recollision times and from short to long trajectories.

In contrast, the analytical phase-mismatch expression based solely on the wavevector mismatch Eq. 2.16 (gray line), fails under our conditions. Nevertheless, it is worth noticing that it describes the contribution of the driving laser phase change (black dashed line) to the phase mismatch surprisingly well. The dipole contribution is given by the difference of the latter with the full expression which helps us to intuitively understand how phase matching is achieved under our conditions. While the rising plasma density causes a positive phase mismatch through the blue-shift leading to an increase of ϕ_{IR}, the decrease of the driving pulse intensity and the blue-shift result in a decrease of ϕ_{dipole}. Thereby, perfect phase-matching is allowed transiently even considerably above the critical ionization fraction.

The suppression of the second XUV burst due to phase-matching, as discussed above, explains the experimental observation that the IAP generation in argon is optimized at a different CEP than expected. This finding is further illustrated in Fig. 6.8 which shows the simulated CEP-dependence of the integrated XUV source term (a) and intensity (b) at the end of the target as well the XUV intensity in the far-field (c). For better comparison, the lineouts for two different CEPs are shown (right panels, black and red lines), as indicated by the dashed lines. In the source term, isolated pulse generation would be optimized at around CEP=0, however, with noticeable pre- and postpulses. Due to the suppression of the later burst visible in the XUV intensity, the optimal CEP (red dashed line), shifts to around 1 rad, as this allows to additionally minimize the prepulse. The remaining CEP-shift of around 0.5 rad in the experiment stems from the focal mirror position adjustment. The far-field XUV intensity shows a similar behavior with the addition that the long-trajectory contribution is quenched due to the increased divergence.

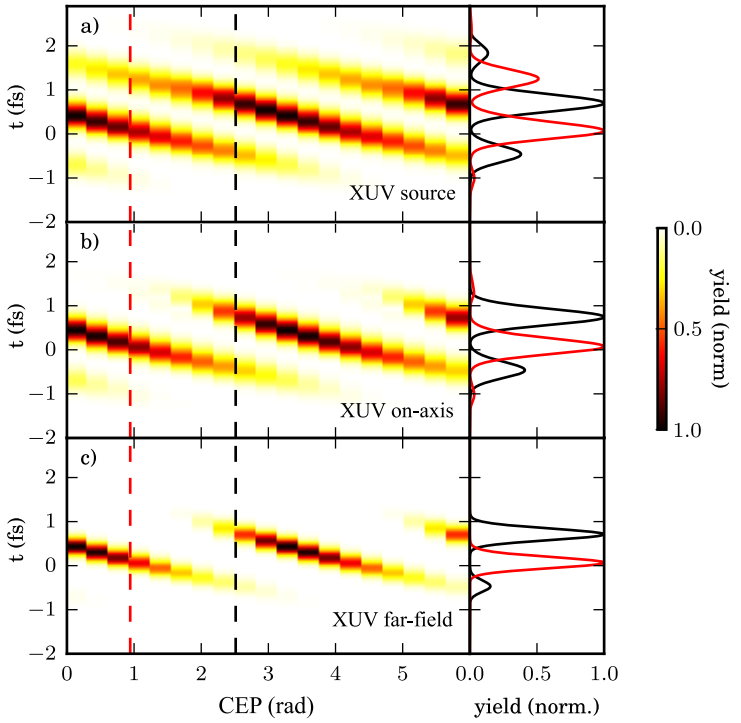

Figure 6.8: Simulations of the CEP-dependence: (a) time-dependence of the source term radially and longitudinally integrated over the whole target and (b) the XUV yield on axis at the end of the target compared to (c) the far-field XUV yield integrated over the inner mirror. All quantities are calculated in the 6.4 eV energy window around 80 eV. The CEP ϕ_0 used to describe the experimental results is shown as red dashed line together with another CEP-value of $\phi_0 + \pi/2$ (black dashed line). The temporal profiles for the respective CEPs are shown in the panels to the right (adapted from Ref. [29]).

6.4.3 Pressure and intensity variation

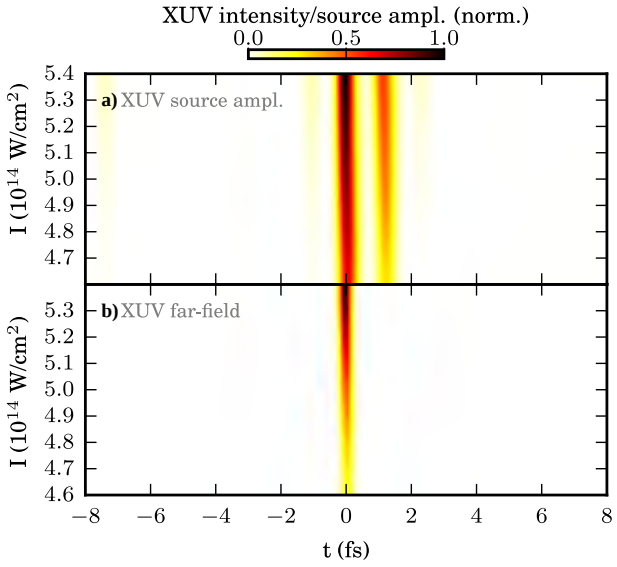

Figure 6.9: The intensity dependence of the XUV generation in argon: a) and b) the time-resolved on-axis XUV source amplitude integrated along the propagation axis and the far-field XUV intensity, respectively. Both quantities are calculated by applying a filter of 80 eV around 6.4 eV bandwidth (adapted from Ref. [29]).

The robustness of the phase-matching effects discussed above with respect to changes in the peak driving intensity is shown in Fig. 6.9. Over an intensity variation from 4.6 to $5.4 \cdot 10^{14}\mathrm{W/cm}^2$ the second burst of the XUV source term (a) is suppressed in the XUV-farfield (b) due to the its increased phase-mismatch.

Furthermore, the evolution of the HHG process in argon in dependence on gas target pressure is discussed in Fig. 6.10. The on-axis XUV source term amplitude along the propagation axis normalized for each pressure is shown in a) for the conditions of our experiment. While for low pressures, it extends over the full target length, already above around 5 mbar the source term gets localized at the entrance of the target, and even shifts into the region of increasing pressure above 100 mbar. This can be explained by the plasma induced reduction of the driving laser pulse intensity, as observed above. At the same time the FWHM of the source distribution (blue line) reduces from the target length down to slightly above 100 μm.

Fig. 6.10 b) shows the XUV yield (blue solid line) and source term (red solid line) together with the contrast (dashed lines) defined as the ratio of the contribution of the main burst to the total yield. While the XUV source keeps increasing with pressure, albeit affected by pulse reshaping, the XUV yield exhibits a maximum at around 20 mbar. At higher pressures, the latter initially drops relatively fast but quickly flattens out above 50 mbar. For the XUV source the contrast varies between 0.6 and 0.8, while the XUV yield quickly reaches 0.95 at around 5 mbar and is close to 1.0 beyond 50 mbar. The maximum

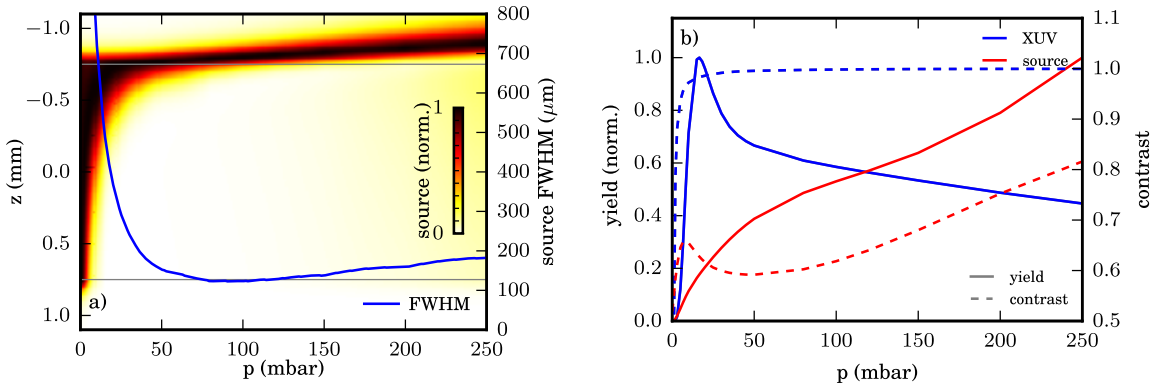

Figure 6.10: Pressure-dependence of the XUV generation in argon (6.4 eV bandwidth at 80 eV): a) spatially resolved XUV source term along the propagation direction (false color plot). Above a few mbar the source term gets localized at the front of the gas target. The FWHM (blue line) drops to around 100 μm at 100 mbar and slightly increases again for higher pressures. The region where the nominal target pressure is reached is indicated by the two thin solid lines. b) Yield (solid lines, left axis) and contrast between main and secondary peak (dashed lines, right axis, see main text for the definition) of the XUV pulse (blue line) and the source term (red line). The figure has been adapted from Ref. [29]

of the XUV yield is reached at conditions where the intensity decrease and blue-shift are such that phase-matching over long distances is possible. In the experiment, we are above this maximum, since the yield quickly drops already for a slight reduction of the pressure whereas it is relatively insensitive at higher pressures. Our findings on the driving pulse dynamics and the phase-matching effects are therefore not affected by the uncertainty in the experimental target pressure determination.

6.5 Phase matching in the overdriven regime with long wavelength driving pulses

Naturally, the question comes up on how our findings scale to different gas types and longer wavelengths, especially in the range of 1.5 μm-2.0 μm, where the overdriven regime was first identified experimentally[28] and where the water window can be reached with few-cycle drivers (see Fig 2.7). To this end, we perform simulations for 1.5-cycle driving pulses in argon at 800 nm central wavelength, in neon at 1400 nm and helium at 1900 nm. This section closely follows the presentation in Ref. [29].

First of all, in order to achieve comparable pulse propagation at least in the linear regime, the same focusing conditions need to be used, i.e. all spatial dimensions are scaled with the driving pulse wavelength. This also includes the gas target parameters. For helium we use a relatively tight focal spotsize of 47.5 μm, a thin target with a length of roughly

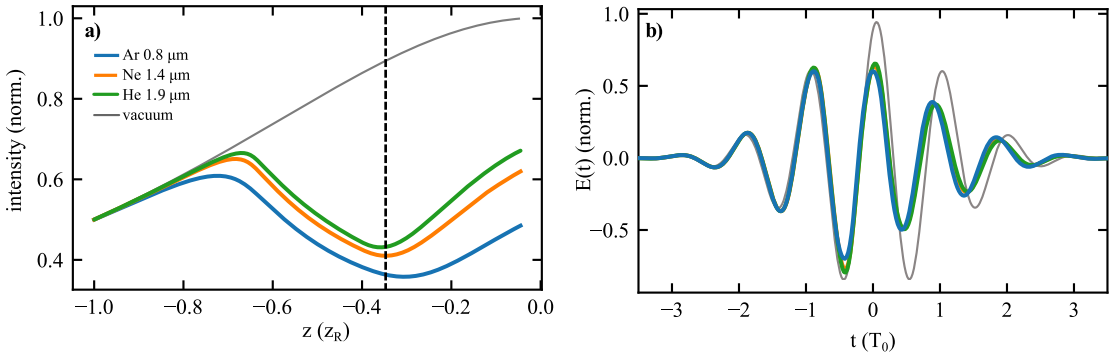

Figure 6.11: Simulated intensity-decay and blue-shift for CEP=0: a) the instantaneous intensity at t=0 along the propagation axis for argon, neon, helium, and a vacuum reference. The propagation axis is expressed in terms of the Rayleigh range and the curves have been normalized to their maximum vacuum intensity of 6.5, 8.9, and $10.7 \times 10^{14}\,\mathrm{W/cm^2}$, respectively. The target is centered at $-0.5\,z_\mathrm{R}$. b) the IR driving pulses at the end of the gastarget at $-0.35\,z_\mathrm{R}$ (as indicated by the black dashed vertical line in a). All pulses, except for a slightly different amplitude, overlap very well, and all show a similar blue-shift and intensity decay around and after t=0 compared to the pulse propagated in vacuum (tin gray line). The figure has been adapted from Ref. [29]

0.8 mm and a half-width of approximately 0.16 mm for the Lorentzian increase/decrease of the pressure distribution. The target center is half the Rayleigh length in front of the focus, as this position has been found to approximately optimize HHG in the overdriven regime[28] (see also discussion below). The scaling of the intensity is slightly less straightforward. Here, since the present work studies phase matching in the overdriven regime, we choose a vacuum peak intensity such that at the main electric field oscillation ten times the critical ionization fraction would be reached. This approach results in vacuum peak intensities of 6.5, 8.9 and $10.7\times10^{14}\mathrm{W/cm^2}$ for argon, neon and helium, respectively.

With the above parameters, the pressure-dependence of HHG is calculated. Interestingly, for the pressures that maximize the considered XUV yield (see next paragraph for details), the evolution of the on-axis peak intensity as well as the laser pulse shape at the end of the target are surprisingly similar, as shown in Fig. 6.11 a) and b), respectively. The peak intensity starts to get severely quenched once the driving pulse enters the pressure distribution and even decreases within the target from about 60 % of its maximum possible value (gray line) to approximately 40 %. This behavior is mainly a consequence of plasma defocussing. After the target, the intensity increases again since the wavevector components away from the optical axis have hardly been affected by the plasma and are still focusing. The driving pulses at the target exit exhibit a strongly decreased intensity after and including the main half-cycle (t=0) compared to the vacuum propagation (gray line). Moreover, a distinct blue-shift is observable. The first few cycles of the pulse are hardly affected. Overall, similar conditions have been found for the simulations of HHG in our experiment (see Fig. 6.6).

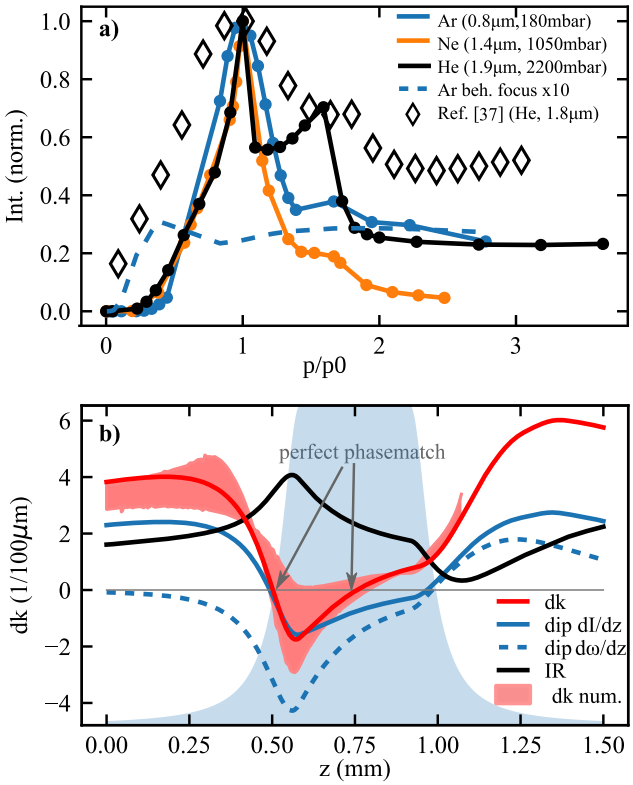

Figure 6.12: Simulated high-harmonic generation dynamics in the tight focusing regime for different wavelengths and gases: (a) the normalized far-field XUV flux in the cutoff region versus normalized pressure for a 1.75-cycle pulse in argon (solid blue line, $p_0 = 180\,\mathrm{mbar}$), in neon (solid orange line, $p_0 = 1050\,\mathrm{mbar}$) and in helium (solid black line, $p_0 = 2200\,\mathrm{mbar}$). The flux in argon for a gas target positioned after the focus is shown (dashed blue line, upscaled by factor 10), as well as the experimental data extracted from Ref. [28] (open diamonds). (b) The different contributions to the total phase-mismatch (thick red line) on-axis for the most intense XUV burst for argon at $p = p_0$ calculated by Eq. 6.1: phase-mismatch IR due to the propagation of the laser driving pulse (black line), dip. $\mathrm{d}I/\mathrm{d}z$ and dip. $\mathrm{d}\omega/\mathrm{d}z$ from the HHG dipole caused by the change of laser intensity (solid blue line) and the blue shift of the laser pulse (dashed blue line), respectively. Also shown is the numerically calculated total phase-mismatch within the half-cycle of the XUV burst (red shaded area) and the gas pressure distribution (blue shaded area). The figure has been adapted from Ref. [29].

The pressure-scaling of the far-field XUV/soft-xray yield is shown in Fig. 6.12 a). For this analysis, the flux is integrated over a divergence angle of approximately 1.5 mrad and an energy-window of 75 - 95 eV in argon, 250 - 320 eV in neon and 550 - 700 eV in helium. The windows correspond to roughly 20 % of the total bandwidth placed at the spectral cutoff. The simulations are carried out only for a single CEP (= 0). The x-axis is normalized to the pressure p_0 of maximum yield. All three curves, for argon (blue solid line), neon (orange) and helium (black), show a qualitatively similar behavior. After an initial strong increase up to the maximum, the flux drops again rapidly but then stabilizes at an almost constant level depending on the gas type. This is consistent with Fig. 6.10 and the calculation and analysis of spatially localized phase-matching in Ref. [96]. There, an effective length of coherent harmonic buildup L_{eff} was defined, that describes the distance over which Δk is close to zero. L_{eff} is inversely proportional to the first derivative of Δk, which in turn is in a coarse approximation proportional to the plasma density, leading to $L_{\text{eff}} \propto 1/p$, where p is the gas pressure. Since the harmonic yield is proportional to the square of the product of the number of contributing emitters $N \propto p$ and the effective coherence length L_{eff}, the deep regime of spatially transient phase-matching results in quasi pressure-independent HHG yields.

For comparison, we show the flux for argon (dashed blue line up-scaled by a factor of 10), when the target is placed at 0.5 Rayleigh length behind the focus at an even increased intensity that corresponds to $15\,\eta_{\text{cr}}$. There, the maximum flux occurs at a lower pressure and is almost two orders of magnitude smaller. Additionally we show the data extracted from Ref. [28] for helium (open diamonds, extracted at 3.3 bar, 410-700eV), which agrees qualitatively very well with our simulations for helium. Note, that averaging over the CEP in the simulations would likely result in smoother curves.

The maximum XUV/soft-x-ray flux is reached for specific phase-matching conditions. Figure 6.12 b) shows the individual contributions to the on-axis phase-matching according to Eq. 6.1 for the peak of the main XUV pulse at p_0. A similar analysis has been done in Ref. [344]. The presented data is for argon, but the conditions for neon and helium are almost identical (see SI of [29]). The contribution of the driving pulse (black solid line) is positive throughout the target due to the strong plasma contribution. The HHG dipole term caused by the intensity change (blue solid line) is first positive followed by a change in sign slightly before the full pressure is reached and subsequently increases again after the target exit. The dipole term due to the blue shift (blue dashed line) is negative before and within the target and then switches to positive at the end of the target. It is important to notice that the blue-shift dipole term that we introduced in Eq. 6.1 dominates here, and is therefore absolutely crucial for the understanding of the total phase-mismatch.

Since the dipole terms counteract the driving laser contribution to the phase mismatch, the overall phase mismatch (red solid line) is close to zero within the gas target. Indeed, a zero crossing slightly in front of the entrance and then close to the middle of the gas target is observed. The zero crossing at the target entrance is located here in the rising edge of the pressure distribution and seems to occur for a wide range of pressures. It explains the results of Ref. [28], that observed an XUV buildup at the target entrance in their simulations. We compare the semi-analytic expression to the full numerical calculation

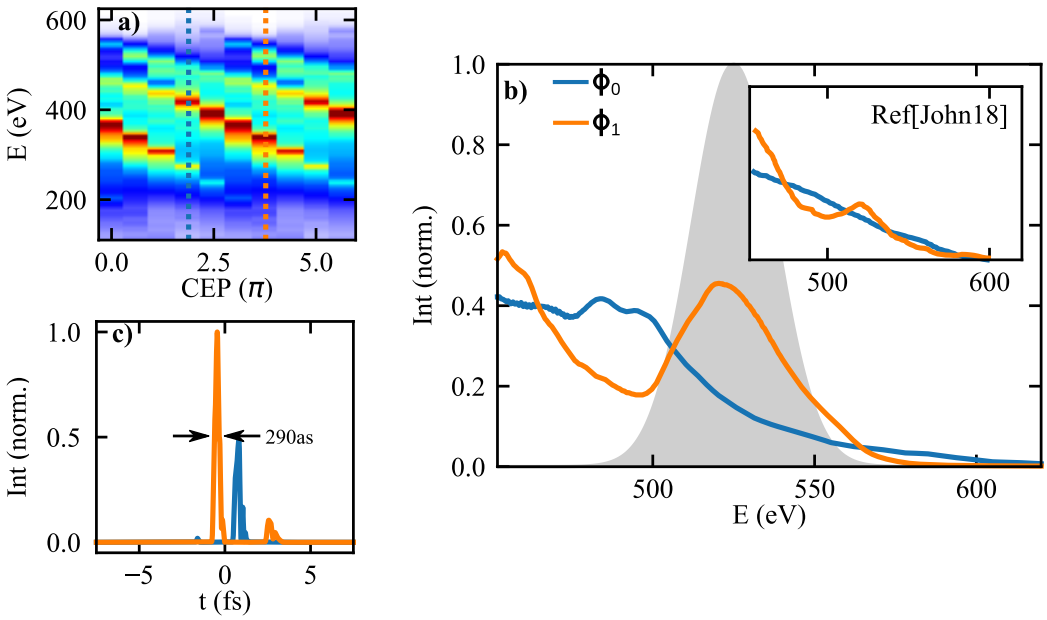

Figure 6.13: Simulated CEP-variation and IAP generation for helium for a driving wavelength of 1800 nm and at p=2000 mbar. (a) CEP-resolved spectra. Transmission through a 0.1 μm aluminum foil has been included to filter out the low energy contribution. The colorscale is the same as in Fig. 6.2. (b) XUV spectra near the cutoff for two different CEP-values of ϕ_0 and ϕ_1 as indicated in a). The inset shows the data extracted from Ref. [28]. The IAPs generated in the energy window illustrated by the gray area, are depicted in (c). The figure has been adapted from Ref. [29].

averaged over the burst (red shaded area). Again, very good agreement is observed. At the condition of maximum flux, shown here, the source term, while starting to be localized towards the target entrance, still extends almost over the whole target length.

The pressure of maximum flux depends on the energy window and we observe that for lower photon energies, higher pressures are required as evident in the data of Ref.[28]. In principle the discussed mechanism would allow to transiently phase match very high photon energies, however, due to the strong intensity clamping at the conditions of maximized photon flux, the HHG cutoff lies in the region of the classical phase-matching cutoff.

In order to demonstrate that these conditions allow IAP generation in the overdriven regime, we investigate the CEP-dependence of the XUV spectra for helium in Fig. 6.13 a). The used parameters are the same as above but scaled to 1.8 μm at 2000 mbar helium. The transmission of a 0.1 μm aluminum filter has been included. A strong CEP-dependence is observed. The spectra in the cutoff region for two specific CEP-values are shown in Fig. 6.13 b). They have a striking resemblance to the experimental data of Ref. [28], shown in the inset. The gray shaded area illustrates the bandwidth for which the resulting soft-x-ray pulses, shown in Fig. 6.13 c), are calculated. Indeed, a very strong isolated pulse is observed for ϕ_1. Surprisingly, even at the complementary phase an nearly isolated pulse is generated. The pulses are slightly positively chirped and therefore longer than the Fourier-limit. For an energy window that covers almost the whole spectrum, the usability of the generated pulses depends on which contrast between the main soft-x-ray burst and satellite bursts is acceptable. As can be seen in Fig. 6.13(a) from the half-cycle cutoffs which are manifested as diagonal stripes, several half-cycles will contribute to the resulting pulses for all energies above 280 eV. Nevertheless, for most CEP values there is always one half-cycle that clearly dominates the spectrum and therefore enables IAP generation with moderate contributions of satellite pulses.

The complexity of the transient phase-matching process is illustrated by the spatio-temporal phase-matching maps in Fig. 6.14 a) which is similar to the approach in Ref. [109]. Here, the on-axis result for the optimized conditions in argon at 80 eV is shown, but similar structures are obtained for the other gases (see SI of Ref. [29]). Here, the phase mismatch is calculated via Eq. 6.1. Perfect phase matching (red areas) can be achieved in several regions. Firstly, at the beginning of the gas target within the region of increasing pressure around z=-0.25 mm, as the ideal relation between the ionization fraction and pressure is reached transiently. Secondly, at around t=-2 fs practically all along the target when the critical ionization fraction is reached within the leading part of the pulse that does not suffer from reshaping. Thirdly, at the exit of the target at z=0.25 mm and finally for later times t=0 fs, when the plasma dispersion starts to dominate the phase-mismatch again, two more regions appear. However, these regions only contribute strongly to the resulting XUV pulse if the source term amplitude is not negligible. The latter (blue line) integrated along the propagation axis is shown in Fig. 6.14 b). Only the central burst at around t=0 fs experiences nearly perfect phase matching over longer distances and therefore contributes the emission in the resulting XUV electric field amplitude (orange line). In contrast the second region connected to the critical ionization fraction, which was attributed to potential IAP generation in Ref. [109], does seem to occur slightly too early for our conditions.

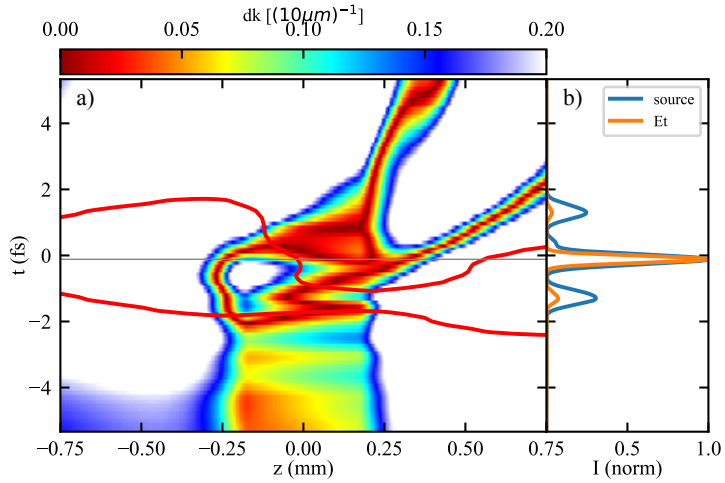

Figure 6.14: Spatio-temporally resolved on-axis phase-matching: a) analytic phase-mismatch along the propagation axis for the central half-cycles of the pulse for argon. The considered XUV energy window is the same as for Fig. 6.12.The red contour line shows the instantaneous intensity where the classical harmonic cutoff lies above the central energy of the investigated energy window. b) source term integrated along the propagation axis (blue line) and the XUV pulse at the end of the target (orange line). The figure has been adapted from Ref. [29].

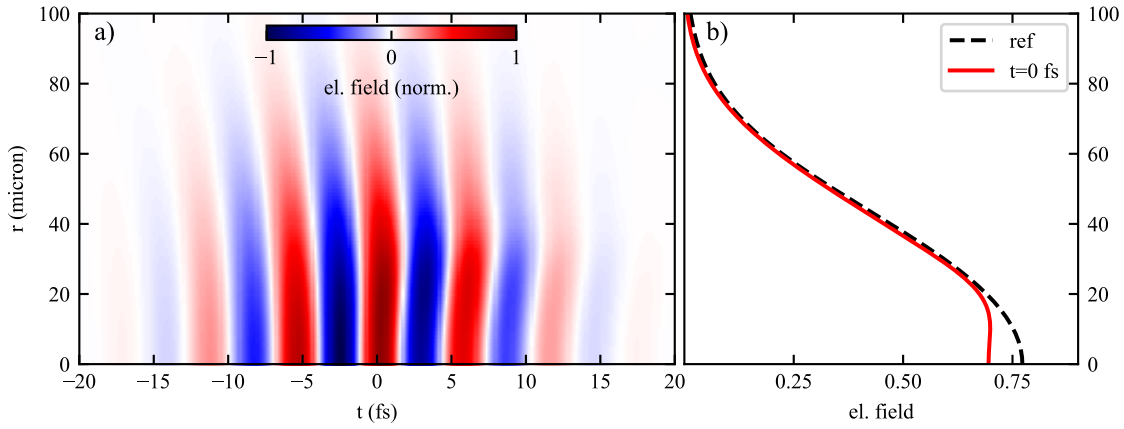

Figure 6.15: Reshaping of the driving laser: a) Spatiotemporal reshaping of the driving laser at the center of the gas target for helium and the driving laser conditions in Fig. 6.13. b) Mode profile at t=0 fs. The plasma-induced defocusing leads to a flat phase-front as well as a flattening of the driving pulse profile.

We want to point out, that unlike in Ref. [345], short trajectory contributions dominate the plateau region of the HHG spectrum in the overdriven regime, even though the gas target is placed in front of the focus,which is consistent with Ref. [28]. This can be explained by the blue-shift dipole term, which is stronger for few-cycle lasers. Similar to Ref. [345], we observe the formation of a flat-top electric field amplitude and flat wavefront for the main cycle, due to plasma-defocussing, as shown in Fig. 6.15. This spatial reshaping should also lead to improved divergence properties of the emitted harmonics. Therefore, this finding can likely also explain observation of Ref. [28] that in the overdriven regime all harmonics seem to originate from a common virtual source point. This is in contrast to conventional HHG, where the intensity decay transversely to the propagation axis and the intensity-dependent HHG dipole phase lead to a strong dependence of the spatial divergence on the harmonic order[121].

6.6 Conclusion

In conclusion, experimentally, our work presents the first unambiguous demonstration of isolated pulse generation in the overdriven regime due to the employed attosecond streaking pulse characterization. Through experimental signatures, simulations and the comparison between argon and neon, we find that in the overdriven regime, due to the driving pulse reshaping, the conditions for high-harmonic generation and phase-matching are strongly modified.

Theoretically, we introduce an analytic expression that is able to describe phase matching in the overdriven regime by including the effect of the driving pulse blue-shift on the HHG dipole phase. Furthermore, a method is presented that allows to extract the phase mismatch from fully numerical calculations with which we validate the analytical expressions. Finally, we extent our findings to longer driving wavelengths through simulations and observe that in the overdriven regime the contribution of the HHG dipole caused by the blue-shift can dominate the phase mismatch.

There are several experiments that have been performed in a regime where our findings would probably have been highly relevant. Apart from the experiments in Refs. [28, 345, 338], we believe that this is likely also the case for Refs. [331, 109].

On both the experimental and theoretical side, several open questions regarding the overdriven regime remain. Firstly, under which conditions is the overdriven regime desirable for HHG? Is it only efficient for tightly focused few-cycle laser pulses? Moreover, which requirements are to be fulfilled by the driving pulse wavefront quality? Recent research seems to indicate that for high energy driving pulses with non-perfect wavefronts, conventional phase-matching schemes could be more efficient[347]. Finally, it remains to be answered which spectral bandwidth for isolated attosecond pulses in the water window can be achieved in the overdriven regime compared to conventional schemes[**?**, 109].

The present work will help to answer these questions and to furthermore understand the limitations of different HHG phase-matching regimes. Therefore, these findings will play a vital role for the development and analysis of current and future experiments that

aim at XUV generation in the water window and beyond, which in turn promises many interesting applications on biological samples in their natural environment.

Chapter 7

Attosecond physics on metallic nanotips

This chapter describes two different experiments on the PHz-scale for the electric field reconstruction on and using nanotips. First, the experimental reconstruction of optical near fields on a nanotaper with attosecond precision is demonstrated. Secondly, the photocurrent-based measurement of the electric field at the nanotip apex is shown. This concept is in turn used to demonstrate the spatio-temporally resolved measurement of a beam with orbital angular momentum (OAM). Since both methods share the same general motivation and the shortcomings of the first technique inspired the latter approach, both experiments and their relation are introduced below. An overview of the outline is given in the respective sections.

7.1 Introduction

The interaction of light with nanostructures exhibits unique features[348, 349]. In plasmonic materials, the excitation of collective oscillations of the electrons with respect to the lattice (i.e. plasmons) may lead to the enhancement of the local near field up to several orders of magnitude in intensity compared to the incident field. At the same time, the enhanced fields are confined to the sharp geometrical features of the nanostructure, well below the diffraction limit of light. These nanoplasmonic phenomena have found a vast range of applications (see Ref. [349] for an overview) including biochemical sensing and detection[350], near-field enhanced optical microscopy with nanometer resolution (nanoscopy)[351], surface-enhanced Raman spectroscopy[352] with detectivity down to the single molecule level[353], thermal cancer treatment[354] and waveguiding of optical energy on the nanometer scale[355]. Moreover, other nano-optical techniques make use of the subwavelength dimension of the nanostructures alone without relying on plasmons, e.g. optical metamaterials[356] or near-field scanning optical microscopy approaches[134]. The progress in nanofabrication in recent years[357, 358, 359] has made nano-optical techniques more widely available and has lead to a better control of the properties of nanostructures.

From the perspective of attosecond physics, nano-optics is especially interesting since it allows to the combine the natural timescale of electron motion (∼1 as-1 fs) with its' natural length scale (∼1 nm). [360]. The demonstration that strong-field photoemission from nanotips[45, 361] and nanospheres can be controlled by the electric field of the driving laser[362, 87] and that the electron dynamics may be strongly modified by the near-field decay[88, 363] has led to the development of attosecond nanophysics as an independent research field[20, 360, 364]. Nanotips illuminated by few-cycle lasers have been used as sources of ultrashort electron pulses for electron microscopy[365, 366, 367] or for the spatially-resolved detection of the CEP of a laser beam[368]. With the advent of solid-state HHG in attosecond physics[369, 370, 371, 372], nano-optics has been used for the enhancement of HHG through nanoplasmonic[373, 374] or all-dielectric[375] nanostructures. Moreover, the focusing of HHG and simultaneous generation of OAM via Fresnel zone plates could be shown[376, 377]. Significant progress has been made in the direction of lightwave electronics[21, 378, 22], i.e. electronics driven by optical fields on the PHz-scale. Based on plasmonic nano-bowtie antennas, the CEP-detection using currents[19, 379, 380] and recently a potential PHz-scale diode[381] have been demonstrated. However, for the further development and optimization of devices and for achieving ultimate control, the development of techniques that can resolve the near-fields on an attosecond temporal and a nanometer spatial scale is crucial.

Several theoretical studies have proposed attosecond streaking[12, 13] for the measurement of nanoscale near fields[382, 383, 384, 385, 386, 387, 388, 389] and some studies noted that for short near-field decay lengths the streaking spectrogram does not sample the vector potential[382, 384, 386]. Within our group the first proof-of-concept experiment using attosecond streaking from a nanotip[24, 25, 26, 27] could be demonstrated, which constitutes an improvement in time resolution by almost three orders of magnitude compared to previous THz experiments[390]. This work is presented in the first section of this chapter (Sec. 7.2). It is shown that attosecond streaking allows the near-field retrieval. The streaking adiabaticity parameter δ is introduced that enables a rigorous classification and description of the near-field streaking regimes and their implication for the field reconstruction. Finally, it is demonstrated that through comparison with reference measurements in gas as well as trajectory simulations, the spectral response function of the nanotaper can be reconstructed.

Despite the success of this experimental demonstration, one major limitation remained: Due to the small XUV photon/photoelectron flux available, the field reconstruction was limited to the shank of the nanotaper and the contribution from the enhanced field at the nanotip apex, which is used in nanoplasmonic applications, could not be resolved. The reason is that XUV photoemission occurs as a linear process. Therefore, even for relatively tightly focused beams, the vast majority of the XUV photoelectrons originate from the nanotaper side which constitutes a much larger illuminated area compared to the apex. Consequently, a method that makes use of the strong-field photoemitted electrons, practically exclusively initiated from the enhanced apex near-field, would allow to overcome this limitation.

Recently a number of alternative attosecond field-resolved measurement techniques

have been developed[34, 35, 36, 32, 168, 33]. Instead of relying on isolated XUV pulses as in attosecond streaking[12, 13], they are based on the realization that the perturbation of a strong-field-driven process by a weak laser pulse shows a linear dependence on the perturbing field. Therefore, the delay-dependent observation of the perturbation allows the reconstruction of the weak field given that the field-driven process can be modeled. One of the first demonstrations is the PHz-oscilloscope[34]. There, a weak perturbing field is focused under a slight angle with respect to a strong laser pulse into an HHG gas target in the attosecond lighthouse scheme[131]. The weak pulse affects the transverse macroscopic phase-matching, leading to a delay-dependent change of the HHG burst emission angle. Other methods make use of the change of the cutoff energy in HHG[35] or of the cutoff energy of rescattering electrons in strong-field photoemission spectra[33]. A particularly intuitive approach is tunneling ionization with a perturbation for the time-domain observation of an electric field (TIPTOE) [32, 168], where, as the name suggests, the change of the tunneling ionization rate is directly proportional to the weak perturbing field. Both, TIPTOE and the streaking of rescattering electrons rely on strong-field emitted photoelectrons and can in principle be used to reconstruct the near-fields at the nanotip apex.

The attosecond field-resolved measurement of the apex near-field on an individual nanotip using the TIPTOE-technique is described in the second part of this chapter, which we refer to as nanoTIPTOE. During our experiments, we have been made aware of related work on nanostructure arrays in the group around Keathley, Berger and Kärtner that has been published[165] during the writing of this thesis. There, the measurement of the near-field of an array of on-chip nano-bowtie structures has been demonstrated and the TIPTOE response function and its CEP-dependence is discussed. Besides differences in the experimental approach, our work goes beyond this study in several regards. First, using the photocurrent in combination with energy-resolved photoelectron spectra, we identify the onset of charge interaction effects in the dynamics of the emitted electrons. Secondly, we demonstrate that the method measures the spectral phase by changing the dispersion of the signal pulse. Moreover, the CEP-dependence of the response function is measured. Furthermore, we study the intensity dependence of both pump and signal pulses. We propose an extension of the current approach for a complete characterization of the nanoTIPTOE response function. Finally, making use of the nanotip as a single nanoscale emitter, we demonstrate the application of the nanoTIPTOE concept to the spatio-temporal-resolved measurement of the focus of a beam with orbital angular momentum (OAM) with a potentially sub-wavelength spatial resolution.

The presented results constitute a major progress both in the experimental demonstration and understanding of attosecond nanoscale near-field measurements, which will boost the further development of these techniques as well as their application in the further development of PHz electronics and nanophotonics.

7.2 Attosecond streaking from a metal nanotip

The following section is structured as follows: First, the experimental setup and approach is described. Subsequently, the numerical modeling is discussed as well as the different near-field streaking regimes and their consequence on the field reconstruction. Then, the experimental results are presented and compared with simulations. Moreover, the reconstruction of the response function of the near field at the nanotaper is demonstrated. Finally, limitations of the approach are discussed and a conclusion and outlook is given. This work has been presented in several publications[24, 25, 26, 27]. The chapter will closely follow Ref. [26] and will focus more on the description of the near-field streaking regimes and the response function reconstruction.

The experiments and the experimental data analysis was performed together with Benjamin Förg (B.F.) and Frederik Süßmann (F.S.). The gold nanotips were produced by Michael Krüger and Michael Förster of the group of Prof. Hommelhoff. The numerical model was developed with initial help from F.S. and expanded and implemented by the author, which was crucial for the understanding of the experimental measurements. The author developed the interpretation of the results in terms of response functions and the categorization of the streaking regimes with the streaking adiabaticity parameter. Finally, the author conducted the numerical simulations and analyzed the results. All experimental and theoretical results were discussed with all authors of Ref. [25].

7.2.1 Experimental setup and approach

For a detailed description of the laser, experimental setup and approach, we refer to Refs. [52, 25, 27]. In short, a Ti:Sa chirped pulse amplifier (CPA) delivers 26 fs pulses with 1.4 mJ pulse energy at either 500 Hz or 1 kHz. The pulses are broadened in a hollow-core fiber from 500 nm up to 1000 nm and subsequently compressed using a set of chirped mirrors (UFI PC70) resulting in pulses with a duration of 4-4.5 fs (FWHM) at a central wavelength of about 720 nm. The experiments were conducted at the AS5-beamline at the Max-Planck-Institute of Quantum Optics, consisting of an HHG chamber where an isolated attosecond pulse is generated, a differential pumping stage, the XUV spectrometer section and the experimental chamber (see Ref. [27] for details).

The experimental scheme is shown in Fig. 7.1 a). An isolated XUV attosecond pulse (blue waveform) at a central photon energy of 95 eV with a bandwidth of 7 eV and pulse duration of 220 as (as reconstructed by a FROG-CRAB-algorithm[143]) and the driving laser pulse (red waveform) are focused at the entrance of a time-of-flight spectrometer (TOF, Stefan Kaesdorf ETF11). A variable time-delay Δt is introduced using a double mirror with a focal length of 12.5 cm. The inner part consists of a custom XUV-multilayer mirror whose reflectivity defines the XUV photon range given above. It can be translated via a closed-loop piezo stage with nanometer precision. The kinetic energy spectrum of the emitted photoelectrons is recorded via the TOF using a time-to-digital converter (FASTComTec P7889). An attosecond streaking spectrogram is constructed from the delay-dependent electron spectra, with which information about the near-fields on the

gold nanotaper can be obtained. The nanotip is positioned in the laser focus using the combination of strong-field and XUV photoemitted electrons as described in Ref. [25]. The gold nanotip is produced via wet chemical etching[137, 51]. The nanotip can be replaced by a neon gas nozzle, allowing the reconstruction of the incident laser pulse as well as the isolated attosecond pulse.

7.2.2 Theoretical approach

Near field description

A proper interpretation of the experimental results requires some prior theoretical considerations, since the interaction of the nanostructure with the optical laser pulse leads to near fields that vary on a nanometer spatial scale. Therefore, the usual assumption of a homogeneous laser field is not valid anymore and the relation between the kinetic energy shift and the local near field can become intricate. Instead, both the near field around the nanotaper, which is the quantity that we aspire to measure, as well as the propagation of the electron in inhomogeneous near fields have to be understood.

The electromagnetic fields around the nanotaper are calculated in the framework of the macroscopic Maxwell's equations using a commercial finite-difference time-domain solver (FDTD, Lumerical FDTD) assuming an incident Gaussian laser pulse of 4.5 fs FWHM at a central wavelength of 720 nm. The nanotip is modeled as a spherical apex with 100 nm radius and either a cylindrical shank or a tapered shank with 10° full opening angle. The conclusions regarding the near fields are not dependent on which geometry is chosen, however the latter corresponds slightly closer to the real situation. The refractive index of gold is taken from Ref. [391].

The calculated maximum electric field strength along the nanotip axis (y-axis) normalized by the incident field is shown in Fig. 7.1 b) together with the outline of the nanotip (white line). The nanotip is illuminated from the left. As can be seen, the field at the apex is enhanced by almost a factor of 3. The maximum occurs slightly behind the apex which is caused by a field propagation effect due to the relatively large apex size. In contrast, the field on the side of the nanotip is reduced in magnitude to about 0.6. Intuitively, this finding can be understood by considering the shank as an extremely deformed mirror. The reflected field destructively interferes partially with the incident field at the surface. The field normal to the surface at the apex is strongly suppressed inside the nanotip when crossing the surface while the parallel field component at the nanotaper side is continuous. This is a consequence of the Maxwell boundary conditions and the implications for attosecond streaking are further discussed below.

In order to obtain a description of the near-fields as a property of the nanostructure that is independent of the incident laser pulse shape, in the spectral domain, the near-field $E_{\mathrm{nf}}(r,\omega)$ can be described in terms of the complex linear response function $H(r,\omega)$ and the incident field $E_0(\omega)$:

$$E_{\mathrm{nf}}(r,\omega) = H(r,\omega) \cdot E_0(\omega). \tag{7.1}$$

Due to the three possible electric-field polarization directions, the response function is gen-

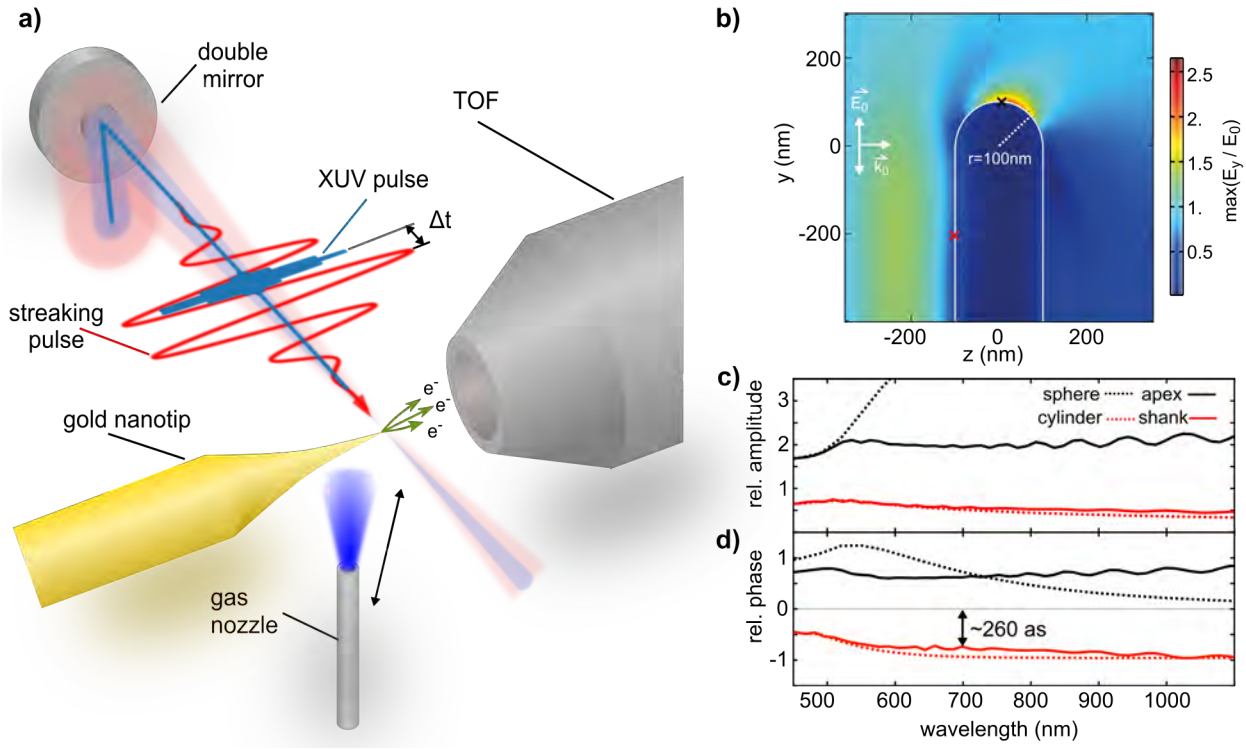

Figure 7.1: Experimental setup and approach: a) experimental setup including the double mirror, tapered nanotip and TOF. The nanotaper can be replaced by a gas nozzle for reference measurements. b) FDTD simulation of the field enhancement on a nanotaper illuminated from the left. c) and d) Amplitude and phase of the response at the apex (black solid line) and shank (red solid line) of the nanotip (black and red cross in b, respectively) and comparison to the Mie solution for a sphere (black dotted line) and an infinite cylinder (red dotted line). b)-d) are adapted from Ref. [26].

erally a 3×3-tensor. In the above expression, we consider a fixed incident beam geometry where the incident field is fully characterized by the value in the focus $E_0(\omega)$. Otherwise, for arbitrary input beam geometries a dyadic Green's function approach would be necessary[134]. In our calculations, we calculate the response with an x-position dependent time-shift, as would be seen by the co-propagating XUV pulse. For linearly polarized incident pulses and if only one near-field direction is considered, $H(r, \omega)$ is a position dependent complex scalar function. The response is characterized by the absolute value, corresponding to the field enhancement, and the relative phase. Once the response function is known, the resulting near-field can be calculated for any input pulse shape. At the end of this section, we will show the experimental reconstruction of the linear response for the nanotaper based on our streaking measurements.

The amplitude and phase of the calculated response function at the two positions indicated in Fig. 7.1 b) at the apex (black cross) and the frontside of the nanotip shank (red cross) are shown in c) and d) as black and red solid lines, respectively. The enhancement at the apex does not show a resonance but is quite constant down to about 500 nm, where interband transitions start to play a role. Small oscillations occur due to the excitation of a surface plasmon traveling away from the apex. The same statement holds for the field at the shank. In addition, a relative phase-shift of both fields with respect to the incident field can be seen in d). At the apex, the phase is shifted by almost +1 rad (corresponding to later times), whereas at the shank the shift is almost -1 rad (earlier times). For comparison the analytic Mie-theory[392, 393] solutions for a sphere (black dashed line) and an infinite cylinder (red dashed line) with radius 100 nm calculated by the MatScat-package[394, 395] are also depicted. While there is some difference between the sphere and apex fields, a close correspondence between the field of an infinite cylinder and the nanotip shank is established.

In our measurement, it is those two features of the response function, the relative field strength and phase compared to the incident field, that we want to resolve. Unfortunately, due to the velocity with which the photoelectrons emitted by the XUV radiation ($v(100eV) \simeq 6$nm/fs) leave the surface, the electrons might experience the inhomogeneity (i.e. the change) of the near-field during the laser pulse, rendering the assumptions for Eq. 3.3 invalid. Therefore, relating the streaking trace to the local vector potential at the emission position might not be possible. An identification of the different streaking regimes and their effect on the field reconstruction is given in the following subsection together with a brief description of the numerical simulations. This will be crucial for the interpretation of the experimental results presented afterwards.

Classification of near-field streaking regimes

The classification of the near-field streaking regimes requires a general description of the electric fields and the streaking process therein and is partially based on primary considerations in Ref. [52]. The treatment presented in the following will require some equations, which involve, however, mostly only simple math and Fourier transformations. The total field E_{tot} around a nanostructure can be separated into the incident field E_{inc} and scat-

tered field E_{scatt}. We will restrict our discussion to the emission direction of the electron x, apply the dipole approximation for the incident field, i.e. $E_{\mathrm{inc}}(x) = E_{\mathrm{inc}}$ and assume an exponential decay of the scattered field with the near-field decay length l_{f}:

$$E_{\mathrm{tot}}(x,t) = E_{\mathrm{incident}}(t) + E_{\mathrm{scattered}}(t) \cdot \exp(-x/l_{\mathrm{f}}), \tag{7.2}$$

as illustrated in Fig. 7.2 a). In attosecond streaking, the kinetic energy of the electron is only slightly changed by the streaking field. Therefore, the classical equation of motion can be Taylor-expanded in terms of the streaking field with the perturbation ϵ:

$$v(t) = v_0 + \epsilon \cdot v_1(t) + \mathcal{O}(\epsilon^2) \tag{7.3}$$

$$x(t) = v_0 \cdot (t - t_0) + \epsilon \cdot \int_{t_0}^{t} v_1(t)\mathrm{d}t + \mathcal{O}(\epsilon^2), \tag{7.4}$$

where t_0 is the emission time and the surface is assumed to be at $x = 0$. To first order, the change in velocity $v_1 = \Delta v$ can now be described by inserting the zeroth order solution for x into Newton's equation of motion:

$$\frac{\mathrm{d}v_1}{\mathrm{d}t} = -\frac{e}{m}\Big[E_{\mathrm{inc}}(t) + E_{\mathrm{scatt}}(t) \cdot \exp\Big(-v_0(t - t_0)/l_f\Big)\Big], \tag{7.5}$$

which is equivalent to neglecting the change of the velocity in the description of the position of the photoelectron in the equation of motion. Using the spectral representation of the field, i.e. $E(t) = \int \mathrm{d}\omega E(\omega) \exp(-i\omega t)$ in the above equation, the velocity change Δv for an electron emitted at t_0 yields:

$$\Delta v(t_0) = +\frac{e}{m}\int_{-\infty}^{\infty} \mathrm{d}\omega \exp(-i\omega t_0)\Big[\frac{E_{\mathrm{inc}}(\omega)}{-i\omega} + \frac{E_{\mathrm{scatt}}}{-i\omega - v_0/l_{\mathrm{f}}}\Big], \tag{7.6}$$

where the integral expression, in analogy to the homogeneous case, can be interpreted as an effective vector potential A_{eff}. Consequently, the Fourier transform of Δv with respect to the delay t_0, multiplied by $\frac{m\omega}{e}$, corresponds to the spectral representation of the effective electric field $E_{\mathrm{eff}}(\omega)$ measured by attosecond near-field streaking:

$$\begin{aligned} E_{\mathrm{eff}}(\omega) &= \frac{E_{\mathrm{inc}}(\omega) + E_{\mathrm{scatt}}(\omega)}{1 - i\frac{v_0}{l_f \cdot \omega}} + \frac{E_{\mathrm{inc}}(\omega)}{1 + i\frac{l_f \cdot \omega}{v_0}} \\ &= \frac{E_{\mathrm{surf}}(\omega)}{1 - i\frac{1}{2\pi\delta(\omega)}} + \frac{E_{\mathrm{inc}}(\omega)}{1 + i2\pi\delta(\omega)}, \end{aligned} \tag{7.7}$$

where we have used the field at the surface $E_{\mathrm{surf}} = E_{\mathrm{inc}} + E_{\mathrm{scatt}}(x = 0)$ and introduced the near-field streaking adiabaticity parameter δ:

$$\delta(\omega) = \frac{l_f}{v_0 \cdot T_0} = \frac{T_{\mathrm{esc}}}{T_0} = \frac{l_{\mathrm{f}}}{l_0} \tag{7.8}$$

$T_0 = 2\pi/\omega$ is the oscillation period, T_{esc} is the escape time from the near field defined as $T_{\mathrm{esc}} = l_{\mathrm{f}}/v_0$, and $l_0 = v_0 \cdot T_0$ is the distance that the electron covers during an oscillation

period. The relation to the strong-field adiabaticity parameter[88], that can directly be deduced from the classical equation of motion, is discussed in Ref. [26]. Different values of the adiabaticity parameter in terms of the distance that an electron travels within an optical cycle, are illustrated in Fig. 7.2. The adiabaticity parameter can be interpreted as the ratio of either the two timescales or the two length scales of the dynamics. As can be seen in Eq. 7.7, for large escape times, i.e. large δ, the effective field corresponds to the near field as expected.

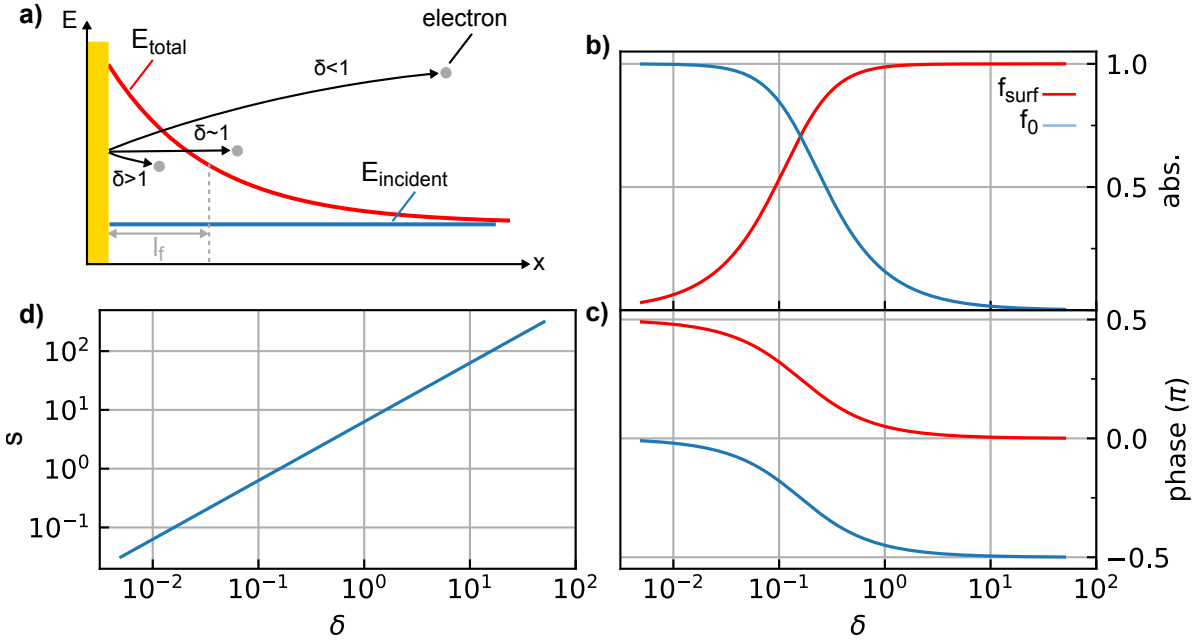

Figure 7.2: Near-field attosecond streaking response function: a) illustration of the geometry and near-field decay model. b) and c) amplitude and phase of the response function of the surface field (red line) and the incident field (blue line), respectively, in dependence on the adiabaticity parameter δ. d) Relative surface field sensitivity s (details in the text).

For decreasing values of δ the interpretation becomes more complicated. For convenience and in order to simplify the discussion, we define the effective response function of the surface field f_{surf} and of the incident field f_{inc}, determining their respective weight and relative phase (see Eq. 7.7) in the effective field:

$$f_{\mathrm{surf}}(\delta) = (1 - i \cdot \frac{1}{2\pi \cdot \delta})^{-1} \tag{7.9}$$

$$f_{\mathrm{inc}}(\delta) = (1 + i \cdot 2\pi \cdot \delta)^{-1}. \tag{7.10}$$

The absolute value and phase of both f_{surf} (red line) and f_{inc} (blue line) are shown in Fig. 7.2 b) and c), respectively. Three different regimes can be identified:

- **ponderomotive regime ($\delta > 1$):** The escape time of the electron from the near field is much larger than the period of the field. The measured effective field reconstructed from the streaking trace is determined in amplitude and phase by the surface field.

- **intermediate regime** ($0.05 < \delta < 5$)**:** The electron starts to experience the inhomogeneity during one cycle and experiences a mixture of the surface field and the incident field. The phase of f_{surf} start to shift from 0 towards π, while a shift from $-\pi$ to 0 occurs for f_{inc}.

- **field-probing regime** ($\delta < 0.05$)**:** The electron leaves the near field almost instantaneously in a fraction of a cycle and sees a quasi-static near field. The naming has been introduced in Ref. [382]. As the phase of the surface field function is π out of phase with E_{eff}, the shift in the measured streaking trace due to the near field is directly proportional to the surface electric field and not the surface vector potential.

The simple interpretation of the field-probing regime is, however, only true, if the incident field is neglected. This is problematic, since, as can be seen in Fig. 7.2 b), the amplitude of f_{surf} goes to zero in the field probing regime, in contrast to $|f_{\mathrm{inc}}|$ which is close to unity. We therefore define the real-valued surface sensitivity $s(\delta)$ as:

$$s(\delta) = \frac{|f_{\mathrm{surf}}|}{|f_{\mathrm{inc}}|}. \tag{7.11}$$

The surface sensitivity is plotted in Fig. 7.2 d). Indeed, in the field probing regime, $s(\delta) < 10^{-1}$. For the simple interpretation to be valid, in which the incident streaking field can be neglected, the field enhancement needs to be significantly higher than $1/s$.

We want to point out that the shift of the phase of the surface response function can also be interpreted as a streaking delay τ_{inh} caused by the near-field inhomogeneity[314]. The model presented here is capable of predicting τ_{inh} once the near-fields are known without having to rely on numerical simulations.

Trajectory simulations

To gain an even better understanding of our experimental results, we perform trajectory simulations of the XUV-emitted photoelectrons in the near field of the nanotaper. The near fields are calculated with FDTD simulations using the experimental laser pulse parameters: 4.5 fs pulse duration, 15 μm focal spotsize and $10^{12}\,\mathrm{W/cm^2}$ intensity. For an adequate description of the fields at the surface, a fine resolution of the rectangular simulation mesh is necessary around the nanotip, which results in file sizes of several 10 GB. The field files are transformed to the portable HDF5-format and read in by an object-oriented trajectory simulation C++-code. The field class linearly interpolates the fields from the closest meshgrid points in space and in time. The nanostructures are modeled based on an analytical description of geometries with compact volume and a combination thereof. This allows to determine whether a point is within the volume and to efficiently calculate the intersection points with the surface for a given point and a vector including the surface normal which is important for treating the electron propagation.

The isolated attosecond pulse is described as a Gaussian beam with an FWHM of 5 μm and a Gaussian pulse with 220 as FWHM at 95 eV central photon energy (and 7 eV

bandwidth). From the experimental reconstruction, negligible chirp is obtained, which allows a simplified spectro-temporal description of the linear XUV photoemission process: The emission time and the kinetic energy of the photoelectron are randomly generated independently from the Gaussian intensity envelope in time and in photon energy (minus the work function of gold). The emission points on the surface are obtained by projecting a randomly generated point in the XUV beam profile onto the surface of the nanostructure. The emission is assumed to be isotropic. Electrons re-entering the surface are ignored and only electrons within the detection angle (full cone angle 45°) are considered. The electrons are propagated independently using the Velocity-Verlet algorithm[216].

For the simulation of attosecond streaking spectrograms 10^6 electrons were propagated. Although not shown here, simulated streaking spectrograms where extremely valuable for understanding the experiments. In order to assess the contribution of a single point on the nanotaper surface, streaking traces are calculated where electron propagation is started at each delay with a fixed kinetic energy of 89 eV and an emission angle of 15°. For the response function, the mean and standard deviation of the local response function of 10^4 points on the surface weighted by the XUV beam profile are calculated.

The tapered nanowire is modeled as a cone with an opening angle of 10° and a hemisphere of 50 nm radius for the response function calculation. Extremely fine meshing is necessary to avoid numerical hotspots in the nanocone geometry which impedes electron trajectory calculations. For the streaking trace simulations, the nanotip is modeled as a cylinder with a hemisphere at the end. The conclusions of this section, as mentioned above, are not affected by the choice of either geometry.

7.2.3 Experimental results

The experimentally measured attosecond streaking spectrograms from the gold nanotaper and the gas target are shown in Fig. 7.3 a) and b), respectively. The countrates from the nanotaper are more than an order of magnitude smaller than from the gastarget. Therefore, for reasonable statistics, overall acquisition times of up to a few hours are required. In order to exclude the influence of phase drifts and instabilities, several nanotaper streaking spectrograms are recorded with a gastarget streaking measurement before and after. If stable conditions are observed, the nanotaper streaking spectrograms are superimposed. Overall, several sets of attosecond streaking spectrograms are recorded on different days and for different nanotips.

The photoelectron spectrum from the nanotaper is significantly broadened compared to the gas target due to the extended density of states as well as inelastic scattering of the photoelectrons within the medium. Moreover, there is a potential contribution of adsorption and passivation layers on the surface that have a higher work function[51, 27] and contribute to the lower energy region. We assign the high-energy edge of the photoelectron spectrum to electrons from gold dominated by the Au-4d band due to the density of states. The photoemitted electrons have to overcome the work function of gold ($\phi \approx 5.4\,eV$)[396] which largely explains the energy of the cutoff of approximately 89 eV. The central energy of the neon streaking trace is shifted to around 74 eV due to the higher

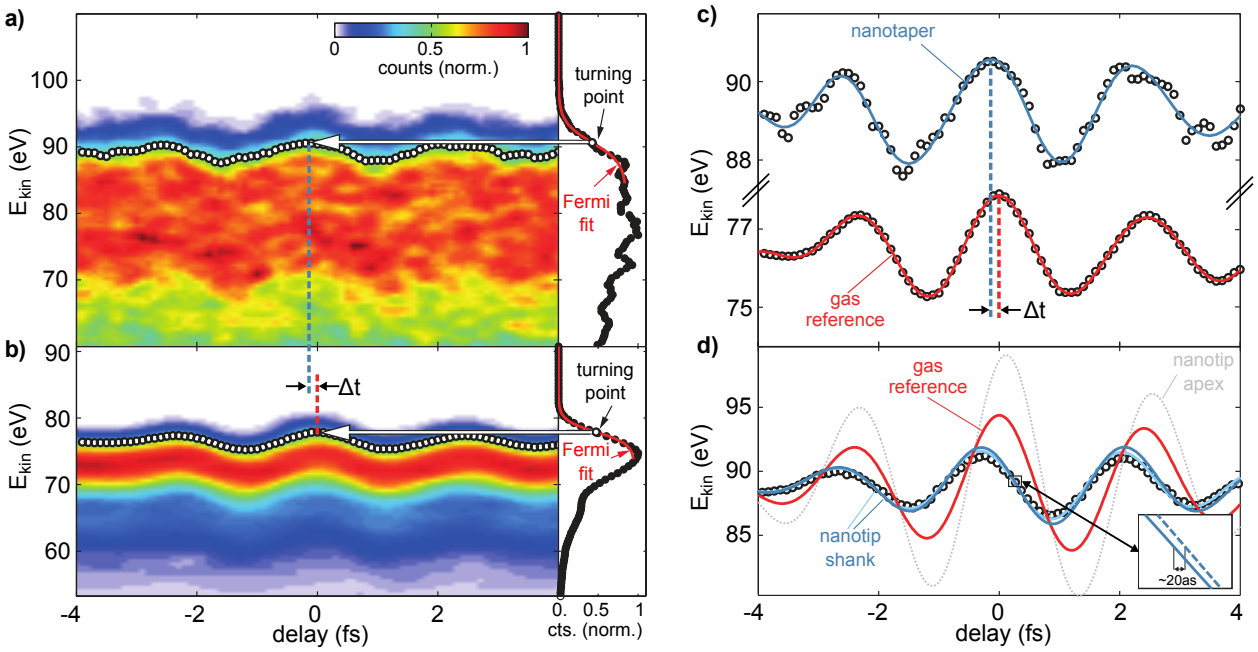

Figure 7.3: Experimental results and comparison to simulations: a) and b) streaking spectrogram from the nanotip and the neon gas reference, respectively. The right panels show the extraction of the streaking trace (black dots) from a Fermi-fit to the high-energy cutoff of the electron kinetic energy spectrum. A delay between the two streaking curves is evident. c) Fourier-filtered streaking traces and delay. d) The streaking curve retrieved via the same approach from a Monte Carlo simulation (symbols) and the calculated streaking curve for electrons emitted from the front of the nanowire at y=-200 nm (dark blue line) and y=-3,000 nm (light blue line), respectively. The latter two curves practically coincide. The simulated reference streaking trace in neon gas (red line) has been upshifted in energy to aid comparison. The inset shows the relation between the simulated streaking curve (dark blue solid line) and the local vector potential of the near-field (dark blue dashed line) at the emission point. The figure has been adapted from Ref. [25].

ionization potential of neon ($I_p = 21.56\,eV$)[397].

Clear streaking oscillations can be observed for both nanotip and gas measurements. The streaking amplitude was set deliberately low, in order to avoid damage of the nanotip. The traditional FROG-CRAB approach[143, 146] can not be applied for the extraction of the streaking pulse for photoelectron spectra with a large incoherent background, as is the case for scattering contribution in the nanotip streaking spectrograms discussed above (see Ref. [156] for a density matrix description). Therefore, as illustrated in the panels right of Fig, 7.3 a) and b), we devised a different approach which consists of fitting a Fermi-function (red line) to the positive cutoff of the spectrum (black line) for each delay. The turning points of the Fermi-function are then used to define the raw streaking curve (open dots in the main panels). For the gas streaking spectrogram, this approach is tested against a FROG-CRAB algorithm[143, 146] as well as against fitting the photoelectron peak with a Gaussian function and excellent agreement is observed[25].

The extracted raw streaking curves are Fourier-filtered by excluding the wavelength components outside the laser spectrum below 400 nm to eliminate noise in the nanotaper data caused by the limited statistics. As can be seen in Fig. 7.4 c), clear temporal shift $\Delta t = 200 \pm 50$ as to smaller delays is observed for the nanotaper curve (blue line) compared to the gas reference (red line).

7.2.4 Discussion

For a better understanding of the experimental results, trajectory simulations in the near-field of the nanotaper were performed as shown in Fig. 7.3 d). The streaking curve retrieved from a Monte-Carlo simulation of the streaking spectrogram from the nanotaper and subsequent application of the same reconstruction algorithm as for the experiment is represented by open dots. In addition, streaking curve calculations for the gas reference in the focus of the incident beam (red line) and for single emission points on the shank of the nanotip, 200 nm (dark blue line) and 3000 nm (light blue line) below the apex, as well as from the apex (gray dashed line) are shown. There are two immediate findings further discussed below. Firstly, the streaking curves from the nanotip shank agree very well with the Monte-Carlo simulation, while a potential contribution of the apex with significantly higher streaking amplitude and a temporal delay compared to the gas reference is not visible neither in the simulated nor experimental streaking spectrogram (see Fig 7.3 a)). Secondly, good agreement of the simulated average temporal shift of around 260 as between gas reference and Monte-Carlo nanotip streaking curve with the experimental result of 200 ± 50 as (see Fig. 7.3 c)) is observed.

The first finding implies that the streaking spectrograms are dominated by electrons originating from the side of the nanotaper, while the apex contribution is negligible. An estimate of the relative weight of both contributions in the experiment can be obtained by a simple consideration based on the geometrical cross section as seen by the incident XUV beam and on the linearity of the XUV photoemission process, while neglecting further details of the latter. The number of detected XUV-emitted photoelectrons from a certain

region on the nanotip n_{region} with an effective cross-sectional area A_{region} is given by:

$$n_{\mathrm{region}} \propto \frac{n_{\mathrm{XUV}}}{\omega_{0,\mathrm{XUV}}^2} \cdot A_{\mathrm{region}} \cdot f_{\mathrm{rep}} \cdot T_{\mathrm{acq}}, \tag{7.12}$$

where n_{XUV} is the number of XUV-photoelectrons per shot, $\omega_{0,\mathrm{XUV}}$ is the waist radius of the XUV beam, f_{rep} is the repetition rate of the laser and T_{acq} is the total acquisition time. The maximum (illuminated) effective area is limited by the XUV spotsize. The illuminated area on the nanotaper shank A_{shank} can be estimated by the product of the average diameter of the nanocone ($\sim$150-300 nm) and the FWHM of the XUV beam ($\sim 5\,\mu$m). In contrast, the region of the enhanced field on the apex A_{enh} is limited to a fraction of the hemisphere area ($\sim \pi[50 - 100\,\mathrm{nm}]^2$). This estimate suggests that around a factor of 250-2000 more electrons originating from the shank are detected compared to the enhanced apex region. Given that our streaking spectrograms typically consist of only a few hundred electrons per delay and even less close to the cutoff, resulting in less than an electron on average from the apex per delay, we can not expect to see this contribution in our measurements. Nevertheless, the contribution from the near field of the shank of the nanotaper is clearly resolved.

The observed correspondence of the experimentally measured and simulated temporal shifts and the agreement with the expected shift of the calculated nanotaper electric near-field response function at the shank of 260 as (see Fig. 7.4 d)), already suggest that the near field on the nanotaper can be extracted from streaking measurements. However, before being able to draw this conclusion, several consideration regarding the intrinsic streaking delays of neon and the gold surface as well as the near-field streaking regime and have to be made.

The intrinsic delays of the photoemission process measured by attosecond streaking that lead to a shift of the streaking curve with respect to the vector potential, could in principle influence our measurements (see Sec. 3.3.1). Theoretical studies for neon suggest an absolute time delay below 10 as at 95 eV photon energy[153, 154]. A large number of experimental studies exist for attosecond streaking from surfaces[15, 158, 398, 82, 161, 157]. While attosecond streaking measures only relative time-delays, the absolute photoemission delays from surfaces has been demonstrated[157] by comparing the bulk emission to an adsorbate, and then subsequently the adsorbate to helium, which can be calculated exactly without approximations. The surface streaking experiments are performed at grazing incidence of the laser onto the bulk surface. There, it could be shown that the laser field is screened within one or two atomic layers[398] and that the delay is caused by the time it takes the electrons to travel from the bulk to the field[158, 398, 82]. At our photon energies, for valence band photoemission, absolute delays below a few tens of attoseconds are expected[157]. At the nanotaper shank the incident laser polarization is parallel to the surface and therefore the field is continuous through the surface, as observed in the near-field calculations above. In the above interpretation, this finding implies that an even lower streaking delay is expected[26, 399]. Overall, we can conclude that the photoemission streaking delays are negligible compared to the measured streaking curve time shifts in our experiment and we treat the photoemission process as instantaneous.

For an estimation of the near-field streaking regime, several parameters are needed (see Sec. 7.2.2). The kinetic energy (∼90 eV) of the XUV-emitted photoelectrons leads to an escape velocity of approximately 5.5 nm/fs. A near-field decay length of around 50-100 nm is obtained from the electromagnetic near-field calculations in agreement with the expectations from the length scale of the nanotip geometry. The oscillation period at the central laser wavelength is around 2.4 fs. Taking into account, that the comparatively small emission angle relative to the surface (<22.5°) for the detected electrons from the shank leads to a reduction of the effective escape velocity, an estimate for the streaking adiabaticity parameter $\delta \approx 10 - 30$ is obtained. This is clearly in the ponderomotive regime. Indeed, as the inset in Fig 7.3 d) shows, a shift of only around 20 as between the streaking curve (solid line) compared to the local vector potential (dashed line) is obtained, which is negligible for our purpose. This finding implies that the nanotip streaking curve represents the local vector potential from which the near field on the nanotaper can easily be extracted.

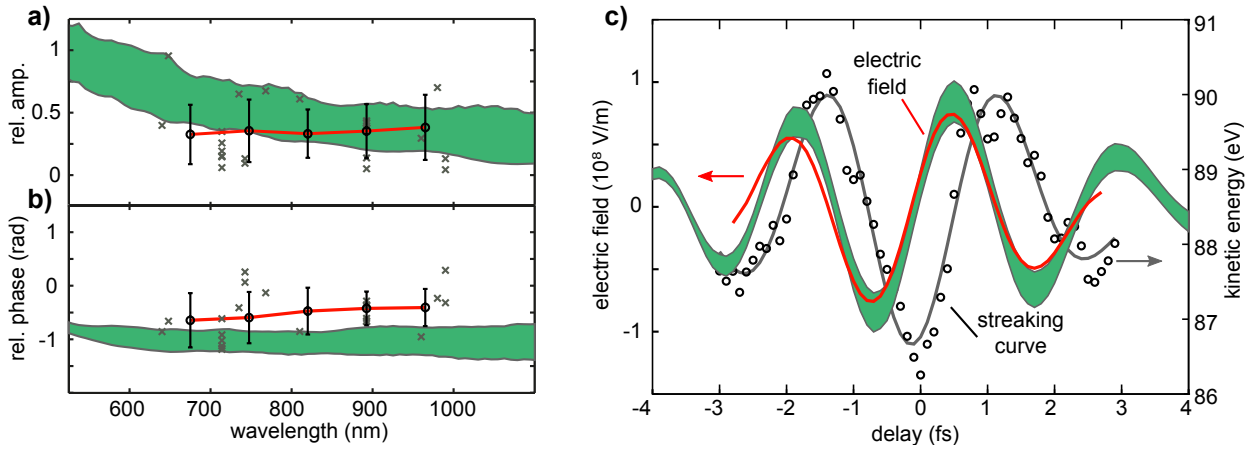

Figure 7.4: Experimental reconstruction of the nanotaper response function: a) and b) experimentally retrieved amplitude and phase of the response function of the shank of the nanotaper. The individual measurements (black crosses) extracted by Fourier analysis with their average and standard deviation (red lines and errorbars). The prediction of the Monte-Carlo simulation is shown as green area indicating the standard deviation around the mean value. c) Comparison of the reconstructed electric field (red line) from the retrieved streaking trace (symbols and gray line) with the expectation, calculated from the Monte-Carlo response function (green area). The figure has been adapted from Ref. [26].

By comparing Fig, 7.3 c) and d), it can be seen that the gas streaking amplitude in the simulation is significantly higher than for the nanotip, in contrast to what is observed in experiment. This apparent discrepancy can be resolved by considering that for the gas streaking, the laser intensity is averaged all over the focal volume, whereas the nanotaper alignment procedure makes sure that the nanotip is placed in the highest intensity. A similiar underestimation of the laser peak intensity from the gas streaking amplitude has

been observed in previous experiments, where additionally ATI has been measured[400]. In order to obtain correction factors, we compare the expected intensities from the gas streaking amplitude to the expected intensities from the observed cutoff energies of the ATI from the nanotip apex in the nanotip streaking measurements, for every set of measurements. Similar to Ref. [400] field amplitude correction factors of around 3 are obtained.

Finally, we can now calculate the incident electric field of the incident laser pulse and the near field on the nanotaper shank from the gas and nanotip streaking measurements, respectively. Moreover, via inversion of Eq. 7.1 the response function of the near field at the nanotaper can be calculated by Fourier-transforming the reconstructed electric fields. The phase and amplitude of the reconstructed response function are shown in Fig. 7.4 a) and b), respectively. Datapoints from different measurement sets (gray crosses) are averaged in order to obtain the mean response function (red lines, black dots) and the standard deviation (errorbars). The simulated average response function and standard deviation (green shaded areas) are also shown. The simulated relative phase slightly overestimates the measured phase-shift. Good agreement is observed between the reconstructed and expected relative amplitude of the response function.

The response function allows to calculate the near field on the nanotaper shank for any incident pulse. This is demonstrated in Fig. 7.4 c) where the expected electric field on the nanotaper calculated from the measured gas reference streaking electric field and the simulated response function (green shaded area) is compared to the experimentally reconstructed electric field (red line) from the measured streaking curve (open dots and gray line).

7.2.5 Conclusion and Outlook

In conclusion, we have demonstrated the first successful experimental streaking measurement of nanoscale near fields using a gold nanotip. A simple theoretical model has been developed that allows the classification of different near-field streaking regimes. Furthermore, the model provides a description of the relation between the near fields and experimentally measured streaking curves. Using numerical simulations, the experimental streaking curves are shown to originate from the side of the nanotaper. Finally, the successful demonstration of the experimental retrieval of the near-field reponse function is demonstrated. Our results constitute a milestone in the experimental realization of and a major step in the theoretical understanding of attosecond streaking spectroscopy of nanoscale near fields, which will be of considerable importance for the further development of this and related techniques.

In our experiments, the limited photoelectron countrate obstructed the observation of the enhanced near fields at the apex. Different knobs to increase the electron flux are given in Eq. 7.12. The most promising approach is likely the increase of the XUV photon flux by going to lower photon energies and different generating gases. Indeed, attosecond streaking from isolated dielectric nanospheres (50 nm diameter) at XUV photon energies below 40 eV using HHG in xenon has been demonstrated[313, 314]. Under the same experimental conditions also the near fields at the nanotip apex should be resolvable.

However, experiments demonstrating the measurement of enhanced plasmonic near fields have not been done so far. Moreover, while the nanosphere experiments were conducted in the transition region from the intermediate to the ponderomotive streaking regime[314], an experimental investigation of the different streaking regimes is still missing.

Spatial resolution, e.g. for device characterization, could be achieved by combining the attosecond near-field streaking concept demonstrated here with scanning approaches or photoemission electron microscopy (atto-PEEM)[382]. The latter approach is fueled by the development of high-repetition rate XUV sources based on enhancement cavities[401, 402, 403, 404, 405], circumventing space-charge problems that had impeded atto-PEEM measurements so far[406].

Another approach to resolve the enhanced near fields at the apex of the nanotaper and plasmonic hotspots of nanostructures in general based on photocurrents is presented in the next section. The method does not rely on isolated attosecond XUV pulses but utilizes the strong-field photoemitted electrons from the enhanced near fields itself and thereby overcomes the limited sensitivity of the attosecond streaking approach to the nanoscale confined near fields.

7.3 Attosecond field-resolved measurements using photocurrents

This section describes the measurement of enhanced near fields on the nanotip using strong-field photoemission from the apex. The outline is as follows: Firstly, the experimental setup and approach is presented. Secondly, the experimental results are presented which are separated into three distinct sections: i) the onset of charge interaction effects, ii) the demonstration of the reconstruction of the near field at the apex including the investigation of the CEP- and intensity-dependence, as well as the comparison with photoelectron spectra and iii) the application of the nanoTIPTOE approach to the spatially resolved measurement of the focus of a vortex beam. We subsequently devote a special section to the discussion of the nanoTIPTOE approach. Finally, we provide a brief conclusion and outlook.

The experimental setup was built and developed by the author with help from Dmitry Zimin with whom also first experimental feasibility tests were performed. The nanotips were produced together with Johannes Blöchl (JB) and Ancyline Malliakal (AM), using the method described in Chap. 3.1. The TOF/CEP-current intensity-dependence was recorded by the author. The TIPTOE measurements, including TOF pump-probe, were performed together with JB and AM, including the compression of the pulses in the experiment and operation of the laser. The latter was supported by Zilong Wang and Philipp Rosenberger. The preparation of the spatially resolved measurements was done by JB. The experimental data was discussed mostly with JB and AM. The presentation of the data in this chapter has been prepared by the author. The measurements on the effects of space charge has resulted in a manuscript draft[407] which has been discussed with all the authors thereof.

7.3.1 Experimental setup

The experimental setup and approach is illustrated in Fig. 7.5. As depicted in Fig. 7.5 a), a strong pump pulse (red line) and weak signal pulse (blue line) with variable relative delay Δt are focused onto a tungsten nanotip using an off-axis parabola (OAP, f=10 cm). The emitted photoelectrons can be detected using a TOF-spectrometer (Stefan Kaesdorf ETF10) and a time-to-digital-converter (FAST ComTec P7889). Due to the vacuum-requirements for the electron spectra measurements and the microchannel-plate detector of the spectrometer, the setup is placed in a vacuum chamber. The photoemitted electrons lead to a photocurrent within the nanotip. Similar to the measurement of currents in gases described in Chap. 4, the wire of the nanotip is electrically contacted to a BNC pin which in turn is inserted into the plug of a BNC cable. The photocurrent is fed through to the outside of the chamber using a floating BNC feedthrough. It is amplified using a low-noise high-gain transimpedance amplifier (FEMTO DLPCA-200) and finally detected via a lock-in amplifier (Zürich Instruments HF2LI).

The laser frontend SMILE is the same as described in Chap. 4 and in more detail in Ref. [201]. In short, the output of a commercial Ti:Sa chirped pulse amplifier is broadened in a hollow-core fiber, spanning from 500 nm to ∼1000 nm. The pulses are compressed down

to around 4.5 fs at 750 nm central wavelength using chirped mirrors (CM, UFI PC70). The CEP-offset ϕ_0 is stabilized and controlled via a slow-loop that provides feedback to the CEP-stabilization of the laser oscillator.

The pump and signal pulses are generated in a Mach-Zehnder interferometer depicted in Fig. 7.5 b). A broadband 50:50 beamsplitter (BS) separates the pulse into the two arms. Each arm contains a circularly variable neutral density filter (ND) and a pair of fused silica (FS) wedges for the fine tuning of the dispersion in the experimental focus. The pump arm (red line) contains a retroreflector mounted on a piezo stage (MCL OPM100) with 100 μm travel range for the precise control of the delay between signal and pump pulses. The signal arm (blue) additionally contains a telescope consisting of two off-axis parabolas (OAP1 and OAP2). An optical chopper (Thorlabs MC2000B) is placed in the intermediate focus. For most experiments presented below, both mirrors had the same focal length (f=20 cm). In this configuration, the incident intensity calibration of Chap. 4 without telescope applies for the pump beam ($1.1 \cdot 10^{14} \frac{\mathrm{W}}{\mu J \cdot \mathrm{cm}^2} \pm 20\%$). This intensity calibration is not strictly valid for the signal beam due to different dispersive elements. Nevertheless, we will use it for estimations. Optionally, a $\lambda/2$-plate can be placed in the signal arm to rotate the polarization.

For the measurement of the angular momentum beams, a vortex plate (Vx plate, Vortex Photonics V-780-20-1) for a wavelength range around 780 nm that preserves the linear polarization is inserted into the signal arm together with a bandpass (BP, Edmund Optics 86956) with 50 nm bandwidth around a central wavelength of 775 nm. Moreover, a 1:2.5-telescope using a combination of concave and convex mirrors is introduced in front of the interferometer for the reduction of the pump beam size. At the same time OAP1 is replaced by an OAP with f=7.5 cm to increase the size of the signal beam. This way, in the experiment the OAM beam gets tightly focused whereas the smaller incident pump beam results in a bigger focal spot size. Here, the incident intensity calibration with telescope is valid for the pump beam ($0.11 \cdot 10^{14} \frac{\mathrm{W}}{\mu J \cdot \mathrm{cm}^2} \pm 50\%$, see Chap. 4).

For the measurements of the CEP-dependence, the signal arm is blocked and the CEP of consecutive laser pulses is flipped between ϕ_0 and $\phi_0 + \pi$ using a Dazzler. The telescope was in the beam and in the experimental chamber an OAP with f=5 cm was used. In this setting, the arrangement of the HCF, the recollimation and CM compression were slightly different from the above configuration.

For the nanostructures, the dynamics is determined by the enhanced near-field intensity rather than the incident intensity. Fortunately, the local enhanced intensity at the apex of the nanotip can directly be estimated from nonlinearity of the strong-field photoemission rate as has been shown in Refs. [361, 408, 66, 409, 135]. At onset of the tunneling regime (Keldysh parameter $\gamma \approx 1$), a characteristic drop of the nonlinearity below the multiphoton scaling is observed (see also Sec. 2.2.1). We use this approach in the intensity-dependent measurements in Sec. 7.3.3 and Sec. 7.3.4 below. However, we want to mention that the intensity calibration based on that method is expected to exhibit relatively large systematic uncertainties. Firstly, the onset of the tunneling regime is not strictly defined and the identification therefore intrinsically requires estimation. Secondly, the nanotip as a nanoscale emitter is very sensitive to the positioning in the laser focus, which has to be

adjusted on a daily basis. Finally, this approach can be affected, once charge interaction influences the emission probability.

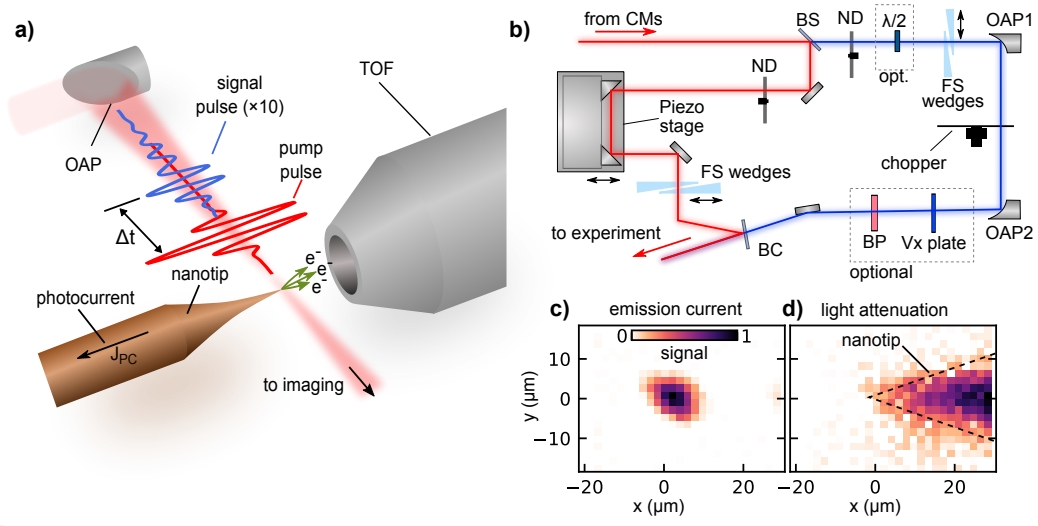

Figure 7.5: Experimental setup and approach for the current measurement from a nanotip: a) Experimental setup with pump and signal pulse. In addition to the photocurrent, the kinetic energy spectrum can be measured using a TOF-spectrometer. b) Interferometer for the pump-probe measurements. c) and d) experimental search for the nanotip apex using both the emission current and the light attenuation.

7.3.2 Experimental approach

Experimentally, an important aspect is to make sure that the apex of the nanotip is positioned in the laser focus and not an occasional hotspot farther down on the shank of the nanotip. Therefore, the nanotip is scanned transversely through the laserbeam and both the electron emission signal and the attenuation of the laser light in the imaging are recorded, as shown in Fig. 7.5 c) and d), respectively. The photocurrent signal is very sensitive to the field enhancement at the apex, whereas the light attenuation allows to get an estimate for the contour of the nanotip and is used to make sure that emission really occurs from the apex at the end of the tip. Without the latter signal, hotspots on the shank of the nanotip can be mistaken for the apex.

The employed digital lock-in amplifier is capable to demodulate the signal input at several frequencies in parallel. For the first demodulation frequency, we choose the laser repetition rate $f_{\mathrm{rep}} = 10\,\mathrm{kHz}$ which results in a signal that is proportional to the total photocurrent. The second demodulation frequency is the chopping frequency f_{chop} or the CEP-flipping frequency f_{CEP} which is set to 5 kHz, making sure that we are as far as possible from the 1/f-noise region at lower frequencies (see Sec. 3.2.2 for a more detailed discussion of lock-in amplification). For scanning applications, demodulation bandwidths

between 2-10 Hz are used.

The detection limit of the photocurrent measurement approach has to be considered. We observed the best signal-to-noise performance at the maximum gain of 10^9V/A of the transimpedance amplifier even though the nominal gain bandwidth ($f_{-3\mathrm{dB}}$) is below 5 kHz. For simplicity, we will, nevertheless, use the value of 10^9 for conversion between voltage and current, but want to point out that the effective gain will be slightly reduced. Moreover, the gain at 10 kHz will be lower than at 5 kHz. The conversion factor between signal amplitude and electrons per shot is approximately given by $0.6\,\mathrm{electrons}\cdot\mathrm{shot}^{-1}\mu\mathrm{V}^{-1}$. The transimpedance amplifier specifies an equivalent input noise current density of $4.3\,\mathrm{fA}/\sqrt{\mathrm{Hz}}$ which translates at the lock-in amplifier into $4.3\,\mu\mathrm{V}/\sqrt{\mathrm{Hz}}$ close to the observed voltage noise density of around 5-7 $\mu\mathrm{V}/\sqrt{\mathrm{Hz}}$.

In order to estimate the number of electrons required per shot in to get a detectable signal, we make a striaght-forward consideration. For simplicity, we assume a lock-in demodulation bandwidth of 1 Hz, a measurement of the signal in a 1 Hz window around the demodulation frequency. Taking into account the repetition rate of the laser and the input current noise density level stated above, roughly means that a change of around 3 electrons per shot can be detected (neglecting any other noise contributions). For higher repetition rate lasers, the sensitivity would increase accordingly due to the higher total number of emitted electrons. As a consequence, in order to be able to measure a modulation of the total photocurrent as required in the TIPTOE experiments, a (maximum) modulation by several tens of electrons per shot has to be achieved which consequently results in a total photocurrent of at least several hundred electrons per shot. Our experiments are therefore necessarily conducted in the multi-electron emission regime. The same, however, seems to be true also for the nano-bowtie current experiments that are driven at MHz repetition rates[165, 380]. While the work on TIPTOE[165] from a nanostructure array does not discuss total electron emission rates, the study on the on-chip CEP-measurements employing similar nanostructure arrays[380] indirectly indicates 10^3 to 10^4 electrons per shot per nanostructure, based on the CEP-current per shot and nanostructure (0.11 electrons) and the ratio of CEP-current to total current (10^{-4} to 10^{-5}).

7.3.3 Onset of space-charge effects

Based on the considerations above that the nanoTIPTOE approach in our implementation requires multi-electron emission, we first turn our attention to the investigation of charge interaction effects before demonstrating the attosecond near-field measurements via the photocurrent further below. Space-charge interaction affects both the tunnel emission process and the subsequent electron dynamics in the continuum. The former effect is hard to assess directly. However, the latter leaves a trace in the kinetic energy spectra of the photoelectrons which we can measure using a TOF spectrometer. For all measurements presented in this section, the photocurrent and the TOF-spectrum were measured simultaneously. Some part of the material presented below has led to a manuscript submission[407] and the presentation below partly follows the one therein.

Experimental results

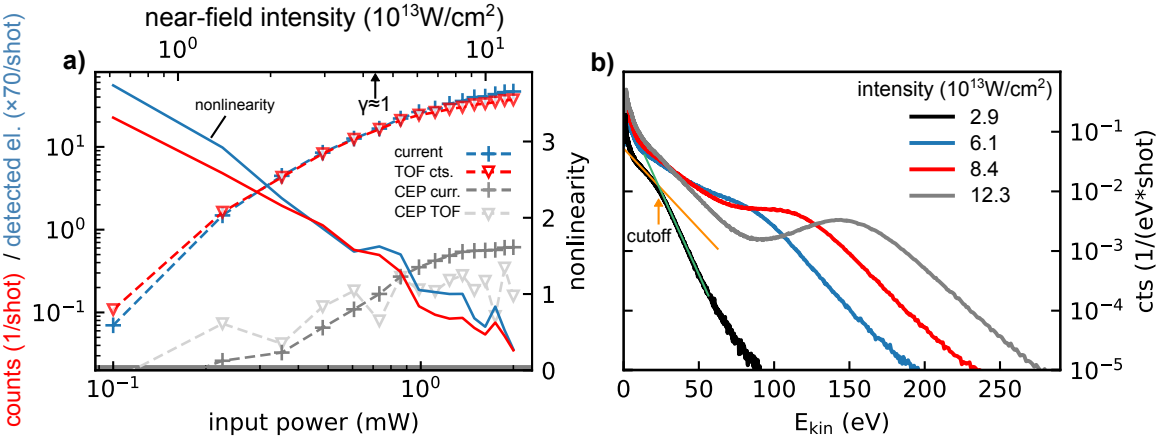

Figure 7.6: TOF-measurements and evidence of charge interaction in the electron spectra: a) TOF (red dashed line) and current (blue dashed line) countrate and nonlinearities (solid lines) together with the detected CEP dependence (light and dark gray dashed lines). Around a factor of 70 more electrons are detected in the photocurrent compared to the TOF. The x-axis at the top shows the near-field intensity calibration based on the onset of the tunneling regime (black arrow). b) Electron spectra for different values of the near-field intensity.

The connection between the photocurrent and the TOF measurements is established in Fig. 7.6 a), which shows the intensity dependence of the number of detected electrons. The signal arm is blocked. Both photocurrent (blue cross and dashed line) and TOF (red triangles and dashed line) approach show a very similar evolution. However, in the photocurrent, approximately a factor 70 more electrons are detected. The main reason is likely that the TOF spectrometer has an acceptance angle of only around 2.5° since we did not apply a lens voltage in order to avoid distortions of the spectra. From a rough comparison with the measured emission angles of Ref. [361], a factor of 40 would be expected, which is close to our observation. This exemplifies one advantage of the photocurrent approach where all emitted electrons contribute to the signal.

The total number of detected electrons per shot in the photocurrent increases from below 5 at the lowest input power of 0.1 mW to above 3000 at 2 mW. The nonlinearity (solid lines), calculated in a finite-difference scheme from the countrate scaling, decreases with increasing input power. The change of the slope can be interpreted as the transition from the multiphoton to the tunneling regime[361]. The slightly higher slope in the multiphoton regime than would be expected from the photon energy ($\hbar\omega = 1.7\,\mathrm{eV}$) and work function of tungsten ($\phi = 4.5\mathrm{eV}$)[410] can be explained by the presence of the surface and rescattering of the photoelectrons[408]. Additionally, since our nanotips are not cleaned in-situ, an increase of the work function (up to 6.5 eV) caused by oxidized adlayers is also expected to contribute[407, 82, 87].

As discussed in Sec. 2.2.1, the onset of the tunneling regime can be identified with a Keldysh parameter of $\gamma \simeq 1$[361, 408] which in turn can be used to obtain an estimate of the enhanced local intensity at the apex as shown in Refs. [66, 409, 135] (see Eq. 2.4). The thereby obtained local intensities for our experiment are shown on the top axis and the power identified with $\gamma = 1$ (black arrow) is also indicated. We estimate a potential systematic error of the intensity calibration of up to almost a factor 2 due to the uncertainty of where to place the onset of the tunneling regime. At the highest intensities the nonlinearity drops below 1, which has been identified as the regime where not only the electron dynamics is affected by charge interaction but also the tunneling emission process is suppressed[409]. However, already below, some suppression of the emission might occur, which has to be kept in mind, when using this calibration procedure. As discussed below in Sec. 7.3.4, our experimental conditions allow to achieve high intensities without damaging the nanotip. We believe that no significant damage occured to the nanotip even at the highest intensities.

We also show the experimental CEP-dependence in the photocurrent (dark gray triangles and dashed line) and the TOF measurement (light gray crosses and dashed line) Fig. 7.6 a) by scanning the CEP over 20 values between 0 and 2π and flipping the CEP for consecutive pulses. The statistical error in the TOF measurements is significantly higher (not shown for the sake of clarity of the figure; on the order of the oscillations between consecutive datapoints) since in the present approach it is affected by slow laser power drifts and fluctuations unlike the photocurrent that is measured with a lock-in amplifier. A ratio of CEP-dependent to total countrate of around 10^{-2} is measured, which is more than an order of magnitude, probably rather two, above what has been reported in other studies using nano-bowtie structures and MHz repetition rate sources[379, 379]. The reason could be twofold. Firstly, it has been reported that in MHz repetition rate nanotip experiments the strong-field emission is suppressed due to accumulative heating[411]. Secondly, we use shorter input pulses and non-resonant field enhancement that translates into enhanced near fields with approximately the same pulse duration. We observe a flip by π in the photocurrent CEP-dependence between the first ($\sim 1.1 \cdot 10^{13} \mathrm{W/cm^2}$) and second ($\sim 2.0 \cdot 10^{13} \mathrm{W/cm^2}$) datapoints that lie above the noise limit (thick horizontal gray line), which can be attributed to the vanishing CEP-effect[219].

The CEP-averaged photoelectron spectrum measured by the TOF for various local intensities is shown in Fig 7.6 b). At low intensities (black line), a low-energy peak connected to a plateau is observed, reminiscent of the direct electron and rescattering contributions of strong-field photoemission corresponding to the $2\,U_\mathrm{p}$ and $10\,U_\mathrm{p}$-cutoffs (see Sec. 2.2.3), similar to e.g. Refs. [87]. Beyond the plateau the spectra decrease rapidly but can still reach quite far in kinetic energy. This is measurable due to the high dynamic range of the spectrometer. For each intensity, the value of the cutoff of the plateau is evaluated by fitting straight lines to the logarithmic data below (orange) and above (green) the apparent cutoff and determining their intersection point, as illustrated here for the lowest intensity shown. As the intensity is increased the cutoff of the plateau evolves into a peak structure (gray line).

The formation of the peak indicates that space-charge effects play a role. A short time

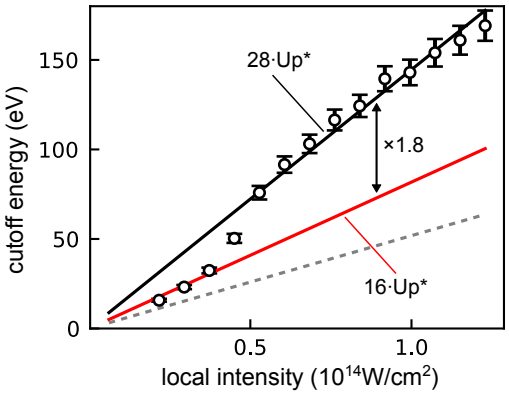

Figure 7.7: Scaling of the plateau cutoff: linear fit to the lowest three datapoints (red line) and the upper eight (black line). The slope is given in terms of the near-field ponderomotive potential. The gray dashed line is the expectation from the $10\,U_{\mathrm{p}}^{*}$-law based on the near-field intensity calibration, where U_{p}^{*} is the ponderomotive potential of the enhanced near-field. Note that the uncertainty in the intensity calibration and therefore the slope is around a factor 2. The ratio of the slopes (black arrow) is unaffected by this uncertainty.

after emission, slower electrons which are still closer to the nanostructure are decelerated by both the positive image charges in the nanostructure as well as the faster electrons that are further away. In turn the faster electrons are accelerated by the slower ones. This effect is also evident in the intensity scaling of the plateau cutoff (open dots) shown in Fig. 7.7. For the lowest intensities, a linear scaling of the cutoff is observed, which is only about a factor 1.6 above what would be expected from the near-field intensity calibration above and using the $10\,U\mathrm{p}^{*}$-cutoff law (gray dashed line), where $U\mathrm{p}^{*}$ is the enhanced near-field ponderomotive potential. Given the estimated uncertainty of up to a factor of 2 of the intensity calibration, which in this case seems to be underestimating the real near-field intensity, the experimental scaling is in agreement with the $10\,\mathrm{U}_{\mathrm{p}}^{*}$-law. Once the charge interaction peak at the cutoff starts to be formed above $0.4 \cdot 10^{14}\mathrm{W/cm}^2$, or above approximately 1000 electrons/shot, a nonlinear shift of the cutoff is observed. At even higher intensities, again a nearly linear scaling is recovered. The cutoff is about a factor 2.8 above the expectation which can be explained by the additional acceleration caused by space-charge interaction. The relative increase of the cutoff due to charge interaction, which is not affected by the uncertainty of the intensity calibration, is about 1.8 which is in remarkably good agreement to the simulation result for nanospheres of around 1.7[362]. However, unlike for dielectric nanospheres a suppression of the low-energy peak is not observed here. This could potentially be explained by differences in the charge interaction, as further discussed below.

The evolution and influence of the space-charge interaction is even more evident in the CEP-resolved spectra. For a better visualization of the CEP-dependence in the signal varying by several orders of magnitude, we investigate the asymmetry $A(\phi_{\mathrm{CEP}}, E)$ calculated

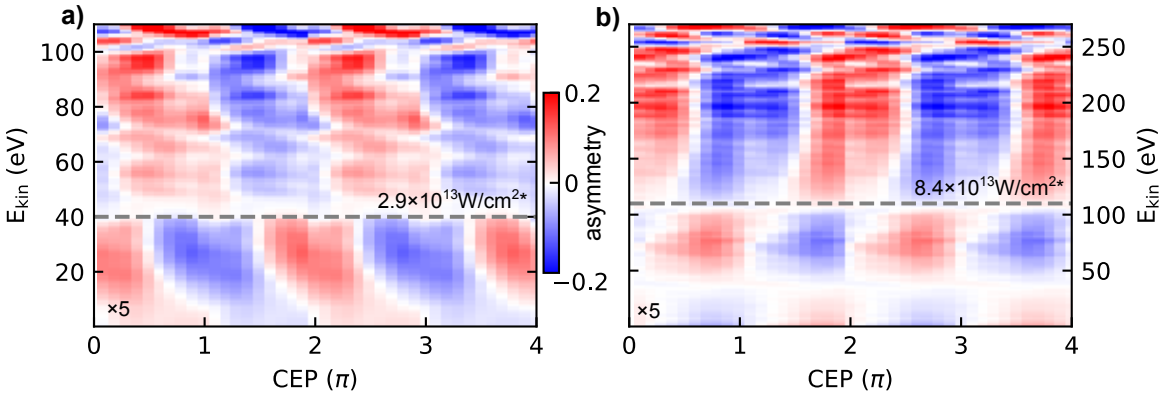

Figure 7.8: CEP-dependence of the electron spectra: CEP-asymmetry maps for near-field intensities of a) $2.9 \cdot 10^{13}\mathrm{W/cm^2}$ and b) $8.4 \cdot 10^{13}\mathrm{W/cm^2}$. The CEP asymmetry for the energies below the gray dashed lines has been increased by a factor of 5 for better visibility. The shown colorbar applies to both a) and b).

from the energy-resolved photoelectron spectrum at CEP=ϕ_{CEP} using:

$$A(\phi_{\mathrm{CEP}}, E) = \frac{S(\phi_{\mathrm{CEP}}, E) - S(\phi_{\mathrm{CEP}} + \pi, E)}{S(\phi_{\mathrm{CEP}}, E) + S(\phi_{\mathrm{CEP}} + \pi, E) + \epsilon}, \tag{7.13}$$

where ϵ is a small regularization parameter to avoid division by zero. Intuitively, A indicates how strongly the spectra depend on the CEP. The asymmetries for an intensity of $2.9 \cdot 10^{13}\mathrm{W/cm^2}$ and $8.4 \cdot 10^{13}\mathrm{W/cm^2}$ are shown in Fig.7.8 c) and d), respectively. For a better visibility, the asymmetry-maps have been multiplied by a factor of 5 below 40 eV and 110 eV, respectively, as indicated by the gray line. Generally, the CEP-dependence increases with higher electron energies.

For the higher intensity a checkerboard-like structure, caused by phase jumps of π at distinct energies, is observed which has been identified as a clear signature of charge interaction in Ref. [66] (see SI and Fig. S7 therein). For the right CEP, only one electron burst is emitted, increasing the interaction between slow and fast electrons which leads to a maximum of the asymmetry at the lowest and highest electron energies. In the case of two emission bursts, the interaction is reduced and electrons at intermediate energies are less affected. For the lower intensity a smooth, tilted asymmetry is observed up to slightly beyond the plateau cutoff. Only above, a sudden phase-flip occurs, followed by a quasi-straight CEP-dependence that extends up to 100 eV. Additionally taking into account that the cutoff peak is around $10\,U_{\mathrm{p}}^*$, we speculate that for the lower intensity shown here the spectrum within the plateau and below is still dominantly laser driven. In contrast, we believe that the electrons at the highest energies beyond the plateau cutoff, show clear signatures of charge interaction.

Sudden phase jumps in the asymmetry were not visible in studies of CEP-resolved strong-field photoemission and charge interaction on isolated nanospheres[362, 52, 412, 413]. We account a part of the difference to the absence of focal averaging in our experiments but again also to different characteristics of the charge interaction.

A simple estimate for the space-charge induced spectral broadening and shift ΔE_{sc} can be obtained from the Long-Itchkawitz-Kabler-model (LIK)[414, 415] that we also used for the estimates in Ref. [405]. In its' adaption to the high-energy edge of a uniform kinetic energy distribution, it is given by[405, 415]:

$$\Delta E_{\mathrm{sc}}[\mathrm{eV}] \approx 0.5 \cdot 10^{-3} N_{\mathrm{e}}/d_{\mathrm{em}}[\mu\mathrm{m}], \tag{7.14}$$

where N_{e} is the total number of emitted electrons and d_{em} is the diameter of the emission spot. We identify the latter with the estimated diameter of the apex 40-60 nm. Using the detected number of electrons in the photocurrent, we obtain a ΔE_{sc} of around 5 eV for $2.9 \cdot 10^{13}\mathrm{W/cm}^2$ and 21 eV for $8.4 \cdot 10^{13}\mathrm{W/cm}^2$ which appears to be a decent estimate for the order magnitude of the space charge interaction observed in our experiment.

Discussion

Our measurements indicate that charge interaction starts to affect the electron dynamics above a near-field intensity of $0.5 \cdot 10^{13}\mathrm{W/cm}^2$ or around 1000 e^-/shot. At intensities above $0.8 \cdot 10^{13}\mathrm{W/cm}^2$ even the tunneling emission process itself seems to be affected. While the strong-field tunneling photocurrent experiments on nano-bowties and triangles[19, 219, 416, 381, 165] focus mainly on the CEP-dependent current which is on the order of one electron per shot, the total number of charges per shot is typically several orders of magnitude higher[379, 219, 380] and therefore in a similar regime as for our experiment. The discussion of charge interaction given here is therefore of high relevance to these experiments as well.

So far, most systematic studies focusing on charge interaction in strong-field photoemission were performed on isolated nanospheres[362, 52, 412, 413]. Despite the differences in the strong-field photoemission process between metallic nanotips and dielectric nanospheres, as discussed below, a comparison is very instructive. In the studies for nanospheres experiments, several effects could be identified by thorough analysis of the experimental results and extensive numerical simulations.

Firstly, the cutoff is increased by a factor of around 1.7 compared to what would be expected from the enhanced near fields[362]. We make a similar finding (factor around 1.8). Moreover, we seem to experimentally observe the onset of the charge interaction with increasing electron numbers.

Secondly, the low-energy direct electron peak is suppressed due to trapping in the combined potential of the holes and the faster rescattered electrons in the case of nanospheres [362, 52, 412, 413]. In contrast, we do not observe a suppression of the low-energy peak.

The disagreement of our experiment with the latter finding could potentially be explained by different behaviors of the photohole inside the medium. In dielectrics the hole is not screened effectively and interacts with the photoelectrons via the quasi-bare Coulomb force over long distances and longer timescales. The isolated nanospheres effectively charge up and stay charged. On the other hand, in the grounded metal nanotip hole screening occurs on the sub-femtosecond timescale[417, 418]. Afterwards, the interaction with the nanostructure solely occurs via the image charge that quickly decays with increasing distance from the surface. As a consequence, at the nanotip a trapping potential is present over

short time and length scales, which could contribute to the increase of the cutoff energy by affecting the electron trajectories between emission and rescattering as for dielectric nanospheres[362]. In addition, the interaction of fast electrons with slower electrons on longer timescales should not be affected significantly. Those two considerations can potentially explain why a similar cutoff extension is observed. On the other hand, we speculate that the low-energy peak is not suppressed due to the photohole screening dynamics and grounding of the metallic nanotip, which should lead to a quick decay of the trapping potential over intermediate timescales. Additionally, the so-called delayed emission channel could contribute to the low-energy peak[419], where electrons are initially scattered back into the nanotip and are released into the vacuum through a series of scattering events. In contrast, emission from the side of the shank observed in Ref. [420], seems to be negligible, as can be seen from the position scans (see Fig. 7.5 c).

Thirdly, for nanospheres, it was found that the nonlinearity of the electron emission decreases to around one once significant charge interaction sets in, both due to trapping and suppression of emission rate. A similar drop of the nonlinearity to a sub-linear scaling, that was attributed to charge interaction suppressed tunneling emission, was observed from nanotip-arrays[409]. For our experiments, a photoemission nonlinearity <1 is also observed for the highest intensities in the CEP-dependent TOF measurements. In contrast, the change from the initial multiphoton-scaling to a nonlinearity of around 2 can be attributed to the onset of tunneling[361, 66, 409, 135].

However, the details of the emission process on the metallic nanotip are different to dielectric nanospheres. The initial multiphoton nonlinearity is significantly smaller due to the lower work function of around 4.5 eV for tungsten[410], compared to the effective ionization potential of 9 eV for SiO_2[412]. Moreover, the laserfield inside the metallic nanotip is screened on the length scale of an atomic layer, whereas significant field strengths are reached within dielectric nanospheres. Therefore, for nanotips charge creation by the laser fields only happens at the surface, whereas in nanospheres potentially the whole volume cose to the surface can contribute. In Refs. [361, 409] it has been argued that emission suppression does only play a minor role around the tunneling transition for nanotips. Indeed, even the study presented in Ref.[419] on electron emission from large nanotips (r=100 nm), where the shape of the kinetic energy spectrum was argued to be completely dominated by charge interaction, did neglect space-charge suppression of the emission rate in the simulations.

The argument, that the small dimension of the nano-emission site leads to highly divergent trajectories, is often used to justify the neglect of charge interaction[361, 66, 219]. On the other hand, the electron kinetic energy spectrum from large nanotips (r$\sim$100 nm) seems to be completely dominated by Coulomb interaction[419, 421]. Therefore a systematic study of the intensity-dependence as presented above in Sec. 7.3.3 but for several different nanotip sizes would be highly desirable.

From a theoretical perspective, a model which allows numerical simulations of our results including laser-matter and charge interaction similar to Refs.[362, 409, 66, 419], would be beneficial for a deeper fundamental understanding. Especially interesting would be a comparison of different photohole screening dynamics.

7.3.4 Characterization of near fields at the apex of a nanotip

Field-resolved measurements

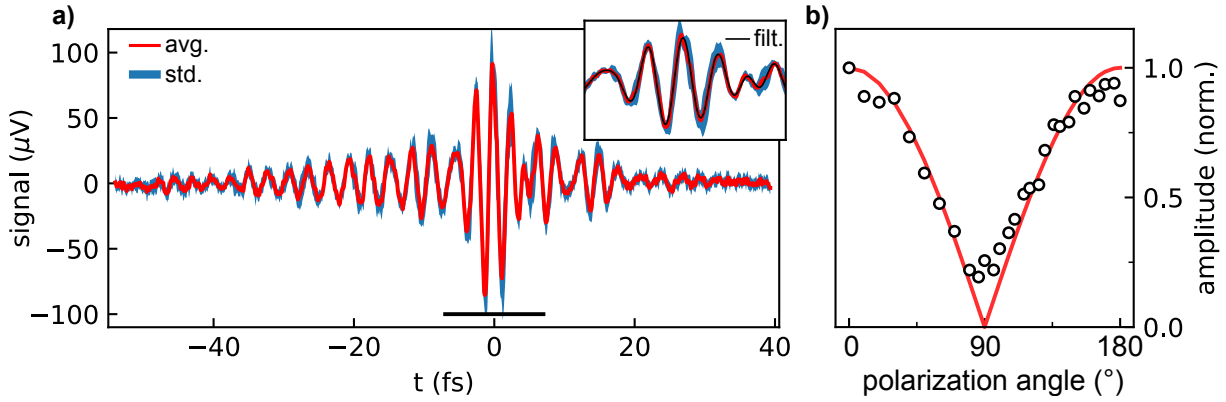

Figure 7.9: Experimental photocurrent signal and polarization dependence: a) average (red line) of the photocurrent signal over 10 scans. The thickness of the blue curve shows the standard deviation (gain 10^9V/A). The inset shows a closeup around t=0 (indicated by the black bar in the main panel) together with a Fourier-filtered curve (thin black line). b) Signal amplitude (symbols) versus polarization angle ϕ controlled by the half-waveplate together with the expected $|\cos(\phi)|$-dependence (red line).

The nanoTIPTOE pump-probe approach described above, where the weak signal pulse perturbatively changes the tunneling photoemission current, allows to measure the enhanced near field at the apex with attosecond resolution. A representative measurement is depicted in Fig. 7.9 a) which has been obtained at an incident pump intensity of around $2 \cdot 10^{12}$W/cm^2 (18 nJ/pulse) and an estimated incident signal intensity of around $2 \cdot 10^{10}$W/cm^2 (0.2 nJ/pulse). Note that the required pulse energies could be significantly reduced by using a higher numerical aperture (currently ~ 0.05). The curve (red line) has been obtained by averaging over 10 scans. The thickness of the blue line indicates the standard deviation. The measured signal is proportional to the electric field of the signal pulse (see Sec. 3.3.3). Here, we obtain a pulse duration of 4.8 fs (intensity-FWHM). A maximum signal amplitude of around 100 μV is observed, corresponding to a signal pulse induced modulation of the photoemission yield of slightly more than 60 electrons per laser shot. The maximum modulation is about 16% of the total emitted photoelectron signal measured at the repetition rate (see Sec. 7.3.2 for further details). The inset shows a closeup around t=0 together with a Fourier-filtered curve (black line) where spectral components below 475 nm have been filtered out. The good agreement with the original curve (red line) illustrates that despite the relatively high signal power compared to the pump pulse for TIPTOE, no significant harmonic distortion occurs at the employed intensity. This is also confirmed in the spectral domain (not shown), where the signal at the second harmonic is at the noise level of our measurements. As further discussed below, this finding can be explained by the low nonlinearity of photoemission in the tunneling regime.

Figure 7.9 b) shows the polarization dependence at a slightly higher incident signal intensity of around $6 \cdot 10^{10}\mathrm{W/cm^2}$ (0.6nJ/pulse) measured by inserting the half-waveplate (HWP) in the signal arm and compensating for the added dispersion by moving the wedges. The waveplate rotates the polarization angle of the signal pulse and the waveplate angle is calibrated with respect to the incident pump beam polarization. As the signal polarization angle ϕ is increased to 90°, the nanoTIPTOE signal amplitude (open dots) experiences a minimum and recovers for a polarization angle of 180°. Overall, excellent agreement between the experimental data and the theoretical expectation $|\cos(\phi)|$ (red line) for the signal field amplitude along the polarization direction of the pump field is observed. A small field amplitude remains even at $\phi = 90°$, which could potentially be explained by the slight residual overlap of the surface normal near fields on the nanotip apex for perpendicular input polarizations and, in addition, to a slightly asymmetric nanotip geometry. In intensity, this contribution is only around 1%. While this could pose a limit on the sensitivity in arbitrary polarized signal fields, it could potentially be overcome by improvements in the nanotip symmetry. For the proof-of-principle experiment presented here, it is negligible.

In the context of polarization sensitivity, we also want to point out that due to the presence of the surface which breaks the inversion symmetry of free-space, tunneling emission is only possible when the electric field vector points into the surface. As a consequence, the nanoTIPTOE measurements do not exhibit directional ambiguity as the gas phase counterparts, but also provide information on the field direction.

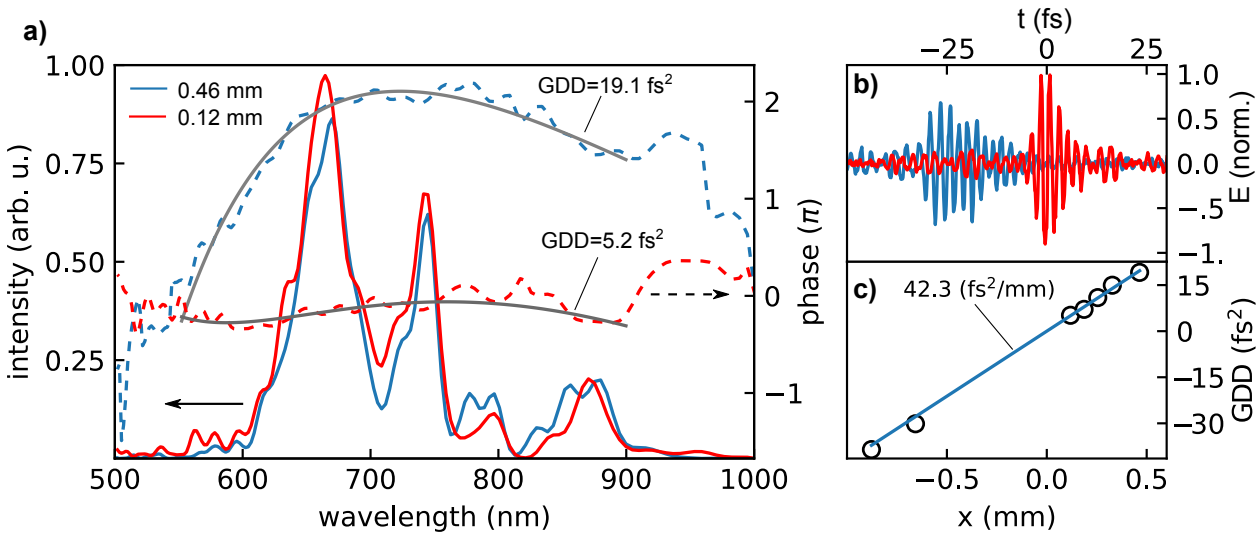

Figure 7.10: Pulse characterization and dispersion optimization of the signal pulse: a) Measured amplitude (solid line) and phase (dashed line) for fused silica insertion of 0.12 mm (red) and 0.46 mm (blue). The fit of the spectral phase (gray line) and extracted GDD at 725 nm is also shown. b) Measured pulses from which the spectral phase and amplitude in a) are retrieved. c) Measured GDD for different fused silica insertion and fit showing the GVD. The literature value is $42.6\,\mathrm{fs^2/mm}$[422].

We also measured the change of the signal upon changing the dispersion in the signal arm by moving the wedges and adding a 1 mm fused silica window into the beampath. The spectral amplitude (solid line) and phase (dashed line) for a fused silica insertion of 0.12 mm (red lines) and 0.46 mm (blue lines), respectively, are shown in Fig. 7.10 a). The insertion is defined relative to the amount for zero group-delay dispersion, discussed further below. Decent agreement of the spectral intensities is observed. The remaining discrepancy could, amongst other reasons, be explained by the limited sampling time window of around 133 fs and the shift of the absolute delay when changing the dispersion. Compared to the input spectrum as measured by a grating spectrometer (not shown), the typical oscillations of the spectral intensity are reproduced, however, the longer wavelength contributions seem to suppressed in the nanotip measurements. Several factors could play a role here. Firstly, the nanotip apex measures only a very localized fraction of the focus and longer wavelength components get focused weaker (scaling as $1/\lambda^2$ in intensity). Secondly, for these measurements the half-waveplate was placed in the beam which, however, is only specified up to 950 nm and which could also be connected to the observed jump of the spectral phase around that wavelength. In principle, the field response function of the nanotip apex could also contribute. However, as shown in Sec. 2.4 the amplitude of the response function of the tungsten tip apex exhibits a slight increase with longer wavelengths.

In the spectral phase (dashed lines in Fig 7.10 a)), a higher second order contribution is visible for the larger fused silica insertion (blue dashed line), indicative of an increased group-delay dispersion (GDD). A third order polynomial fit at a central wavelength of 725 nm (gray lines) reveals a GDD of 19.1 fs^2 compared to 5.2 fs^2 for the reduced glass insertion (red dashed line). The effect on the pulse shape in the temporal domain is shown in Fig.7.10 b). As expected, the pulse with less GDD (red line) exhibits a considerably shorter pulse duration and a higher amplitude. Note that there is an arbitrary relative time delay between both curves due to the required coarse delay correction with the manual stage. The extracted GDD values for a number of pulse measurements with different glass insertion is shown in Fig. 7.10 c). A linear fit to the data points (blue line) yields a group-velocity dispersion of 42.3 fs^2/mm which is very close to the literature value of 42.6 fs^2/mm[422]. These results indicate that the spectral phase and therefore indeed the electric field oscillations of the signal pulse, at least up to a phase offset, are measured.

CEP dependence of the nanoTIPTOE-response

In order to investigate the relation between photocurrent signal and the electric field of the signal pulse, i.e. the TIPTOE response function, further field measurements were conducted, where the CEP of both the pump and the signal pulse, was changed using the slow-loop feedback to the oscillator. The extracted CEP of the signal pulse from the TIPTOE measurement (open dots) versus the CEP set-value of the slow-loop is shown in Fig. 7.11 a) together with the mean value (gray dashed line) and standard deviation (gray shaded area). The measurement was obtained at an incident pump intensity of around $2 \cdot 10^{12}$W/cm^2 (18 nJ/pulse), and a signal intensity of approximately $2 \cdot 10^{10}$W/cm^2 (0.2 nJ/pulse). The measurements show a quasi constant value of the carrier-envelope

phase. In contrast, for a pump pulse with varying CEP and a signal pulse with constant CEP=0, based on the discussion in Sec. 3.3.3, a linear dependence (red line) of the measured CEP would be expected.

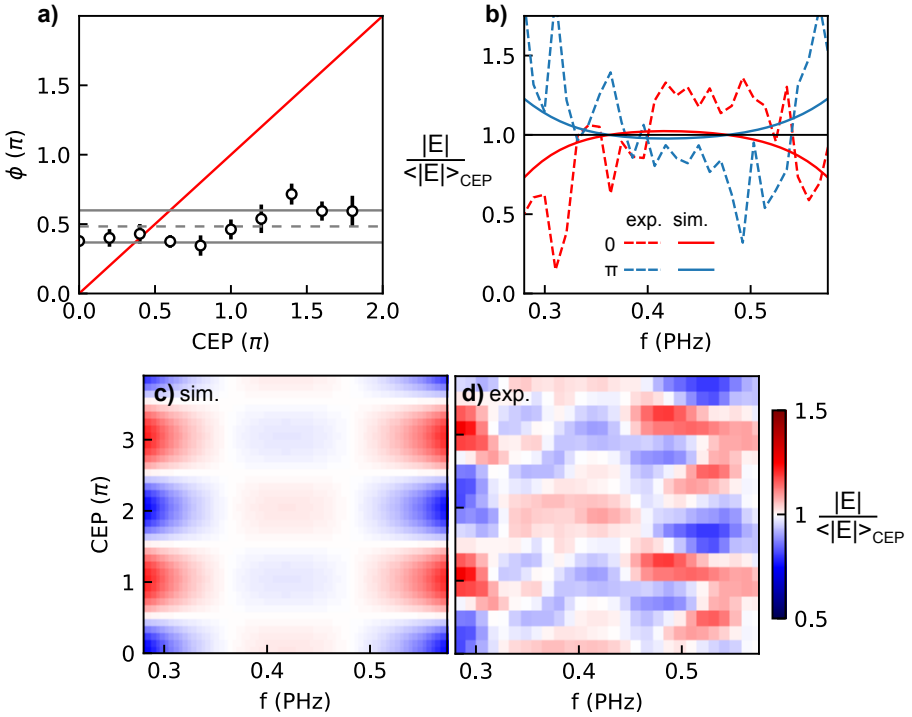

Figure 7.11: CEP-dependence of the response function of the measurement technique: a) Measured CEP (symbols) versus set-value of the CEP stabilization together with the mean (gray dashed line) and standard deviation (solid lines) calculated within 0.37-0.47 PHz. If both pulses derive from the same source, as here, a constant value is expected. By contrast, if the signal pulse was CEP-stable, a linear evolution(red line) would be expected. b) Measured (dashed line) and simulated (solid line) relative spectral amplitude for CEP=0 (red) and π (blue), respectively. c) and d) CEP-resolved simulated and measured relative spectral amplitude. A Gaussian filter has been applied to the experimental data for noise-reduction. Pump intensity for the simulations $5.5 \cdot 10^{13}\mathrm{W/cm^2}$, work function 4.5 eV, laser FHWM 3.75 fs).

As shown in the discussion in Ref. [165] (and also here in Sec. 3.3.3), the TIPTOE response function only allows the measurement of the relative phase, which is caused by the time/phase shift of the tunnel emission burst with the CEP of the pump pulse. In order to really measure the electric field of the signal field in nano-TIPTOE, the CEP of the pump pulse must be calibrated and set to π, which in principle should be possible by measuring the CEP-dependence of the photocurrent[379, 219, 380]. However, if both pulses are derived from the same laser source and exhibit the same CEP-variation (i.e. not involving DFG or SHG) as in our experiments, the relative phase between both pulses

does not change with CEP and the measured signal exhibits a constant ϕ_{CEP}. This can be interpreted as a feature that TIPTOE inherits from autocorrelation measurements. This, however, allows for a simple interpretation, as pointed out in Ref. [165]. When varying the CEP of both pulses simultaneously, the situation is met where the carrier-envelope phase of the pump pulse is π and therefore the true waveform of the signal pulse is measured. With the observation above, this implies, that irrespective of the actual pump CEP, all measurements represent this case and a CEP-stabilization is not necessarily required in these auto-TIPTOE-measurements. For arbitrary signal pulses, however, CEP stability is required.

So far, we have only considered the phase of the response function and neglected the spectral amplitude. This approach is justified if the signal pulse has the same central wavelength λ_0 as the pump pulse and is considerably narrower than an octave[167]. However, as has been discussed in Fig. 3.8 c), for few-cycle pulses a strong CEP-dependence of the amplitude response is observed, amongst others, at $2\lambda_0$ and $2/3\lambda_0$ caused by the switching between single and double tunneling emission bursts. Thus, in our measurements a CEP-dependence can be expected at the edges of the spectrum. Indeed, as shown in Fig. 7.11 b), the measured relative photocurrent spectral amplitude $|E|/ < |E| >_{\mathrm{CEP}}$, where $< |E| >_{\mathrm{CEP}}$ is the CEP-averaged spectral amplitude, significantly differs for CEP=0 (red dashed line) and CEP=π (blue dashed line). As expected, the former decreases at the edges of the covered spectral range, while the latter increases. A comparison with theoretical calculations (solid lines) based on the Fowler-Nordheim-rate[66] qualitatively shows decent agreement, especially towards the edges. Additionally, the slightly increased (reduced) response in the frequency range from around 0.35 PHz to 0.5 PHz for CEP=0 (CEP=π) is reproduced, albeit with a lower magnitude.

The good qualitative agreement is further illustrated by the CEP-resolved relative spectral amplitude shown in Fig. 7.11 c) and d) for the theoretical model and the experimental measurement, respectively. In agreement with the above observation, at the edges of the frequency range, i.e. below 0.32 PHz and above 0.5 PHz, a strong CEP-dependence with an amplitude of up to 0.5 is observed. It peaks at CEP=π, when a single emission burst is expected. The substructure in the experimental data might be due to noise in the measurement. In contrast, close to the central frequency, between 0.35 PHz and 0.45 PHz a weaker CEP-dependence is observed that is π out of phase with the former. Note that this measurement could in principle also be used for the calibration of the CEP.

For a better agreement with theory, more involved simulations than the simple Fowler-Nordheim calculation is likely to be necessary. A more complete information about the response function could be obtained by measuring a signal pulse at a different central wavelength than for the pump pulse similar to Ref. [30], ideally around $0.5\,\lambda_0$, since there the phase and amplitude response show a strong CEP-dependence (see Fig. 3.8 c)). In our experimental setup, this could be achieved rather easily by placing a nonlinear crystal in the signal arm focus for the generation of DFG. We leave this to future work, but it is especially interesting in order to quantify the influence of the charge interaction on the emission process, as further discussed below.

Intensity dependence

For a deeper understanding of the photoemission process and the signal formation mechanism under our conditions, the dependence of the photocurrent on signal and pump intensity is investigated. The current signal, demodulated at the repetition rate, which is proportional to the total photoemission current versus the pump power is shown in Fig. 7.12 a). Here, the number of detected electrons per shot (blue line) has been calculated from the nominal transimpedance and the total number of electrons should be slightly higher, as mentioned above. The thickness of the line indicates the uncertainty. The signal arm has been blocked. When increasing the pump power from 70 μW to 300 μW (incident intensity from 0.8 to $3.3 \cdot 10^{12}$W/cm^2) an increase of the number of detected electrons by almost two orders of magnitude is observed from approximately 10 up to around 1000 per shot. At around 140 μW (14 nJ/pulse), there is a noticeable change of the slope of the curve, which is equivalent to the nonlinearity of the photoemission process. The nonlinearity (gray triangles), calculated using finite differences between neighboring datapoints, changes from around 4.2 to roughly 1.8, as confirmed by fitting the slope of the measured photoemission current over the region indicated by the black lines.

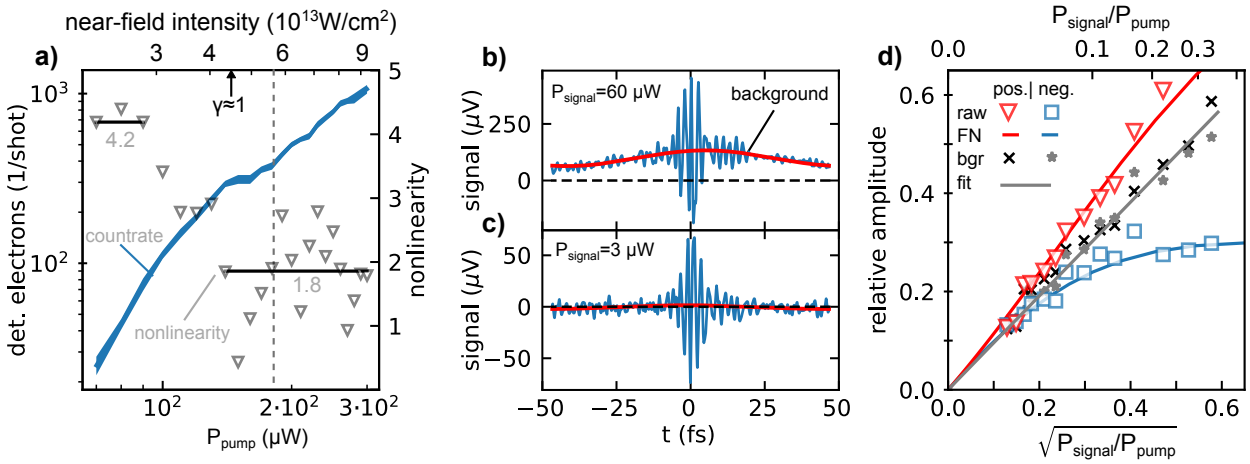

Figure 7.12: Intensity-dependence: a) detected emitted electrons per shot (blue line), the thickness shows the uncertainty. Calculated nonlinearity (symbols), as well as the nonlinearity extracted from a fit at the lowest and highest power values (black lines). The near-field intensity (top x-axis) has been calibrated by identifying the onset of tunneling emission (black arrow). b) The nanoTIPTOE-signals for two different driving powers at a pump power of 180 μW (gray vertical dashed line in a)). The slowly varying background is shown as red line. c) Amplitude of the nanoTIPTOE-signal in positive (red signals) and negative direction (blue symbols) versus the squareroot of power together with Fowler Nordheim calculations (red and blue solid lines). After background correction, the amplitudes both in the negative and positive direction (black and gray symbols) lie quasi on a straight line (gray line).

An almost identical curve, both in the total number of emitted electrons and evolution of the nonlinearity, has been measured in the first work demonstrating tunneling emission from a nanotip[361]. We use the same approach as discussed above (see Fig. 7.7 a)) to obtain the near-field intensity by identifying the change of the photoemission nonlinearity with the transition from the multiphoton regime to the tunneling regime at a Keldysh parameter $\gamma = 1$ (black arrow)[361, 408, 66, 409, 135]. The obtained enhanced near-field intensities for our experiment are shown on the top axis. Again, a relative high systematic error of the near-field intensity calibration of around 2 is to be expected due to the uncertainty of where to place the onset of tunneling. The scaling of the nonlinearity is similar to the measurements investigating the onset of space-charge effects, presented in Fig. 7.7 a). However, due to the slightly smaller intensity range, the nonlinearity does not consistently drop below 1, which would indicate Coulomb suppression of the tunneling process, as discussed above. Furthermore, both measurements were taken from different nanotips under slightly different conditions.

From measurements of ATI in the gas phase under the same experimental conditions (see Sec. 4) the intensity calibration for the incident pump field is determined rather precisely ($1.1 \cdot 10^{14}\mathrm{Wcm}^{-2}\mu\mathrm{J}^{-1} \pm 20\%$). At 14 nJ of incident pulse energy, an incident intensity of $1.5 \cdot 10^{12}\mathrm{W/cm}^2$ is expected. By comparison with the determined corresponding local intensity at the apex of about $4 \cdot 10^{13}\mathrm{W/cm}^2$, a field enhancement factor of around 4-6 is obtained. From the nanotip focus scans (see Fig. 7.5 d), we determine a tip opening angle of around 15-20°. The field enhancement together with the opening angle allows to estimate the nanotip radius from theoretical studies of the near-field enhancement[423]. We obtain a tip radius of 15-30 nm. Unfortunately, the tip used here suffered mechanical damage during unmounting while the tip used above in the TOF measurements was laser damaged in experiments, such that the tip apex radii could not be determined afterwards via an scanning electron microscope (SEM). Otherwise, a comparison of experimentally determined and theoretically predicted field-enhancements[423] would be interesting.

Similar intensities have been reached in other nanotip experiments[66, 368, 361] without observing damage to the nanotip. Specifically Ref.[361] states that, under conditions similar to our experiment, even at intensities up to a factor 6 above the kink, no damage seems to occur to the nanotip. Several studies indicate that one of the major damaging mechanisms for nanostructures is heating by the electric field inside the material in combination with inefficient heat conduction[424, 425, 426]. Acccumulated heating is rather a problem at MHz repetition rates[424] which has also been shown to potentially alter the emission characteristics[411]. In contrast, at kHz rates there is enough time between consecutive pulses for the heat to be dissipated. Moreover, since the nanotip quickly takes on a micron length scale away from the apex due to the conical structure of the shank, a better heat dissipation can be expected compared to e.g. nanowires that, nevertheless, exhibit a damage threshold of around $10^{13}\mathrm{W/cm}^2$ of incident intensity at kHz repetition rates[426]. Finally, as a general rule the damage threshold increases with decreasing pulse length. In this regard, our experimental conditions, a tungsten nanotip irradiated by sub-two-cycle laser pulses at 10 kHz repetition rate and below 300 μW average power seems to be ideal for achieving high local intensities without damage. Indeed, we do not observe significant

changes of the photocurrent over a day of measurements and intensity scans in the range of Fig. 7.12 yield reproducible results.

A comparison of the TIPTOE signal for two different signal powers of 60 μW (6 nJ/pulse) and 3 μW (0.3 nJ/pulse) is shown in Fig. 7.12 b) and c), respectively, for a pump power of 180 μW (18nJ/pulse) corresponding to an enhanced near-field peak intensity of around $0.55 \cdot 10^{13}\mathrm{W/cm}^2$. Originally, TIPTOE has been derived for conditions where the signal field only constitutes a small perturbation of the pump field[32], but has also been extended to conditions where this restriction does not hold at the expense of a more complicated retrieval[167]. For the lower signal pulse powers where our experiments are typically conducted (see Fig. 7.12 c), no offset, asymmetry or harmonic distortion is observed despite relatively high expected electric field ratios of 0.15 between signal and pump pulse. It can be argued that the original TIPTOE conditions are still approximately fulfilled due to the low nonlinearity (<2) in the tunneling regime. In contrast, at the highest signal powers (Fig. 7.12 b), we observe a prominent asymmetry of the TIPTOE signal that is characterized by a low-frequency offset background (red line), reminiscent of an autocorrelation signal.

As illustrated in Fig. 7.12 d), we also investigated the maximum signal in the nanoTIPTOE trace in positive (red triangles) and negative (blue squares) direction normalized by the total photocurrent signal. The x-axis is expressed in terms of the squareroot of the power ratio rather than the electric field ratio, since pump and signal pulses do not exactly exhibit the same dispersion. As long as the signal pulse is only a small perturbation, the datapoints would be expected to lie on a single straight line. As anticipated from the finding above, this is only true for the lowest signal powers. When going to higher signal-pump ratios, the amplitude in negative direction starts to flatten out while the positive amplitude keeps increasing, which is caused by the nonlinearity of the emission process.

This behavior is well reproduced by theoretical calculations of the amplitude ratios (red and blue solid line). Here, we used a Fowler-Nordheim (FN) tunneling rate[66] and a pulse with 4.5 fs FWHM. However, as shown in Ref. [381] using time-dependent DFT calculations (see supplementary Fig. S5 therein) and also observed here, the experimental photoemission rate undergoes a significantly faster evolution of the nonlinearity than predicted by the FN rate. The latter only shows satisfactory agreement only deep in the tunneling regime[381]. In order to obtain a nonlinearity in agreement with the experimental conditions, we therefore had to use an intensity about a factor 5 higher than in the experiment. A better expression for the photoemission rate would thus be desirable[361, 408]. Moreover, we had to scale the theoretical amplitude ratio by 0.3, which, however, can be explained by the lower transimpedance gain at f_{rep} compared to $f_{\mathrm{rep}}/2$ in the experiment. Finally, we note that by subtracting the background offset (red line in Fig. 7.12 b)) a nearly identical linear dependence for both maximum negative (gray star) and positive (black cross) amplitudes is obtained. Some more discussion on the physical reason behind this observation might be necessary, nevertheless we will use the same method later for the correction of a nanoTIPTOE trace exhibiting the same effect.

Comparison of nanoTIPTOE and rescattering streaking

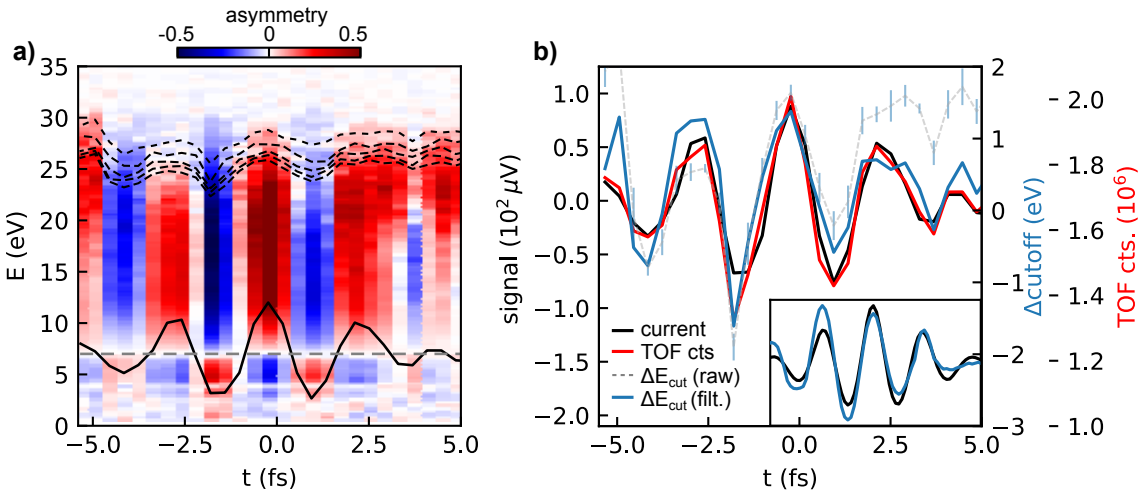

Figure 7.13: Spectrally-resolved pump-probe measurements: a) the delay-dependent asymmetry of the delay-normalized spectra. The current signal is indicated as black line (offset, arbitrary units) together with five different contour lines (black dashed lines). The asymmetry below the gray dashed line has been increased by a factor of 5 for better visibility. b) delay-dependence of the current signal (black line), of the TOF counts (red line), of the raw cutoff energy shift (gray dashed line with errorbars) and of the Fourier-filtered energy shift (blue solid line). The inset compares the cutoff energy shift and current calculated simulated in the 1D-SMM.

In order to obtain a deeper insight into the emission dynamics and the signal generation, we also performed measurements were we simultaneously recorded the TOF-spectrum and the modulated photocurrent under the nanoTIPTOE conditions described before. Due to our chopping rate at $f_{\mathrm{rep}}/2$ for consecutive pump pulses there is either a signal pulse present or not. The TOF acquisition is triggered only when a signal pulse is present. For an increased electron countrate we applied a small lens voltage (100 V) to the TOF. Since the effect of the signal pulse on the spectrum is largely dominated by the change in photoemission rate which obscures changes of the spectral shape, we calculate the pump-probe asymmetry A_{pp}. We define it as the countrate normalized spectrum S_{norm} at delay t subtracted and subsequently divided by the delay-averaged countrate-normalized spectrum:

$$A_{\mathrm{pp}}(E,t) = \frac{S_{\mathrm{norm}}(t,E) - < S_{\mathrm{norm}}(t,E) >_t}{< S_{\mathrm{norm}}(t,E) >_t} \tag{7.15}$$

The result for an estimated incident pump intensity of $1.2 \cdot 10^{12}\mathrm{W/cm^2}$(11 nJ/pulse) (estimated near-field intensity of around $4 - 6 \cdot 10^{13}\mathrm{W/cm^2}$) and incident signal intensity of around $1.6 \cdot 10^{10}\mathrm{W/cm^2}$ (0.15nJ/pulse) is shown in Fig. 7.13 a). The asymmetry below 7 eV (gray dashed line) was multiplied by a factor of 5 for better visibility. The shape of the TIPTOE signal (solid black line) is also shown. Additionally, we determined several

isocontourlines of the countrate-normalized spectra close to the cutoff (dashed lines). Interestingly, the asymmetry also exhibits a phase-jump at 7 eV, above which it is in phase with the current signal and out of phase below. While this could again be a hint at charge interaction, the phase-jump in this case more likely indicates the transition from direct to rescattering electrons. The asymmetry above 7 eV is remarkably high, up to 50% which would also be consistent with rescattering dynamics.

Figure 7.13 b) shows the comparison between the current signal (black line) and the TOF-countrate (red line). Very good agreement is observed. Additionally, the modulation of the cutoff and its standard deviation is depicted (gray dashed line with errorbars), calculated from the isocontourlines in a). In principle, in the absence of charge interaction, this modulation can be used via the rescattering streaking approach as an alternative method to reconstruct the field. In turn, it can be used to gauge the influence of charge interaction by comparing it to the photocurrent signal. While clear oscillations that are in phase with the photocurrent signal are observable, the trace seems to be affected by a slow drift. We took several traces but all with similar problems. For a qualitative comparison of the current signal, we tried to remove this drift by filtering out wavelength components below 250 nm and above 1200 nm via Fourier-transformation. For lower pump-probe delays (negative delay: pump arrives first) the filtered cutoff curve (solid blue line) shows a larger amplitude compared to the current signal which is reversed for larger delays. As shown in the inset, this behavior is qualitatively reproduced in single electron 1D-SMM calculations using an FN emission rate (near-field pump intensity $5 \cdot 10^{13}\mathrm{W/cm}^2$, a Gaussian pulse with 4 fs duration at 750 nm central wavelength, electric field ratio of 3.5%). The observation can be understood by comparing the phase of the TIPTOE and rescattering streaking response function shown in Fig. 3.8 and Fig 3.9, respectively. The nearly linear increase of the phase of the rescattering streaking response function corresponds to a shift of the signal envelope by around $0.7 \cdot T_0 \approx 1.75$ fs to smaller delays. As discussed in Sec. 3.3.4, this leads to the interpretation that the rescattering streaking gate is approximately centered around the instance of electron rescattering, while the TIPTOE gate is localized around the time of the electron tunneling emission burst.

This above observation is again consistent with field-driven electron dynamics despite multi-electron emission. Care should be taken given the limited data quality of the rescattering cutoff trace. Nevertheless, a similar finding is provided by the 1D-SMM description of the nano-bowtie experiments in Ref. [416]. Moreover, this interpretation is also in agreement with the results of Sec. 2, where the corresponding near-field intensity marked only the onset of charge interaction effects on the electron dynamics. A further analysis would require better data quality and a systematic study of the pump pulse CEP-dependence is desirable. For both, rescattering streaking in the single electron picture and the effect of strong charge interaction, a modulation of the cutoff in phase with the countrate change is expected, if signal and pump have the same central wavelength. Therefore, using a signal pulse at half of the pump wavelength and below, as already proposed above, would help to gain additional insight since there not only the rescattering cutoff is shifted in phase but also the CEP-dependence of the amplitude response function is significantly different to TIPTOE. Additionally, in case of several half-cycles adding to the signal, their contribution

would be discernible by different phase-shifts. Therefore, using DFG in the signal arm for future experiments, will help to gain a lot more information about the physical process at the nanotip.

For completeness, we want to mention that the quenching of the quiver motion[88] that could also influence the spectral shape, does not play a role here. Firstly, the quiver amplitude is below 0.8 nm even at the highest intensities whereas the expected field decay length is on the order of 10 nm, resulting a strong-field adiabaticity parameter $\delta_{\mathrm{SF}} > 10$ which is in the quiver regime. Secondly, the influence of the quiver motion quenching would be a reduction of the cutoff compared to the $10\,U_{\mathrm{p}}$-law, which we do not observe.

7.3.5 Field and spatially resolved measurements of an OAM beam

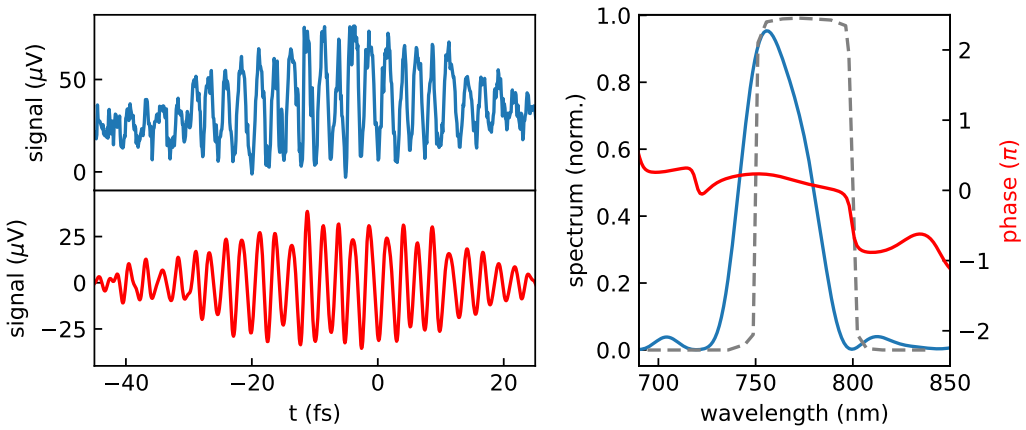

Figure 7.14: nanoTIPTOE signal from the OAM beam: a) and b) raw and Fourier-filtered (background substracted) signal trace, respectively. c) Spectrum (blue line) and phase (red line) together with the transmission of the employed bandpass (gray dashed line).

Having demonstrated that the field at the apex of the nanotip can be reconstructed, we show below that the approach presented above allows spatially resolved measurement of laser fields in free-space is possible. This section is an extension to the spatially resolved CEP-determination based on TOF-measurements presented in Ref. [368]. In our approach, the tip is scanned through the focus, thereby sampling the signal pulse at different positions using nanoTIPTOE.

Ideally, the pump field at the apex should not change while scanning the signal beam focus. Co-moving the pump beam with the tip, or more generally moving both beams relative to another without changing the relative delay is practically almost impossible. Therefore, in our approach we decreased the pump beam input size by a factor of roughly 2.5 (see Sec. 7.3.2). This results in an increase by the same factor in the pump beam focus size, thereby providing an almost uniform field over the length scale of the signal beam spotsize. In addition, we generate an orbital angular momentum (OAM) beam in the signal arm by placing a Vortex plate which results in a donut-shaped focal intensity

and a phase-shift of $2\,\pi$ of the carrier wave when moving around the focus. Additionally, a bandpass filter corresponding to the working range of the Vortex plate is used.

The advantage of the OAM beam for demonstrating the spatially resolved measurements is twofold. Firstly, there is a clear expectation for the mode to be measured due to the singularity in the center which makes it easy to compare theory and experiment. Secondly, a π phase jump occurs across the center which is a result of the singularity and in principle should appear as a sharp step. Moreover, the phase jump is protected by topology, manifested in the orbital angular momentum of the beam, meaning that it will occur even under non-perfect alignment and focusing conditions. Ideally, to show the limit of the spatial resolution, near fields from nanostructures should be used to generate subwavelength features. However, it would not be known what to expect and furthermore they can only be measured in the near field and not in free-space due to the diffraction limit in any imaging setup.

A representative raw signal trace for the employed incident pump intensity of around $3.5 \cdot 10^{12}\mathrm{W/cm}^2$ (320 nJ/pulse) and estimated incident peak signal intensity on the order of $0.5 - 1 \cdot 10^{10}\mathrm{W/cm}^2$(5 nJ/pulse) is shown in Fig. 7.14 a). As before, we remove the offset and noise by Fourier-filtering, resulting in a zero-centered smooth curve (see b)). Again, this approach is motivated by Ref. [167]. The spectral intensity (blue line) and spectral phase (red line) are depicted in Fig. 7.14 c) together with the nominal bandpass transmission (dashed line; left axis).

The spatially resolved, delay-averaged amplitude of the OAM beam is illustrated in Fig. 7.15 a). It has been obtained by spatially scanning the nanotip through the beam while keeping the delay between signal and pump pulse fixed and averaging the absolute value over four different delays. No offset correction has been applied in this case. A clear, typical donut-shaped focus with a minimum in the middle is visible. The slight asymmetry manifested in the diagonal maxima is due to a small astigmatism introduced by the first telescope. For comparison the theoretical expectation for a Laguerre-Gauss mode is illustrated in Fig. 7.15 b). The amplitude of the pump field is shown in Fig. 7.15 c), which is mostly uniform but exhibits some decay towards the edges of the scanning range.

Finally, we demonstrate the attosecond field- and spatially-resolved measurement of the OAM focus by scanning the nanotip apex through the donut mode along the dotted line indicated in Fig. 7.15 a) and performing a delay scan at each position. The result is shown in Fig. 7.16 a). The stepsize is $1\,\mu$m. Two distinct maxima at different positions separated by a minimum are observed, as expected from the mode profile depicted above. Additionally, since the phase changes continuously by $2\,\pi$ when moving around the minimum, there is a phase-jump by π when crossing the minimum of the OAM mode, which upon closer inspection is visible in the data. It can be seen even clearer in the close-up around delay zero, shown in Fig. 7.16 b).

With the help of the spatio-temporal measurements, we calculate the wavelength dependent amplitude (blue line) and phase (red line) of the OAM mode by Fourier-transforming along the time axis, as can be seen in Fig. 7.16 c). While the amplitude (blue solid line) exhibits two maxima roughly separated by roughly $10\,\mu$m and a smooth change in between, the phase (red solid line) undergoes a sudden jump of π across the amplitude minimum.

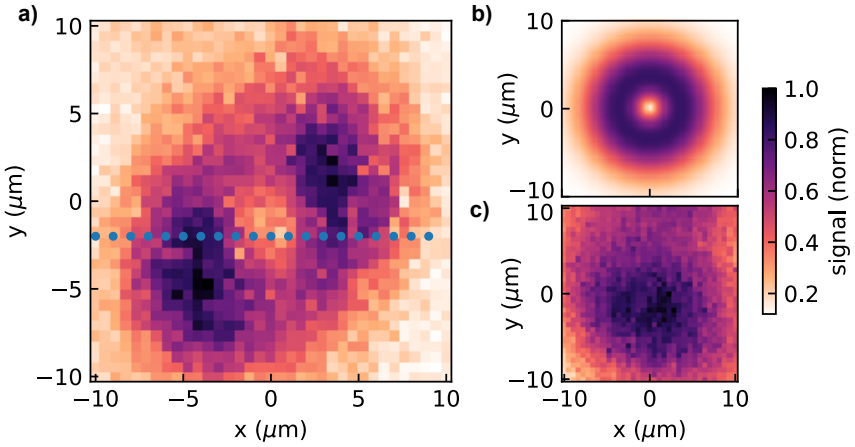

Figure 7.15: Spatially resolved signal from an OAM beam. a) Spatially-resolved nanoTIPTOE-signal by scanning the nanotip apex through the focus of the OAM signal and Gaussian pump beam for four different time-delays. b) Theoretical amplitude of the electric field of a Laguerre-Gauss beam (l=1, p=0, ω_0=5 μm, λ=750 nm). c) Signal strength at the laser repetition rate caused by the Gaussian pump beam.

The jump occurs on the length scale of a single step, i.e. 1 μm. Overall, decent agreement between the theoretical expectation (dashed lines) and the measurement is observed. However, an almost linear phase shift seems to be superimposed on the measured phase. It could originate from a misalignment of both beams, e.g. when propagating under a slight angle or the residual astigmatism of the OAM beam. In the present measurements, we used a bandpass to restrict the signal beam spectrum to the working range of the vortex plate. Without the bandpass the OAM pulses would develop a more complex spatio-temporal behavior. Together with a tighter focusing and ultimately the exploitation of near-fields for demonstrating sub-wavelength resolution and a smaller scanning stepsize, this approach could reveal the full potential of our approach.

In the nanoTIPTOE approach the enhanced field at the apex is measured. In order to obtain the local electric field of the incident signal pulse, the response function of nanotip apex has to be taken into account. As shown in Fig. 2.10 the nanotip near-field response exhibits a slightly increasing amplitude with wavelength, however, with a nearly constant phaseshift of -0.5 π over the visible range. Moreover, in principle the response function could be determined experimentally by comparing TIPTOE measurements on the nanotip and in gas. If only the relative amplitude and phase at individual wavelengths is desired, no calibration is required.

7.4 Discussion

We have demonstrated that the near field on the nanotip apex can be measured using the nanoTIPTOE approach and studied different aspects of the response function. By

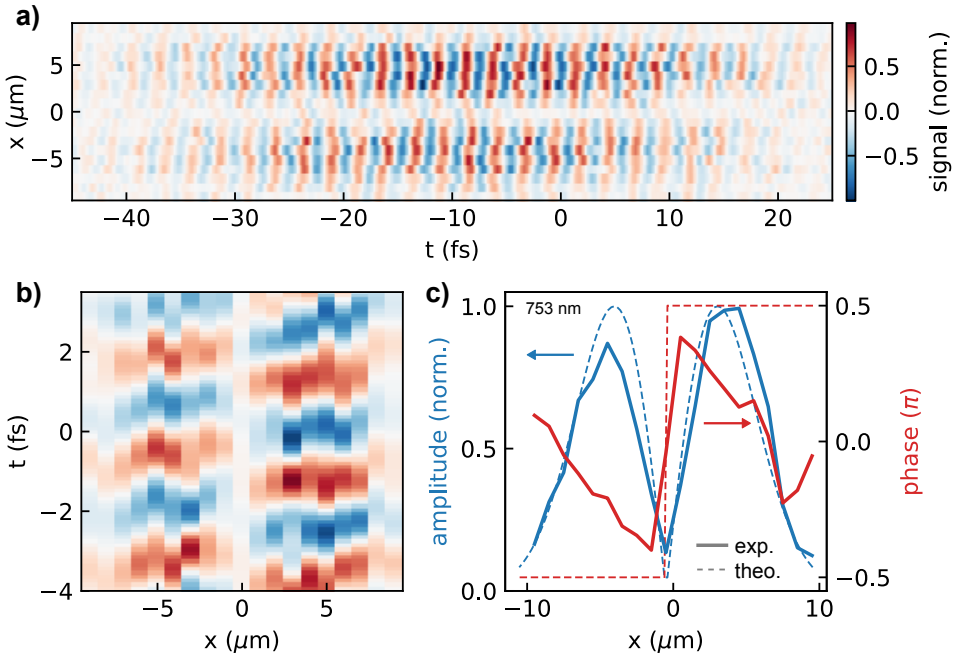

Figure 7.16: Spatio-temporally resolved measurement of the OAM beam: a) scan along the dotted line indicated in Fig. 7.15 a). b) Close-up of the delay-scans around t=0. The plot has been rotated w.r.t. a) for a better comparison with the next panel. c) Spatially resolved amplitude and spectral phase at a wavelength of 753 nm.

investigating the delay-dependent change of the photoemission spectra and comparing the results to the dedicated discussion of charge interaction effects in Sec. 7.3.3, we have found indications that the most of our nanoTIPTOE measurements are taken in a regime that is only weakly affected by space-charge effects. Finally, we have shown that the nanotip can be scanned spatially in order to obtain local measurements of a laser field in free-space. This section will therefore focus on the discussion of the limitations, possible improvements, implementations and applications of the method.

The shortest wavelengths that can be measured with this approach are ultimately limited by the work function of the nanotip (i.e. $4.5\,\mathrm{eV}\hat{=}275\,\mathrm{nm}$), beyond which single photon ionization is possible and likely dominates over the modulation of the tunneling emission. However, already at longer wavelengths, effects such as multipath interference could occur[427]. The same limitation is true for the wavelength range of the pump pulse and staying above a nonlinearity of two in the multiphoton regime ($\hat{=}530\,\mathrm{nm}$) seems advisable. It would be preferential to go to longer wavelengths since the nonlinearity for multiphoton emission is increased and, moreover, the tunneling regime is reached at lower intensities. The latter could avoid damage to the nanotip. While not so important for our setup, it could play a role for high repetition rate experiments. Ultimately, for very long pump wavelengths, the sensitivity for short wavelength signal radiation will be suppressed. For the signal pulse, there seems to be no apparent limit. The minimum relative intensity of signal and pump pulse that can be resolved, is estimated in our setup to lie between $2.5 \cdot 10^{-3}$ and 10^{-2} but could be improved at higher repetition rates or with longer integration times.

Experimentally, as discussed above, supplementing our experiments with signal pulses at longer wavelengths created via DFG would allow a more complete characterization of the nanoTIPTOE response function and, moreover, could reveal in a clearer fashion how strongly the electron continuum dynamics is driven by the near field and affected by charge interactions. Eventually, this approach could also be used to investigate the dynamics of the excited electron distribution inside the nanotip[420], similar to the THz study in Ref. [428], but on a two to three orders of magnitude faster timescale. Theoretically, a fully dimensional numerical model that takes into account charge interaction effects on the nanotip, similar to Refs. [362, 409, 66, 419], would be desirable.

So far, spatial resolution could strictly speaking only be demonstrated down to about 3 micron, the distance between the electric field minimum in the center and the position of the maximum of the donut mode, which is however already about a factor of two below the diffraction limit ($\simeq 7\,\mu\mathrm{m}$) for the given numerical aperture (NA$\simeq 0.05$) used for focusing. A factor of 4-6 harder focusing is should be implementable in our setup with which subwavelength resolution should be possible to demonstrate. Ultimately, the resolution is limited by the interaction of the nanotip with the field close to the apex. In Ref. [423] it has been shown theoretically, that the induced surface charge on the shank can contribute to the field enhancement at the apex. The effect is only important for small tips and large opening angles and limited to a region of about 100 nm from the apex. We therefore expect a maximum resolution on the order of the radius of the nanotip.

For the further development of PHz electronics, the interfacing of lightwave driven devices, such as the nanotip in our experiments or the bowtie structures in Refs. [416, 381,

380, 165] with classical GHz nanoelectronic switches would allow the creation of powerful hybrid ultrafast integrated electronic circuits with an interface to the world of CMOS devices. It is, therefore, instructive to consider the amount of charges needed for switching modern field-effect-transistor (FETs), such as the fin FET (FinFET) or gate-all-around FET (GAAFET) which are found in the latest CPUs[429]. The gate-capacitance of FinFETs is on the order of 1 fF and even lower at switching voltages of around 1 V[430, 431]. The resulting gate-charge is in the range of the total charge of around 0.1 fC per shot observed in our experiments, which means that classical transistors could potentially be switched with the nanotip photocurrent. For fewer electrons per shot, currently developed nanowire transistors[432] or single-electron transistors[433, 434] could be suitable.

There are a lot of immediate applications of the demonstrated approach that should be accessible to a large number of laboratories due to the simplicity of the method which does not require XUV generation and large ultra-high vacuum infrastructures. An example would be the measurement of grating coupled nanoplasmonic fields from nanotapers, or generalizing the approach in Ref. [435] by combining the method with scanning tunneling microscopy for attosecond nanometer resolution. Given that a charge modulation of around 10 % is easily detectable in electron imaging setups, this method could potentially be combined with PEEM, or alternatively with field-electron microscopy (FEM) from a nanotip as in Ref [436], that would allow apex nanoscale emission-site resolved measurement of near fields with attosecond resolution.

7.5 Conclusion and Outlook

In conclusion, we have demonstrated the attosecond field-resolved measurement of the enhanced near fields at the nanotip apex using photocurrents, by extending the approach of Ref. [165]. Since on the order of few 100 to 1000 electrons per shot are detected, we investigated the effect of space-charge on the electron dynamics by combining our approach with TOF-detection. Clear signatures of charge interaction are observed at the highest intensities with hints remaining at lower powers. Secondly, we experimentally investigated the spectral phase reconstruction as well as the CEP-dependence of the amplitude and phase of the nanoTIPTOE response function. Furthermore, we measured the intensity dependence of the total photocurrent and the nanoTIPTOE traces. For the former, good agreement with previous literature is achieved, which allows us to identify the onset of the tunneling regime, where our experiments are conducted. Moreover, the delay-dependent photoelectron spectra were compared to the nanoTIPTOE signal results and agreement with field-controlled dynamics was observed. Finally, the attosecond field and spatially resolved measurement of an OAM mode is demonstrated with a spatial resolution on the order of the wavelength. The latter methodology could become a milestone for spatio-temporal beam characterization. In the context of lightwave electronics, the interfacing of the nanotip with current classical nano-electronic components is discussed.

While charge interaction clearly affects the electron dynamics at higher pump intensities, our results indicate that only minor effects are to be expected at the conditions of

the field-resolved measurements. A further clarification of the effect of charge interaction on both the electron dynamics and the tunneling process, could be obtained by using signal pulses at longer wavelengths. Nevertheless, our results indicate that the field-control of currents is possible even under significant influence of space-charge interaction on the electron dynamics, which is of importance for potential applications.

So far, the demonstrated spatial resolution was limited to above the signal pulse wavelength due to the relatively loose focusing. A harder focusing is possible and should be enough to demonstrate sub-wavelength resolution. In the long-term, combining our approach with the light-triggered CEP-dependent scanning tunneling microscopy demonstrated in Ref. [435], could provide a possibility for attosecond temporal characterization of nanoscale near-field on nano-/optoelectronic devices and many more applications are conceivable.

This work pushes nanoscale near-field resolved measurements and its understanding. The demonstrated applications show the potential of the approach. Together with Ref. [165], our results, therefore, are breaking new grounds and open the door for rapid further development of the field.

Appendix A

Dual-frequency demodulation

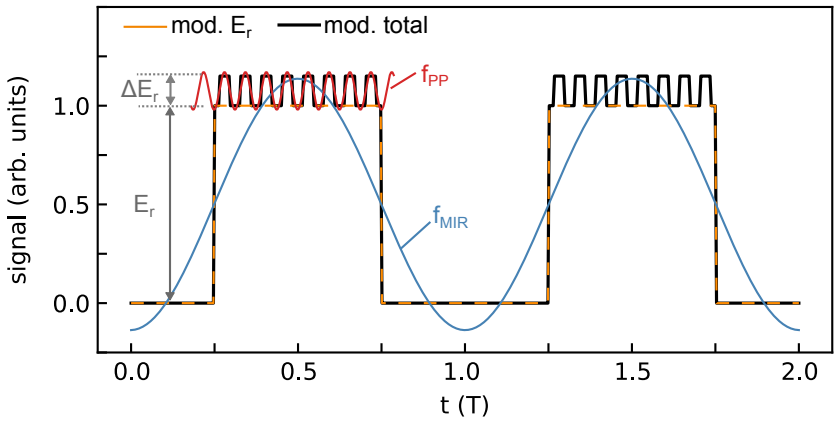

Figure A.1:
Schematic illustration of the dual-frequency demodulation approach used in the solid-state reflectometry setup of Chap. 5.

Figure A.1 illustrates schematically the modulated voltage signal $S(t)$ (black line) at the input of the lock-in amplifier for the solid state reflectometry experiments described in Chap. 5 at a fixed sampling and pump-probe delay. The MIR-pulse is modulated by an optical chopper at a frequency f_{MIR}. The effect of this modulation is shown as orange dashed line which is proportional to the reflected field E_{r} without pump. The pump beam is modulated at another incommensurate frequency f_{PP}. The effect of this modulation is proportional to ΔE_{r}. For simplicity we assumed the modulation to occur in a rectangular fashion, i.e. either fully blocking or fully transmitting the pulses. The modulation functions are denoted as $a(t)$ and $b(t)$, for the MIR- and PP-modulation, respectively. The component at the first harmonic at the respective modulation frequency, as would be measured by the lock-in-amplifier, is illustrated as solid blue and solid red line, respectively.

The signal can be described by:

$$S(t) = a(t) \cdot E_{\mathrm{r}} + a(t) \cdot b(t) \cdot \Delta E_{\mathrm{r}} = a(t)\Big(E_{\mathrm{r}} + b(t)\Delta E_{\mathrm{r}}\Big) \tag{A.1}$$

We can now make use of the Fourier-series expansion of the periodic rectangular function:

$$a(t) = \frac{1}{2} + c_1 \cos(\omega_{\mathrm{MIR}} \cdot t) + \mathcal{O}(3\omega_{\mathrm{MIR}}), \tag{A.2}$$

where c_1 is the coefficient for the first harmonic, which scales with harmonic order k as $|c_\mathrm{k}| \propto 1/k$ and $b(t)$ is expanded analogously. We neglect harmonic orders higher than 2, as indicated by $\mathcal{O}(3\omega_{\mathrm{MIR}})$. We can now insert the expansion into Eq. A.1, in order to obtain the modulation at the frequencies f_{MIR} and f_{PP}:

$$\begin{aligned} S(t) = & \left[\tfrac{1}{2} + c_1 \cos(\omega_{\mathrm{MIR}} t)\right] \cdot \left(E_\mathrm{r} + \left[\tfrac{1}{2} + c_1 \cos(\omega_{\mathrm{PP}} t)\right] \cdot \Delta E_\mathrm{r}\right) + \mathcal{O}(3\omega_{\mathrm{MIR}}, 3\omega_{\mathrm{PP}}) \\ = & \quad \tfrac{1}{2} E_\mathrm{r} + \tfrac{1}{4} \Delta E_\mathrm{r} \\ & + \left(E_\mathrm{r} + \tfrac{1}{2} \Delta E_\mathrm{r}\right) \cdot c_1 \cos(\omega_{\mathrm{MIR}} t) \\ & + \tfrac{1}{2} \Delta E_\mathrm{r} \cdot c_1 \cos(\omega_{\mathrm{PP}} t) \\ & + \Delta E_\mathrm{r} \cdot c_1^2 \cos(\omega_{\mathrm{MIR}} t) \cos(\omega_{\mathrm{PP}} t) \\ & + \mathcal{O}(3\omega_{\mathrm{MIR}}, 3\omega_{\mathrm{PP}}). \end{aligned}$$

Traditional approaches using cascaded demodulation (e.g. [437]), usually measure ΔE_r via the second to last term in the above equation, by first demodulating with ω_{MIR} with a high enough bandwidth (small time constant), such that modulation at the much lower ω_{PP} (in that setting) is detectable on the first demodulated signal. In our case, we obtain ΔE_r through the third to last term and both ω_{MIR} and ω_{PP} are much higher and way above the demodulation bandwidth of either channel. As can be seen, we need to manipulate the demodulated signal, in order to obtain E_r and ΔE_r

$$E_\mathrm{r} \quad \propto < S >_{\mathrm{MIR}} - < S >_{\mathrm{PP}} \tag{A.3}$$

$$\Delta E_\mathrm{r} \propto 2 \cdot < S >_{\mathrm{PP}}, \tag{A.4}$$

where $< ... >_{\mathrm{MIR}}$ and $< ... >_{\mathrm{PP}}$ denote demodulation at f_{MIR} and f_{PP}, respectively. The proportionality constant is $c_1/2$ for both cases, but can be neglected since electro-optic sampling only yields relative amplitudes anyway. The intuitive interpretation of this result is given in the main text.

Bibliography

[1] T. H. Maiman. Stimulated Optical Radiation in Ruby. *Nature*, 187(4736):493–494, 1960.

[2] F. J. McClung and R. W. Hellwarth. Giant Optical Pulsations from Ruby. *J. Appl. Phys.*, 33(3):828–829, 1962.

[3] H. W. Mocker and R. Collins. Mode competition and self-locking effects in aq-switched ruby laser. *Appl. Phys. Lett.*, 7(10):270–273, 1965.

[4] R. Fork, B. Greene, and C. V. Shank. Generation of optical pulses shorter than 0.1 psec by colliding pulse mode locking. *Appl. Phys. Lett.*, 38(9):671–672, 1981.

[5] M. Dantus, M. J. Rosker, and A. H. Zewail. Real-time femtosecond probing of transition statesin chemical reactions. *J. Chem. Phys.*, 87(4):2395–2397, 1987.

[6] A. H. Zewail. Femtochemistry: Atomic-scale dynamics of the chemical bond. *J. Phys. Chem. A*, 104(24):5660–5694, 2000.

[7] T. Brabec and F. Krausz. Intense few-cycle laser fields: Frontiers of nonlinear optics. *Rev. Mod. Phys.*, 72(2):545, 2000.

[8] F. Krausz and M. Ivanov. Attosecond physics. *Rev. Mod. Phys.*, 81(1):163–234, 2009.

[9] M. Hentschel, R. Kienberger, C. Spielmann, G. A. Reider, et al. Attosecond metrology. *Nature*, 414(6863):509, 2001.

[10] A. McPherson, G. Gibson, H. Jara, U. Johann, T. S. Luk, I. A. McIntyre, K. Boyer, and C. K. Rhodes. Studies of multiphoton production of vacuum-ultraviolet radiation in the rare gases. *J. Opt. Soc. Am. B*, 4(4):595–601, 1987.

[11] M. Ferray, A. L'Huillier, X. F. Li, L. A. Lompré, G. Mainfray, and C. Manus. Multiple-harmonic conversion of 1064 nm radiation in rare gases. *J. Phys. B*, 21(3):L31, 1988.

[12] J. Itatani, F. Quéré, G. L. Yudin, M. Y. Ivanov, F. Krausz, and P. B. Corkum. Attosecond Streak Camera. *Phys. Rev. Lett.*, 88(17):173903, 2002.

[13] R. Kienberger, E. Goulielmakis, M. Uiberacker, A. Baltuska, et al. Atomic transient recorder. *Nature*, 427(6977):817, 2004.

[14] M. Schultze, M. Fieß, N. Karpowicz, J. Gagnon, M. Korbman, M. Hofstetter, S. Neppl, A. L. Cavalieri, Y. Komninos, T. Mercouris, C. A. Nicolaides, R. Pazourek, S. Nagele, J. Feist, J. Burgdörfer, A. M. Azzeer, R. Ernstorfer, R. Kienberger, U. Kleineberg, E. Goulielmakis, F. Krausz, and V. S. Yakovlev. Delay in photoemission. *Science*, 328(5986):1658–1662, 2010.

[15] A. L. Cavalieri, N. Müller, T. Uphues, V. S. Yakovlev, A. Baltuška, B. Horvath, B. Schmidt, L. Blümel, R. Holzwarth, S. Hendel, M. Drescher, U. Kleineberg, P. M. Echenique, R. Kienberger, F. Krausz, and U. Heinzmann. Attosecond spectroscopy in condensed matter. *Nature*, 449(7165):1029–1032, 2007.

[16] A. Schiffrin, T. Paasch-Colberg, N. Karpowicz, V. Apalkov, D. Gerster, S. Mühlbrandt, M. Korbman, J. Reichert, M. Schultze, S. Holzner, J. V. Barth, R. Kienberger, R. Ernstorfer, V. S. Yakovlev, M. I. Stockman, and F. Krausz. Optical-field-induced current in dielectrics. *Nature*, 493(7430):70–74, 2013.

[17] T. Paasch-Colberg, S. Y. Kruchinin, Özge Sağlam, S. Kapser, S. Cabrini, S. Muehlbrandt, J. Reichert, J. V. Barth, R. Ernstorfer, R. Kienberger, V. S. Yakovlev, N. Karpowicz, and A. Schiffrin. Sub-cycle optical control of current in a semiconductor: from the multiphoton to the tunneling regime. *Optica*, 3(12):1358–1361, 2016.

[18] C. Heide, T. Higuchi, H. B. Weber, and P. Hommelhoff. Coherent Electron Trajectory Control in Graphene. *Phys. Rev. Lett.*, 121(20):207401, 2018.

[19] T. Rybka, M. Ludwig, M. F. Schmalz, V. Knittel, D. Brida, and A. Leitenstorfer. Sub-cycle optical phase control of nanotunnelling in the single-electron regime. *Nat. Photonics*, 10(10):667–670, 2016.

[20] P. Hommelhoff and M. F. Kling. *Attosecond Nanophysics*. Wiley-VCH Weinheim, 2015.

[21] E. Goulielmakis, V. S. Yakovlev, A. L. Cavalieri, M. Uiberacker, V. Pervak, A. Apolonski, R. Kienberger, U. Kleineberg, and F. Krausz. Attosecond control and measurement: lightwave electronics. *Science*, 317(5839):769–775, 2007.

[22] J. Schötz, Z. Wang, E. Pisanty, M. Lewenstein, M. F. Kling, and M. Ciappina. Perspective on petahertz electronics and attosecond nanoscopy. *ACS Photonics*, 6(12):3057–3069, 2019.

[23] A. Sommer, E. M. Bothschafter, S. A. Sato, C. Jakubeit, T. Latka, O. Razskazovskaya, H. Fattahi, M. Jobst, W. Schweinberger, V. Shirvanyan, V. S. Yakovlev,

R. Kienberger, K. Yabana, N. Karpowicz, M. Schultze, and F. Krausz. Attosecond nonlinear polarization and light-matter energy transfer in solids. *Nature*, 534(7605):86–90, 2016.

[24] J. Schötz. Attosecond experiments on plasmonic nanostructures. *LMU Master Thesis*, 2014.

[25] B. Förg, J. Schötz, F. Süßmann, M. Förster, M. Krüger, B. Ahn, W. Okell, K. Wintersperger, S. Zherebtsov, A. Guggenmos, et al. Attosecond nanoscale near-field sampling. *Nat. Commun.*, 7(1):1–7, 2016.

[26] J. Schötz, B. Förg, M. Förster, W. A. Okell, M. I. Stockman, F. Krausz, P. Hommelhoff, and M. F. Kling. Reconstruction of nanoscale near fields by attosecond streaking. *IEEE J. Sel. Top. Quantum Electron.*, 23(3):77–87, 2016.

[27] B. Förg. *Attosecond dynamics of collective electron effects in nanostructures and molecules*. PhD thesis, Ludwig-Maximilians-Universität München, 2018.

[28] A. S. Johnson, D. R. Austin, D. A. Wood, C. Brahms, A. Gregory, K. B. Holzner, S. Jarosch, E. W. Larsen, S. Parker, C. S. Strüber, et al. High-flux soft x-ray harmonic generation from ionization-shaped few-cycle laser pulses. *Sci. Adv.*, 4(5):eaar3761, 2018.

[29] J. Schötz, B. Förg, W. Schweinberger, I. Liontos, H. A. Masood, A. M. Kamal, C. Jakubeit, N. G. Kling, T. Paasch-Colberg, S. Biswas, M. Högner, I. Pupeza, M. Alharbi, A. M. Azzeer, and M. F. Kling. Phase-Matching for Generation of Isolated Attosecond XUV and Soft-X-Ray Pulses with Few-Cycle Drivers. *Phys. Rev. X*, 10(4):041011, 2020.

[30] S. Sederberg, D. Zimin, S. Keiber, F. Siegrist, M. S. Wismer, V. S. Yakovlev, I. Floss, C. Lemell, J. Burgdörfer, M. Schultze, F. Krausz, and N. Karpowicz. Attosecond optoelectronic field measurement in solids. *Nat. Commun.*, 11(1):430, 2020.

[31] S. Keiber, S. Sederberg, A. Schwarz, M. Trubetskov, V. Pervak, F. Krausz, and N. Karpowicz. Electro-optic sampling of near-infrared waveforms. *Nat. Photonics*, 10(3):159–162, 2016.

[32] S. B. Park, K. Kim, W. Cho, S. I. Hwang, I. Ivanov, C. H. Nam, and K. T. Kim. Direct sampling of a light wave in air. *Optica*, 5(4):402, 2018.

[33] Y. H. Kim, I. A. Ivanov, S. I. Hwang, K. Kim, C. H. Nam, and K. T. Kim. Attosecond streaking using a rescattered electron in an intense laser field. *Sci. Rep.*, 10(1):22075, 2020.

[34] K. T. Kim, C. Zhang, A. D. Shiner, B. E. Schmidt, F. Légaré, D. Villeneuve, and P. Corkum. Petahertz optical oscilloscope. *Nat. Photonics*, 7(12):958–962, 2013.

[35] A. S. Wyatt, T. Witting, A. Schiavi, D. Fabris, P. Matia-Hernando, I. A. Walmsley, J. P. Marangos, and J. W. G. Tisch. Attosecond sampling of arbitrary optical waveforms. *Optica*, 3(3):303, 2016.

[36] P. Carpeggiani, M. Reduzzi, A. Comby, H. Ahmadi, S. Kühn, F. Calegari, M. Nisoli, F. Frassetto, L. Poletto, D. Hoff, J. Ullrich, C. D. Schröter, R. Moshammer, G. G. Paulus, and G. Sansone. Vectorial optical field reconstruction by attosecond spatial interferometry. *Nat. Photonics*, 11(6):383–389, 2017.

[37] D. Auston. Picosecond photoconductors: Physical properties and applications. In *Picosecond Optoelectronic Devices*, pages 73–117. Academic New York, 1984.

[38] P. R. Smith, D. H. Auston, and M. C. Nuss. Subpicosecond photoconducting dipole antennas. *IEEE J. Quantum Electron.*, 24(2):255–260, 1988.

[39] J. Valdmanis, G. Mourou, and C. Gabel. Picosecond electro-optic sampling system. *Appl. Phys. Lett.*, 41(3):211–212, 1982.

[40] D. Auston and M. Nuss. Electrooptical generation and detection of femtosecond electrical transients. *IEEE J. Quantum Electron.*, 24(2):184–197, 1988.

[41] Q. Wu and X.-C. Zhang. Free-space electro-optic sampling of terahertz beams. *Appl. Phys. Lett.*, 67(24):3523–3525, 1995.

[42] Z. Chang. *Fundamentals of attosecond optics*. CRC press, 2016.

[43] J.-C. Diels and W. Rudolph. *Ultrashort laser pulse phenomena*. Elsevier, 2006.

[44] D. Strickland and G. Mourou. Compression of amplified chirped optical pulses. *Opt. Commun.*, 56(3):219–221, 1985.

[45] M. Schenk, M. Krüger, and P. Hommelhoff. Strong-Field Above-Threshold Photoemission from Sharp Metal Tips. *Phys. Rev. Lett.*, 105(25):257601, 2010.

[46] J. Eberly and J. Javanainen. Above-threshold ionisation. *Eu. J. Phys.*, 9(4):265, 1988.

[47] N. Ammosov, MV Delone and V. Krainov. Tunnel ionization of complex atoms and of atomics ions in an alternating electromagnetic field. *Sov. Phys. JETP*, 74(6):1191, 1987.

[48] F. A. Ilkov, J. E. Decker, and S. L. Chin. Ionization of atoms in the tunnelling regime with experimental evidence using Hg atoms. *J. Phys. B*, 25(19):4005–4020, 1992.

[49] D. Bauer and P. Mulser. Exact field ionization rates in the barrier-suppression regime from numerical time-dependent Schrödinger-equation calculations. *Phys. Rev. A*, 59(1):569, 1999.

[50] L. Keldysh et al. Ionization in the field of a strong electromagnetic wave. *Sov. Phys. JETP*, 20(5):1307–1314, 1965.

[51] M. Krüger. *Attosecond physics in strong-field photoemission from metal nanotips*. PhD thesis, Ludwig-Maximilians-Universität München, 2013.

[52] F. Süßmann. *Attosecond dynamics of nano-localized fields probed by photoelectron spectroscopy*. PhD thesis, Ludwig-Maximilians-Universität München, 2013.

[53] F. Bunkin and M. Fedorov. Cold emission of electrons from the surface of a metal in a strong radiation field. *Sov. Phys. JETP*, 21(5):896, 1965.

[54] A. Perelomov, V. Popov, and M. Terentev. Ionization of atoms in an alternating electric field. *Sov. Phys. JETP*, 23(5):924–934, 1966.

[55] A. Perelomov, V. Popov, and M. Terentev. Ionization of atoms in an alternating electric field: II. *Sov. Phys. JETP*, 24(1):207–217, 1967.

[56] A. Perelomov and V. Popov. Ionization of atoms in an alternating electrical field. Ill. *Sov. Phys. JETP*, 25(2), 1967.

[57] Y. H. Lai, J. Xu, U. B. Szafruga, B. K. Talbert, X. Gong, K. Zhang, H. Fuest, M. F. Kling, C. I. Blaga, P. Agostini, et al. Experimental investigation of strong-field-ionization theories for laser fields from visible to midinfrared frequencies. *Phys. Rev. A*, 96(6):063417, 2017.

[58] H. Muller, A. Tip, and M. Van der Wiel. Ponderomotive force and AC Stark shift in multiphoton ionisation. *J. Phys. B*, 16(22):L679, 1983.

[59] P. H. Bucksbaum, R. R. Freeman, M. Bashkansky, and T. J. McIlrath. Role of the ponderomotive potential in above-threshold ionization. *J. Opt. Soc. Am. B*, 4(5):760–764, 1987.

[60] M. Uiberacker, T. Uphues, M. Schultze, A. J. Verhoef, V. Yakovlev, M. F. Kling, J. Rauschenberger, N. M. Kabachnik, H. Schröder, M. Lezius, K. L. Kompa, H. G. Muller, M. J. J. Vrakking, S. Hendel, U. Kleineberg, U. Heinzmann, M. Drescher, and F. Krausz. Attosecond real-time observation of electron tunnelling in atoms. *Nature*, 446(7136):627–632, 2007.

[61] P. Eckle, A. N. Pfeiffer, C. Cirelli, A. Staudte, R. Dörner, H. G. Muller, M. Büttiker, and U. Keller. Attosecond Ionization and Tunneling Delay Time Measurements in Helium. *Science*, 322(5907):1525–1529, 2008.

[62] G. L. Yudin and M. Y. Ivanov. Nonadiabatic tunnel ionization: Looking inside a laser cycle. *Phys. Rev. A*, 64(1):013409, 2001.

[63] O. Smirnova and M. Ivanov. Multielectron High Harmonic Generation: Simple Man on a Complex Plane. In *Attosecond and XUV Physics*, chapter 7, pages 201–256. John Wiley & Sons, Ltd, 2014.

[64] A. S. Landsman, M. Weger, J. Maurer, R. Boge, A. Ludwig, S. Heuser, C. Cirelli, L. Gallmann, and U. Keller. Ultrafast resolution of tunneling delay time. *Optica*, 1(5):343–349, 2014.

[65] X. M. Tong and C. D. Lin. Empirical formula for static field ionization rates of atoms and molecules by lasers in the barrier-suppression regime. *J. Phys. B*, 38(15):2593, 2005.

[66] B. Piglosiewicz, S. Schmidt, D. J. Park, J. Vogelsang, P. Groß, C. Manzoni, P. Farinello, G. Cerullo, and C. Lienau. Carrier-envelope phase effects on the strong-field photoemission of electrons from metallic nanostructures. *Nat. Photonics*, 8(1):37–42, 2014.

[67] P. B. Corkum. Plasma perspective on strong field multiphoton ionization. *Phys. Rev. Lett.*, 71(13):1994–1997, 1993.

[68] A. L'Huillier, L. A. Lompre, G. Mainfray, and C. Manus. Multiply Charged Ions Formed by Multiphoton Absorption Processes in the Continuum. *Phys. Rev. Lett.*, 48(26):1814–1817, 1982.

[69] A. l'Huillier, L. A. Lompre, G. Mainfray, and C. Manus. Multiply charged ions induced by multiphoton absorption in rare gases at 0.53 μm. *Phys. Rev. A*, 27(5):2503–2512, 1983.

[70] B. Walker, E. Mevel, B. Yang, P. Breger, J. P. Chambaret, A. Antonetti, L. F. DiMauro, and P. Agostini. Double ionization in the perturbative and tunneling regimes. *Phys. Rev. A*, 48(2):R894–R897, 1993.

[71] B. Bergues, M. Kübel, N. G. Kling, C. Burger, and M. F. Kling. Single-cycle nonsequential double ionization. *IEEE J. Sel. Top. Quantum Electron.*, 21(5):1–9, 2015.

[72] M. Kohler, T. Pfeifer, K. Hatsagortsyan, and C. Heitel. Frontiers of Atomic High-Harmonic Generation. In P. Berman, E. Arimondo, and C. Lin, editors, *Advances in Atomic, Molecular, and Optical Physics*, pages 159–208. Elsevier Science.

[73] Z. Chen, Y. Wang, T. Morishita, X. Hao, J. Chen, O. Zatsarinny, and K. Bartschat. Revisiting the recollisional excitation-tunneling process in strong-field nonsequential double ionization of helium. *Phys. Rev. A*, 100(2):023405, 2019.

[74] M. Krüger, M. Schenk, P. Hommelhoff, G. Wachter, C. Lemell, and J. Burgdörfer. Interaction of ultrashort laser pulses with metal nanotips: a model system for strong-field phenomena. *New J. Phys.*, 14(8):085019, 2012.

[75] A. Scrinzi. Lecture Notes: Attosecond Physics - Theory. `https://www.physik.uni-muenchen.de/lehre/vorlesungen/wise_11_12/attophysics_theory/script/attophysics.pdf`, 2011. Accessed: 2021-01-09.

[76] W. Becker, F. Grasbon, R. Kopold, D. Milošević, G. Paulus, and H. Walther. Above-threshold ionization: From classical features to quantum effects. *Adv. At. Mol. Opt. Phys.*, 48:35–98, 2002.

[77] M. Ivanov. Ionization in Strong Low-Frequency Fields. In *Attosecond and XUV Physics*, chapter 6, pages 177–200. John Wiley & Sons, Ltd, 2014.

[78] M. Lewenstein, K. C. Kulander, K. J. Schafer, and P. H. Bucksbaum. Rings in above-threshold ionization: A quasiclassical analysis. *Phys. Rev. A*, 51(2):1495–1507, 1995.

[79] M. Lewenstein, P. Balcou, M. Y. Ivanov, A. L'Huillier, and P. B. Corkum. Theory of high-harmonic generation by low-frequency laser fields. *Phys. Rev. A*, 49(3):2117–2132, 1994.

[80] P. Salières, B. Carré, L. Le Déroff, F. Grasbon, G. G. Paulus, H. Walther, R. Kopold, W. Becker, D. B. Milošević, A. Sanpera, and M. Lewenstein. Feynman's Path-Integral Approach for Intense-Laser-Atom Interactions. *Science*, 292(5518):902–905, 2001.

[81] A. Scrinzi. Time-Dependent Schrödinger Equation. In *Attosecond and XUV Physics*, chapter 8, pages 257–292. John Wiley & Sons, Ltd, 2014.

[82] G. Wachter. *Simulation of condensed matter dynamics in strong femtosecond laser pulses*. PhD thesis, Technische Universität Wien, 2014.

[83] B. Willenberg, J. Maurer, B. W. Mayer, and U. Keller. Sub-cycle time resolution of multi-photon momentum transfer in strong-field ionization. *Nat. Commun.*, 10:5548, 2019.

[84] S. Biswas, B. Förg, L. Ortmann, J. Schötz, W. Schweinberger, T. Zimmermann, L. Pi, D. Baykusheva, H. A. Masood, I. Liontos, A. M. Kamal, N. G. Kling, A. F. Alharbi, M. Alharbi, A. M. Azzeer, G. Hartmann, H. J. Wörner, A. S. Landsman, and M. F. Kling. Probing molecular environment through photoemission delays. *Nat. Phys.*, 16(7):778–783, 2020.

[85] G. G. Paulus, W. Nicklich, H. Xu, P. Lambropoulos, and H. Walther. Plateau in above threshold ionization spectra. *Phys. Rev. Lett.*, 72(18):2851–2854, 1994.

[86] C. I. Blaga, F. Catoire, P. Colosimo, G. G. Paulus, H. G. Muller, P. Agostini, and L. F. Dimauro. Strong-field photoionization revisited. *Nat. Phys.*, 5(5):335–338, 2009.

[87] M. Krüger, M. Schenk, and P. Hommelhoff. Attosecond control of electrons emitted from a nanoscale metal tip. *Nature*, 475(7354):78–81, 2011.

[88] G. Herink, D. R. Solli, M. Gulde, and C. Ropers. Field-driven photoemission from nanostructures quenches the quiver motion. *Nature*, 483(7388):190–193, 2012.

[89] J. Schötz, S. Mitra, H. Fuest, M. Neuhaus, W. A. Okell, M. Förster, T. Paschen, M. F. Ciappina, H. Yanagisawa, P. Wnuk, P. Hommelhoff, and M. F. Kling. Nonadiabatic ponderomotive effects in photoemission from nanotips in intense midinfrared laser fields. *Phys. Rev. A*, 97(1):013413, 2018.

[90] B. Walker, B. Sheehy, K. C. Kulander, and L. F. Dimauro. Elastic Rescattering in the Strong Field Tunneling Limit. *Phys. Rev. Lett.*, 77(25):5031–5034, 1996.

[91] C. D. Lin, A.-T. Le, C. Jin, and H. Wei. Elements of the quantitative rescattering theory. *J. Phys. B*, 51(10):104001, 2018.

[92] F. Süßmann, S. Zherebtsov, J. Plenge, N. G. Johnson, M. Kbel, A. M. Sayler, V. Mondes, C. Graf, E. Rhl, G. G. Paulus, D. Schmischke, P. Swrschek, and M. F. Kling. Single-shot velocity-map imaging of attosecond light-field control at kilohertz rate. *Rev. Sci. Instrum.*, 82(9):093109, 2011.

[93] M. Högner. Optical high-order harmonic generation in gas targets with spatially tailored driving fields. Master's thesis, LMU München, 2013.

[94] S. Mitra, S. Biswas, J. Schötz, E. Pisanty, B. Förg, G. A. Kavuri, C. Burger, W. Okell, M. Högner, I. Pupeza, V. Pervak, M. Lewenstein, P. Wnuk, and M. F. Kling. Suppression of individual peaks in two-colour high harmonic generation. *J. Phys. B*, 53(13):134004, 2020.

[95] M. Y. Ivanov, T. Brabec, and N. Burnett. Coulomb corrections and polarization effects in high-intensity high-harmonic emission. *Phys. Rev. A*, 54(1):742–745, 1996.

[96] V. S. Yakovlev, M. Ivanov, and F. Krausz. Enhanced phase-matching for generation of soft X-ray harmonics and attosecond pulses in atomic gases. *Opt. Express*, 15(23):15351–15364, 2007.

[97] S. Kim, J. Jin, Y.-J. Kim, I.-Y. Park, Y. Kim, and S.-W. Kim. High-harmonic generation by resonant plasmon field enhancement. *Nature*, 453(7196):757–760, 2008.

[98] I.-Y. Park, S. Kim, J. Choi, D.-H. Lee, Y.-J. Kim, M. F. Kling, M. I. Stockman, and S.-W. Kim. Plasmonic generation of ultrashort extreme-ultraviolet light pulses. *Nat. Photonics*, 5(11):677–681, 2011.

[99] M. Sivis, M. Duwe, B. Abel, and C. Ropers. Nanostructure-enhanced atomic line emission. *Nature*, 485(7397):E1, 2012.

[100] M. Sivis, M. Duwe, B. Abel, and C. Ropers. Extreme-ultraviolet light generation in plasmonic nanostructures. *Nat. Phys.*, 9(5):304–309, 2013.

[101] M. B. Raschke. High-harmonic generation with plasmonics: feasible or unphysical? *Ann. Phys.*, 525(3):A40–A42, 2013.

[102] J. Tate, T. Auguste, H. G. Muller, P. Salières, P. Agostini, and L. F. DiMauro. Scaling of Wave-Packet Dynamics in an Intense Midinfrared Field. *Phys. Rev. Lett.*, 98(1):013901, 2007.

[103] M. Frolov, N. Manakov, and A. F. Starace. Wavelength scaling of high-harmonic yield: threshold phenomena and bound state symmetry dependence. *Phys. Rev. Lett.*, 100(17):173001, 2008.

[104] A. Shiner, C. Trallero-Herrero, N. Kajumba, H.-C. Bandulet, D. Comtois, F. Légaré, M. Giguère, J. Kieffer, P. Corkum, and D. Villeneuve. Wavelength scaling of high harmonic generation efficiency. *Phys. Rev. Lett.*, 103(7):073902, 2009.

[105] M. B. Gaarde, J. L. Tate, and K. J. Schafer. Macroscopic aspects of attosecond pulse generation. *J. Phys. B*, 41(13):132001, 2008.

[106] T. Popmintchev, M.-C. Chen, A. Bahabad, M. Gerrity, P. Sidorenko, O. Cohen, I. P. Christov, M. M. Murnane, and H. C. Kapteyn. Phase matching of high harmonic generation in the soft and hard X-ray regions of the spectrum. *Proc. Natl. Acad. Sci. U.S.A.*, 106(26):10516–10521, 2009.

[107] C. Hernández-García, T. Popmintchev, M. Murnane, H. Kapteyn, L. Plaja, A. Becker, and A. Jaron-Becker. Isolated broadband attosecond pulse generation with near-and mid-infrared driver pulses via time-gated phase matching. *Opt. Express*, 25(10):11855–11866, 2017.

[108] M.-C. Chen, C. Mancuso, C. Hernández-García, F. Dollar, B. Galloway, D. Popmintchev, P.-C. Huang, B. Walker, L. Plaja, A. A. Jaroń-Becker, A. Becker, M. M. Murnane, H. C. Kapteyn, and T. Popmintchev. Generation of bright isolated attosecond soft X-ray pulses driven by multicycle midinfrared lasers. *Proc. Natl. Acad. Sci. U.S.A.*, 111(23):E2361–E2367, 2014.

[109] S. M. Teichmann, F. Silva, S. L. Cousin, M. Hemmer, and J. Biegert. 0.5-keV Soft X-ray attosecond continua. *Nat. Commun.*, 7(1):11493, 2016.

[110] T. Popmintchev, M.-C. Chen, D. Popmintchev, P. Arpin, S. Brown, S. Ališauskas, G. Andriukaitis, T. Balčiunas, O. D. Mücke, A. Pugzlys, A. Baltuška, B. Shim, S. E. Schrauth, A. Gaeta, C. Hernández-García, L. Plaja, A. Becker, A. Jaron-Becker, M. M. Murnane, and H. C. Kapteyn. Bright Coherent Ultrahigh Harmonics in the keV X-ray Regime from Mid-Infrared Femtosecond Lasers. *Science*, 336(6086):1287–1291, 2012.

[111] E. Constant, D. Garzella, P. Breger, E. Mével, C. Dorrer, C. Le Blanc, F. Salin, and P. Agostini. Optimizing high harmonic generation in absorbing gases: Model and experiment. *Phys. Rev. Lett.*, 82(8):1668, 1999.

[112] S. Kazamias, D. Douillet, F. Weihe, C. Valentin, A. Rousse, S. Sebban, G. Grillon, F. Augé, D. Hulin, and P. Balcou. Global optimization of high harmonic generation. *Phys. Rev. Lett.*, 90(19):193901, 2003.

[113] A. S. Sandhu, E. Gagnon, A. Paul, I. Thomann, A. Lytle, T. Keep, M. M. Murnane, H. C. Kapteyn, and I. P. Christov. Generation of sub-optical-cycle, carrier-envelope-phaseinsensitive, extreme-UV pulses via nonlinear stabilization in a waveguide. *Phys. Rev. A*, 74(6):061803(R), 2006.

[114] M. J. Abel, T. Pfeifer, P. M. Nagel, W. Boutu, M. J. Bell, C. P. Steiner, D. M. Neumark, and S. R. Leone. Isolated attosecond pulses from ionization gating of high-harmonic emission. *Chem. Phys.*, 366(1):9–14, 2009.

[115] A. Bideau-Mehu, Y. Guern, R. Abjean, and A. Johannin-Gilles. Measurement of refractive indices of neon, argon, krypton and xenon in the 253.7–140.4 nm wavelength range. Dispersion relations and estimated oscillator strengths of the resonance lines. *J. Quant. Spectrosc. Radiat. Transfer*, 25(5):395–402, 1981.

[116] C. R. Mansfield and E. R. Peck. Dispersion of helium. *J. Opt. Soc. Am. A*, 59(2):199–204, 1969.

[117] E. Pisanty, M. F. Ciappina, and M. Lewenstein. The imaginary part of the high-harmonic cutoff. *J. Phys. Photonics*, 2(3):034013, 2020.

[118] Y. Okajima, O. I. Tolstikhin, and T. Morishita. Adiabatic theory of high-order harmonic generation: One-dimensional zero-range-potential model. *Phys. Rev. A*, 85(6):063406, 2012.

[119] M. Bellini, C. Lyngå, A. Tozzi, M. B. Gaarde, T. W. Hänsch, A. L'Huillier, and C.-G. Wahlström. Temporal Coherence of Ultrashort High-Order Harmonic Pulses. *Phys. Rev. Lett.*, 81(2):297–300, 1998.

[120] M. B. Gaarde, F. Salin, E. Constant, P. Balcou, K. J. Schafer, K. C. Kulander, and A. L'Huillier. Spatiotemporal separation of high harmonic radiation into two quantum path components. *Phys. Rev. A*, 59(2):1367–1373, 1999.

[121] E. Frumker, G. G. Paulus, H. Niikura, A. Naumov, D. M. Villeneuve, and P. B. Corkum. Order-dependent structure of high harmonic wavefronts. *Opt. Express*, 20(13):13870–13877, 2012.

[122] F. Calegari, G. Sansone, S. Stagira, C. Vozzi, and M. Nisoli. Advances in attosecond science. *J. Phys. B*, 49(6):062001, 2016.

[123] M. Kovacev, Y. Mairesse, E. Priori, H. Merdji, O. Tcherbakoff, P. Monchicourt, P. Breger, E. Mével, E. Constant, P. Salières, B. Carré, and P. Agostini. Temporal confinement of the harmonic emission through polarization gating. *Eur. Phys. J. D*, 26(1):79–82, 2003.

[124] G. Sansone, E. Benedetti, F. Calegari, C. Vozzi, L. Avaldi, R. Flammini, L. Poletto, P. Villoresi, C. Altucci, R. Velotta, S. Stagira, S. De Silvestri, and M. Nisoli. Isolated Single-Cycle Attosecond Pulses. *Science*, 314(5798):443–446, 2006.

[125] Z. Chang. Controlling attosecond pulse generation with a double optical gating. *Phys. Rev. A*, 76(5):051403, 2007.

[126] H. Mashiko, S. Gilbertson, C. Li, S. D. Khan, M. M. Shakya, E. Moon, and Z. Chang. Double Optical Gating of High-Order Harmonic Generation with Carrier-Envelope Phase Stabilized Lasers. *Phys. Rev. Lett.*, 100(10):103906, 2008.

[127] X. Feng, S. Gilbertson, H. Mashiko, H. Wang, S. D. Khan, M. Chini, Y. Wu, K. Zhao, and Z. Chang. Generation of Isolated Attosecond Pulses with 20 to 28 Femtosecond Lasers. *Phys. Rev. Lett.*, 103(18):183901, 2009.

[128] F. Ferrari, F. Calegari, M. Lucchini, C. Vozzi, S. Stagira, G. Sansone, and M. Nisoli. High-energy isolated attosecond pulses generated by above-saturation few-cycle fields. *Nat. Photonics*, 4(12):875–879, 2010.

[129] T. Pfeifer, A. Jullien, M. J. Abel, P. M. Nagel, L. Gallmann, D. M. Neumark, and S. R. Leone. Generating coherent broadband continuum soft-x-ray radiation by attosecond ionization gating. *Opt. Express*, 15(25):17120–17128, 2007.

[130] I. Thomann, A. Bahabad, X. Liu, R. Trebino, M. M. Murnane, and H. C. Kapteyn. Characterizing isolated attosecond pulses from hollow-core waveguides using multi-cycle driving pulses. *Opt. Express*, 17(6):4611, 2009.

[131] K. T. Kim, C. Zhang, T. Ruchon, J.-F. Hergott, T. Auguste, D. M. Villeneuve, P. B. Corkum, and F. Quéré. Photonic streaking of attosecond pulse trains. *Nat. Photonics*, 7(8):651–656, 2013.

[132] F. Silva, S. M. Teichmann, S. L. Cousin, M. Hemmer, and J. Biegert. Spatiotemporal isolation of attosecond soft X-ray pulses in the water window. *Nat. Commun.*, 6(1):6611, 2015.

[133] T. Gaumnitz, A. Jain, Y. Pertot, M. Huppert, I. Jordan, F. Ardana-Lamas, and H. J. Wörner. Streaking of 43-attosecond soft-X-ray pulses generated by a passively CEP-stable mid-infrared driver. *Opt. Express*, 25(22):27506–27518, 2017.

[134] L. Novotny and B. Hecht. *Principles of nano-optics*. Cambridge university press, 2012.

[135] M. Krüger, C. Lemell, G. Wachter, J. Burgdörfer, and P. Hommelhoff. Attosecond physics phenomena at nanometric tips. *J. Phys. B*, 51(17):172001, 2018.

[136] J. Ibe, P. Bey Jr, S. Brandow, R. Brizzolara, N. Burnham, D. DiLella, K. Lee, C. Marrian, and R. Colton. On the electrochemical etching of tips for scanning tunneling microscopy. *J. Vac. Sci. Technol. A*, 8(4):3570–3575, 1990.

[137] M. Eisele, M. Krüger, M. Schenk, A. Ziegler, and P. Hommelhoff. Note: Production of sharp gold tips with high surface quality. *Rev. Sci. Instrum.*, 82(2):026101, 2011.

[138] Cosinus Messtechnik GmbH. Low Noise Amplifier SA Series. product overview, Cosinus Messtechnik GmbH. `https://www.cosinus.de/_downloads/NF-SA-200-400-600Serie.pdf`, last accessed: 2021-04-29.

[139] E. Säckinger. *Analysis and design of transimpedance amplifiers for optical receivers*. John Wiley & Sons, 2017.

[140] T. Wang and B. Erhman. Compensate Transimpedance Amplifiers Intuitively. application note, Texas Instruments, 2005. `https://www.ti.com/lit/an/sboa055a/sboa055a.pdf`, last accessed: 2021-05-01.

[141] Zurich Instruments. Principles of lock-in detection and the state of the art. white paper, Zurich Instruments, 2016. `https://www.zhinst.com/sites/default/files/li_primer/zi_whitepaper_principles_of_lock-in_detection.pdf`, last accessed: 2021-04-29.

[142] Zurich Instruments. Basics of Boxcar Averaging. application note, Zurich Instruments. `https://www.zhinst.com/europe/en/basics-of-boxcar-averaging`, last accessed: 2021-05-01.

[143] J. Gagnon, E. Goulielmakis, and V. S. Yakovlev. The accurate FROG characterization of attosecond pulses from streaking measurements. *Appl. Phys. B*, 92(1):25–32, 2008.

[144] P. D. Keathley, S. Bhardwaj, J. Moses, G. Laurent, and F. X. Krtner. Volkov transform generalized projection algorithm for attosecond pulse characterization. *New J. Phys.*, 18(7):073009, 2016.

[145] Y. Mairesse and F. Quéré. Frequency-resolved optical gating for complete reconstruction of attosecond bursts. *Phys. Rev. A*, 71(1):011401, 2005.

[146] J. Gagnon and V. S. Yakovlev. The robustness of attosecond streaking measurements. *Opt. Express*, 17(20):17678, 2009.

[147] M. Lucchini, M. Brügmann, A. Ludwig, L. Gallmann, U. Keller, and T. Feurer. Ptychographic reconstruction of attosecond pulses. *Opt. Express*, 23(23):29502–29513, 2015.

[148] L. Cattaneo, J. Vos, M. Lucchini, L. Gallmann, C. Cirelli, and U. Keller. Comparison of attosecond streaking and RABBITT. *Opt. Express*, 24(25):29060–29076, 2016.

[149] L. Pedrelli, P. D. Keathley, L. Cattaneo, F. X. Kärtner, and U. Keller. Complete phase retrieval of photoelectron wavepackets. *New J. Phys.*, 22(5):053028, 2020.

[150] P. M. Paul, E. S. Toma, P. Breger, G. Mullot, F. Augé, P. Balcou, H. G. Muller, and P. Agostini. Observation of a Train of Attosecond Pulses from High Harmonic Generation. *Science*, 292(5522):1689–1692, 2001.

[151] M. Chini, S. Gilbertson, S. D. Khan, and Z. Chang. Characterizing ultrabroadband attosecond lasers. *Opt. Express*, 18(12):13006–13016, 2010.

[152] G. Laurent, W. Cao, I. Ben-Itzhak, and C. L. Cocke. Attosecond pulse characterization. *Opt. Express*, 21(14):16914–16927, 2013.

[153] J. Feist, O. Zatsarinny, S. Nagele, R. Pazourek, J. Burgdörfer, X. Guan, K. Bartschat, and B. I. Schneider. Time delays for attosecond streaking in photoionization of neon. *Phys. Rev. A*, 89(3):033417, 2014.

[154] M. Isinger, R. J. Squibb, D. Busto, S. Zhong, A. Harth, D. Kroon, S. Nandi, C. L. Arnold, M. Miranda, J. M. Dahlström, E. Lindroth, R. Feifel, M. Gisselbrecht, and A. L'Huillier. Photoionization in the time and frequency domain. *Science*, 358(6365):893–896, 2017.

[155] M. Ossiander, F. Siegrist, V. Shirvanyan, R. Pazourek, A. Sommer, T. Latka, A. Guggenmos, S. Nagele, J. Feist, J. Burgdörfer, R. Kienberger, and M. Schultze. Attosecond correlation dynamics. *Nat. Phys.*, 13(3):280–285, 2017.

[156] C. Bourassin-Bouchet, L. Barreau, V. Gruson, J.-F. Hergott, F. Quéré, P. Salières, and T. Ruchon. Quantifying Decoherence in Attosecond Metrology. *Phys. Rev. X*, 10(3):031048, 2020.

[157] M. Ossiander, J. Riemensberger, S. Neppl, M. Mittermair, M. Schäffer, A. Duensing, M. S. Wagner, R. Heider, M. Wurzer, M. Gerl, M. Schnitzenbaumer, J. V. Barth, F. Libisch, C. Lemell, J. Burgdörfer, P. Feulner, and R. Kienberger. Absolute timing of the photoelectric effect. *Nature*, 561(7723):374–377, 2018.

[158] M. Ossiander. *Absolute Photoemission Timing*. PhD thesis, Technische Universität München, 2018.

[159] R. Pazourek, S. Nagele, and J. Burgdörfer. Attosecond chronoscopy of photoemission. *Rev. Mod. Phys.*, 87(3):765–802, 2015.

[160] C. Goldsmith, A. Jaroń-Becker, and A. Becker. Attosecond Streaking Time Delays: Finite-Range Interpretation and Applications. *Appl. Sci.*, 9(3):492, 2019.

[161] F. Siek, S. Neb, P. Bartz, M. Hensen, C. Strüber, S. Fiechter, M. Torrent-Sucarrat, V. M. Silkin, E. E. Krasovskii, N. M. Kabachnik, et al. Angular momentum–induced delays in solid-state photoemission enhanced by intra-atomic interactions. *Science*, 357(6357):1274–1277, 2017.

[162] S. Keiber. *Novel metrology techniques resolve strong-field-driven electron dynamics in solids*. PhD thesis, Ludwig Maximilians Universität München, 2016.

[163] I. Pupeza, M. Huber, M. Trubetskov, W. Schweinberger, S. A. Hussain, C. Hofer, K. Fritsch, M. Poetzlberger, L. Vamos, E. Fill, et al. Field-resolved infrared spectroscopy of biological systems. *Nature*, 577(7788):52–59, 2020.

[164] C. Riek, D. Seletskiy, A. S. Moskalenko, J. Schmidt, P. Krauspe, S. Eckart, S. Eggert, G. Burkard, and A. Leitenstorfer. Direct sampling of electric-field vacuum fluctuations. *Science*, 350(6259):420–423, 2015.

[165] M. R. Bionta, F. Ritzkowsky, M. Turchetti, Y. Yang, D. C. Mor, W. P. Putnam, F. X. Kärtner, K. K. Berggren, and P. D. Keathley. On-chip sampling of optical fields with attosecond resolution. *Nat. Photonics*, 15(6):456–460, 2021.

[166] S. I. Hwang, S. B. Park, J. Mun, W. Cho, C. H. Nam, and K. T. Kim. Generation of a single-cycle pulse using a two-stage compressor and its temporal characterization using a tunnelling ionization method. *Sci. Rep.*, 9(1):1–6, 2019.

[167] W. Cho, S. I. Hwang, C. H. Nam, M. R. Bionta, P. Lassonde, B. E. Schmidt, H. Ibrahim, F. Légaré, and K. T. Kim. Temporal characterization of femtosecond laser pulses using tunneling ionization in the UV, visible, and mid-IR ranges. *Sci. Rep.*, 9(1), 2019.

[168] N. Saito, N. Ishii, T. Kanai, and J. Itatani. All-optical characterization of the two-dimensional waveform and the Gouy phase of an infrared pulse based on plasma fluorescence of gas. *Opt. Express*, 26(19):24591–24601, 2018.

[169] D. H. Auston. Picosecond optoelectronic switching and gating in silicon. *Appl. Phys. Lett.*, 26(3):101–103, 1975.

[170] M. Kubullek, Z. Wang, K. von der Brelje, D. Zimin, P. Rosenberger, J. Schötz, M. Neuhaus, S. Sederberg, A. Staudte, N. Karpowicz, M. F. Kling, and B. Bergues. Single-shot carrier–envelope-phase measurement in ambient air. *Optica*, 7(1):35–39, 2020.

[171] A. Korobenko, K. Johnston, M. Kubullek, L. Arissian, Z. Dube, T. Wang, M. Kübel, A. Y. Naumov, D. M. Villeneuve, M. F. Kling, P. B. Corkum, A. Staudte, and B. Bergues. Femtosecond streaking in ambient air. *Optica*, 7(10):1372–1376, 2020.

[172] D. Zimin, M. Weidman, J. Schötz, M. F. Kling, V. S. Yakovlev, F. Krausz, and N. Karpowicz. Petahertz-scale nonlinear photoconductive sampling in air. *Optica*, 8(5):586–590, 2021.

[173] S. R. Leone and D. M. Neumark. Attosecond science in atomic, molecular, and condensed matter physics. *Faraday Discuss.*, 194(0):15–39, 2016.

[174] E. Magerl, S. Neppl, A. L. Cavalieri, E. M. Bothschafter, M. Stanislawski, T. Uphues, M. Hofstetter, U. Kleineberg, J. V. Barth, D. Menzel, F. Krausz, R. Ernstorfer, R. Kienberger, and P. Feulner. A flexible apparatus for attosecond photoelectron spectroscopy of solids and surfaces. *Rev. Sci. Instrum.*, 82(6):063104–063104–6, 2011.

[175] M. Huppert, I. Jordan, and H. J. Wörner. Attosecond beamline with actively stabilized and spatially separated beam paths. *Rev. Sci. Instrum.*, 86(12):123106, 2015.

[176] G. D. Lucarelli, B. Moio, G. Inzani, N. Fabris, L. Moscardi, F. Frassetto, L. Poletto, M. Nisoli, and M. Lucchini. Novel beamline for attosecond transient reflection spectroscopy in a sequential two-foci geometry. *Rev. Sci. Instrum.*, 91(5):053002, 2020.

[177] M. Schultze, E. M. Bothschafter, A. Sommer, S. Holzner, W. Schweinberger, M. Fiess, M. Hofstetter, R. Kienberger, V. Apalkov, V. S. Yakovlev, M. I. Stockman, and F. Krausz. Controlling dielectrics with the electric field of light. *Nature*, 493(7430):75–78, 2013.

[178] O. Kwon and D. Kim. PHz current switching in calcium fluoride single crystal. *Appl. Phys. Lett.*, 108(19):191112, 2016.

[179] O. Kwon, T. Paasch-Colberg, V. Apalkov, B.-K. Kim, J.-J. Kim, M. I. Stockman, and D. Kim. Semimetallization of dielectrics in strong optical fields. *Sci. Rep.*, 6(1):21272, 2016.

[180] F. Langer, Y.-P. Liu, Z. Ren, V. Flodgren, C. Guo, J. Vogelsang, S. Mikaelsson, I. Sytcevich, J. Ahrens, A. L'Huillier, C. L. Arnold, and A. Mikkelsen. Few-cycle lightwave-driven currents in a semiconductor at high repetition rate. *Optica*, 7(4):276, 2020.

[181] E. Castro-Camus and M. Alfaro. Photoconductive devices for terahertz pulsed spectroscopy: a review. *Photon. Res.*, 4(3):A36–A42, 2016.

[182] D. J. Cook and R. M. Hochstrasser. Intense terahertz pulses by four-wave rectification in air. *Opt. Lett.*, 25(16):1210–1212, 2000.

[183] M. Kreß, T. Löffler, S. Eden, M. Thomson, and H. G. Roskos. Terahertz-pulse generation by photoionization of air with laser pulses composed of both fundamental and second-harmonic waves. *Opt. Lett.*, 29(10):1120–1122, 2004.

[184] M. Kreß, T. Löffler, M. D. Thomson, R. Dörner, H. Gimpel, K. Zrost, T. Ergler, R. Moshammer, U. Morgner, J. Ullrich, and H. G. Roskos. Determination of the carrier-envelope phase of few-cycle laser pulses with terahertz-emission spectroscopy. *Nat. Phys.*, 2(5):327–331, 2006.

[185] A. R. Hanna and E. R. Fisher. Investigating recent developments and applications of optical plasma spectroscopy: A review. *J. Vac. Sci. Technol. A*, 38(2):020806, 2020.

[186] A. Bogaerts, E. Neyts, R. Gijbels, and J. van der Mullen. Gas discharge plasmas and their applications. *Spectrochim. Acta B*, 57(4):609–658, 2002.

[187] A. Bogaerts, X. Tu, J. C. Whitehead, G. Centi, L. Lefferts, O. Guaitella, F. Azzolina-Jury, H.-H. Kim, A. B. Murphy, W. F. Schneider, T. Nozaki, J. C. Hicks, A. Rousseau, F. Thevenet, A. Khacef, and M. Carreon. The 2020 plasma catalysis roadmap. *J. Phys. D*, 53(44):443001, 2020.

[188] J. Šimončicová, S. Kryštofová, V. Medvecká, K. Ďurišová, and B. Kaliňáková. Technical applications of plasma treatments: current state and perspectives. *Appl. Microbiol. Biotechnol.*, 103(13):5117–5129, 2019.

[189] T. von Woedtke, S. Emmert, H.-R. Metelmann, S. Rupf, and K.-D. Weltmann. Perspectives on cold atmospheric plasma (CAP) applications in medicine. *Phys. Plasmas*, 27(7):070601, 2020.

[190] F.-G. Chizoba Ekezie, D.-W. Sun, and J.-H. Cheng. A review on recent advances in cold plasma technology for the food industry: Current applications and future trends. *Trends Food Sci. Technol.*, 69:46–58, 2017.

[191] T. Boolakee, C. Heide, F. Wagner, C. Ott, M. Schlecht, J. Ristein, H. B. Weber, and P. Hommelhoff. Length-dependence of light-induced currents in graphene. *J. Phys. B*, 53(15):154001, 2020.

[192] Z. He. Review of the Shockley-Ramo theorem and its application in semiconductor gamma-ray detectors. *Nucl. Instrum. Methods Phys. Res. A*, 463(1-2):250–267, 2001.

[193] W. Riegler. An application of extensions of the Ramo-Shockley theorem to signals in silicon sensors. *Nucl. Instrum. Methods Phys. Res. A*, 940:453–461, 2019.

[194] S. Ramo. Currents Induced by Electron Motion. *Proc. IRE*, 27(9):584–585, 1939.

[195] W. Shockley. Currents to Conductors Induced by a Moving Point Charge. *J. Appl. Phys.*, 9(10):635–636, 1938.

[196] J. Schötz, A. Maliakkal, J. Blöchl, D. Zimin, Z. Wang, P. Rosenberger, M. Alharbi, A. M. Azzeer, M. Weidman, V. S. Yakovlev, B. Bergues, and M. F. Kling. The emergence of macroscopic currents in photoconductive sampling of optical fields. *arXiv preprints arXiv:2105.10010*, 2021.

[197] W. Möller. Fundamentals of Plasma Physics. `https://www.hzdr.de/db/Cms?pOid=23689`, 2006. lecture notes; last accessed: 2020-02-11.

[198] U. Schumacher. Basics of Plasma Physics. In A. Dinklage, T. Klinger, G. Marx, and L. Schweikhard, editors, *Plasma Physics: Confinement, Transport and Collective Effects*, pages 1–20. Springer Berlin Heidelberg, Berlin, Heidelberg, 2005.

[199] A. Piel. *Plasma Physics*. Springer-Verlag Berlin Heidelberg, 2010.

[200] J. Bittencourt. *Fundamentals of Plasma Physics*. Springer-Verlag New York, 2004.

[201] C. Burger. *Laser-induced nuclear dynamics in hydrocarbons*. PhD thesis, lmu, 2018.

[202] C. Geuzaine and J.-F. Remacle. Gmsh: A 3-D finite element mesh generator with built-in pre-and post-processing facilities. *Int. J. Numer. Methods Eng.*, 79(11):1309–1331, 2009.

[203] C. Geuzaine and J.-F. Remacle. gmsh. `https://gmsh.info/`. last accessed 2020-02-12.

[204] M. T. Homer Reid and S. G. Johnson. Efficient Computation of Power, Force, and Torque in BEM Scattering Calculations. *ArXiv e-prints*, 2013.

[205] H. Reid. scuff-em. `http://github.com/homerreid/scuff-EM`. last accessed 2020-02-12.

[206] C. J. Schmidt. Lecture on Particle Detectors and Electronic Readout - 5th International FAIR School. `https://indico.gsi.de/event/6416/contributions/29455/attachments/21371/26925/FAIR-School_Detectors.pdf`, 2017. Accessed: 2021-05-14.

[207] E. Gatti, G. Padovini, and V. Radeka. Signal evaluation in multielectrode radiation detectors by means of a time dependent weighting vector. *Nucl. Instrum. Methods Phys. Res.*, 193(3):651–653, 1982.

[208] W. Riegler. Extended theorems for signal induction in particle detectors VCI 2004. *Nucl. Instrum. Methods Phys. Res. A*, 535(1-2):287–293, 2004.

[209] J. Bortfeldt, O. Biebel, B. Flierl, R. Hertenberger, F. Klitzner, P. Lösel, L. Magallanes, R. Müller, K. Parodi, T. Schlüter, B. Voss, and A. Zibell. Low material budget floating strip Micromegas for ion transmission radiography. *Nucl. Instrum. Methods Phys. Res. A*, 845:210–214, 2017.

[210] P. Seifert, M. Kundinger, G. Shi, X. He, K. Wu, Y. Li, A. Holleitner, and C. Kastl. Quantized Conductance in Topological Insulators Revealed by the Shockley-Ramo Theorem. *Phys. Rev. Lett.*, 122(14):146804, 2019.

[211] E. Castro-Camus, M. B. Johnston, and J. Lloyd-Hughes. Simulation of fluence-dependent photocurrent in terahertz photoconductive receivers. *Semicond. Sci. Technol.*, 27(11):115011, 2012.

[212] T. K. Nguyen, W. T. Kim, B. J. Kang, H. S. Bark, K. Kim, J. Lee, I. Park, T.-I. Jeon, and F. Rotermund. Photoconductive dipole antennas for efficient terahertz receiver. *Opt. Commun.*, 383:50–56, 2017.

[213] R. A. Lewis. A review of terahertz detectors. *J. Phys. D*, 52(43):433001, 2019.

[214] B. Shan, X.-M. Tong, Z. Zhao, Z. Chang, and C.-D. Lin. High-order harmonic cutoff extension of the O2 molecule due to ionization suppression. *Phys. Rev. A*, 66(6):061401, 2002.

[215] J. G. Calvert. Glossary of atmospheric chemistry terms (Recommendations 1990). *Pure Appl. Chem.*, 62(11):2167–2219, 1990.

[216] W. C. Swope, H. C. Andersen, P. H. Berens, and K. R. Wilson. A computer simulation method for the calculation of equilibrium constants for the formation of physical clusters of molecules: Application to small water clusters. *J. Chem. Phys.*, 76(1):637–649, 1982.

[217] Fortran program, MAGBOLTZ v8.97. https://magboltz.web.cern.ch/magboltz/.

[218] Biagi database. www.lxcat.net. Retrieved on 2020-05-12.

[219] P. D. Keathley, W. P. Putnam, P. Vasireddy, R. G. Hobbs, Y. Yang, K. K. Berggren, and F. X. Kärtner. Vanishing carrier-envelope-phase-sensitive response in optical-field photoemission from plasmonic nanoantennas. *Nat. Phys.*, 15(11):1128–1133, 2019.

[220] M. C. Nuss and J. Orenstein. Terahertz time-domain spectroscopy. In G. Grüner, editor, *Millimeter and Submillimeter Wave Spectroscopy of Solids*, pages 7–50. Springer Berlin Heidelberg, Berlin, Heidelberg, 1998.

[221] R. M. Smith and M. A. Arnold. Terahertz time-domain spectroscopy of solid samples: principles, applications, and challenges. *Appl. Spectrosc. Rev.*, 46(8):636–679, 2011.

[222] H. Němec, F. Kadlec, and P. Kužel. Methodology of an optical pump-terahertz probe experiment: An analytical frequency-domain approach. *J. Chem. Phys.*, 117(18):8454–8466, 2002.

[223] R. Ulbricht, E. Hendry, J. Shan, T. F. Heinz, and M. Bonn. Carrier dynamics in semiconductors studied with time-resolved terahertz spectroscopy. *Rev. Mod. Phys.*, 83(2):543, 2011.

[224] S. Wietzke, C. Jansen, M. Reuter, T. Jung, D. Kraft, S. Chatterjee, B. Fischer, and M. Koch. Terahertz spectroscopy on polymers: A review of morphological studies. *J. Mol. Struct.*, 1006(1-3):41–51, 2011.

[225] O. Cherkasova, M. Nazarov, A. Shkurinov, and V. Fedorov. Terahertz spectroscopy of biological molecules. *Radiophys. Quantum Electron.*, 52(7):518, 2009.

[226] J. Demsar, R. Averitt, A. Taylor, V. Kabanov, W. Kang, H. Kim, E. Choi, and S. Lee. Pair-Breaking and Superconducting State Recovery Dynamics in MgB2. *Phys. Rev. Lett.*, 91(26):267002, 2003.

[227] R. Huber, F. Tauser, A. Brodschelm, M. Bichler, G. Abstreiter, and A. Leitenstorfer. How many-particle interactions develop after ultrafast excitation of an electron-hole plasma. *Nature*, 414(6861):286–289, 2001.

[228] R. Huber, C. Kübler, S. Tübel, A. Leitenstorfer, Q. Vu, H. Haug, F. Köhler, and M.-C. Amann. Femtosecond formation of coupled phonon-plasmon modes in InP: Ultrabroadband THz experiment and quantum kinetic theory. *Phys. Rev. Lett.*, 94(2):027401, 2005.

[229] C. A. Schmuttenmaer. Exploring dynamics in the far-infrared with terahertz spectroscopy. *Chem. Rev.*, 104(4):1759–1780, 2004.

[230] M. Neuhaus, J. Schötz, M. Aulich, A. Srivastava, D. Kimbaras, V. Pervak, A. Alharbi, M. Alharbi, A. M. Azzeer, Z. Wang, and M. Kling. Transient field-resolved mid-infrared reflectometry for probing highly-excited carrier dynamics in solids. in preparation, 2021.

[231] T. Zentgraf, R. Huber, N. C. Nielsen, D. S. Chemla, and R. A. Kaindl. Ultrabroadband 50-130 THz pulses generated via phase-matched difference frequency mixing in LiIO3. *Opt. Express*, 15(9):5775–5781, 2007.

[232] R. Kochanov, I. Gordon, L. Rothman, P. Wciso, C. Hill, and J. Wilzewski. HITRAN Application Programming Interface (HAPI): A comprehensive approach to working with spectroscopic data. *J. Quant. Spectrosc. Radiat. Transfer*, 177:15–30, 2016. XVIIIth Symposium on High Resolution Molecular Spectroscopy (HighRus-2015), Tomsk, Russia.

[233] M. Huber, W. Schweinberger, F. Stutzki, J. Limpert, I. Pupeza, and O. Pronin. Active intensity noise suppression for a broadband mid-infrared laser source. *Opt. Express*, 25(19):22499–22509, 2017.

[234] H. Roskos, B. Rieck, A. Seilmeier, and W. Kaiser. Cooling of a carrier plasma in germanium investigated with subpicosecond infrared pulses. *Appl. Phys. Lett.*, 53(24):2406–2408, 1988.

[235] H. Roskos, B. Rieck, A. Seilmeier, and W. Kaiser. Carrier cooling in nonpolar semiconductors studied with subpicosecond time-resolution. *Solid State Electron.*, 32(12):1437–1441, 1989.

[236] A. Othonos. Probing ultrafast carrier and phonon dynamics in semiconductors. *J. Appl. Phys.*, 83(4):1789–1830, 1998.

[237] D. W. Bailey and C. J. Stanton. Calculations of femtosecond differential optical transmission in germanium. *J. Appl. Phys.*, 77(5):2107–2115, 1995.

[238] S. Zollner, K. Myers, K. Jensen, J. Dolan, D. Bailey, and C. Stanton. Femtosecond interband hole scattering in Ge studied by pump-probe reflectivity. *Solid State Commun.*, 104(1):51–55, 1997.

[239] A. Urbanowicz, R. Adomavičius, A. Krotkus, and V. Malevich. Electron dynamics in Ge crystals studied by terahertz emission from photoexcited surfaces. *Semicond. Sci. Technol.*, 20(10):1010, 2005.

[240] J. H. Davies. *The Physics of Low-dimensional Semiconductors: An Introduction*. Cambridge University Press, 1997.

[241] M. Zürch, H.-T. Chang, L. J. Borja, P. M. Kraus, S. K. Cushing, A. Gandman, C. J. Kaplan, M. H. Oh, J. S. Prell, D. Prendergast, C. D. Pemmaraju, D. M. Neumark, and S. R. Leone. Direct and simultaneous observation of ultrafast electron and hole dynamics in germanium. *Nat. Commun.*, 8(1):15734, 2017.

[242] Ioffe Institute, database of semiconductor properties. http://www.ioffe.ru/SVA/NSM/Semicond/. Accessed: 2021-02-23.

[243] S. Smirnov. *Physical Modeling of Electron Transport in Strained Silicon and Silicon-Germanium*. PhD thesis, TU Wien, 2003.

[244] A. Dargys and J. Kundrotas. *Handbook on physical properties of Ge, Si, GaAs and InP*. Science and Encyclopedia Publ., 1994.

[245] M. A. Green. Intrinsic concentration, effective densities of states, and effective mass in silicon. *J. Appl. Phys.*, 67(6):2944–2954, 1990.

[246] S. Sundaram and E. Mazur. Inducing and probing non-thermal transitions in semiconductors using femtosecond laser pulses. *Nat. Mater.*, 1(4):217–224, 2002.

[247] H. Haug and S. W. Koch. *Quantum theory of the optical and electronic properties of semiconductors*. World Scientific, 1990.

[248] Gallium arsenide (GaAs), intrinsic carrier concentration, electrical and thermal conductivity: Datasheet from Landolt-Börnstein - Group III Condensed Matter · Volume 41A1β: "Group IV Elements, IV-IV and III-V Compounds. Part b - Electronic, Transport, Optical and Other Properties" in SpringerMaterials, 2002.

[249] Germanium (Ge), intrinsic carrier concentration: Datasheet from Landolt-Börnstein - Group III Condensed Matter · Volume 41A1β: "Group IV Elements, IV-IV and III-V Compounds. Part b - Electronic, Transport, Optical and Other Properties" in SpringerMaterials, 2002.

[250] M. S. Dresselhaus. Lecture Notes: Solid state physics - part II - optical properties of solids. http://web.mit.edu/course/6/6.732/www/6.732-pt2.pdf, 2001. Accessed: 2021-04-24.

[251] F. Ganikhanov, K. C. Burr, D. J. Hilton, and C. L. Tang. Femtosecond optical-pulse-induced absorption and refractive-index changes in GaAs in the midinfrared. *Phys. Rev. B*, 60(12):8890–8896, 1999.

[252] S. Sato, K. Yabana, Y. Shinohara, T. Otobe, and G. F. Bertsch. Numerical pump-probe experiments of laser-excited silicon in nonequilibrium phase. *Phys. Rev. B*, 89(6):064304, 2014.

[253] K. Sokolowski-Tinten and D. von der Linde. Generation of dense electron-hole plasmas in silicon. *Phys. Rev. B*, 61(4):2643–2650, 2000.

[254] S. Anisimov, B. Kapeliovich, T. Perelman, et al. Electron emission from metal surfaces exposed to ultrashort laser pulses. *Zh. Eksp. Teor. Fiz*, 66(2):375–377, 1974.

[255] T. Shin, S. W. Teitelbaum, J. Wolfson, M. Kandyla, and K. A. Nelson. Extended two-temperature model for ultrafast thermal response of band gap materials upon impulsive optical excitation. *J. Chem. Phys.*, 143(19):194705, 2015.

[256] C. Jacoboni and L. Reggiani. The Monte Carlo method for the solution of charge transport in semiconductors with applications to covalent materials. *Rev. Mod. Phys.*, 55(3):645, 1983.

[257] R. N. Hall. Electron-hole recombination in germanium. *Phys. Rev.*, 87(2):387, 1952.

[258] W. Shockley and W. Read Jr. Statistics of the recombinations of holes and electrons. *Phys. Rev.*, 87(5):835, 1952.

[259] P. Auger. Sur les rayons β; secondaires produits dans un gaz par des rayons X. *C. R. Acad. Sci.*, 177:169–171, 1923.

[260] L. Zhou, B. Bo, X. Yan, C. Wang, Y. Chi, and X. Yang. Brief review of surface passivation on III-V semiconductor. *Crystals*, 8(5):226, 2018.

[261] R. Haight and M. Baeumler. Ultrafast-electron dynamics and recombination on the Ge (111)(2× 1) π-bonded surface. *Phys. Rev. B*, 46(3):1543, 1992.

[262] S. Sato, Y. Shinohara, T. Otobe, and K. Yabana. Dielectric response of laser-excited silicon at finite electron temperature. *Phys. Rev. B*, 90(17):174303, 2014.

[263] M. Qasim, M. S. Wismer, M. Agarwal, and V. S. Yakovlev. Ensemble properties of charge carriers injected by an ultrashort laser pulse. *Phys. Rev. B*, 98(21):214304, 2018.

[264] J. Kitagawa, Y. Kadoya, M. Tsubota, F. Iga, and T. Takabatake. Terahertz conductivity of localized photoinduced carriers in a Mott insulator YTiO3 at low excitation density, contrasted with the metallic nature in a band semiconductor Si. *J. Condens*, 19(40):406224, 2007.

[265] M. Born and E. Wolf. *Principles of optics: electromagnetic theory of propagation, interference and diffraction of light*. Elsevier, 2013.

[266] F. Meng, M. D. Thomson, B. E. Sernelius, M. Jörger, and H. G. Roskos. Ultrafast dynamic conductivity and scattering rate saturation of photoexcited charge carriers in silicon investigated with a midinfrared continuum probe. *Phys. Rev. B*, 91(7):075201, 2015.

[267] J. Vinet, M. Combescot, and C. Tanguy. Influence of the electron-hole density profile on the reflectivity of laser irradiated silicon. *Solid State Commun.*, 51(3):171–173, 1984.

[268] J. Vaitkus. The nonequilibrium hall effect and related transport phenomena in semiconductors under inhomogeneous excitation by a laser pulse. *Phys. Status Solidi A*, 34(2):769–775, 1976.

[269] T.-T. Yeh, H. Shirai, C.-M. Tu, T. Fuji, T. Kobayashi, and C.-W. Luo. Ultrafast carrier dynamics in Ge by ultra-broadband mid-infrared probe spectroscopy. *Sci. Rep.*, 7(1):1–10, 2017.

[270] J. Lloyd-Hughes and T.-I. Jeon. A review of the terahertz conductivity of bulk and nano-materials. *J. Infrared Millim. Terahertz Waves*, 33(9):871–925, 2012.

[271] H. Dember. Photoelectromotive force in cuprous oxide crystals. *Phys. Z*, 32(1):554–556, 1931.

[272] M. B. Johnston, D. M. Whittaker, A. Corchia, A. G. Davies, and E. H. Linfield. Simulation of terahertz generation at semiconductor surfaces. *Phys. Rev. B*, 65(16):165301, 2002.

[273] B. Hönerlage. Diffusion and recombination of bipolar plasmas in highly excited semiconductors. *Opt. Mater.*, 1(3):133–140, 1992.

[274] E. Najafi, V. Ivanov, A. Zewail, and M. Bernardi. Super-diffusion of excited carriers in semiconductors. *Nat. Commun.*, 8(1):1–7, 2017.

[275] K. Chen, N. Sheehan, F. He, X. Meng, S. C. Mason, S. R. Bank, and Y. Wang. Measurement of ambipolar diffusion coefficient of photoexcited carriers with ultrafast reflective grating-imaging technique. *ACS Photonics*, 4(6):1440–1446, 2017.

[276] D. Steiauf, E. Kioupakis, and C. G. Van de Walle. Auger recombination in GaAs from first principles. *ACS Photonics*, 1(8):643–646, 2014.

[277] F. Schlaepfer, M. Lucchini, S. A. Sato, M. Volkov, L. Kasmi, N. Hartmann, A. Rubio, L. Gallmann, and U. Keller. Attosecond optical-field-enhanced carrier injection into the GaAs conduction band. *Nat. Phys.*, 14(6):560–564, 2018.

[278] R. K. Ahrenkiel. Chapter 2 Minority-Carrier Lifetime in IIIV Semiconductors. In R. K. Ahrenkiel and M. S. Lundstrom, editors, *Minority Carriers In III-V Semiconductors: Physics and Applications*, volume 39 of *Semiconductors and Semimetals*, pages 39–150. Elsevier, 1993.

[279] H. Ito and T. Ishibashi. Surface recombination velocity in p-type GaAs. *Jpn. J. Appl. Phys.*, 33(1R):88, 1994.

[280] M. Passlack, M. Hong, J. Mannaerts, J. Kwo, and L. Tu. Recombination velocity at oxide–GaAs interfaces fabricated by in situ molecular beam epitaxy. *Appl. Phys. Lett.*, 68(25):3605–3607, 1996.

[281] W. S. Werner. Electron transport in solids for quantitative surface analysis. *Surf. Interface Anal.*, 31(3):141–176, 2001.

[282] R. Shimizu and D. Ze-Jun. Monte Carlo modelling of electron-solid interactions. *Rep. Prog. Phys.*, 55(4):487, 1992.

[283] H. Ghimire, P. Jayaweera, D. Somvanshi, Y. Lao, and A. Perera. Recent Progress on Extended Wavelength and Split-Off Band Heterostructure Infrared Detectors. *Micromachines*, 11(6):547, 2020.

[284] A. Leblanc, P. Lassonde, S. Petit, J.-C. Delagnes, E. Haddad, G. Ernotte, M. Bionta, V. Gruson, B. Schmidt, H. Ibrahim, et al. Phase-matching-free pulse retrieval based on transient absorption in solids. *Opt. Express*, 27(20):28998–29015, 2019.

[285] C. J. Kaplan, P. M. Kraus, A. D. Ross, M. Zürch, S. K. Cushing, M. F. Jager, H.-T. Chang, E. M. Gullikson, D. M. Neumark, and S. R. Leone. Femtosecond tracking of carrier relaxation in germanium with extreme ultraviolet transient reflectivity. *Phys. Rev. B*, 97(20):205202, 2018.

[286] P. U. Jepsen, D. G. Cooke, and M. Koch. Terahertz spectroscopy and imaging–Modern techniques and applications. *Laser Photonics Rev.*, 5(1):124–166, 2011.

[287] T. Pfeifer, W. Kütt, H. Kurz, and R. Scholz. Generation and detection of coherent optical phonons in germanium. *Phys. Rev. Lett.*, 69(22):3248, 1992.

[288] A. V. Kuznetsov and C. J. Stanton. Theory of coherent phonon oscillations in semiconductors. *Phys. Rev. Lett.*, 73(24):3243, 1994.

[289] G. Cho, W. Kütt, and H. Kurz. Subpicosecond time-resolved coherent-phonon oscillations in GaAs. *Phys. Rev. Lett.*, 65(6):764, 1990.

[290] T. Terashige, H. Yada, Y. Matsui, T. Miyamoto, N. Kida, and H. Okamoto. Temperature and carrier-density dependence of electron-hole scattering in silicon investigated by optical-pump terahertz-probe spectroscopy. *Phys. Rev. B*, 91(24):241201, 2015.

[291] D. Hulin, M. Combescot, J. Bok, A. Migus, J. Vinet, and A. Antonetti. Energy transfer during silicon irradiation by femtosecond laser pulse. *Phys. Rev. Lett.*, 52(22):1998, 1984.

[292] E. Hendry, M. Koeberg, J. Pijpers, and M. Bonn. Reduction of carrier mobility in semiconductors caused by charge-charge interactions. *Phys. Rev. B*, 75(23):233202, 2007.

[293] M. Bernardi, D. Vigil-Fowler, C. S. Ong, J. B. Neaton, and S. G. Louie. Ab initio study of hot electrons in GaAs. *Proc. Natl. Acad. Sci. U.S.A.*, 112(17):5291–5296, 2015.

[294] L. Kim, S. Kim, P. K. Jha, V. W. Brar, and H. A. Atwater. Mid-infrared radiative emission from bright hot plasmons in graphene. *Nat. Mater.*, 20(6):805–811.

[295] J. G. Smith. Mass Spectrometry and Infrared Spectroscopy. *Org. Chem.*, 3:463–488, 2011.

[296] X. F. Li, A. L'Huillier, M. Ferray, L. A. Lompré, and G. Mainfray. Multiple-harmonic generation in rare gases at high laser intensity. *Phys. Rev. A*, 39(11):5751–5761, 1989.

[297] L. Gallmann, C. Cirelli, and U. Keller. Attosecond Science: Recent Highlights and Future Trends. *Annu. Rev. Phys. Chem.*, 63(1):447–469, 2012.

[298] I. Orfanos, I. Makos, I. Liontos, E. Skantzakis, B. Förg, D. Charalambidis, and P. Tzallas. Attosecond pulse metrology. *APL Photonics*, 4(8):080901, 2019.

[299] G. Steinmeyer, D. Sutter, L. Gallmann, N. Matuschek, and U. Keller. Frontiers in ultrashort pulse generation: pushing the limits in linear and nonlinear optics. *Science*, 286(5444):1507–1512, 1999.

[300] M. Kitzler, N. Milosevic, A. Scrinzi, F. Krausz, and T. Brabec. Quantum theory of attosecond XUV pulse measurement by laser dressed photoionization. *Phys. Rev. Lett.*, 88(17):173904, 2002.

[301] E. Goulielmakis, M. Uiberacker, R. Kienberger, A. Baltuska, V. Yakovlev, A. Scrinzi, T. Westerwalbesloh, U. Kleineberg, U. Heinzmann, M. Drescher, and F. Krausz. Direct Measurement of Light Waves. *Science*, 305(5688):1267–1269, 2004.

[302] C. Cirelli, M. Sabbar, S. Heuser, R. Boge, M. Lucchini, L. Gallmann, and U. Keller. Energy-Dependent Photoemission Time Delays of Noble Gas Atoms Using Coincidence Attosecond Streaking. *IEEE J. Sel. Top. Quantum Electron.*, 21(5):1–7, 2015.

[303] W. A. Okell, T. Witting, D. Fabris, C. A. Arrell, J. Hengster, S. Ibrahimkutty, A. Seiler, M. Barthelmess, S. Stankov, D. Y. Lei, Y. Sonnefraud, M. Rahmani, T. Uphues, S. A. Maier, J. P. Marangos, and J. W. G. Tisch. Temporal broadening of attosecond photoelectron wavepackets from solid surfaces. *Optica*, 2(4):383–387, 2015.

[304] E. Goulielmakis, Z.-H. Loh, A. Wirth, R. Santra, N. Rohringer, V. S. Yakovlev, S. Zherebtsov, T. Pfeifer, A. M. Azzeer, M. F. Kling, S. R. Leone, and F. Krausz. Real-time observation of valence electron motion. *Nature*, 466(7307):739–743, 2010.

[305] M. Schultze, K. Ramasesha, C. Pemmaraju, S. Sato, D. Whitmore, A. Gandman, J. S. Prell, L. J. Borja, D. Prendergast, K. Yabana, D. M. Neumark, and S. R. Leone. Attosecond band-gap dynamics in silicon. *Science*, 346(6215):1348–1352, 2014.

[306] H. Mashiko, K. Oguri, T. Yamaguchi, A. Suda, and H. Gotoh. Petahertz optical drive with wide-bandgap semiconductor. *Nat. Phys.*, 12(8):741–745, 2016.

[307] M. Lucchini, S. A. Sato, A. Ludwig, J. Herrmann, M. Volkov, L. Kasmi, Y. Shinohara, K. Yabana, L. Gallmann, and U. Keller. Attosecond dynamical Franz-Keldysh effect in polycrystalline diamond. *Science*, 353(6302):916–919, 2016.

[308] A. Moulet, J. B. Bertrand, T. Klostermann, A. Guggenmos, N. Karpowicz, and E. Goulielmakis. Soft x-ray excitonics. *Science*, 357(6356):1134–1138, 2017.

[309] M. Volkov, S. A. Sato, F. Schlaepfer, L. Kasmi, N. Hartmann, M. Lucchini, L. Gallmann, A. Rubio, and U. Keller. Attosecond screening dynamics mediated by electron localization in transition metals. *Nat. Phys.*, 15(11):1145–1149, 2019.

[310] F. Siegrist, J. A. Gessner, M. Ossiander, C. Denker, Y.-P. Chang, M. C. Schröder, A. Guggenmos, Y. Cui, J. Walowski, U. Martens, U. Martens, J. K. Dewhurst, U. Kleineberg, M. Münzenberg, S. Sharma, and M. Schultze. Light-wave dynamic control of magnetism. *Nature*, 571(7764):240–244, 2019.

[311] K. F. Chang, M. Reduzzi, H. Wang, S. M. Poullain, Y. Kobayashi, L. Barreau, D. Prendergast, D. M. Neumark, and S. R. Leone. Revealing electronic state-switching at conical intersections in alkyl iodides by ultrafast XUV transient absorption spectroscopy. *arXiv preprint arXiv:2005.00668*, 2020.

[312] M. Lucchini, S. A. Sato, G. D. Lucarelli, B. Moio, G. Inzani, R. Borrego-Varillas, F. Frassetto, L. Poletto, H. Hübener, U. D. Giovannini, A. Rubio, and M. Nisoli. Unravelling the intertwined atomic and bulk nature of localised excitons by attosecond spectroscopy. *arXiv preprint: arXiv:2006.16008*, 2020.

[313] L. Seiffert, Q. Liu, S. Zherebtsov, A. Trabattoni, P. Rupp, M. C. Castrovilli, M. Galli, F. Süßmann, K. Wintersperger, J. Stierle, G. Sansone, L. Poletto, F. Frassetto, I. Halfpap, V. Mondes, C. Graf, E. Rühl, F. Krausz, M. Nisoli, T. Fennel, F. Calegari, and M. F. Kling. Attosecond chronoscopy of electron scattering in dielectric nanoparticles. *Nat. Phys.*, 13(8):766–770, 2017.

[314] Q. Liu, L. Seiffert, A. Trabattoni, M. C. Castrovilli, M. Galli, P. Rupp, F. Frassetto, L. Poletto, M. Nisoli, E. Rühl, F. Krausz, T. Fennel, S. Zherebtsov, F. Calegari, and M. F. Kling. Attosecond streaking metrology with isolated nanotargets. *J. Opt.*, 20(2):024002, 2018.

[315] Y. Mairesse, A. de Bohan, L. J. Frasinski, H. Merdji, L. C. Dinu, P. Monchicourt, P. Breger, M. Kovačev, R. Taïeb, B. Carré, H. G. Muller, P. Agostini, and P. Salières. Attosecond Synchronization of High-Harmonic Soft X-rays. *Science*, 302(5650):1540–1543, 2003.

[316] J. M. Dahlström, D. Guénot, K. Klünder, M. Gisselbrecht, J. Mauritsson, A. LHuillier, A. Maquet, and R. Taïeb. Theory of attosecond delays in laser-assisted photoionization. *Chem. Phys.*, 414:53–64, 2013.

[317] Z. Tao, C. Chen, T. Szilvási, M. Keller, M. Mavrikakis, H. Kapteyn, and M. Murnane. Direct time-domain observation of attosecond final-state lifetimes in photoemission from solids. *Science*, 353(6294):62–67, 2016.

[318] C. Chen, Z. Tao, A. Carr, P. Matyba, T. Szilvási, S. Emmerich, M. Piecuch, M. Keller, D. Zusin, S. Eich, et al. Distinguishing attosecond electron–electron scattering and screening in transition metals. *Proc. Natl. Acad. Sci. U.S.A.*, 114(27):E5300–E5307, 2017.

[319] S. Nandi, E. Plésiat, S. Zhong, A. Palacios, D. Busto, M. Isinger, L. Neoričić, C. L. Arnold, R. J. Squibb, R. Feifel, P. Decleva, A. L'Huillier, F. Martín, and M. Gisselbrecht. Attosecond timing of electron emission from a molecular shape resonance. 6(31):1–7.

[320] I. Jordan, M. Huppert, D. Rattenbacher, M. Peper, D. Jelovina, C. Perry, A. von Conta, A. Schild, and H. J. Wörner. Attosecond spectroscopy of liquid water. *Science*, 369(6506):974–979, 2020.

[321] L. J. Borja, M. Zürch, C. D. Pemmaraju, M. Schultze, K. Ramasesha, A. Gandman, J. S. Prell, D. Prendergast, D. M. Neumark, and S. R. Leone. Extreme ultraviolet transient absorption of solids from femtosecond to attosecond timescales. *J. Opt. Soc. Am. B*, 33(7):C57–C64, 2016.

[322] Y. Pertot, C. Schmidt, M. Matthews, A. Chauvet, M. Huppert, V. Svoboda, A. Von Conta, A. Tehlar, D. Baykusheva, J.-P. Wolf, et al. Time-resolved x-ray absorption spectroscopy with a water window high-harmonic source. *Science*, 355(6322):264–267, 2017.

[323] R. M. Karl, G. F. Mancini, J. L. Knobloch, T. D. Frazer, J. N. Hernandez-Charpak, B. Abad, D. F. Gardner, E. R. Shanblatt, M. Tanksalvala, C. L. Porter, et al. Full-field imaging of thermal and acoustic dynamics in an individual nanostructure using tabletop high harmonic beams. *Sci. Adv.*, 4(10):eaau4295, 2018.

[324] L. Young, K. Ueda, M. Gühr, P. H. Bucksbaum, M. Simon, S. Mukamel, N. Rohringer, K. C. Prince, C. Masciovecchio, M. Meyer, A. Rudenko, D. Rolles, C. Bostedt, M. Fuchs, D. A. Reis, R. Santra, H. Kapteyn, M. Murnane, H. Ibrahim, F. Légaré, M. Vrakking, M. Isinger, D. Kroon, M. Gisselbrecht, A. L'Huillier, H. J.

Wörner, and S. R. Leone. Roadmap of ultrafast x-ray atomic and molecular physics. *J. Phys. B*, 51(3):032003, 2018.

[325] J. Duris, S. Li, T. Driver, E. G. Champenois, J. P. MacArthur, A. A. Lutman, Z. Zhang, P. Rosenberger, J. W. Aldrich, R. Coffee, et al. Tunable isolated attosecond X-ray pulses with gigawatt peak power from a free-electron laser. *Nat. Photonics*, 14(1):30–36, 2020.

[326] P. K. Maroju, C. Grazioli, M. Di Fraia, M. Moioli, D. Ertel, H. Ahmadi, O. Plekan, P. Finetti, E. Allaria, L. Giannessi, et al. Attosecond pulse shaping using a seeded free-electron laser. *Nature*, 578(7795):386–391, 2020.

[327] S. Schulz, I. Grguraš, C. Behrens, H. Bromberger, J. T. Costello, M. Czwalinna, M. Felber, M. Hoffmann, M. Ilchen, H. Liu, et al. Femtosecond all-optical synchronization of an X-ray free-electron laser. *Nat. Commun.*, 6(1):1–11, 2015.

[328] N. Hartmann, G. Hartmann, R. Heider, M. Wagner, M. Ilchen, J. Buck, A. Lindahl, C. Benko, J. Grünert, J. Krzywinski, et al. Attosecond time–energy structure of X-ray free-electron laser pulses. *Nat. Photonics*, 12(4):215–220, 2018.

[329] H.-S. Kang and I. S. Ko. Attosecond XFEL for pump–probe experiments. *Nat. Photonics*, 14(1):7–8, 2020.

[330] C. Spielmann, N. H. Burnett, S. Sartania, R. Koppitsch, M. Schnürer, C. Kan, M. Lenzner, P. Wobrauschek, and F. Krausz. Generation of Coherent X-rays in the Water Window Using 5-Femtosecond Laser Pulses. *Science*, 278(5338):661–664, 1997.

[331] N. Ishii, K. Kaneshima, K. Kitano, T. Kanai, S. Watanabe, and J. Itatani. Carrier-envelope phase-dependent high harmonic generation in the water window using few-cycle infrared pulses. *Nat. Commun.*, 5(1):3331, 2014.

[332] G. J. Stein, P. D. Keathley, P. Krogen, H. Liang, J. P. Siqueira, C.-L. Chang, C.-J. Lai, K.-H. Hong, G. M. Laurent, and F. X. Kärtner. Water-window soft x-ray high-harmonic generation up to the nitrogen K-edge driven by a kHz, 2.1 μm OPCPA source. *J. Phys. B*, 49(15):155601, 2016.

[333] J. Pupeikis, P.-A. Chevreuil, N. Bigler, L. Gallmann, C. R. Phillips, and U. Keller. Water window soft x-ray source enabled by a 25W few-cycle 2.2 μm OPCPA at 100kHz. *Optica*, 7(2):168–171, 2020.

[334] S. L. Cousin, N. Di Palo, B. Buades, S. M. Teichmann, M. Reduzzi, M. Devetta, A. Kheifets, G. Sansone, and J. Biegert. Attosecond Streaking in the Water Window: A New Regime of Attosecond Pulse Characterization. *Phys. Rev. X*, 7(4):041030, 2017.

[335] R. Schoenlein, T. Elsaesser, K. Holldack, Z. Huang, H. Kapteyn, M. Murnane, and M. Woerner. Recent advances in ultrafast X-ray sources. *Philos. Trans. R. Soc. A*, 377(2145):20180384, 2019.

[336] M. Högner, V. Tosa, and I. Pupeza. Generation of isolated attosecond pulses with enhancement cavities - a theoretical study. *New J. Phys.*, 19(3):033040, 2017.

[337] M. Högner. HHGmax. `https://mhoegner.gitlab.io/hhgmax-homepage`. last accessed on 2021-05-01.

[338] H.-W. Sun, P.-C. Huang, Y.-H. Tzeng, J.-T. Huang, C. D. Lin, C. Jin, and M.-C. Chen. Extended phase matching of high harmonic generation by plasma-induced defocusing. *Optica*, 4(8):976–981, 2017.

[339] G. Tempea, M. Geissler, M. Schnürer, and T. Brabec. Self-Phase-Matched High Harmonic Generation. *Phys. Rev. Lett.*, 84(19):4329–4332, 2000.

[340] M. Schnürer, C. Spielmann, P. Wobrauschek, C. Streli, N. H. Burnett, C. Kan, K. Ferencz, R. Koppitsch, Z. Cheng, T. Brabec, and F. Krausz. Coherent 0.5-keV X-Ray Emission from Helium Driven by a Sub-10-fs Laser. *Phys. Rev. Lett.*, 80(15):3236–3239, 1998.

[341] E. Seres, J. Seres, F. Krausz, and C. Spielmann. Generation of coherent soft-X-ray radiation extending far beyond the titanium L edge. *Phys. Rev. Lett.*, 92(16):163002, 2004.

[342] J. Seres, E. Seres, A. J. Verhoef, G. Tempea, C. Streli, P. Wobrauschek, V. Yakovlev, A. Scrinzi, C. Spielmann, and F. Krausz. Laser technology: Source of coherent kiloelectronvolt X-rays. *Nature*, 433(7026):596, 2005.

[343] E. Seres, J. Seres, and C. Spielmann. X-ray absorption spectroscopy in the keV range with laser generated high harmonic radiation. *Appl. Phys. Lett.*, 89(18):181919, 2006.

[344] C.-J. Lai and F. X. Kärtner. The influence of plasma defocusing in high harmonic generation. *Opt. Express*, 19(23):22377–22387, 2011.

[345] C. Vozzi, M. Negro, F. Calegari, S. Stagira, K. Kovács, and V. Tosa. Phase-matching effects in the generation of high-energy photons by mid-infrared few-cycle laser pulses. *New J. Phys.*, 13(7):073003, 2011.

[346] M. Geissler, G. Tempea, and T. Brabec. Phase-matched high-order harmonic generation in the nonadiabatic limit. *Phys. Rev. A*, 62(3):033817, 2000.

[347] Y. Fu, K. Nishimura, R. Shao, A. Suda, K. Midorikawa, P. Lan, and E. J. Takahashi. High efficiency ultrafast water-window harmonic generation for single-shot soft X-ray spectroscopy. *Commun. Phys.*, 3(1):92, 2020.

[348] S. A. Maier. *Plasmonics: fundamentals and applications*. Springer Science & Business Media, 2007.

[349] M. I. Stockman, K. Kneipp, S. I. Bozhevolnyi, S. Saha, A. Dutta, J. Ndukaife, N. Kinsey, H. Reddy, U. Guler, V. M. Shalaev, et al. Roadmap on plasmonics. *J. Opt.*, 20(4):043001, 2018.

[350] M. I. Stockman. Nanoplasmonic sensing and detection. *Science*, 348(6232):287–288, 2015.

[351] R. J. Hermann and M. J. Gordon. Nanoscale Optical Microscopy and Spectroscopy Using Near-Field Probes. *Annu. Rev. Chem. Biomol. Eng.*, 9(1):365–387, 2018.

[352] J. Langer, D. Jimenez de Aberasturi, J. Aizpurua, R. A. Alvarez-Puebla, B. Auguié, J. J. Baumberg, G. C. Bazan, S. E. Bell, A. Boisen, A. G. Brolo, et al. Present and future of surface-enhanced Raman scattering. *ACS nano*, 14(1):28–117, 2019.

[353] K. Kneipp, Y. Wang, H. Kneipp, L. T. Perelman, I. Itzkan, R. R. Dasari, and M. S. Feld. Single molecule detection using surface-enhanced Raman scattering (SERS). *Phys. Rev. Lett.*, 78(9):1667, 1997.

[354] A. M. Gobin, M. H. Lee, N. J. Halas, W. D. James, R. A. Drezek, and J. L. West. Near-infrared resonant nanoshells for combined optical imaging and photothermal cancer therapy. *Nano Lett.*, 7(7):1929–1934, 2007.

[355] Z. Han and S. I. Bozhevolnyi. Radiation guiding with surface plasmon polaritons. *Rep. Prog. Phys.*, 76(1):016402, 2013.

[356] W. Cai and V. M. Shalaev. *Optical metamaterials*, volume 10. Springer, 2010.

[357] M. Stepanova and S. Dew. *Nanofabrication: Techniques and Principles*. Springer Vienna, 2014.

[358] A. Sarangan. 5 - Nanofabrication. In J. W. Haus, editor, *Fundamentals and Applications of Nanophotonics*, pages 149–184. Woodhead Publishing, 2016.

[359] C. Papadopoulos. *Nanofabrication: principles and applications*. Springer, 2016.

[360] M. F. Ciappina, J. A. Pérez-Hernández, A. S. Landsman, W. A. Okell, S. Zherebtsov, B. Förg, J. Schötz, L. Seiffert, T. Fennel, T. Shaaran, T. Zimmermann, A. Chacón, R. Guichard, A. Zaïr, J. W. G. Tisch, J. P. Marangos, T. Witting, A. Braun, S. A. Maier, L. Roso, M. Krüger, P. Hommelhoff, M. F. Kling, F. Krausz, and M. Lewenstein. Attosecond physics at the nanoscale. *Rep. Prog. Phys.*, 80(5):054401, 2017.

[361] R. Bormann, M. Gulde, A. Weismann, S. Yalunin, and C. Ropers. Tip-enhanced strong-field photoemission. *Phys. Rev. Lett.*, 105(14):147601, 2010.

[362] S. Zherebtsov, T. Fennel, J. Plenge, E. Antonsson, I. Znakovskaya, A. Wirth, O. Herrwerth, F. Süßmann, C. Peltz, I. Ahmad, S. A. Trushin, V. Pervak, S. Karsch, M. J. J. Vrakking, B. Langer, C. Graf, M. I. Stockman, F. Krausz, E. Rühl, and M. F. Kling. Controlled near-field enhanced electron acceleration from dielectric nanospheres with intense few-cycle laser fields. *Nat. Phys.*, 7(8):656–662, 2011.

[363] K. E. Echternkamp, G. Herink, S. V. Yalunin, K. Rademann, S. Schäfer, and C. Ropers. Strong-field photoemission in nanotip near-fields: from quiver to sub-cycle electron dynamics. *Appl. Phys. B*, 122(4):80, 2016.

[364] P. Dombi, Z. Pápa, J. Vogelsang, S. V. Yalunin, M. Sivis, G. Herink, S. Schäfer, P. Groß, C. Ropers, and C. Lienau. Strong-field nano-optics. *Rev. Mod. Phys.*, 92(2):025003, 2020.

[365] M. Müller, A. Paarmann, and R. Ernstorfer. Femtosecond electrons probing currents and atomic structure in nanomaterials. *Nat. Commun.*, 5(1):1–8, 2014.

[366] J. Vogelsang, G. Hergert, D. Wang, P. Groß, and C. Lienau. Observing charge separation in nanoantennas via ultrafast point-projection electron microscopy. *Light Sci. Appl.*, 7(1):1–8, 2018.

[367] A. Feist, G. Storeck, S. Schäfer, and C. Ropers. Structural dynamics probed by high-coherence electron pulses. *MRS Bulletin*, 43(7):504–511, 2018.

[368] D. Hoff, M. Krüger, L. Maisenbacher, A. M. Sayler, G. G. Paulus, and P. Hommelhoff. Tracing the phase of focused broadband laser pulses. *Nat. Phys.*, 13(10):947–951, 2017.

[369] A. H. Chin, O. G. Calderón, and J. Kono. Extreme midinfrared nonlinear optics in semiconductors. *Phys. Rev. Lett.*, 86(15):3292, 2001.

[370] S. Ghimire, A. D. DiChiara, E. Sistrunk, P. Agostini, L. F. DiMauro, and D. A. Reis. Observation of high-order harmonic generation in a bulk crystal. *Nat. Phys.*, 7(2):138–141, 2011.

[371] O. Schubert, M. Hohenleutner, F. Langer, B. Urbanek, C. Lange, U. Huttner, D. Golde, T. Meier, M. Kira, S. W. Koch, and R. Huber. Sub-cycle control of terahertz high-harmonic generation by dynamical Bloch oscillations. *Nat. Photonics*, 8(2):119–123, 2014.

[372] T. T. Luu, M. Garg, S. Y. Kruchinin, A. Moulet, M. T. Hassan, and E. Goulielmakis. Extreme ultraviolet high-harmonic spectroscopy of solids. *Nature*, 521(7553):498–502, 2015.

[373] S. Han, H. Kim, Y. W. Kim, Y.-J. Kim, S. Kim, I.-Y. Park, and S.-W. Kim. High-harmonic generation by field enhanced femtosecond pulses in metal-sapphire nanostructure. *Nat. Commun.*, 7(1):1–7, 2016.

[374] G. Vampa, B. G. Ghamsari, S. Siadat Mousavi, T. J. Hammond, A. Olivieri, E. Lisicka-Skrek, A. Y. Naumov, D. M. Villeneuve, A. Staudte, P. Berini, and P. B. Corkum. Plasmon-enhanced high-harmonic generation from silicon. *Nat. Phys.*, 13(7):659–662, 2017.

[375] H. Liu, C. Guo, G. Vampa, J. L. Zhang, T. Sarmiento, M. Xiao, P. H. Bucksbaum, J. Vučković, S. Fan, and D. A. Reis. Enhanced high-harmonic generation from an all-dielectric metasurface. *Nat. Phys.*, 14(10):1006–1010, 2018.

[376] M. Sivis, M. Taucer, G. Vampa, K. Johnston, A. Staudte, A. Y. Naumov, D. Villeneuve, C. Ropers, and P. Corkum. Tailored semiconductors for high-harmonic optoelectronics. *Science*, 357(6348):303–306, 2017.

[377] D. Gauthier, S. Kaassamani, D. Franz, R. Nicolas, J.-T. Gomes, L. Lavoute, D. Gaponov, S. Février, G. Jargot, M. Hanna, W. Boutu, and H. Merdji. Orbital angular momentum from semiconductor high-order harmonics. *Opt. Lett.*, 44(3):546, 2019.

[378] F. Krausz and M. I. Stockman. Attosecond metrology: from electron capture to future signal processing. *Nat. Photonics*, 8(3):205–213, 2014.

[379] W. P. Putnam, R. G. Hobbs, P. D. Keathley, K. K. Berggren, and F. X. Kärtner. Optical-field-controlled photoemission from plasmonic nanoparticles. *Nat. Phys.*, 13(4):335–339, 2017.

[380] Y. Yang, M. Turchetti, P. Vasireddy, W. P. Putnam, O. Karnbach, A. Nardi, F. X. Kärtner, K. K. Berggren, and P. D. Keathley. Light phase detection with on-chip petahertz electronic networks. *Nat. Commun.*, 11(1):3407, 2020.

[381] M. Ludwig, G. Aguirregabiria, F. Ritzkowsky, T. Rybka, D. C. Marinica, J. Aizpurua, A. G. Borisov, A. Leitenstorfer, and D. Brida. Sub-femtosecond electron transport in a nanoscale gap. *Nat. Phys.*, 16(3):341–345, 2019.

[382] M. I. Stockman, M. F. Kling, U. Kleineberg, and F. Krausz. Attosecond nanoplasmonic-field microscope. *Nat. Photonics*, 1(9):539–544, 2007.

[383] E. Skopalová, D. Lei, T. Witting, C. Arrell, F. Frank, Y. Sonnefraud, S. Maier, J. Tisch, and J. Marangos. Numerical simulation of attosecond nanoplasmonic streaking. *New J. Phys.*, 13(8):083003, 2011.

[384] F. Süßmann and M. F. Kling. Attosecond nanoplasmonic streaking of localized fields near metal nanospheres. *Phys. Rev. B*, 84(12):121406, 2011.

[385] A. G. Borisov, P. M. Echenique, and A. K. Kazansky. Attostreaking with metallic nano-objects. *New J. Phys.*, 14(2):023036, 2012.

[386] F. Kelkensberg, A. Koenderink, and M. Vrakking. Attosecond streaking in a nanoplasmonic field. *New J. Phys.*, 14(9):093034, 2012.

[387] J. S. Prell, L. J. Borja, D. M. Neumark, and S. R. Leone. Simulation of attosecond-resolved imaging of the plasmon electric field in metallic nanoparticles. *Ann. Phys.*, 525(1-2):151–161, 2013.

[388] M. Lupetti, J. Hengster, T. Uphues, and A. Scrinzi. Attosecond photoscopy of plasmonic excitations. *Phys. Rev. Lett.*, 113(11):113903, 2014.

[389] J. Li, E. Saydanzad, and U. Thumm. Retrieving plasmonic near-field information: A quantum-mechanical model for streaking photoelectron spectroscopy of gold nanospheres. *Phys. Rev. A*, 94(5):051401, 2016.

[390] L. Wimmer, G. Herink, D. R. Solli, S. V. Yalunin, K. Echternkamp, and C. Ropers. Terahertz control of nanotip photoemission. *Nat. Phys.*, 10(6):432–436, 2014.

[391] P. B. Johnson and R.-W. Christy. Optical constants of the noble metals. *Phys. Rev. B*, 6(12):4370, 1972.

[392] C. F. Bohren and D. R. Huffman. *Absorption and scattering of light by small particles*. John Wiley & Sons, 2008.

[393] S.-C. Lee. Dependent scattering of an obliquely incident plane wave by a collection of parallel cylinders. *J. Appl. Phys.*, 68(10):4952–4957, 1990.

[394] J.-P. Schäfer. *Implementierung und Anwendung analytischer und numerischer Verfahren zur Lösung der Maxwellgleichungen für die Untersuchung der Lichtausbreitung in biologischem Gewebe*. PhD thesis, Universität Ulm, 2011.

[395] J. Schaefer, S.-C. Lee, and A. Kienle. Calculation of the near fields for the scattering of electromagnetic waves by multiple infinite cylinders at perpendicular incidence. *J. Quant. Spectrosc. Radiat. Transfer*, 113(16):2113–2123, 2012.

[396] W. M. H. Sachtler, G. J. H. Dorgelo, and A. A. Holscher. The work function of gold. *Surf. Sci.*, 5(2):221–229, 1966.

[397] V. Kaufman and L. Minnhagen. Accurate ground-term combinations in Ne i. *J. Opt. Soc. Am. A*, 62(1):92–95, 1972.

[398] S. Neppl, R. Ernstorfer, A. L. Cavalieri, C. Lemell, G. Wachter, E. Magerl, E. M. Bothschafter, M. Jobst, M. Hofstetter, U. Kleineberg, J. V. Barth, D. Menzel, J. Burgdörfer, P. Feulner, F. Krausz, and R. Kienberger. Direct observation of electron propagation and dielectric screening on the atomic length scale. *Nature*, 517(7534):342–346, 2015.

[399] M. Lucchini, L. Castiglioni, L. Kasmi, P. Kliuiev, A. Ludwig, M. Greif, J. Osterwalder, M. Hengsberger, L. Gallmann, and U. Keller. Light-Matter Interaction at Surfaces in the Spatiotemporal Limit of Macroscopic Models. *Phys. Rev. Lett.*, 115(13):137401, 2015.

[400] S. Zherebtsov, A. Wirth, T. Uphues, I. Znakovskaya, O. Herrwerth, J. Gagnon, M. Korbman, V. S. Yakovlev, M. J. J. Vrakking, M. Drescher, and M. F. Kling. Attosecond imaging of XUV-induced atomic photoemission and Auger decay in strong laser fields. *J. Phys. B*, 44(10):105601, 2011.

[401] C.-T. Chiang, M. Huth, A. Trützschler, M. Kiel, F. O. Schumann, J. Kirschner, and W. Widdra. Boosting laboratory photoelectron spectroscopy by megahertz high-order harmonics. *New J. Phys.*, 17(1):013035, 2015.

[402] A. K. Mills, S. Zhdanovich, A. Sheyerman, G. Levy, A. Damascelli, and D. J. Jones. An XUV source using a femtosecond enhancement cavity for photoemission spectroscopy. In *Advances in X-ray Free-Electron Lasers Instrumentation III*, volume 9512, page 95121I. International Society for Optics and Photonics, 2015.

[403] M. Högner, V. Tosa, and I. Pupeza. Generation of isolated attosecond pulses with enhancement cavities—a theoretical study. *New J. Phys.*, 19(3):033040, 2017.

[404] C. Corder, P. Zhao, J. Bakalis, X. Li, M. D. Kershis, A. R. Muraca, M. G. White, and T. K. Allison. Ultrafast extreme ultraviolet photoemission without space charge. *Struct. Dyn.*, 5(5):054301, 2018.

[405] T. Saule, S. Heinrich, J. Schötz, N. Lilienfein, M. Högner, O. deVries, M. Plötner, J. Weitenberg, D. Esser, J. Schulte, P. Russbueldt, J. Limpert, M. F. Kling, U. Kleineberg, and I. Pupeza. High-flux ultrafast extreme-ultraviolet photoemission spectroscopy at 18.4 MHz pulse repetition rate. *Nat. Commun.*, 10(1):458, 2019.

[406] S. H. Chew, F. Süßmann, C. Späth, A. Wirth, J. Schmidt, S. Zherebtsov, A. Guggenmos, A. Oelsner, N. Weber, J. Kapaldo, A. Gliserin, M. I. Stockman, M. F. Kling, and U. Kleineberg. Time-of-flight-photoelectron emission microscopy on plasmonic structures using attosecond extreme ultraviolet pulses. *Appl. Phys. Lett.*, 100(5):051904, 2012.

[407] J. Schötz, L. Seiffert, A. Maliakkal, J. Blöchl, D. Zimin, P. Rosenberger, B. Bergues, P. Hommelhoff, F. Krausz, T. Fennel, and M. F. Kling. Onset of space-charge effects in strong-field photocurrents from nanometric needle tips. *arXiv preprints arXiv:2106.00503*, 2021.

[408] S. V. Yalunin, M. Gulde, and C. Ropers. Strong-field photoemission from surfaces: Theoretical approaches. *Phys. Rev. B*, 84(19):195426, 2011.

[409] M. E. Swanwick, P. D. Keathley, A. Fallahi, P. R. Krogen, G. Laurent, J. Moses, F. X. Kärtner, and L. F. Velásquez-García. Nanostructured Ultrafast Silicon-Tip Optical Field-Emitter Arrays. *Nano Lett.*, 14(9):5035–5043, 2014.

[410] G. N. Derry, M. E. Kern, and E. H. Worth. Recommended values of clean metal surface work functions. *J. Vac. Sci. Technol. A*, 33(6):060801, 2015.

[411] M. Bionta, S. J. Weber, I. Blum, J. Mauchain, B. Chatel, and B. Chalopin. Wavelength and shape dependent strong-field photoemission from silver nanotips. *New J. Phys.*, 18(10):103010, 2016.

[412] F. Süßmann, L. Seiffert, S. Zherebtsov, V. Mondes, J. Stierle, M. Arbeiter, J. Plenge, P. Rupp, C. Peltz, A. Kessel, et al. Field propagation-induced directionality of carrier-envelope phase-controlled photoemission from nanospheres. *Nat. Commun.*, 6(1):1–9, 2015.

[413] Q. Liu, L. Seiffert, F. Sußmann, S. Zherebtsov, J. Passig, A. Kessel, S. A. Trushin, N. G. Kling, I. Ben-Itzhak, V. Mondes, et al. Ionization-Induced Subcycle Metallization of Nanoparticles in Few-Cycle Pulses. *ACS Photonics*, 7(11):3207–3215, 2020.

[414] J. P. Long, B. S. Itchkawitz, and M. N. Kabler. Photoelectron spectroscopy of laser-excited surfaces by synchrotron radiation. *J. Opt. Soc. Am. B*, 13(1):201–208, 1996.

[415] S. Hellmann, K. Rossnagel, M. Marczynski-Bühlow, and L. Kipp. Vacuum space-charge effects in solid-state photoemission. *Phys. Rev. B*, 79(3):035402, 2009.

[416] M. Ludwig, A. K. Kazansky, G. Aguirregabiria, D. C. Marinica, M. Falk, A. Leitenstorfer, D. Brida, J. Aizpurua, and A. G. Borisov. Active control of ultrafast electron dynamics in plasmonic gaps using an applied bias. *Phys. Rev. B.*, 101(24):241412, 2020.

[417] R. D. Muino, D. Sanchez-Portal, V. M. Silkin, E. V. Chulkov, and P. M. Echenique. Surface Chemistry Special Feature: Time-dependent electron phenomena at surfaces. *Proc. Natl. Acad. Sci. U.S.A.*, 108(3):971–976, 2011.

[418] A. Borisov, D. Sánchez-Portal, R. Díez Muiño, and P. M. Echenique. Building up the screening below the femtosecond scale. *Chem. Phys. Lett.*, 387(1):95–100, 2004.

[419] H. Yanagisawa, S. Schnepp, C. Hafner, M. Hengsberger, D. E. Kim, M. F. Kling, A. Landsman, L. Gallmann, and J. Osterwalder. Delayed electron emission in strong-field driven tunnelling from a metallic nanotip in the multi-electron regime. *Sci. Rep.*, 6(1):35877, 2016.

[420] H. Yanagisawa, M. Hengsberger, D. Leuenberger, M. Klöckner, C. Hafner, T. Greber, and J. Osterwalder. Energy Distribution Curves of Ultrafast Laser-Induced

Field Emission and Their Implications for Electron Dynamics. *Phys. Rev. Lett.*, 107(8):087601, 2011.

[421] H. Yanagisawa, T. Greber, C. Hafner, and J. Osterwalder. Laser-induced field emission from a tungsten nanotip by circularly polarized femtosecond laser pulses. *Phys. Rev. B*, 101(4):045406, 2020.

[422] I. H. Malitson. Interspecimen Comparison of the Refractive Index of Fused Silica∗,. *J. Opt. Soc. Am.*, 55(10):1205–1209, 1965.

[423] S. Thomas, G. Wachter, C. Lemell, J. Burgdörfer, and P. Hommelhoff. Large optical field enhancement for nanotips with large opening angles. *New J. Phys.*, 17(6):063010, 2015.

[424] N. Pfullmann, C. Waltermann, M. Noack, S. Rausch, T. Nagy, C. Reinhardt, M. Kovačev, V. Knittel, R. Bratschitsch, D. Akemeier, A. Hütten, A. Leitenstorfer, and U. Morgner. Bow-tie nano-antenna assisted generation of extreme ultraviolet radiation. *New J. Phys.*, 15(9):093027, 2013.

[425] L. Liu, P. Peng, A. Hu, G. Zou, W. Duley, and Y. N. Zhou. Highly localized heat generation by femtosecond laser induced plasmon excitation in Ag nanowires. *Appl. Phys. Lett.*, 102(7):073107, 2013.

[426] A. M. Summers, A. S. Ramm, G. Paneru, M. F. Kling, B. N. Flanders, and C. A. Trallero-Herrero. Optical damage threshold of Au nanowires in strong femtosecond laser fields. *Opt. Express*, 22(4):4235–4246, 2014.

[427] M. Förster, T. Paschen, M. Krüger, C. Lemell, G. Wachter, F. Libisch, T. Madlener, J. Burgdörfer, and P. Hommelhoff. Two-Color Coherent Control of Femtosecond Above-Threshold Photoemission from a Tungsten Nanotip. *Phys. Rev. Lett.*, 117(21):217601, 2016.

[428] G. Herink, L. Wimmer, and C. Ropers. Field emission at terahertz frequencies: AC-tunneling and ultrafast carrier dynamics. *New J. Phys.*, 16(12):123005, 2014.

[429] H. H. Radamson, H. Zhu, Z. Wu, X. He, H. Lin, J. Liu, J. Xiang, Z. Kong, W. Xiong, J. Li, H. Cui, J. Gao, H. Yang, Y. Du, B. Xu, B. Li, X. Zhao, J. Yu, Y. Dong, and G. Wang. State of the art and future perspectives in advanced CMOS technology. *Nanomaterials*, 10(8):1555, 2020.

[430] S. Venugopalan. *From poisson to silicon-advancing compact SPICE models for ic design*. PhD thesis, UC Berkeley, 2013.

[431] S. Sinha, G. Yeric, V. Chandra, B. Cline, and Y. Cao. Exploring sub-20nm FinFET design with predictive technology models. In *DAC Design Automation Conference 2012*, pages 283–288. IEEE, 2012.

[432] A. Bindal and S. Hamedi-Hagh. *Silicon Nanowire Transistors*. Springer International Publishing, 2016.

[433] M. A. Kastner. The single-electron transistor. *Rev. Mod. Phys.*, 64(3):849–858, 1992.

[434] R. Patel, Y. Agrawal, and R. Parekh. Single-electron transistor: review in perspective of theory, modelling, design and fabrication. *Microsyst. Technol.*, 25(5):1863–1875, 2020.

[435] M. Garg and K. Kern. Attosecond coherent manipulation of electrons in tunneling microscopy. *Science*, 367(6476):411–415, 2020.

[436] H. Yanagisawa, C. Hafner, P. Doná, M. Klöckner, D. Leuenberger, T. Greber, J. Osterwalder, and M. Hengsberger. Laser-induced field emission from a tungsten tip: Optical control of emission sites and the emission process. *Phys. Rev. B*, 81(11):115429, 2010.

[437] P. Steinleitner, P. Merkl, P. Nagler, J. Mornhinweg, C. Schuller, T. Korn, A. Chernikov, and R. Huber. Direct observation of ultrafast exciton formation in a monolayer of WSe2. *Nano Lett.*, 17(3):1455–1460, 2017.